Finite Element Modelling of Reinforced Concrete Beams with Corroded Shear Reinforcement

By

Sebastien Bernard

A thesis

Presented to the University of Ottawa in fulfillment of the requirements for Master of Applied Science in Civil Engineering

Department of Civil Engineering

University of Ottawa

Ottawa, Canada

K1N 6N5

August 2013

Abstract

This thesis presents a finite element (FE) modelling approach investigating the effects of corroded shear reinforcement on the capacity and behaviour of shear critical reinforced concrete (RC) beams. Shear reinforcement was modelled using a "locally smeared" approach, wherein the shear reinforcement is smeared within a series of plane-stress concrete elements at the specific stirrup location. This was done with the objective of incorporating both the reduction in cross-sectional area due to corrosion and the corresponding expansion of corrosion products build up. Corrosion damage was incorporated through equivalent straining induced by the corrosion build up on the affected surrounding concrete where the concrete cover was treated as a thick-wall cylinder subjected to internal pressure. Strains were introduced in the FE model using fictitious smeared horizontal pre-stressing steel, with a compressive pre-straining level related to the degree of corrosion penetration of the reinforcement. The FE modelling approach was first validated against published test data of shear critical RC beams with and without stirrup corrosion. The proposed modelling approach successfully reproduces the load deformation response as well as the failure mode and cracking patterns of the published experimental tests.

Upon validation of the FE model, the work was extended to a parametric analysis of important shear design variables, such as the shear span-to-depth ratio, beam width and stirrup spacing The FE analyses were carried out for three increasing levels of corrosion (low, moderate and high) applied to affected stirrups within the critical section of the beams and based on steel mass loss (10%, 30% and 50%, respectively).

In general, the results show a reduction in load carrying capacity accompanied by a softening of the load-deformation curves with each increasing level of corrosion. In most of the cases, a reduction in deflection associated to peak loads was also observed for moderate and high levels of corrosion. The impact of the various parameters was studied with respect to strength and deformation, as well as crack angle and mid-height horizontal strain. This was done in an effort to compare FE values to those provided by the CSA A23.3 design equations. The CSA A23.3 shear design equations were compared against FE analysis data in terms of residual shear strength estimation and individual component contributions to shear resistance (i.e., concrete and steel). The comparisons revealed an over conservative estimation for both strength and concrete contributions and an overestimation of the steel contribution. This divergence was attributed to a transition in shear behaviour within the critical section. Based on the progression of the concrete compressive struts with increasing corrosion and predicted crack angle, it was found that stresses in affected sections are redistributed towards adjacent undamaged material. The shear resistance mechanism generally transitioned from typical beam behaviour towards an arching-dominated one. Finally, based on important findings from the literature and the work conducted within this research, important considerations for assessment practice are suggested.

Acknowledgements

I would first like to thank my thesis supervisor Dr. Beatriz Martín-Pérez for all of her support throughout my studies. Her dedication toward the advancement in engineering is tremendous and is reflected by her work ethics. She was always there to help me in the hardest times of this research project, and provided useful encouragement which helped me successfully complete my master's studies.

I would also like to thank the members of the thesis defence committee, Dr. Elena Dragomirescu from the University of Ottawa and Dr. Ted Sherwood from the University of Carlton for their insights, advice and valuable comments about this research in general.

I would like to acknowledge the Natural Sciences and Engineering Research Council of Canada (NSERC), the Queen Elizabeth II Graduate Scholarship in Science and Technology, and the University of Ottawa Admission Scholarship for their financial support.

Finally, and most importantly, I would like to thank my friends and family for their support and understanding throughout my studies. Your countless words of encouragement helped me focus on the task at hand and complete my work more efficiently. I dedicate this work to my parents who I have had to turn to countless times, for guidance and help during my studies. Without them, it would not have been possible accomplish what I have done and become the person I am today.

Table of Contents

Abstract ..... **ii**

Acknowledgements ..... **iv**

List of Tables ..... **viii**

List of Figures ..... **ix**

Notation ..... **xvii**

Chapter 1 Introduction **21**

1.1 Background 21
1.2 Scope of Research 22
1.3 Organization of Thesis 23

Chapter 2 Literature Review **25**

2.1 Corrosion of Reinforcing Steel 25
2.2 Corrosion-Induced Damage 28
2.3 Effects of Corrosion on Resistance to Shear 30
2.4 Modelling Corrosion in RC Beams 35
2.5 Current Assessment Practices 39
2.6 Need for Research 47

Chapter 3 Finite Element Modelling **51**

3.1 Introduction 51
3.2 Finite Element Types and Mesh 51
3.3 Modelling Corrosion-Induced Damage 56
3.4 Material Models 59
3.4.1 Concrete Constitutive Behaviour 60
3.4.2 Steel Constitutive Behaviour 66
3.4.3 Shear Behaviour 67
3.5 Summary of Modelling Methodology 76

Chapter 4 Finite Element Model Validation ... 78
4.1 Introduction ... 78
4.2 Modeling Shear-Critical RC Beams ... 78
4.3 Test Specimens ... 80
4.4 Validation of LS model ... 82
4.5 Validation of Corroded Beams ... 84
4.5.1 Low Corrosion ... 85
4.5.2 Moderate Corrosion ... 87
4.5.3 High Corrosion ... 88
4.6 Validation Summary ... 90
Chapter 5 Parametric Analysis ... 91
5.1 Introduction ... 91
5.2 Parametric Testing Grid ... 92
5.2.1 Oregon Beams ... 92
5.2.2 Toronto Beams ... 94
5.3 Shear Capacity ... 103
5.3.1 Oregon Beams ... 104
5.3.2 Toronto Beams ... 105
5.3.3 Shear Strength Summary ... 126
5.4 Flexural Rigidity ... 128
5.4.1 Oregon Beams ... 128
5.4.2 Toronto Beams ... 130
5.4.3 Flexural Rigidity Summary ... 135
5.5 Ductility ... 135
5.5.1 Oregon Beams ... 135
5.5.2 Toronto Beams ... 136
5.5.3 Ductility Summary ... 139
Chapter 6 Discussion of Parametric Results ... 141
6.1 Introduction ... 141
6.2 Shear Resistance in CSA A23.3-04 ... 141
6.3 Oregon Beams ... 143
6.4 Shear Span-to-Depth Ratio (*a/d*) ... 145

6.4.1 Effects on Strength and Deformability ... 145
6.4.2 Effects on θ and ε_x ... 150
6.4.3 *a/d* Summary ... 154
6.5 Beam Width (b_w) ... 157
6.5.1 Effects on Strength and Deformability ... 157
6.5.2 Effects on θ and ε_x ... 160
6.5.3 Beam Width Summary ... 165
6.6 Stirrup Spacing (s) ... 166
6.6.1 Effects on Strength and Deformability ... 166
6.6.2 Effects on θ and ε_x ... 168
6.6.3 Stirrup Spacing Summary ... 169
6.7 Effects of Corrosion on Shear Resistance ... 170
6.7.1 Oregon Beams ... 171
6.7.2 Toronto Beams ... 174
6.7.3 Shear Resistance Summary ... 193
6.8 Comparison to Design Equations ... 194
6.8.1 Total Shear Strength ... 194
6.8.2 Steel Contribution to Shear Strength ... 196
6.8.3 Concrete Contribution to Shear Strength ... 198
6.8.4 Design Equation Summary ... 200
6.9 Comparison to Experimental Tests ... 201
6.10 Assessment Considerations ... 202
Chapter 7 Concluding Remarks ... 206
7.1 Conclusions ... 206
7.2 Future Work ... 210
References ... 211

List of Tables

Table 2.1: Corrosion products and relative densities (reproduced from (Higgins et al. 2003) 26

Table 4.1: Recorded Area and Mass Loss (Higgins et al. 2003)... 82

Table 4.2: Pre-strains inducing cracking.. 85

Table 5.1: Oregon Beam Properties.. 93

Table 5.2: Toronto Beams Series A Properties.. 97

Table 5.3: Toronto Beams Series B Properties.. 98

Table 5.4: Toronto Beams Series C Properties.. 99

Table 5.5: Corrosion Details and Strains (only span series 1 and 2) 102

Table 5.6: Corrosion Details and Strains (for span series 3)... 103

List of Figures

Figure 2.1: a) General corrosion mechanism (reproduced from Dekoster et al. (2003)), b) Pitting corrosion mechanism (reproduced from Stewart (2009))......................... 27

Figure 2.2: a) Effects of corrosion on steel constitutive properties due to pitting (Coronelli and Gambarova 2004) b) The effects of corrosion on steel properties (Cairns et al. 2005).. 29

Figure 2.3: a) Residual bond-slip relationship (Coronelli and Gambarova 2004) b) Evolution of maximum bond strength based on corrosion penetration (Coronelli and Gambarova 2004).. 30

Figure 2.4: Decrease in concrete compressive strength (reproduced from Coronelli and Gambarova 2004).. 39

Figure 3.1: Concrete plane-stress element (reproduced from VecTor2 manual)................... 53

Figure 3.2: Typical finite element mesh 55

Figure 3.3:(a) Corrosion products build up; (b) Concrete cover treated as a thick-wall cylinder subjected to internal pressure (reproduced from Martín-Pérez 1999) ... 57

Figure 3.4: Corroding stirrup legs in RC beam... 58

Figure 3.5: Oregon beam test setup and FEM grid of test setup... 60

Figure 3.6: Effect of peak strain on load-deformation using Hognestad's parabola 62

Figure 3.7: Effects of peak strain on the load deformation using Popovic's model............... 62

Figure 3.8: Effect of tangential modulus on load deformation (Hognestad's) 63

Figure 3.9: Effect of tangential modulus on load deformation (Popovic's) 63

Figure 3.10: Peak stress effect on load deformation (Popovic's Model) 64

Figure 3.11: Effect of concrete tensile strength on load deformation using Hognestad's model for concrete in compression 65

Figure 3.12: Effects of concrete tensile strength on load deformation using Popovic's model for concrete in compression 66

Figure 3.13: The effect of yield strength on the load-deformation response 67

Figure 3.14: The effect of limiting the shear stress at a crack (MCFT) 70

Figure 3.15: The effect of analytical model choice (MCFT vs. DSFM) on the load deformation curve 71

Figure 3.16: The effect of crack width limit on the load-deformation response using MCFT 72

Figure 3.17: The effect of crack width limit on the load-deformation response using DSFM 73

Figure 3.18: Effect of tension softening model on load deformation (MCFT) 74

Figure 3.19: Effect of tension softening model on load deformation (DSFM) 75

Figure 3.20: The effect of dowel action on load deformation 76

Figure 4.1: Test setup from Higgins et al. (2011) 81

Figure 4.2: Load-deformation curves from Higgins et al. (2003) 81

Figure 4.3: Load-deformation for control beam and LS model 83

Figure 4.4:(a) Cracking generated by finite element model at failure; (b) Cracking map at failure for test specimen (Higgins et al. 2003) 83

Figure 4.5: Validation of FEM for low levels of corrosion 86

Figure 4.6: a) Cracking prediction for low corrosion without pre-straining, b) Crack map for beam 10RB (Higgins et al. 2003).. 86

Figure 4.7: a) Cracking prediction for low corrosion with pre-straining, b) Crack map for beam 10RB (Higgins et al. 2003).. 86

Figure 4.8: Validation of FEM for moderate levels of corrosion 87

Figure 4.9: a) Cracking prediction for moderate corrosion without pre-straining, b) Crack map for beam 10RC (Higgins et al. 2003) 88

Figure 4.10 a) Cracking prediction for moderate corrosion with pre-straining, b) Crack map for beam 10RC (Higgins et al. 2003) 88

Figure 4.11 Validation of FEM for high levels of corrosion 89

Figure 4.12 a) Cracking prediction for high corrosion without pre-straining, b) Crack map for beam 10RD (Higgins et al. 2003) 89

Figure 4.13 a) Cracking prediction for high corrosion with pre-straining, b) Crack map for beam 10RD (Higgins et al. 2003)... 89

Figure 5.1: Toronto beams sectional properties (Vecchio and Shim 2004)........................... 96

Figure 5.2: Test setup and span lengths used in Toronto beams (Vecchio and Shim 2004) . 96

Figure 5.3: Toronto Beam FE mesh 100

Figure 5.4: Shear strength prediction of the FEM against experimental data...................... 101

Figure 5.5: Load deformation response of Oregon beams obtained from FE analysis........ 104

Figure 5.6: Strength degradation for beam 10R.. 105

Figure 5.7: Load deformation response for specimen A1 106

Figure 5.8: Cracking pattern at ultimate load for specimen A1 107

Figure 5.9: Load deformation response for specimen A2 108

Figure 5.10: Cracking pattern at ultimate load for specimen A2 109

Figure 5.11: Load deformation response for specimen A3 110

Figure 5.12: Crack pattern at ultimate load for specimen A3 111

Figure 5.13: Shear strength degradation for series A 112

Figure 5.14: Load-deformation response for specimens B1 113

Figure 5.15: Cracking pattern at ultimate load for specimens B1 114

Figure 5.16: Load-deformation response for specimen B2 115

Figure 5.17: Cracking pattern at ultimate load for specimen B2 116

Figure 5.18: Load-deformation response for specimen B3 117

Figure 5.19: Cracking pattern at ultimate load for specimen B3 118

Figure 5.20: Shear strength degradation for series B 119

Figure 5.21: Load-deformation for specimen C1 120

Figure 5.22: Cracking pattern at ultimate load for specimen C1 121

Figure 5.23: Load-deformation response for specimen C2 122

Figure 5.24: Cracking pattern at ultimate load for specimen C2 123

Figure 5.25: Load-deformation response for specimen C3 124

Figure 5.26: Cracking pattern at ultimate load for specimen C3 125

Figure 5.27: Shear strength degradation for series C 126

Figure 5.28: Stiffness-curvature relationship obtained from experimental data of Oregon beams 129

Figure 5.29: Stiffness-curvature relationship for Oregon beams without accounting for corrosion-induced cracking in FE 129

Figure 5.30: Stiffness-curvature relationship for Oregon beams accounting for corrosion-induced cracking in FE 130

Figure 5.31: Stiffness-curvature relationships for series A 132

Figure 5.32: Stiffness-curvature relationship for series B 133

Figure 5.33: Stiffness-curvature relationship for series C 134

Figure 5.34: Corrosion effects on relative peak deflection for Oregon beams 136

Figure 5.35: Decrease of mid-span deflection at ultimate load for series A 137

Figure 5.36: Decrease of mid-span deflection at ultimate load for series B 138

Figure 5.37: Decrease of mid-span deflection at ultimate load for series C 139

Figure 6.1: Effects of mass loss on crack angle for Oregon beam 10R 144

Figure 6.2: Effects of mass loss on mid-height horizontal strain for Oregon Beam 10R 145

Figure 6.3: Effects of *a/d* and mass loss on strength and deformability 147

Figure 6.4: The effects of *a/d* on the relative strength 148

Figure 6.5: The effects of *a/d* on deformability 149

Figure 6.6: Effects of *a/d* and mass loss on cracking angle ... 151

Figure 6.7: Effects of *a/d* on crack angle ... 152

Figure 6.8: Effects of *a/d* on mid-height horizontal strain ... 153

Figure 6.9: Effects of *a/d* on average mid-height strain within d_v of point load ... 154

Figure 6.10: Effects of b_w and mass loss on strength and deformability ... 158

Figure 6.11: Effect of beam width on shear strength ... 159

Figure 6.12: Effects of beam width on deformability ... 160

Figure 6.13: Effects of b_w on cracking angles ... 161

Figure 6.14: Effects of beam width on crack angle ... 162

Figure 6.15: Effects of b_w and mass loss on mid-height horizontal strain (FE and MCFT) 164

Figure 6.16: Effects of beam width on mid-height horizontal strain ... 166

Figure 6.17: Effects of stirrup spacing (s) on shear strength ... 167

Figure 6.18: Effects of stirrup spacing (s) on deformability ... 168

Figure 6.19: Effects of stirrup spacing (s) on crack angle ... 169

Figure 6.20: Effects of stirrup spacing (s) on mid-height horizontal strain ... 169

Figure 6.21: Contributions of concrete and steel to shear resistance and crack angle for Oregon beams ... 172

Figure 6.22: Principal compressive stress orientation at ultimate load for Oregon beams .. 173

Figure 6.23: Contributions of concrete and steel to shear resistance for Series A1 ... 177

Figure 6.24: Contributions of concrete and steel to shear resistance for Series A2............ 177

Figure 6.25: Contributions of concrete and steel to shear resistance for Series A3............ 177

Figure 6.26: Principal concrete compressive stress orientation for Series A1..................... 178

Figure 6.27: Principal concrete compressive stress orientation for Series A2..................... 179

Figure 6.28: Principal concrete compressive stress orientation for Series A3..................... 180

Figure 6.29: Contributions of concrete and steel to shear resistance for Series B1............ 183

Figure 6.30: Contributions of concrete and steel to shear resistance for Series B2............ 183

Figure 6.31: Contributions of concrete and steel to shear resistance for Series B3............ 183

Figure 6.32: Principal concrete compressive stress orientation for Series B1 184

Figure 6.33: Principal concrete compressive stress orientation of Series B2 185

Figure 6.34: Principal concrete compressive stress orientation of Series B3 186

Figure 6.35: Contributions of concrete and steel to shear resistance for Series C1............ 189

Figure 6.36: Contributions of concrete and steel to shear resistance for Series C2............ 189

Figure 6.37: Contributions of concrete and steel to shear resistance for Series C3............ 189

Figure 6.38: Principal concrete compressive stress orientation of Series C1 190

Figure 6.39: Principal concrete compressive stress orientation of Series C2 191

Figure 6.40: Principal concrete compressive stress orientation of Series C3 192

Figure 6.41: Code equation estimation for shear strength (general method, cl. 11.3.6.4) ... 195

Figure 6.42: Code estimation of shear strength (simplified method, Cl. 11.3.6.3)............. 196

Figure 6.43: Estimation of steel contribution to shear strength (general method, cl. 11.3.6.4) 197

Figure 6.44: Estimation of steel contribution to shear strength (Simplified method, Cl. 11.3.6.3).. 198

Figure 6.45: Estimation of concrete contribution to shear resistance (general method, cl. 11.3.6.4).. 199

Figure 6.46: Estimation of concrete contribution to shear resistance (simplified method, Cl. 11.3.6.3).. 200

Figure 6.47: Comparison of experimental and numerical data of effects of mass loss on shear strength 202

Notation

a_g	=	aggregate size
a	=	shear span
A_s	=	flexural reinforcement
A_s'	=	compression reinforcement
$A_s(t)$	=	area at time t
A_{sloss}	=	loss of steel area
A_v	=	shear reinforcement area
A_v'	=	expanded shear reinforcement area
b_w	=	beam width
b_e	=	effective beam width
c	=	concrete cover thickness
d	=	depth to flexural reinforcement
d'	=	expanded area diameter
d_o	=	initial bar diameter
d_v	=	shear depth
E_c	=	concrete tangential modulus
$\overline{E}_{c1}$	=	concrete secant moduli in tension
$\overline{E}_{c2}$	=	concrete secant moduli in compression
ε_o	=	concrete peak compressive strain
E_{sec}	=	concrete secant modulus
E_{si}	=	modulus of elasticity of steel in the i^{th} direction
F	=	Faraday's constant
f_c'	=	concrete compressive strength

f_{c1} = concrete principle tensile stress

f_{c2} = concrete principle compression stress

f_{sx} = steel stress in the x direction

$f_{sxyield}$ = yield strength in the x direction

f_{sy} = steel stress in the y direction

$f_{syyield}$ = yield strength in the y direction

f_t' = concrete tensile strength

f_u = specific ultimate strength

f_{uo} = initial ultimate strength

f_y = specific yield strength

f_{yo} = initial yield strength

f_{yv} = yield strength of shear reinforcement

$\overline{G}_c$ = concrete shear modulus

I = moment of inertia

I_{cor} = corrosion current

i_{cor} = corrosion current density

L = span length

m = Mass loss

M = atomic mass

M_a = applied moment

M_{loss} = steel mass loss

n = curve fitting parameter

P = applied load

Q_{corr} = average section loss

s = stirrup spacing

s_{ze}	=	equivalent crack spacing
t	=	time after initiation
V	=	applied shear
V_c	=	concrete contribution to shear strength
v_{ci}	=	shear stress transferred by aggregate interlock
V_n	=	Total nominal shear resistance
V_s	=	steel contribution to shear strength
w	=	crack width
x_{cor}	=	corrosion penetration
z	=	valence
α_1	=	empirical parameter for loss in strain
α_u	=	empirical parameter for loss in ultimate strength
α_y	=	empirical parameter for loss in yield strength
β	=	modified compression field theory factor for concrete
δ	=	mid span deflection
δ_{cor}	=	deflection associated to a corroded member
δ_{val}	=	deflection associated to an uncorroded member
ε_{c2}	=	concrete principle compression strain
ε_{ci}	=	concrete compressive strain
ε_{cor}	=	strain induced by corrosion within thick wall cylinder
$\bar{\varepsilon}_{cor}$	=	average corrosion induced strain
ε_{cx}	=	net concrete axial strain in the x direction
ε_{cy}	=	net concrete axial strain in the y direction
ε_o	=	concrete peak compressive strain

ε_u = specific ultimate strain

ε_{uo} = initial ultimate strain

ε_x = mid height horizontal strain

ε_x^t = total axial strain in the x direction

ε_x^s = strain due to shear slip in the x direction

ε_y = specific yield strain

ε_y = total axial strain in the y direction

ε_{yo} = initial yield strain

ε_y^s = strain due to shear slip in the y direction

γ_{cxy} = net concrete shear strain

γ^s_{xy} = shear strain due to slip

γ_{xy} = total shear strain

μ = density ratio

π = pi constant

θ = crack angle

ρ_i = percentage of steel incorporated

ρ_s = flexural reinforcement ratio

ρ_v = shear reinforcement ratio

ρ_x = steel reinforcement ratio in the x direction

ρ_y = steel reinforcement ratio in the y direction

Chapter 1 Introduction

1.1 Background

A large part of the Canadian reinforced concrete (RC) infrastructure is in a suffering state. The combination of harsh winter conditions and de-icing salts to prevent ice buildups on our roads make for a difficult environment for RC structures. Amongst all the sources of degradation, the most severe source that affects RC structures is reinforcement corrosion (Berto et al. 2008; Kobayashi 2006). Large amounts of RC structures show signs of degradation as a direct cause of reinforcement corrosion. This directly impacts the budgeting of provincial and Canadian governments. Resources are required to either retrofit or replace damaged structures before the end of their design life, especially in essential and lifeline structures (Gohier 2011) (Delcan 2011). These resources should be spent on improving the state of the infrastructure instead of simply maintaining it. In the United States, it is estimated that 15% of the RC structures are affected by corrosion degradation with a rehabilitation cost increasing by approximately $ 8.3 billion per year (H. Koch et al. 2002). In Canada is it estimated that currently a total of $74 billion would be needed to just restore deteriorated RC infrastructure back to its original state (NSERC 2012). Not only is this a reoccurring problem when budgeting, but it is also of great importance to the safety of the public.

The trigger for the onset of reinforcing steel corrosion is the accumulation of chlorides at the steel level above a threshold value. Once corrosion is initiated, the steel bars' cross-sectional area start to decrease, and an accumulation of corrosion buildup around the rebar eventually leads to cracking, spalling, and/or delamination of the concrete cover, and to the eventual decommission of the structure. Although this process is naturally slow, it is can be greatly accelerated when contaminants such as chloride (e.g. de-icing salts) are present (Dekoster et al. 2003). The time to initiation of corrosion is influenced by the level of contaminants present as well as the protection measures to the reinforcement. These protection techniques, such as increase in concrete cover and epoxy coatings, have been only implemented as a solution from lessons learned from the past. The combination of the harsh Canadian winter, repetitive freeze-thaw actions with a lack in detailing, poor construction practices, and little to no maintenance work, have led to the degradation of RC structures with either costly rehabilitation implemented or not reaching the end of the intended design life (Zhao et al. (2009)).

1.2 Scope of Research

Practicing engineers require the proper tools to assess the effect of reinforcing steel corrosion on the capacity and behavior of RC structures. This is essential for the proper assessment of the health condition and safety of affected structures. Practicing engineers face questions like the following when assessing a RC structure affected by corrosion:

- Is this structure safe for use?
- What is the maximum load that it can carry?
- What are the effects on serviceability?
- Is it up to the current standards for safety?
- If not, what type of work is required to make this structure safe?
- What maintenance work is required?
- Will this structure reach the end of its design life?

Although some of these questions are meant to be addressed primarily from a durability standpoint, the residual strength estimation is essential for the proper assessment of safety.

One of the tools that can be used for these types of assessment is finite element (FE) modeling. Although FE modeling is more often used in research applications, it can provide useful information in stress distribution, capacity and ductility estimation, which can all assist in drawing proper conclusions on the state of the structure. Previous research has been performed on multiple structural elements such as columns and beams to understand the effects of corrosion on the behavior and strength of these elements. The effects on concrete confinement (Hanjari et al. 2013), axial capacity, ductility (Torres-Acosta et al. 2004), cracking, flexural strength and bond strength (Berto et al. 2008; Hanjari et al. 2013; Val and Chernin 2012) have been studied in an effort to develop adequate models to be incorporated in analysis. However, little information is available on the effects of stirrup corrosion on the capacity of RC beams, and how this can be accounted in FE modeling when faced with such a situation.

This research aims at modelling shear reinforcement corrosion and ensuing concrete cover cracking within a two-dimensional plane-stress FE model when analyzing shear critical RC beams. As an ultimate goal, it aims at determining the effects of shear reinforcement corrosion on the capacity and behavior of RC beams to provide a prescriptive guide for the shear assessment of such structures.

1.3 Organization of Thesis

Chapter two will present a literature review on relevant topics of the research. First, the corrosion mechanism and degradation process is presented in detail. An overview of available literature on the effects of corrosion on different mechanical properties for both concrete and steel is then introduced. A review of the effects of steel corrosion on the shear capacity of RC beams, and the FE model implication in modeling corrosion cracking, as well as corrosion effects is also presented. Finally an overview of available documentation on the assessment of corroded RC structures is reviewed and the need for further research is outlined.

Chapter three presents the FE model, elements and meshing. It also presents the cracking model introduced within the FE framework to simulate corrosion-induced cover cracking. The sensitivity of the finite model is studied, and the effects of the different modeling parameters on the predicted strength, ductility, stiffness and overall behavior of the RC beams are presented.

Chapter four contains the validation of the proposed FE model. First, the experimental data from the literature is presented, and then the model is tested against the published data. Once confidence in the model is confirmed, the effects of corrosion are introduced. The model is then tested against published data for two corrosion scenarios: one accounting for the reduction in cross-sectional area without the concrete cracking model and another in which the corrosion-cracking model is accounted for.

Chapter five presents a parametric analysis of the problem using FE simulation. It introduces the important selected design parameters and presents the results. It present the collected data from FE model and highlights important behavioural characteristic.

The Chapter six discusses the results from the parametric analysis. It presents the data with respect to important shear design parameter in an effort to identify important trends, and explains behavioural patterns within the data. This chapter also looks at CSA A23.3 design equations precision in estimating residual strength. Furthermore, the FE data is analyzed for modified compression field theory parameters such as crack angle and mid height horizontal strains. These parameters are compared to estimated values from code equations. The chapter is concluded by highlighting important assessment consideration.

Finally, Chapter seven presents the thesis conclusions and identifies important future considerations for research.

Chapter 2 Literature Review

This chapter provides background information on the problem of corrosion of reinforcing steel and corrosion-induced damage in RC structures. A review of the literature on the effects of steel corrosion on the resistance of flexural members to shear and on modelling of the associated mechanics is also presented. This chapter also provides a summary of current practices on the assessment of corrosion-damaged RC structures, and it identifies research needs based on the state-of-the-art.

2.1 Corrosion of Reinforcing Steel

Corrosion of steel embedded in concrete can be initiated either by carbonation of the concrete cover, which lowers its natural high alkalinity to a pH of 9, or by chloride contamination of the concrete cover above a threshold concentration. Once steel corrosion is triggered, it is an electrochemical process which requires of an anode, cathode, an electrolyte (concrete pore solution) and an electrical conductor (reinforcing steel itself). The anodic reaction, in which iron is oxidized, is given by:

$$Fe \rightarrow Fe^{2+} + 2e^{-} \qquad 2.1$$

For RC exposed to the atmosphere, oxygen reduction is the most common cathodic reaction, which proceeds by consuming the electrons released at the anode:

$$O_2 + 2H_2O + 4e^{-} \rightarrow 4OH^{-} \qquad 2.2$$

Ferrous ions combine with the hydroxide to form ferrous hydroxide according to:

$$Fe^{2+} + 2H_2O \rightarrow Fe(OH)_2 + 2H^{+} \qquad 2.3$$

Upon further oxidation, ferrous hydroxide can convert into other corrosion by-products, as listed in Table 2.1. Depending on the rust by-product, the density can range from 2 to 4 times less than that of the original steel (Guzman et al. 2011) .

Table 2.1: Corrosion products and relative densities (reproduced from (Higgins et al. 2003)

Iron oxide	Molar volume, cm^3/mol	Fe Volume Ratio (μ)	Characteristic colour
α-Fe	7.1	1	Metallic silver
Fe_3O_4, magnetite	14.9	2.10	Black
α-Fe_2O_3, hematite	15.2	2.14	Earthy red or black
α-FeOOH, goethite	21.3	3.00	Blackish, yellowish, or reddish brown
γ-FeOOH, lepidocrocite	22.4	2.15	Deep red to reddish brown
β-FeOOH, akaganeite	27.5	3.87	Brown to rusty brown
$Fe(OH)_2$	26.4	3.72	Pale green or white

Two types of steel corrosion are commonly observed in RC structures (see Figure 2.1). The first type is a localized corrosion called pitting (Figure 2.1 (b)). This is most commonly observed at locations where large cracks typically form. Contaminants, such as chlorides, penetrate through these cracks, exposing the rebar to a higher concentration of contaminants at these specific locations and initiating a greater mass loss (Stewart 2009). The second type is general corrosion (Figure 2.1 (a)), in which the reinforcing bar corrodes uniformly throughout. This type of corrosion is more frequently observed when carbonation of the concrete cover takes place, but it can also be caused by chloride-induced corrosion when several pits coalesce together.

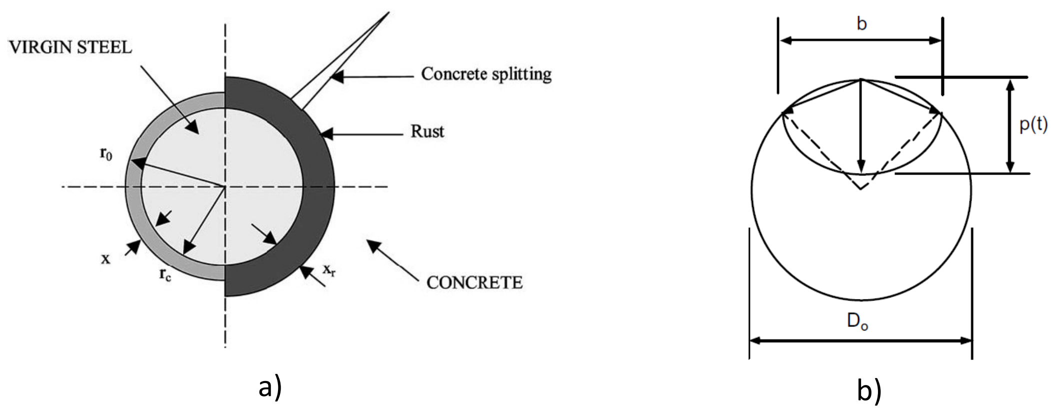

Figure 2.1: a) General corrosion mechanism (reproduced from Dekoster et al. (2003)), b) Pitting corrosion mechanism (reproduced from Stewart (2009))

The amount of reinforcing steel loss due to corrosion is governed by Faraday's law:

$$m = \frac{M\, I_{cor}\, t}{zF} \qquad 2.4$$

where m is the mass loss (g), M is the atomic mass (55.85 g/mol for iron), I_{cor} is the corrosion current (A), t is the time during which corrosion has taken place (s), z is the valence (z = 2 for iron oxidation), and F is Faraday's constant (96,487 C/mol). Based on Faraday's law, the remaining cross-sectional area of the reinforcing bar at time t, $A_s(t)$, can be determined from:

$$A_s(t) = \frac{\pi\left(d_o - 0.0232 i_{cor}\, t\right)^2}{4} \qquad 2.5$$

where $A_s(t)$ is given in mm^2, d_o is the original rebar diameter (mm), i_{cor} is the corrosion current density (μA/cm^2), and t is the time during which corrosion has proceeded (years). Corrosion currents densities encountered in the field range from 0.1 μA/cm^2 for low corrosion environments to 1 μA/cm^2 in highly corrosive areas, and they vary throughout the service life of an affected RC structure (Dekoster et al. 2003).

2.2 Corrosion-Induced Damage

Once the corrosion process is initiated, corrosion products start accumulating around the reinforcing steel. Since their density is much lower than the original steel, the ensuing volume expansion exerts a pressure against the concrete cover, which eventually cracks once its tensile resistance is exceeded, leading to longitudinal cracking and/or spalling/delamination of the cover. In addition to cover cracking, reinforcing steel corrosion can also affect the mechanical behaviour of RC by:

- reducing the steel cross-sectional area;
- decreasing the steel ductility; and
- reducing the bond action between the steel and the concrete.

Depending on the type and location of damage within a specific element (e.g., which steel reinforcement is corroding), the overall behavior of the RC member might be affected in different ways, such as:

- decrease in member stiffness (as a result of cracking, and loss in available material);
- reduction in load carrying capacity;
- decrease in the ability to deform (i.e., a shift to less ductile behaviour);
- redistribution of stresses; and
- change in failure mechanism (e.g., from flexural to shear failure).

It is important to recognize that reinforcing steel corrosion is a time-dependent process, and the measurement of the corrosion rate i_{cor} only reflects the state of the RC member at the time of the measurement. This information is key in properly assessing the health and safety of affected structures at any stage within their service lives.

Experimental studies of the mechanical behaviour of corroded steel have shown that steel undergoes a change in behaviour under uniaxial loads, with a reduction in yield strength and deformation capacity (see Figure 2.2). It has been observed that pitting affects the steel's ductility, while uniform corrosion affects both yield and ultimate strengths in addition to ductility.

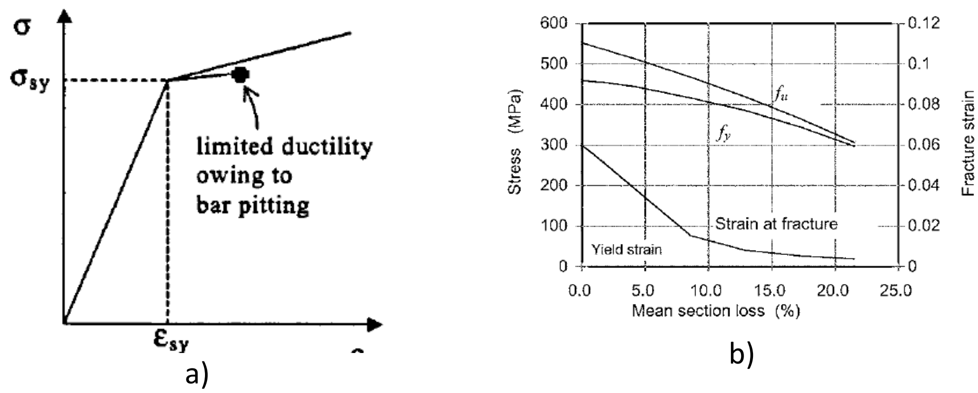

Figure 2.2: a) Effects of corrosion on steel constitutive properties due to pitting (Coronelli and Gambarova 2004) b) The effects of corrosion on steel properties (Cairns et al. 2005)

In order to account for these effects, Cairns et al. (2005) proposed the following equations to adjust the steel properties based on the level of corrosion:

$$f_y = \left(1.0 - \alpha_y \cdot Q_{corr}\right) f_{y0} \tag{2.6}$$

$$f_u = \left(1.0 - \alpha_u \cdot Q_{corr}\right) f_{u0} \tag{2.7}$$

$$\varepsilon_u = \left(1.0 - \alpha_1 \cdot Q_{corr}\right) \varepsilon_0 \tag{2.8}$$

where f_y, f_u and ε_u are respectively the yield stress, ultimate stress, and ultimate strain, f_{y0}, f_{u0} and ε_0 represent the initial values of yield strength, ultimate strength and ultimate elongation, respectively, Q_{corr} is the average section loss expressed as percentage of original section, and α_y, α_u and α_1 are empirical parameters. Values for α_y and α_u range between 0 and 0.015, while values for α_1 have been reported to be within 0 and 0.039 (Cairns et al. 2005).

The decrease of bond action between steel and concrete has been mostly attributed to the decrease in lug size and a reduction in confinement due to concrete cracking. Although there is an increase in strength in early stages of corrosion, as shown in Figure 2.3, the effect quickly reverses once cracking begins.

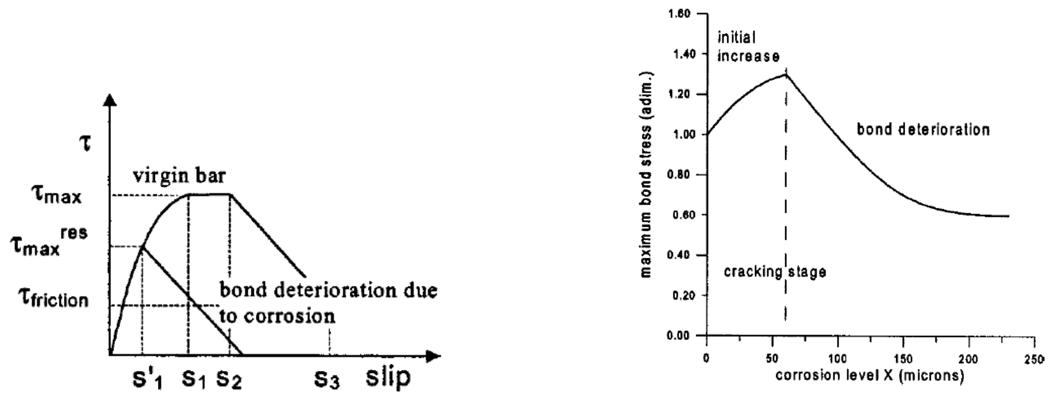

a) b)

Figure 2.3: a) Residual bond-slip relationship (Coronelli and Gambarova 2004) b) Evolution of maximum bond strength based on corrosion penetration (Coronelli and Gambarova 2004)

Proposed bond-slip models that account for corrosion-induced damage reduce the maximum bond strength based on the corrosion level (Figure 2.3 (b)). At low levels of corrosion, bond strength actually increases due to the initial increase in bar diameter leading to higher level of friction between both materials. As soon as the surrounding concrete begins to crack, the bond strength quickly decreases.

2.3 Effects of Corrosion on Resistance to Shear

A number of studies have been performed on the effect of reinforcing steel corrosion on RC flexural members (Coronelli and Gambarova 2004); (Yamamoto et al. 2011); (Azam and Soudki 2012), with three important conclusions being:

- a reduction in load carrying capacity;
- a softer response; and
- an increase in deflection (when flexural steel is properly anchored).

The general consensus within the research community attributes this change in response mainly to the degradation of bond properties. It is important to note that, while examining the effects of corrosion on flexurally dominant beams, a change in failure mechanism was often observed. In some cases, the expected excessive deflection, flexural steel yielding and eventual concrete crushing in flexural failure mechanisms were replaced by sudden failure with no warning signs (Coronelli and Gambarova 2004). This is an important factor to consider as the typical design requirement seeks to provide warning signs when a member is overloaded in order to ensure public safety. Therefore, this could create an increased safety risk in corroded members.

When a shift from flexural failure to shear failure has been observed (especially when 2.5 < shear span-to-depth ratio < 5) ((Coronelli and Gambarova 2004), this change in failure mode has been attributed to:

- excessive cracking near anchorage zones;
- loss in available concrete (spalling or delamination of cover);
- loss in shear reinforcing steel available area; and
- excessive slip in flexural reinforcement (due to loss of bond).

Only in the past decade has there has been an increase in research on the shear behavior of RC elements affected by corrosion of reinforcing steel. In an effort to quantify the effects of corrosion on shear strength, experimental testing specifically designed to determine the cause and effects of this phenomenon have been explored (Higgins et al. (2003), Suffern et al. (2010), Wang et al. (2011), Azam and Soudki (2012), Azam and Soudki (2013)).

In an early attempt, Cairns (1995) developed an analysis procedure in determining residual strength of beams affected by reinforcement corrosion. His procedure is aimed at determining the strength of members with de-bonded flexural properly anchored reinforcement. A simplified analysis in combination with the semi empirical procedure of the BS 8110 (1985) is used to estimate shear strength. He formulates his approach by considering that shear stresses need to be resisted by the bonded section of the beams. This procedure was specifically developed to estimate residual capacity for beams with major deterioration, or for cases where repairs are require completely remove concrete cover in an effort to expose longitudinal reinforcement for maintenance. It is tested against experimental work and a series of beams were specially developed to test the precision of this procedure. This was achieved by artificially removing the cover and exposing the flexural reinforcement prior to testing. Provided that the bars are properly anchored at the ends, experimental data show that a loss of strength of only 10% is to be expected. In some cases, when beams were designed to be shear-dominant, the exposure of flexural reinforcement increased the capacity of the beams.

Higgins et al. (2003) tested a series of shear-critical RC beams using accelerated corrosion on the shear reinforcement. Three series of rectangular section beams were tested at different levels of accelerated corrosion. The series consist of beams with the same sectional design but having three different stirrup spacing (203 mm, 254 mm and 303 mm) within the test span. These beams are 600 mm in height and 254 mm in width. They all have a clear span of 2,438 mm and underwent 4-point loading, yielding a shear span-to-depth ratio a/d of 2.04. The beams were cast with a salt rich concrete and underwent accelerated corrosion with levels of corrosion ranging from 13.6 to 33.8% average mass loss of the stirrups. The data from the series with stirrup spacing of 254 mm was further analyzed through FE modeling (Miller et al. 2011). The general findings were a reduction in shear strength, stiffness and deformability. Reduction of load carrying capacity was observed with increasing corrosion in all cases, with an associated reduction in ultimate deflections.

Similar to Higgins et al. (2003), Suffern et al. (2010) tested a series of 9 shear critical beams in which the shear reinforcement was subjected to accelerated corrosion. The shear span-to-depth ratio of these beams was 1.0, 1.5 and 2.0. The specimens had a height of 350 mm and a width of 125 mm. In each of the specimens, they noted a decrease in shear strength with respect to the control (no corrosion) counterpart. The strength degradation was more significant for smaller a/d ratios. An important finding was that the shear capacities of the corroded beams were in fact lower than that of a beam without shear reinforcement, indicating that simply neglecting the steel contribution to the shear strength in corroded specimens would in fact overestimate the capacity. This indicates the importance of considering cracking effects on the concrete when estimating the residual capacity of a corroded member. The authors also reported relatively uniform mass loss along the length of each leg of the stirrups.

Zhao et al. (2009) proposed a design procedure for the shear strength of corroded RC beams. In this publication, the work from previous authors was reviewed. The authors developed an empirical relationship using the degradation phenomenon to determine residual strength of RC beams. The empirical equation suggests simply using the original shear strength of a member but reducing it to a residual value based on the level of damage imposed on the section. This reduction was developed using a statistical regression of published data.

Wang et al. (2011) studied the effects of partially un-bonded flexural reinforcement on the shear capacity of RC beams. The beams were designed to fail in shear, and accelerated corrosion was induced along different lengths of the flexural reinforcement. Three degrees of corrosion were selected: fully un-bonded, 10% in average weight loss, and 25 % in average weight loss. Two shear span-to-depth ratios were chosen: 2 and 3. The beams were tested using a four-point loading scheme, where only the mid span loading points were modified to create the different shear span-to-depth ratios. The main observations found were an increase in strength and ductility at low levels corrosion, a large decrease in strength and ductility at high corrosion levels, and an abrupt change in failure mode. Larger un-bonded lengths of flexural reinforcement due to corrosion yielded lower relative strength in every case.

Juarez et al. (2011) tested a series of beams using accelerated corrosion on the stirrups. They tested two series of beams with shear span-to-depth ratios of 2, each having 150-mm and 200-mm stirrup spacing, respectively. The specimens were corroded to 3 different levels of mass loss. The results show a change in cracking patterns at failure indicating a change in shear mechanism. A change from rather uniform cracking for control specimens to localized cracking at higher levels of corrosion resulted in a reduction if deformability and strength. The measured shear strength was compared to the shear strength estimated according to ACI 318-08 (2008), in which only reductions in the stirrup cross section were applied in the calculations. In almost every case, the shear capacity was overestimated when the average area loss was used in the calculations. However, if only critical cross-sectional area losses were applied, the predictions led to conservative estimates. This highlights the importance of properly accounting for corrosion-induced damage in assessment calculations.

Azam and Soudki (2012) looked at the performance of shear critical beams with corroded longitudinal steel reinforcement. A total of 8 specimens measuring 350 mm in depth by 150 mm in width, with a clear span of 1,400 mm, were tested under 3-point loading (a/d = 1.7). Some of the specimens were reinforced in shear, some were not. With the exception of the control specimens, the beams underwent accelerated corrosion on their flexural reinforcement at mid span. The main conclusion from the study was that the load transfer mechanism changed from a combination of beam and arch action to pure arch action in the corroded beams, where the longitudinal flexural steel was properly anchored. Corrosion of the longitudinal steel at mid span also changed the cracking pattern of the beams under loading. The specimens did not experience shear cracking when corrosion was present. Rather, the shear stresses were transferred through compression struts. This change in load paths resulted in the splitting of the struts, instead of the shear crack extending to the compression zone and the beam failing in a shear-compression manner. The change in stress distribution within the disturbed region actually led to an increase in the load carrying capacity for the specimens without any stirrups, while the beams with stirrups did not show this increase. The beams with stirrups, however, did have an increase in deformability relative to its control counterpart. An analytical procedure was proposed by Azam and Soudki (2012) which adapts the CSA A23.3-04 (2004) strut-and-tie model to account for the effects of corrosion of the longitudinal ties. This is done by simply applying a reduction in the area of the longitudinal steel based on corrosion damage of these elements.

Azam and Soudki (2013) extended their work to study the effects of properly anchored corroded longitudinal reinforcement on shear-critical RC slender beams. In this study, a total of 10 beams were tested in a very similar format as their 2012 study. Two series of beams were tested, one without stirrups and the other including them. The beams were 350 mm by 150 mm with a span of 2,400 mm and were tested under 3-point loading (a/d = 3). Accelerated corrosion was applied on the longitudinal reinforcement up to three different levels of damage: 0%, 2.5%, 5.0% and 7.5% of mass loss. The general finding from this work is that corrosion of properly anchored longitudinal steel changed the load transfer mechanism to a pure arch action, increasing the load carrying capacity of the beam. Whereas the control un-corroded specimens failed by diagonal tension, the corroded beams without stirrups failed by anchorage failure and those with stirrups failed by yielding of the longitudinal steel. With an increasing level of corrosion, an increase in ductility of the beams was observed. An analytical procedure was also provided in this work. It uses the strut-and tie model from CSA A23.3-04 (2004) by incorporating the effects of bond loss of the longitudinal reinforcement (tied arch analysis). The effect of corrosion is simply incorporated by reducing the available area of the longitudinal steel.

Khan et al. (2013) tested 26 year old beams subject to a controlled environment, which simulated a coastal salt rich scenario. These beams were 280 mm in height by 150 mm in width and were tested under 3 point loading up to failure. Based on the loading setup, the specimens had a/d ratios of 2.33. A reduction both in terms of strength and ductility was observed compared to the control specimen.

2.4 Modelling Corrosion in RC Beams

Most of the attempts to estimate residual strength in RC members affected by corrosion are based on the application of existing design capacity equations, in which material and geometric properties are modified to reflect the level of attained deterioration. Higgins et al. (2011) calculated the residual shear strength of the RC beams tested in Higgins and Farrow (2010) by using the equations provided in the ACI code and the AASHTO LRFD bridge design specifications, the latter being based on the Modified Compression Field Theory, on which the CSA A23.3 (2004) is also developed. The authors incorporated corrosion effects in these equations by reducing the beams width and effective depth due to spalling of the concrete cover, and by reducing the cross-sectional area of affected stirrups. The loss in steel cross-sectional area was introduced by using both an average loss and actual minimum stirrup area measured on completion of the experimental tests. Both approaches provided conservative estimates compared to experimental results, although the use of average loss of stirrup area correlated better with the measured values. Higgins et al. (2010) also used the

Strut-and-Tie Method to estimate residual shear capacity. Corrosion-induced damage was incorporated into the model by reducing the tension tie areas, to reflect stirrup area loss, and by decreasing the strut widths, to reflect concrete cover spalling. The Strut-and-Tie Method proved to be a simple tool to assess the residual shear strength of affected beams with a low shear span-to-depth ratio.

Azam and Soudki (2012, 2013) also used the CSA 23.3-04 strut-and-tie procedure to model shear-critical deep and slender beams. Corrosion effects were incorporated in both models by reducing the area of available longitudinal steel. When analyzing slender beams, the authors incorporated an arching mechanism as observed in their experimental work. In both cases, the residual strength of the corroded specimens estimated from the strut-and-tie model was in good agreement with experimental data, with estimates being around 20% lower than experimental values. These beams however did not have damage to their stirrups, which adds a level of uncertainty caused by the increase in cracking of the strut type elements.

Khan et al. (2013) investigated the precision of the ACI 318-08 (2008) and Eurocode 2 shear design equations in estimating the residual strength of their test specimens. In addition, they also looked at the use of the strut-and-tie model from the ACI 318-08 (2008). In the case of the design equations, both the ACI 318-08 (2008) and Eurocode 2 greatly under estimated strength, while the strut-and-tie method slightly over estimated strength. In each case, corrosion effects were accounted for by reducing the steel area and concrete section.

Nevertheless, it has been found that sectional analysis of corroded flexural members with modified material and geometric properties to account for corrosion effects might not give realistic predictions, because both corrosion-induced concrete cracking and bond loss lead to nonlinear behaviour of these members (Coronelli and Gambarova 2004). Corrosion also triggers behavioral change where stress paths are altered to avoid and compensate for damaged areas, which makes it very difficult to predict behaviour simply based on reduction in available material. It is for this reason that finite element modelling of the effect of corrosion on structural behaviour of RC flexural members is a better tool to capture and simulate the observed corrosion-induced phenomena.

Higgins et al. (2003) extended their experimental work to 3-D finite element modelling, in which reduction in the area of the stirrups and concrete cover, based on visible damage, was applied (Potisuk et al. 2011). The analysis used a smeared cracking model for concrete and assumed perfect bond between reinforcing steel and concrete. In general, they found that the finite element analysis was able to capture the observed behaviour in their experimental tests. Conducting what-if scenarios using their finite element model, Potisuk et al. (2011) found that applying a maximum localized stirrup area loss can result in a significant decrease in shear strength when the location of maximum section loss occurs close to a major shear crack. The authors also studied the effect of partially de-bonding stirrups from the surrounding concrete by only connecting to the concrete elements the two end nodes of the truss elements representing the stirrups. The combination of removing concrete cover elements due to spalling, de-bonding stirrups and decreasing stirrups cross-sectional area up to 50% led to a reduction in strength of 33%.

Dekoster et al. (2003) investigated the effects of corrosion on bond properties. A FE model was proposed and tested against experimental results for both general and pitting corrosion. In each case, corrosion was treated separately in the FE model and incorporated as separate elements at the steel concrete interface. These elements mimic the presence of corrosion by reducing their properties to small but non-zero values. The corrosion elements effects were studied with respect to an increase in corrosion element thickness and compared to the section loss only model. Two types of modeling strategies were investigated in this work, the damaged approach and the elastic plastic approach. The elastic-plastic method is based on smeared crack approach and uses limit state criterions for compression and traction of concrete, while the damage model is a history based analysis where the damage from previous loading stages is considered for strength calculation at a present stage. In general, good agreement with the test data was found.

Corronelli and Gambarova (2004) used nonlinear finite element analysis to study the effects of steel corrosion in RC beams. The authors accounted for corrosion-induced damage in their analyses by reducing the geometry of both concrete and steel, and by modifying the constitutive material relationships for concrete, reinforcing steel and bond. The methodology was tested against flexural dominant beams data from Rodriguez et al. (1995). In general, the FE analyses provided acceptable estimation of residual strength of the beams against which it was tested. Although shear failure was not obtained in the analyses, Rodriguez et al. (1995) reported reversal shift of failure from flexural to shear in beams with a larger flexural steel ratio and attributed this change in failure to stirrup pitting.

Maaddawy et al. (2005) proposed an analytical procedure in estimating residual strength of RC members. This was specifically designed for under reinforced members affected by corrosion of the flexural reinforcement. The procedure uses mostly sectional analysis (plane sections remain plane) but incorporates the effects of residual bond on strength and cracking behaviour. The beam is separated into elements based on the average crack spacing, and then the average stress and strain values within the length of a crack spacing is used for strength and deflection calculations. There was generally good agreement between test data and the FE results.

In a similar fashion, Kallias and Rafiq (2010) investigated the structural response of RC beams using 2D nonlinear FE analysis. The experimental data from the Rodriguez et al. (1995) and Du et al. (2007) was used for this work. The effects of corrosion deterioration were introduced in their analyses by reducing the geometry of both concrete and steel, and by modifying the constitutive material relationships for concrete, reinforcing steel and bond properties. In general, good agreement was found between the FE results and the test data in terms of load deflection characteristics. The effect on both serviceability and ultimate limit states was investigated. For the ultimate limit state, the loss in strength was attributed to the loss in steel and concrete area because of corrosion damage. When corrosion was accounted for in compression longitudinal steel, an overall softening response was observed with increasing levels of corrosion. For the serviceability limit state, the response was generally unaffected between cases of localised and general bond loss. Neglecting the effects of corrosion on the concrete cover in the compression zone led to an overestimation of residual capacity.

It is worth noting that several analytical models have also been proposed to simulate corrosion-induced cracking of the concrete cover. These models are based on the assumption that the concrete cover is analogous to a thick-wall cylinder subjected to the internal pressure caused by the accumulation of corrosion products around the reinforcing (Chemin and Val 2010; Hanjari et al. 2011). This internal pressure generates radial (compressive) and tangential (tensile) stresses in the concrete cover. The pressure distribution within the concrete around the bar is a function of the distance from the concrete-steel interface. Once the tensile capacity of the concrete cover is reached, cracking is initiated. The effects of corrosion-induced cracking on the concrete strength has been applied in FE analysis of beams (Corronelli and Gamarova 2004; Kallias and Rafiq 2010), wherein a compression softening model (Vecchio and Collins 1986) was applied by introducing out of plane deformation caused by cracking in the compression zones (see Figure 2.4). The out of plane strain is simply calculated based on the increase in sectional width, which is analogous to the expansion mechanism of the corroding reinforcement.

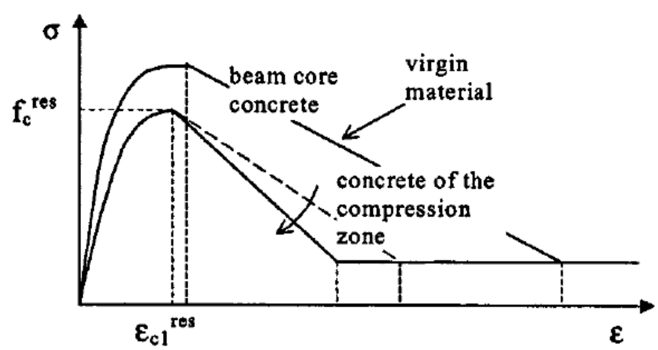

Figure 2.4: Decrease in concrete compressive strength (reproduced from Coronelli and Gambarova 2004)

2.5 Current Assessment Practices

In the Canadian engineering community, few documents (CSA S6 (2006) and OSIM (2008)) exist to help engineers in the assessment of corroded RC structures. The documentation available on assessment of affected structures mostly serves to educate users and provide general guidelines. These documents only provide basic information, requiring the engineer to use judgement to a great extent. In general, there are three steps to successfully complete an assessment of a damaged structure. The first step consists of inspecting the structure, in which data is collected to get an indication on the material and structural state. The second step is the assessment of the structure, in which the data collected from the previous step is analyzed and organised to determine its structural integrity. Finally, the information is transferred back to the client with recommendations in the form of a detailed report.

A great deal of information is required to successfully estimate the residual capacity of a corroded RC member. In practice, this information is either known, if a thorough inspection and evaluation on the structure has been performed, or assumed if it is not available through condition assessment. Great effort and resources are required to properly inspect and assess affected structures. There are generally two systematic procedures accepted by the engineering community for inspecting RC structures. Although the first is mostly used for smaller highway structures, it provides useful information on the types of damages expected, and it associates a qualitative level of damaged based on measured properties. The guideline for inspecting these types of structures is the Ontario Structures Inspection Manual (OSIM, 2008), which involves a visual inspection of the structure. This assessment determines the condition of the structure based on the level of observed damage. When dealing with a concrete component or structure, the OSIM document provides basic guidance regarding typical damage types and level of damage. The typical types of damages observed in concrete structures as described in the OSIM are:

- scaling;
- disintegration;
- erosion;
- corrosion of reinforcement;
- delamination;
- spalling;
- cracking;
- alkali-aggregate reaction; and

- surface defects (mostly construction defects including bees nesting, pop outs, construction and cold joints).

The different observed damages are rated and given a qualitative description based on quantitative values for observed damage (e.g., 1 mm-width cracks are described as large cracks by the OSIM). As required by the Ministry of Transportation of Ontario (MTO), all road structures with a 3-m clear span or greater are required to be inspected and assessed every two years. It is required by authorities in charge of these structures to keep and document an inventory of all structures with their current condition and required work for budgeting and safety purposes. Although this procedure does provide useful information of the degradation of RC structures, it does not take into account any degradation values in terms of material strength, and it is only useful in determining if the structure is visibly damaged.

The second approach is a more detailed inspection and evaluation of the condition of highway structures, and it is prescribed by Section 14 of the Canadian Highway Bridge Design Code (CSA S6 (2006)). In this approach, the discretion of the assessing engineer is encouraged; however, it also requires the use of non-destructive testing and material sampling. In Clause 14.6.1, the code states that an inspection of the structure is required and be sufficiently detailed to provide insight on its condition. Clause 14.6.4 deals with deterioration and implies that sufficient data be collected in order to properly consider the deterioration effects during the evaluation.

In Section 14 of the Canadian Highway Bridge Design Code (CSA S6 2006), procedures are also described to guide an engineer in determining the capacity of an existing structure. In general, the approach is based on a statistical approach, where each element of a structure is given a reliability index based on its impact effect on structural behaviour if it were to fail. Then this element is linked to its current condition based on the availability of inspection information and accessibility. The loads are developed, amplified and weighted based on the previously determined reliability and condition. To calculate capacity, the code requires the consideration of deterioration of materials. The deterioration is based on the collection of data at the inspection phase of the process, and it provides very limited guidance through this aspect of the assessment. Clause 14.7 provides guidance when material strength of an existing member is estimated. When no deterioration is observed during the inspection sage, values for material strength are based on the following (Cl 14.7.1):

a) construction plans
b) test samples
c) estimated with respect to the year of construction
d) an approved method

However, Clause 14.7.5 specifically states that special provisions are required to determine the strength of a deteriorating material and refers to Clause 14.14.3. Furthermore, Clause 14.7.5 requires the use of non-destructive testing and specialty equipment to correlate the deteriorated material back to present undamaged materials. It also implies the use of uncertainty factors to predict residual strength.

Clause 14.14 provides guidance concerning the resistance of a member. A special provision for the shear capacity estimation of RC beams is mentioned under Clause 14.14.1.6. The minimum reinforcement area is amplified here based on the shear stress demand of the section. The contribution of the steel reinforcement to shear capacity is fully considered if the area of stirrups satisfies this new upper bound limit. If it does not and falls below a prescribed lower bound, the beam is to be considered unreinforced and the steel contribution is neglected. If, however, the section provides shear reinforcement amounts between these two limit values, a linear interpolation is to be used to determine residual shear strength. In any case, the clause refers back to the design equations under Clause 8.9.3.6 and 8.9.3.7.

The deterioration and defects of the materials are to be considered under Clause 14.14.3, where a resistance adjustment factor is to be applied on the strength calculation based on the type of material. This clause also limits the designer to the use of sound material only when strength is calculated, and the reliability index needs to be adjusted based on these adjustment factors as well. For concrete members, the adjustment factor is 1.05 when shear strength is estimated and the minimum amount of stirrups is provided. This also stipulates that if additional deterioration is expected before the next evaluation of the structure, then it is to be considered in the present evaluation.

ACI 562-12 (2012) provides guidance in the evaluation, repair and rehabilitation of concrete buildings. Chapter 5 of ACI 562-12 (2012) describes the procedure in developing loads and load factors, but it does not go into reliability considerations as the CSA S6 (2006) does. This chapter also introduces strength reduction factors. It specifically states that the load factors and strength reduction factors cannot be used with other design codes, indicating that these were specifically developed for assessment purposes. Regarding the application of strength reduction factors, ACI 562-12 prescribes different values based on the type of member being evaluated, which are then multiplied to its calculated nominal strength. Chapter 6 details the evaluation and analysis stage of the assessment procedure. An evaluation of the current condition of the structure is required and needs to address the following information (Cl 6.1.4):

a) Determine the condition of all the members and the extent and location of degradation.
b) Determine load paths in order to satisfy structural integrity.
c) Determine as built information for the purpose of establishing strength reduction factors from Chapter 5.
d) Determine the orientation of structural members, displacement, construction deviation and dimension.
e) Determine material properties from available:
    i. Construction documents
    ii. Drawing specifications
    iii. By testing
f) Determine additional information regarding surrounding structures load bearing partition walls and other limitations for rehabilitation.
g) Determine necessary information for the proper seismic evaluation of the structure.

Similar to the CSA S6 (2006), if information on material properties is missing, Clause 6.3 provides guidance in making the proper assumptions based on the construction year of the structure and type of element (e.g. column, beam or footing). However, this clause provides additional requirements in terms of testing and sampling procedures.

In the analysis stage, although Clause 6.5.4 requires the assessing engineer to use deteriorated properties, including the consideration of material deterioration, bond loss and redistribution of forces in the member and within the structural system as a whole, this clause however does not provide additional information as to the procedure in addressing this deterioration. Emphasis is given to the proper sampling and testing of material components.

ACI 562-12 (2012) extends into repair and rehabilitation design, but it remains vague in determining the residual strength of member, which requires the engineer to use judgment in applying a reduced nominal strength of the member. No special mention is provided for shear residual strength calculations.

A third document available for guidance in assessment practices of RC structures affected by reinforcement corrosion is Contecvet (2000). It is a prescribed manual for assessing the residual life of concrete structures affected by reinforcing steel corrosion. This document is separated into two distinct procedures, a simplified method and a detailed method. The selection of the method in the assessment should be based on:

- the importance of the assessment;
- the complexity of the assessment;
- the damage level of the structure;
- previous inspection reports;
- required information; and
- financial reasons.

The two procedures use the same analogy as both CSA S6 (2006) and ACI 562-12 (2012), where a great deal of importance is attributed to the proper inspection of the current state of a structure. Data collection and deterioration identification is a key part of the two procedures.

The simplified method is an importance-based procedure. Similar to the load development procedure of CSA S6 Section 14, the importance of a member is evaluated and based on its impact if it were to fail. The manual prescribes and determines the state of a member based on reliability or risk indexes. First, a simplified corrosion index (SCI) is determined, based on the environment aggressiveness and actual damage of the structure. The member is then classified into either flexural member or compression member, and with the help of the inspection information it is given a structural index (SI). This index is based on the condition and individual index of components of the member being evaluated (e.g., flexural members are given an index with respect to transverse reinforcement, longitudinal reinforcement and bond condition). From these indexes and evaluation, a simplified index of structural damage (SISD) is determined based on the SCI and the SI, as well as on its impact if it were to fail. The ratings are qualitative and describe damage as negligible, moderate, severe, and very severe. The SISD is refined based on a safety margin index (SMI), which is simply the nominal resistance to the nominal loading ratio of the element. Finally, the SISD is used in determining the urgency of intervention. This is described as the number of years after which remedial action is required, and it also provides guidance in what type of action is required. The simplified method has a similarity to the OSIM (2008), although the OSIM uses quantitative values of observed damage to determine a qualitative description of damage.

The detailed method of the Contecvet assessment manual addresses the problem from both a material and structural viewpoints. First and foremost, it prescribes a detailed inspection of the structure and its environment. Then the corrosion effects on steel and concrete are treated separately. Here the sectional loss, constitutive behaviour and bond properties are evaluated based on corrosion. Next, the load and analysis of the structure is presented and modified sectional properties are discussed. Afterwards the strength of the members is discussed with the modified material properties. Finally, the verification of the structural behaviour is made based on residual strength estimation and future deterioration. Case studies and examples are presented in the appendices of the manual.

The structural assessment section of the detailed method provides guidance in determining the residual strength of members based on information gathered during the inspection phase. The detailed method is based on the Eurocode 1 and 2. It details both ultimate limit state and serviceability limit sate considerations in the assessment. It aims at determining the level of damage and if it is above acceptable values in terms of strength, which are based on prescribed minimum levels from the design code or on predetermined performance level from the structures owner.

Loads are developed based on Chapter 5 of the Eurocode 2 (Structural Analysis), but they are modified for assessment purposes. It suggests the use of modified sectional member properties based on the loss in available section of both concrete and steel. Loss in ductility is also considered in the analysis. It also suggests the use of linear elastic as it is deemed conservative in the design and assessment. The use of the transformed section is suggested in the analysis stage, as damage, usually in the form of cracking, is known from the inspection phase. Consistency from the analysis to strength assessment in terms of sectional properties between the two stages is suggested. Load safety factors in the detailed method imply the use of less strict factors compared to the initial design, as it is suggested that since a thorough inspection was made of the structure, large deviation from actual loading is unlikely. It is suggested that this modification mainly be applied in terms of building loads, and it should be avoided when assessing bridges and only be made using engineering judgement if the uncertainties at the design stage were thoroughly addressed.

When the residual strength of a member with corroding reinforcing steel is estimated, the method uses the penetration of corrosion to modify the value of various properties of RC. Annex F provides useful information regarding corrosion effects on the mechanical properties of both steel and concrete, which are all based on the corrosion penetration of the reinforcement. It also mentions structural behaviour change because of composite action degradation. The redistribution of stresses is mentioned here with respect to beams transitioning from beam type stress distribution to arching action.

An example of residual shear strength calculation is provided under Sections F1.6. and F3.3. Here, the design equations from the Eurocode 2 are used but with modified material properties. The steel area is reduced, the effective depth is also reduced based on concrete cover cracking, and bond is modified when crack angles are lower than 45 degrees, as it can be critical for the element if the bars are not properly anchored.

Once loads are developed and strength is estimated, an ultimate limit state lower bound and higher bound values are suggested based on the inequality equation. It is suggested that if the resistance is greater than the demand, that no immediate action is required until the estimated time to re-examination is reached. If the demand is higher than the resistance but lower than 1.1 times the resistance, then reassessment is required within a year. If however the demand is greater than 1.1 times the resistance, urgent repairs are needed.

Out of the three documents, the Contecvet manual provides the most information on the assessment of RC structures under corrosion attacks. It guides the user in a thorough way, with mentions of important considerations, of the potential effects of corrosion on material and structural properties. Both ACI 562-12 (2012) and CSA S6 (2006) codes incorporate a wider range of deterioration and are rather elusive in dealing specifically with reinforcement corrosion. Such a document should be available to North American engineers.

2.6 Need for Research

From the literature review, it has been found that a great deal of effort has been dedicated to understanding reinforcing steel corrosion and its effects on RC members. Typically, the research has been focused on two main areas: concrete cracking and deterioration of the structural behaviour at the member level. First, the corrosion process and its effects on the surrounding concrete have been studied through the simulation of cracking. From these studies, important parameters that have been reported are:

- time to cracking, spalling and delamination of the concrete cover;
- loss of mass to cracking;
- loss of mass to spalling or delamination; and

- surface crack width.

The second area of focus has been the impact of steel corrosion on the mechanical properties and member behaviour of RC. The effects of corrosion have been found to decrease the yield strength in steel as well as its ductility. It has been observed that concrete loses strength because of the presence of cracks with increasing corrosion levels, and that bond strength between the steel and concrete decreases with increasing corrosion levels as well.

The strength and deformation capabilities of RC beams have been reported to decrease with an increasing level of corrosion. In flexurally dominant members, the main behavioural changes have been the reduction in load carrying capacity, reduction in ductility and possible change in failure mode (from bending to shear). These changes have been mainly attributed to the increase in concrete cracking, stirrup pitting and loss of bond. In the case of failure mode reversal, this change in behaviour has been reported of being caused mostly by a loss in anchorage strength by excessive cracking in these regions and stirrup pitting. This reversal of failure mode has led to the exploration of the shear strength reduction in shear-critical beams. Similar to flexural cases, a reduction in strength and deformability has been observed; however, this reduction has been instead attributed to the loss of steel reinforcement and reduction of available concrete as a result of cover spalling/delamination.

The use of finite element modelling as an estimation tool can provide important information on residual strength of affected members. It can also be successful in reproducing cracking caused by corrosion in RC members. In general, in order to properly model the residual strength of these types of damaged structural members, it is important to always keep in mind the ensuing effects on the material constitutive properties and change in behavior. It is also important to acknowledge limitations in finite element analysis in order to make sound engineering decisions.

Evaluation tools currently available for practicing engineers require a great deal of information that is rarely available from the inspection of a structure (e.g., the amount of steel loss and the actual location of that loss). Existing standards do not provide guidelines in the estimation of residual shear strength, and it is current practice to use current shear design equations in which material and geometric properties are modified. The CSA A23.3 (2004) procedure for shear strength calculation requires a minimum amount of shear reinforcement when the factored shear force exceeds the contribution provided by the concrete. However, it has been observed that the strength of reinforced members can fall below unreinforced values (Suffern et al. 2010), which does not account for the effects of cracking on the concrete properties. This lack of standardized assessment procedures requires a great deal of experience and engineering judgement to successfully estimate the residual shear strength of corroded RC flexural members.

When code equations are used to estimate residual capacity of a corrosion-affected beam, do these equations provide acceptable values for strength? Is simply modifying the area of available shear reinforcing steel acceptable? Is there also an impact on the concrete contribution to shear capacity? And how can this be incorporated using current design equations? These questions need to be answered prior to provide a successful prescribed assessment procedure.

The analysis methodology using finite elements requires input parameters that have to be measured through either destructive testing or reinforcement retrieval after the specimen has been tested to failure. It is important to link the process to actual engineering assessment practice, while keeping in mind the availability and accessibility of information that is provided to the assessing engineer. This requires a thorough inspection in combination with proper material sampling of the affected structure to extract the required parameters. Can this process be improved? Is there a method that can be developed to estimate the residual strength without having to go through the tedious task of inspection?

There is a definite need to link both aspects of corrosion in the assessment procedure (i.e., cracking and material strength deterioration to member behaviour). This is especially true in shear strength estimation, as RC strength depends on the amount of cracking present to successfully transfer shear stresses especially in disturbed regions. The effects of cracking within concrete might not be fully captured by simply removing detached concrete (e.g., by spalling or delamination of the concrete cover) from the calculations, and strength might be overestimated. In this work, it is proposed to incorporate a corrosion-induced cracking model within a two-dimensional plane-stress finite element model. The cracking model is indicative of the level of corrosion-induced damage in the concrete, and, therefore, the strength and behavioral changes can be studied. The model is then validated against experimental results of shear-critical RC beams affected by web reinforcement corrosion. Upon validation, the analyses are then extended to a parametric study of design parameters to determine their effects on strength and deformation capacity. Engineers are in need of an assessment tool to first assist in estimating residual strength and second simulate the progress of strength degradation due to corrosion.

Chapter 3 Finite Element Modelling

3.1 Introduction

This chapter presents the finite element (FE) modelling procedures implemented to simulate the shear resistance of shear-critical RC beams with corrosion-damaged stirrups. The nonlinear FE package VecTor2, developed at the University of Toronto, has been used for this purpose (Wong and Vecchio 2002). VecTor2 is a two-dimensional FE program to analyze RC members subjected to in-plane normal and shear stresses. The program utilizes an incremental total load, iterative secant stiffness algorithm to produce an efficient and robust nonlinear solution.

3.2 Finite Element Types and Mesh

There are two commonly accepted FE modeling techniques in RC. The first is incorporating reinforcing steel within the concrete element, also known as "smearing". This is often done because it is a quicker solution when meshing and yields acceptable results for both flexural and shear-reinforcing applications as long as the steel is uniformly distributed. However, this technique has its limitations, because the steel component is directly incorporated within the elements. A major disadvantage is that certain mechanical properties cannot be properly modeled (e.g., bond between steel and concrete). The second method consists of using distinct truss bar elements for the reinforcement, where the steel is incorporated separately within the model as truss bars, only capable of carrying axial loads. These elements are connected to concrete elements by either assuming perfect bond (i.e., concrete and steel elements share nodes) or using link elements between the two to simulate bond effects. This technique is more commonly used for flexural applications, as the bond mechanism is predominant in the interaction between flexural reinforcement and concrete, especially for improperly anchored bars. The FE methodology in this study uses a combination of the two techniques, with a slight modification in the application of the reinforcement smearing technique.

Plain concrete elements were modelled using a 4-node rectangular plane stress element, with 2 degrees of freedom at each node, as shown in Figure 3.1. For regions where shear reinforcement is well distributed and assumed to be smeared across the element, the material matrix for the plane stress element [D] is modified in VecTor2 to account for both the concrete [D_c] and steel [D_s] contributions as follows:

$$[D] = [D_c] + \sum_{i=1}^{n} [D_s]_i \tag{3.1}$$

where the subscript i refers to the different steel orientations. Concrete is treated as an orthotropic material along the principal directions, and the concrete material matrix [D_c] is defined for a given load stage as:

$$[D_c] = \begin{bmatrix} \overline{E}_{c1} & 0 & 0 \\ 0 & \overline{E}_{c2} & 0 \\ 0 & 0 & \overline{G}_c \end{bmatrix} \tag{3.2}$$

where $\overline{E}_{c1}$, $\overline{E}_{c2}$ and $\overline{G}_c$ are the secant moduli in tension, compression and shear, respectively. These moduli are calculated based on the current values of principal stresses and strains at any given load stage, i.e.,

$$\overline{E}_{c1} = \frac{f_{c1}}{\varepsilon_{c1}}, \quad \overline{E}_{c2} = \frac{f_{c2}}{\varepsilon_{c2}}, \quad \overline{G}_c = \frac{\overline{E}_{c1} \cdot \overline{E}_{c2}}{\overline{E}_{c1} + \overline{E}_{c2}} \tag{3.3}$$

where f_{c1} and f_{c2} are principal stresses, and ε_{c1} and ε_{c2} are principal strains. The [D_s]$_i$ matrix in Eq. 3.1 describes the steel contribution along the i^{th} direction and for a given load stage is defined as follows:

$$[D_s]_i = \begin{bmatrix} \rho_i \overline{E}_{si} & 0 & 0 \\ 0 & 0 & 0 \\ 0 & 0 & 0 \end{bmatrix} \tag{3.4}$$

where $\overline{E}_{si}$ is the modulus of elasticity of the steel in the i^{th} direction, and ρ_i is the percentage of steel distributed within the element along the same direction. The stresses in the reinforced concrete element $\{\sigma\}$ are related to the total strains $\{\varepsilon\}$ through the composite material stiffness matrix $[D]$ as follows:

$$\{\sigma\} = [D]\{\varepsilon\} - \{\sigma^o\} \tag{3.5}$$

where $\{\sigma^o\}$ represents the stress contribution of strain offsets and shear slip strains (Wong and Vecchio 2002). This stress vector $\{\sigma^o\}$ is obtained from:

$$[\sigma^o] = [D_c]\{[\varepsilon_c^o] + [\varepsilon_c^p] + [\varepsilon^s]\} + \sum_{i=1}^{n}[D_s]_i\{[\varepsilon_s^o]_i + [\varepsilon_s^p]_i\} \tag{3.6}$$

where $\{\varepsilon_c^o\}$ is the concrete elastic strain offset (due to thermal, prestrains, shrinkage and lateral expansion effects), $\{\varepsilon_c^p\}$ is the concrete plastic strain offset (due to cyclic loading or damage), and $\{\varepsilon^s\}$ represents the strain due to crack shear slip (Wong and Vecchio 2002). Likewise, $\{\varepsilon_s^o\}_i$ and $\{\varepsilon_s^p\}_i$ are respectively the elastic and plastic strain offsets in the i^{th} direction of the reinforcing steel.

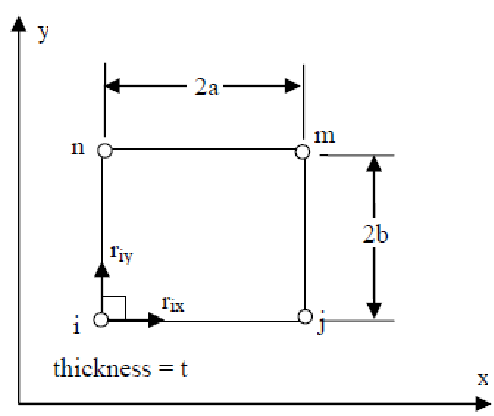

Figure 3.1: Concrete plane-stress element (reproduced from VecTor2 manual)

The shear reinforcement was modelled using rectangular plane-stress elements with the composite material matrix in Eq. 3.1. However, depending on where the shear reinforcement is located within the beam, two distinct modelling approaches were used. For sections that are considered non-critical in terms of stirrup corrosion, the shear reinforcement was smeared across the elements. It was incorporated as a percentage of steel reinforcement distributed equally throughout the elements in the region. For sections that are critical, wherein corrosion in the stirrup needs to be introduced, the stirrups were isolated by means of composite elements with a width equal to the stirrup diameter. This generates two types of elements within the critical section, plain unreinforced concrete elements and "locally smeared" (LS) RC elements. This was done for two reasons. First, the material and geometric properties for each stirrup can be modified independently based on the degree of corrosion. Second, a corrosion-induced cracking model, as described in Section 3.3, can be introduced by means of simulating the expansion caused by corrosion build up on the stirrup legs.

Compression and tension flexural reinforcement were modelled using 2-node truss elements, with one degree of freedom per node. These elements can only transfer axial loads. If corrosion is considered along the longitudinal reinforcement, the properties of the truss elements can be modified accordingly. Furthermore, truss elements also lend themselves to incorporate a bond element (e.g., a spring) within the model, if bond is chosen to be a critical factor in modeling the member's behaviour. However, since the focus of this research is to study the effect of corrosion on shear reinforcement, flexural reinforcement was assumed unaffected by corrosion, and thus none of its properties were modified. Furthermore, perfect bond was assumed for all reinforcement.

A typical finite element mesh of an RC beam is shown in Figure 3.2. The light green elements at the beam's ends as well as the blue right side section are modelled with composite non-critical elements, in which the shear reinforcement is smeared throughout these regions based on the percentage of steel that was intended in the design. The light blue on the left side of the beam represents plain unreinforced concrete elements. The shear reinforcement in this critical region is modelled by LS elements, in which the reinforcement in smeared along a width equivalent to the diameter of the stirrup legs at the original location of the stirrups.

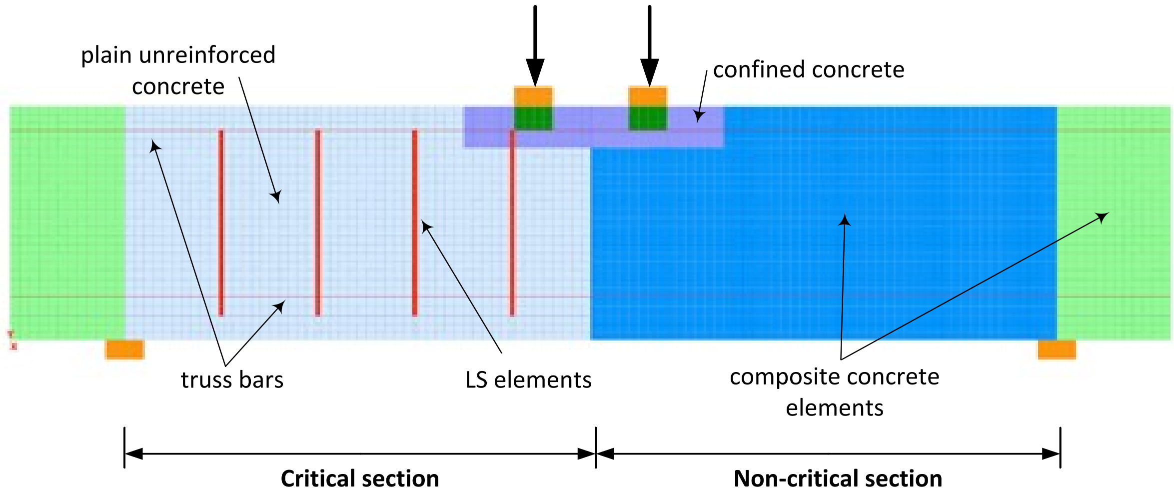

Figure 3.2: Typical finite element mesh

An aspect ratio between 1 and 1.5 was used when meshing with rectangular plane-stress elements. To accommodate the geometry of LS elements, an aspect ratio of 2 was allowed when meshing with these elements. Initially, the width of LS elements was set to the diameter of the stirrup legs. By applying the height-to-width ratio limit of 2, the average size for the remainder rectangular concrete elements was approximately double the stirrup diameter, with an aspect ratio of 1. For FE analyses where the stirrup diameter was small, it was deemed satisfactory to set the width of the LS elements equal to half the width of the concrete elements, as long as they properly simulated the behaviour and cracking pattern once the model was validated. A minimum number of element rows over the height of the section are required to do so accordingly. A general rule of thumb is 24 elements over the height of the RC beam. This is especially true for shear critical beams, as the stress distribution estimation is paramount in providing acceptable behavioral characteristic and strength estimation. The length of truss elements representing longitudinal reinforcement was governed by the dimension of the concrete elements to which they were connected.

3.3 Modelling Corrosion-Induced Damage

Corrosion-induced damage was introduced in the FE methodology by reducing the cross-sectional area of the stirrups and by inducing concrete cracking as a result of corrosion products build-up around the shear reinforcement (Figure 3.3). The loss of steel cross-sectional area A_{sLoss} due to corrosion is obtained from:

$$A_{sLoss} = A_s - \frac{\pi\left(d - 2x_{cor}\right)^2}{4} \tag{3.7}$$

where A_s is the original cross-sectional area of the stirrup, d is the reinforcing steel diameter, and x_{cor} is the depth of corrosion attack penetration. The original cross-sectional area A_s is given by:

$$A_s = \frac{\pi d^2}{4} \tag{3.8}$$

Corrosion-induced cracking is simulated by using the analogy for the concrete cover of a thick-wall cylinder subjected to internal pressure (see Figure 3.3(b)). The internal pressure is the result of the volume increase of corrosion by-products, which have a lower density than the original reinforcing steel. As corrosion by-products build-up, the pressure at the steel-concrete interface increases against the surrounding concrete. Once the tensile limit of the concrete is reached at the steel/concrete interface, the concrete starts to crack and dissipates this accumulated energy from the initial pressure p_i to an effective pressure p_e at the crack limit (see Figure 3.3(b)). It is assumed that the pressure is fully released once the crack reaches the surface of the thick-wall cylinder.

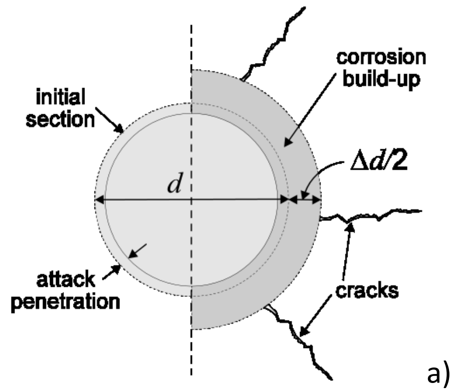

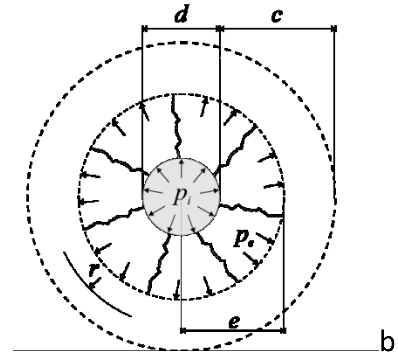

Figure 3.3:(a) Corrosion products build up; (b) Concrete cover treated as a thick-wall cylinder subjected to internal pressure (reproduced from Martín-Pérez 1999)

This process is introduced in the FE model in the form of equivalent strains. Here, fictitious horizontal steel is smeared within the affected LS elements, and this fictitious steel is pre-strained in compression prior to loading to simulate the natural expansion of corrosion build up. The compressed steel elements are then released prior to loading of the RC beam, so that they expand and induce tensile stress in the surrounding concrete elements. This is done as an effort to mimic hoop deformations within the concrete cover surrounding the reinforcement caused by the corrosion mechanism and include theme in analysis. The magnitude of pre-strain is calculated based on the percentage of corrosion attack and associated volume build-up, but only for the longitudinal deformation. These compressive pre-strains are then distributed over the affected surrounding concrete, i.e., within the thick-wall cylinder representing the concrete cover based on the area occupied by the cylinders within the member section.

The total expanded area $A_s^{'}$ resulting from corrosion products build-up can be obtained by assuming a ratio of steel-to-corrosion product density μ according to:

$$A_s^{'} = \mu A_{s\,Loss} + \frac{\pi\left(d - 2x_{cor}\right)^2}{4} \tag{3.9}$$

The ratio μ has been reported of having values between 2 and 4 (Rosenberg 1989). The value for this model was set at 2. This value was selected based on fact that the majority of the work is focused around accelerated corrosion where density ratios are typically closer to 2. The expanded diameter d' is calculated as follows:

$$d' = \sqrt{\frac{4A_s'}{\pi}} \tag{3.10}$$

Finally, the strain induced in the thick-wall cylinder is calculated from:

$$\varepsilon_{cor} = \frac{d' - d}{d + 2c} \tag{3.11}$$

where ε_{cor} is the corrosion-induced strain in a single leg of the stirrup, and c is the concrete cover to the respective leg. In the two-dimensional plane-stress problem modelled in this study, both legs in the stirrup are assumed to be corroding at the same rate and level, and therefore the resulting compressive pre-strain is adjusted by averaging the strains in each leg over the width b of the beam (see Figure 3.4), i.e.,

$$\bar{\varepsilon}_{cor} = (\varepsilon_{cor1} + \varepsilon_{cor2}) \times \left[\frac{2(d + 2c)}{b}\right] \tag{3.12}$$

where b represents the beam's width. Once the strains are calculated based on the percentage of corrosion attack, they are incorporated in the FE model as previously discussed.

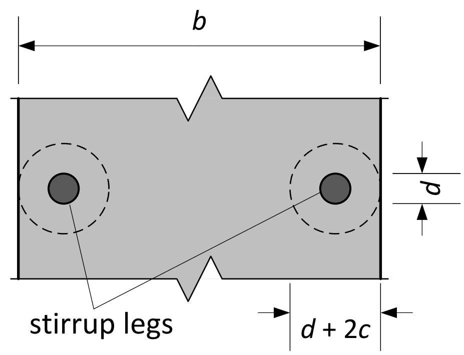

Figure 3.4: Corroding stirrup legs in RC beam

3.4 Material Models

The FE software VecTor2 offers a variety of constitutive material models; it is important to carefully and strategically select the proper combination of available models in order to best represent and simulate the behaviour and strength of shear critical RC beams. As part of the validation task of the FE methodology presented here, it was apparent the need to explore the effect of the various constitutive models on the behaviour of the selected RC test data (Higgins et al. 2003) due to the lack of enough information provided in the literature. The limited information directly impacted the validation task of the FE analyses, which required numerous trials of input parameters to successfully reproduce the test data. The initial analysis results deviated from the actual strength and stiffness observed in the tests, and, therefore, it led to an exploration and adaptation of different modelling parameters and constitutive models to capture the behaviour exhibited during testing. A parametric analysis of the different material models and input parameters was therefore conducted to have a good understanding of the effects of each parameter on the behaviour of shear critical RC flexural members and select those most appropriate to analyze them.

The RC beam used in this parametric study is one tested by Higgins et al. (2003). It is a shear critical beam with a shear-span-to-depth ratio of 2.04. It was tested under a 4-point loading scheme, with a critically designed span to ensure failure of the beam occurred within the test section (see Figure 3.5). The cross-section is 600-mm deep by 254-mm wide. In the critical section, the beam is reinforced in shear using #13 bars at 254 mm spacing, while in the non-critical span #13 bars are placed at 203 mm and at 100 mm at point loads. The flexural reinforcement consists of 5 #25 bars distributed over two layers, one containing 2 bars and the other 3. The 3 #25 are placed in the lower part of the beam and are properly anchored using 90-degree hooks past the supports, while the layer containing 2 #25 are simply straight bars. The compressive strength of the concrete was 33.4 MPa (Potisuk et al. 2011). The beam was modeled using the elements and techniques previously described, and it was loaded using an incremental displacement at the mid-span loading plates (see Figure 3.5). The effect of different constitutive model parameters on the resulting load-displacement curve is presented and discussed in the following sub-sections. Note that the mid span deflections are based on the orientation convention indicating that negative values represent downwards deformations.

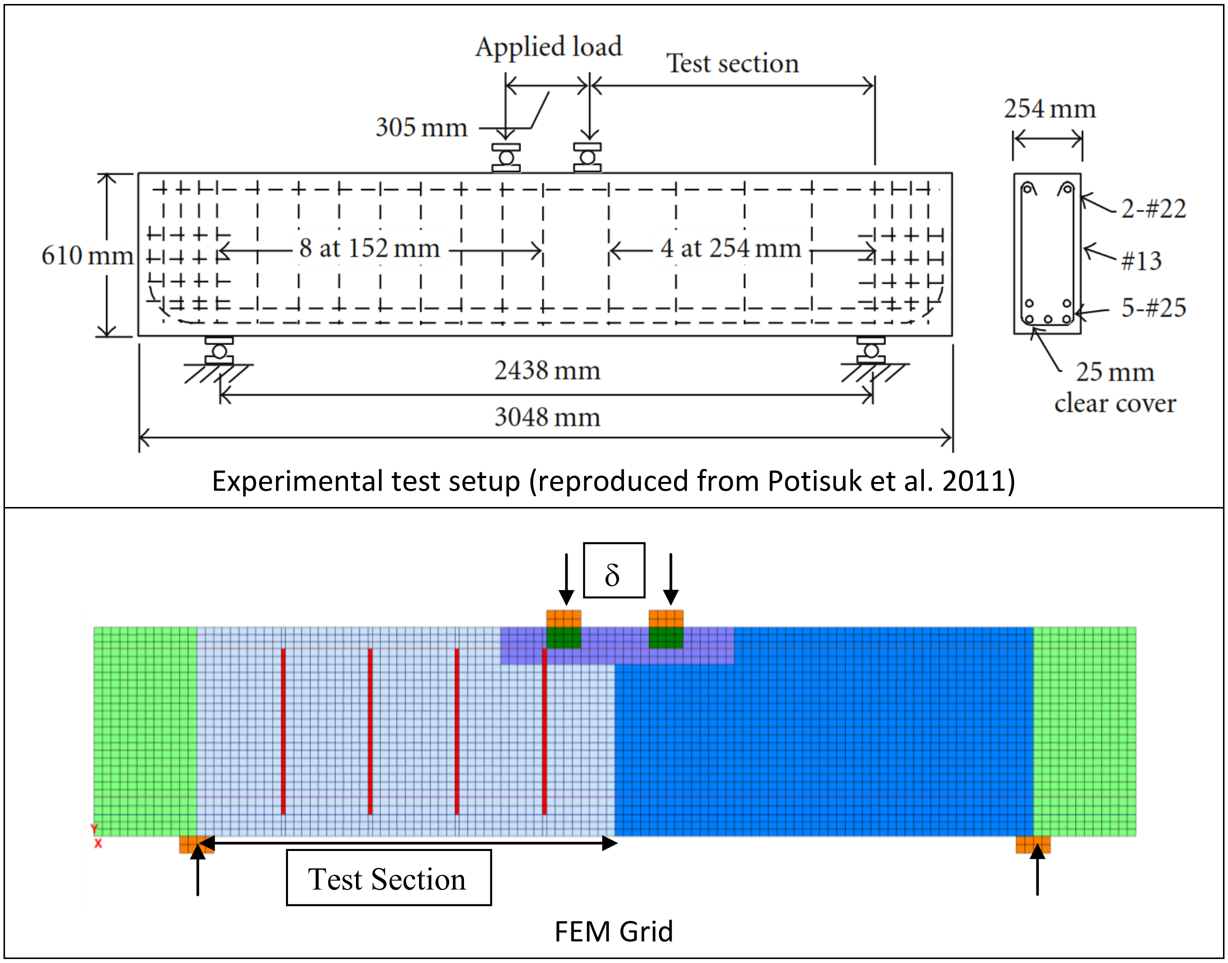

Experimental test setup (reproduced from Potisuk et al. 2011)

FEM Grid

Figure 3.5: Oregon beam test setup and FEM grid of test setup

3.4.1 Concrete Constitutive Behaviour

The FE software VecTor2 allows for a selection of various well-known constitutive models for both pre-peak and post-peak behaviour for concrete in compression. Although these models were not explored extensively here, a sensitivity analysis of model parameters was performed to help understand effects at the FE level. The two basic pre-peak models that were explored are Hognestad's and Popovic's models. Both the effects of peak strain and modulus of elasticity as input parameters were studied. Hognestad's model is given by:

$$f_{ci} = -f_c' \left\{ 2\left(\frac{\varepsilon_{ci}}{\varepsilon_o}\right) - \left(\frac{\varepsilon_{ci}}{\varepsilon_o}\right)^2 \right\} < 0 \tag{3.13}$$

where f_{ci} is the concrete compressive stress, f'_c is the concrete compressive strength, ε_{ci} is the concrete compressive strain, and ε_o is the strain corresponding to f'_c. Popovic's model represents the pre-peak compressive response of concrete as:

$$f_{ci} = -\left(\frac{\varepsilon_{ci}}{\varepsilon_o}\right) f_c' \frac{n}{n-1+\left(\varepsilon_{ci}/\varepsilon_o\right)^n} \tag{3.14}$$

where n is a curve fitting parameter defined as:

$$n = \frac{E_c}{E_c - E_{\sec}} \tag{3.15}$$

where E_c is the tangential elastic modulus and E_{sec} is the secant modulus. The tangential modulus E_c is an input parameter; however, if not defined, it is calculated by default as $E_c = 2f_c'/\varepsilon_o$. The secant modulus is calculated based on the peak stress and strain as $E_{sec} = f_c'/\varepsilon_o$.

The effect of the value of the concrete peak strain ε_o on the load deformation response of the RC beam previously described was studied using both Eqs. 3.13 and 3.14. If no input value for ε_o is provided, VecTor2 calculates the peak strain ε_o based on the concrete compressive strength f'_c as $\varepsilon_o = 1.8 + 0.0075 f'_c$ ($\times 10^{-3}$). Thus for f'_c = 33.4 MPa, ε_o becomes 2.05×10^{-3}. The peak strain was varied from the default value of 2.05×10^{-3} to 4×10^{-3}. Figure 3.6 and Figure 3.7 illustrate the effect of varying ε_o on the load-deformation response using Hognestad's and Popovic's model, respectively. By comparing both graphs, it is observed that Popovic's model is less sensitive to this parameter, providing the same capacity and deformation for both cases. Since the test data used to validate the FE methodology only provided a value for f'_c, it was decided that Popovic's model would be used to model concrete in compression, as it shows less sensitivity to other input parameters.

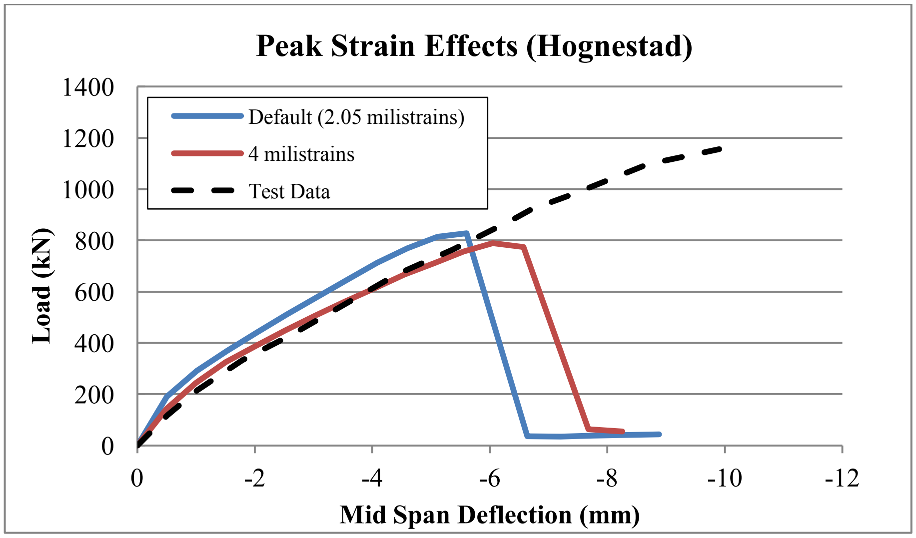

Figure 3.6: Effect of peak strain on load-deformation using Hognestad's parabola

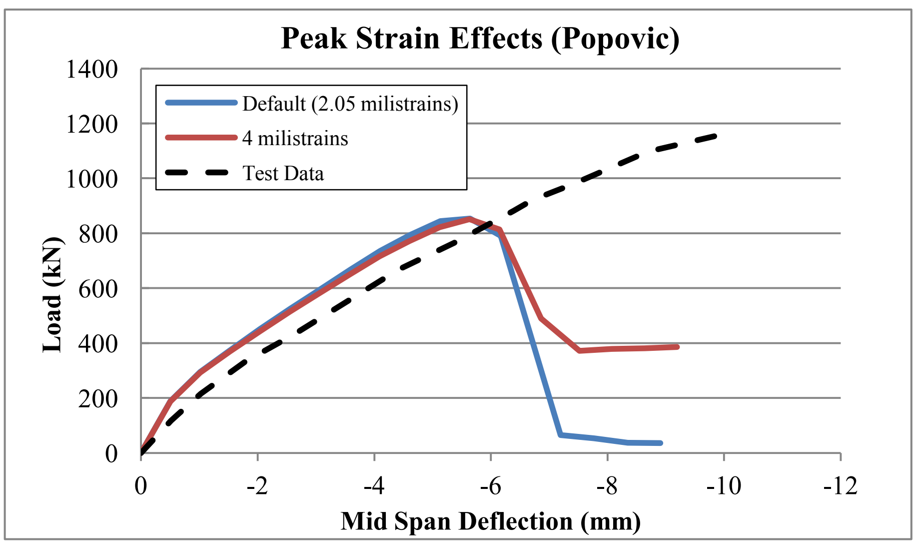

Figure 3.7: Effects of peak strain on the load deformation using Popovic's model

Likewise, the effect of varying the concrete elastic modulus E_c on the load deformation response of an RC beam was also studied. The default value for this parameter is calculated as $E_c = 5{,}500\sqrt{f_c^{'}}$ (GPa). The values for E_c were varied from $4{,}000\sqrt{f_c^{'}}$ to $6{,}000\sqrt{f_c^{'}}$. The effect of this parameter on the load-deformation curve can be observed in Figure 3.8 and

Figure 3.9 for Hognestad's and Popovic's models, respectively. When using Hognestad's model, the value of E_c does not have an effect on the resulting load-deformation response, as Hognestad's model does not use this parameter directly in modelling the compressive behaviour of concrete (see Eq. 3.13). In the case of Popovic's model, the decrease in stiffness and increase in ultimate load and deflection with a decrease in E_c is attributed to the increase in allowable straining in tension as the concrete softens.

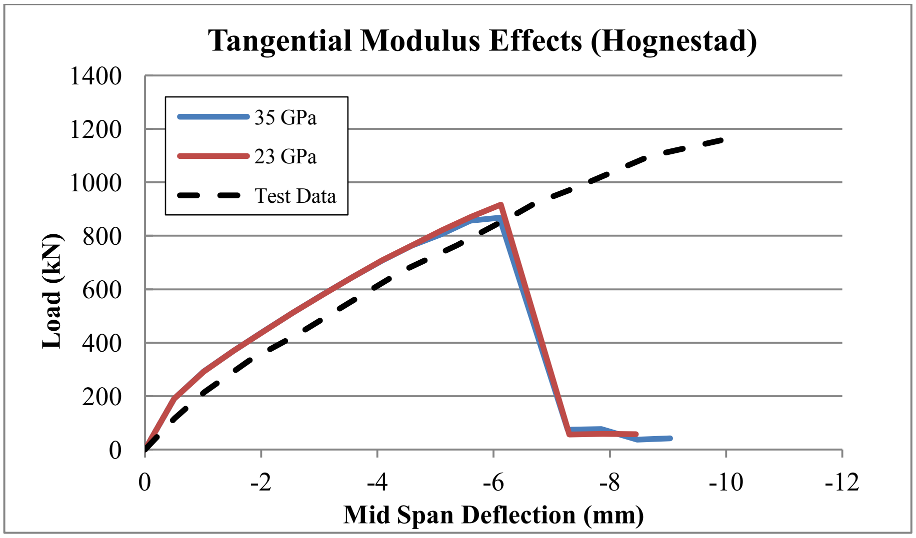

Figure 3.8: Effect of tangential modulus on load deformation (Hognestad's)

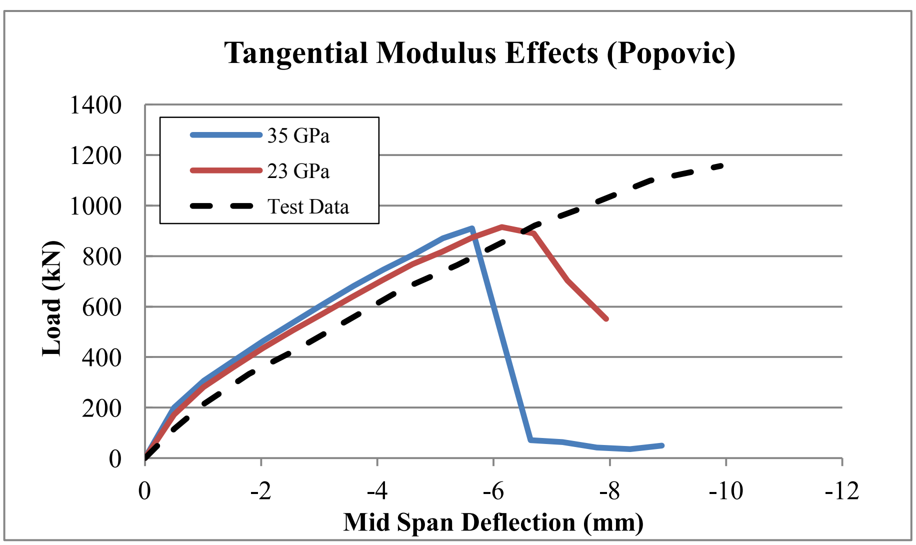

Figure 3.9: Effect of tangential modulus on load deformation (Popovic's)

The effect of the peak stress is mostly reflected by the default calculation of other model parameters (such as E_c, ε_o or tensile strength f'_t). In shear critical beams, the magnitude of f'_c is mostly reflected through the calculation of the concrete tensile strength. Increasing the concrete peak stress by default increases the tensile capacity and ductility of the concrete. The impact of increasing f'_c on the load-deformation response can be observed in Figure 3.10. In this figure, all default values were selected for low and high f'_c values of 25 and 45 MPa, respectively. As it can be observed from the figure, reducing the compressive strength of concrete softens the response and reduces the load and deformation capacity of the beam. VecTor2 also allows inputting tensile-related properties directly, without being calculated from f'_c. In this case, the impact is less significant, and the load-deformation response shows less sensitivity to the variation in compressive strength.

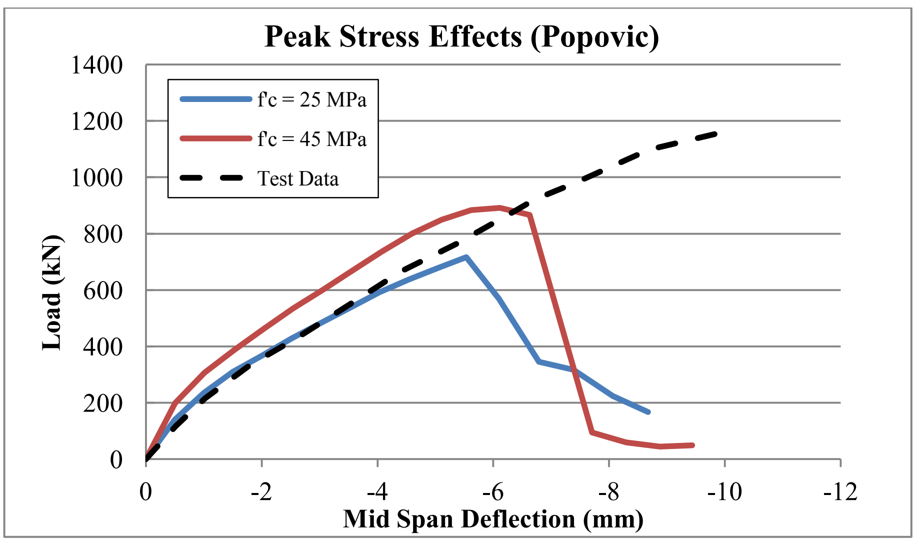

Figure 3.10: Peak stress effect on load deformation (Popovic's Model)

The value of the concrete tensile strength has a noticeable impact on the behaviour and strength of shear critical members. It is the governing factor in most cases for the cracking criterion, and it impacts the stiffness, overall load-deformation response and failure mechanism. Because the moment of inertia changes as cracking progresses in RC beams, a lower tensile limit leads to early cracking and increase in deflection, resulting in an early drop in member stiffness. The default input value for the concrete tensile strength in

VecTor2 is calculated from $f_t' = 0.33\sqrt{f_c'}$ (MPa). To show the effect of the input tensile strength on the load deformation response, the concrete tensile strength f'_t was varied from the default value to the flexural rupture strength of $0.6\sqrt{f_c'}$ (MPa). The results are presented in Figure 3.11 when Hognestad's model for concrete in compression is used and in Figure 3.12 when Popovic's model is selected instead. A similar outcome is observed for both models when the tensile strength of the concrete is increased. Two effects are observed when f'_t increases: the first is the increase in ultimate strength and deflection, and the second is the increase in overall stiffness. The increase in strength is directly attributed to the tensile resistance of the compressive struts, thus allowing greater strength and deformability with increasing tensile strength. The change in stiffness is attributed to the degree of concrete cracking, wherein a higher tensile strength leads to greater resistance to cracking and thus an increase in the flexural rigidity of the section.

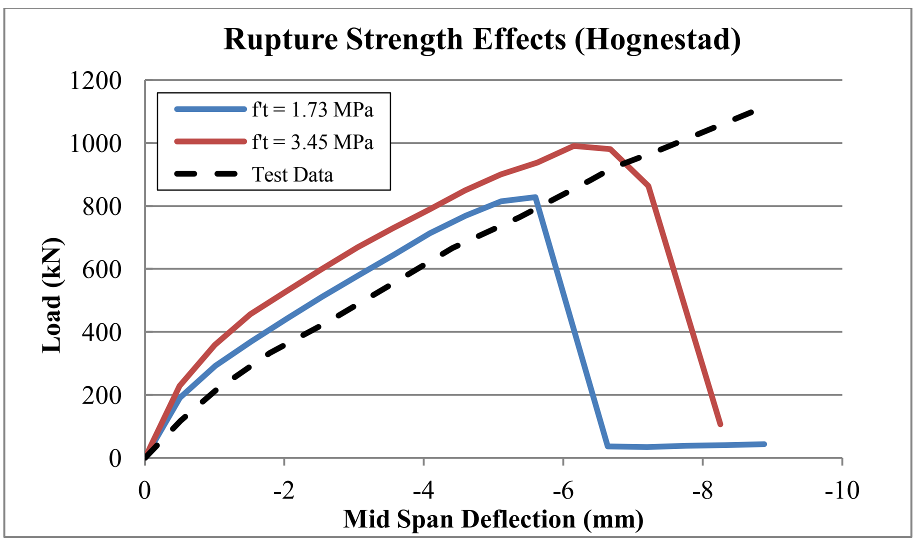

Figure 3.11: Effect of concrete tensile strength on load deformation using Hognestad's model for concrete in compression

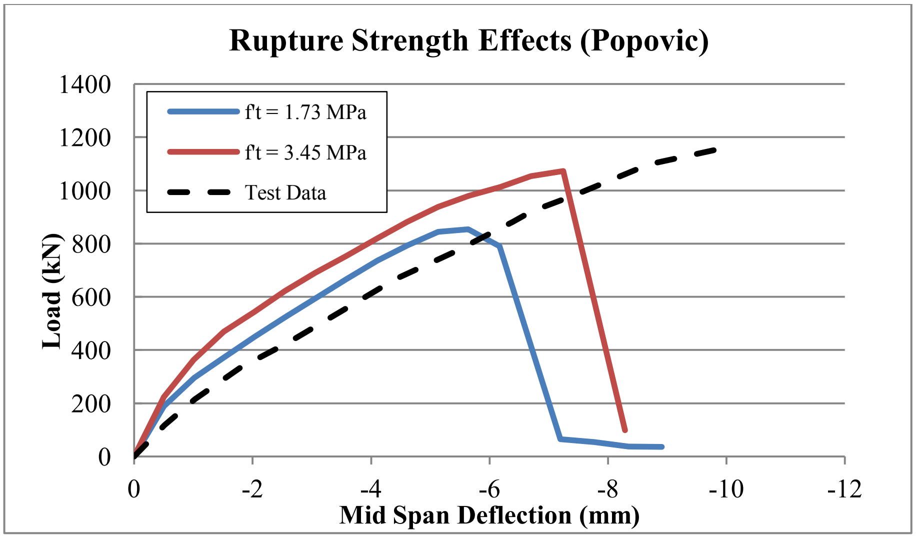

Figure 3.12: Effects of concrete tensile strength on load deformation using Popovic's model for concrete in compression

3.4.2 Steel Constitutive Behaviour

The steel constitutive behaviour in the FE analysis follows a tri-linear relationship. Here, the sensitivity of the load-deformation response to the yield stress in the ductile steel model (tri-linear relationship) was tested. To show the effects of modifying the yield strength of the different steel reinforcements, four scenarios were selected: (i) all default values were selected with the yield strength set to 400 MPa for all the steel; (ii) only the flexural steel yield strength was increased to 500 MPa; (iii) all the steel yield strengths were set to 500 MPa; and, (iv) the shear reinforcement yield strength was set to 500 MPa, whereas the flexural steel had a yield strength of 400 MPa. The results are shown in Figure 3.13.

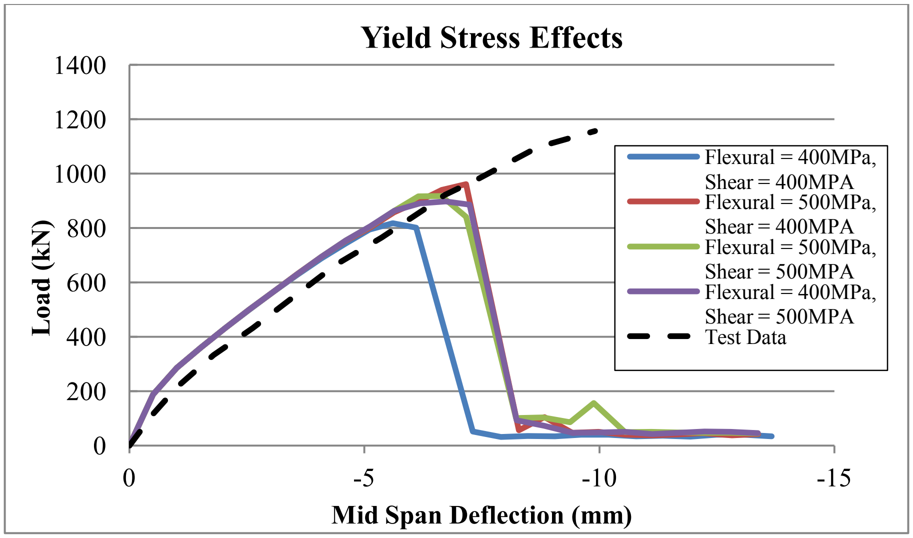

Figure 3.13: The effect of yield strength on the load-deformation response

Increasing the value of the yielding stress of the longitudinal reinforcement increases the depth of the compression block in order to equilibrate the forces within the section. The capacity is therefore increased with the increasing yield strength, unless a compression failure is triggered first. As shown in Figure 3.13, increasing the yield strength of the shear reinforcement over that of the longitudinal reinforcement also leads to higher capacity.

3.4.3 Shear Behaviour

The shear strength and behaviour of RC beams is a very complex phenomenon as concrete undergoes non-linear behavior under shear stresses. Depending on the configuration of loading, as well as flexural and shear reinforcement, the shear stresses are distributed and transferred using a combination of different mechanisms. These stresses are distributed among the compression zone, aggregate interlock, shear reinforcement, and dowel action of the flexural tension reinforcement. It is important when modeling shear critical beams to understand how the FE software considers and incorporates these different mechanisms, and to strategically select the appropriate models for the problem at hand. The distribution ratio among the different shear mechanisms directly impacts the failure mechanism of shear critical beams, which is typically a function of the shear span-to-depth ratio.

FE program VecTor2 uses as its theoretical basis two analytical models to simulate the behaviour of RC subjected to in-plane normal and shear stresses. These analytical models are the Modified Compression Field Theory (MCFT) and the Disturbed Stress Field Model (DSFM). Both models treat cracked concrete as an orthotropic material with smeared, rotating cracks and with material directions aligned to principal stresses directions. Likewise, the two models are built on three sets of relationships:

- compatibility relationships for concrete and reinforcement average strains;
- equilibrium relationships involving average stresses in the concrete and reinforcement; and
- constitutive relationships for cracked concrete and reinforcement.

The assumptions under the MCFT are:

- uniformly distributed reinforcement;
- uniformly distributed and rotating cracks (smeared cracking);
- uniformly applied shear and normal stresses;
- unique stress state for each strain state, without consideration of strain history;
- strains and stresses are averaged over a distance including several cracks;
- the orientation of principal strains coincide with the orientation of principal stresses;
- a perfect bond between reinforcement and concrete;
- independent constitutive relationships for concrete and reinforcement. Concrete constitutive features include compression softening due to tensile stresses and tension stiffening; and
- negligible shear stresses in reinforcement.

Although the MCFT assumes cracks to be smeared and formulates its equilibrium and compatibility equations in terms of average stresses and strains, it also considers local stress conditions at the cracks by checking if the reinforcement crossing a crack is yielding or if sliding shear failure occurs at a crack. These checks are performed by imposing a limit on:

1. The average concrete tensile stress f_{c1}

$$f_{c1} \leq \rho_x \left(f_{sxyield} - f_{sx}\right)\cos^2\theta_{nx} + \rho_y \left(f_{syyield} - f_{sy}\right)\cos^2\theta_{ny} \qquad 3.16$$

   where ρ_x and ρ_y are the reinforcement ratios along the x- and y-direction, respectively; $f_{sxyield}$ and $f_{syyield}$ are the yielding stresses along the x- and y-direction, respectively; f_{sx} and f_{sy} are the average stresses of the reinforcement along the x- and y-direction, respectively; and, θ_{nx} and θ_{ny} are the angles between the normal to the crack and the reinforcement along the x- and y-direction, respectively.

2. The local shear stresses at a crack v_{ci} transferred by aggregate interlock. These stresses decrease as the crack width w increases or the maximum aggregate size a decreases. The limiting criterion was developed by Vecchio and Collins 1988 but based on the work of Walraven (1981):

$$v_{ci} \leq \frac{0.18\sqrt{f'_c}}{0.31 + 24w/\left(a+26\right)} \qquad 3.17$$

The effect of selecting the MCFT as the basis for the analysis and omitting the shear stress check at a crack is highlighted in Figure 3.14. All default values were selected for both cases. As expected, limiting v_{ci} at the crack reduces both the strength and deformation capacity at failure.

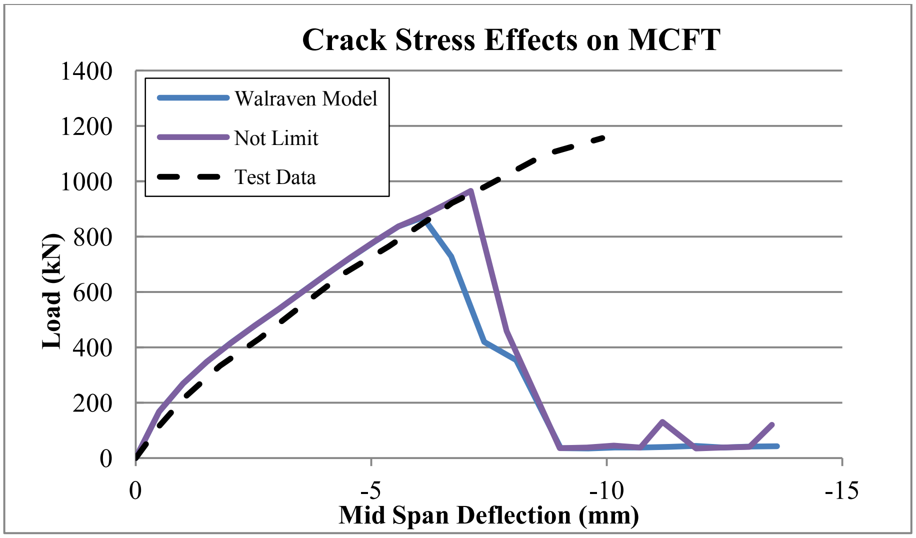

Figure 3.14: The effect of limiting the shear stress at a crack (MCFT)

The DSFM is formulated similarly to the MCFT; however, it incorporates the effects of lag between principal stresses and principal strains orientations. In RC members lightly reinforced, where shear slip at the crack can be significant, the orientation of principal stresses lags that of principal strains (Wong and Vecchio 2002). To account for this lag, DSFM accounts for shear slip deformations at the crack by formulating the total concrete strains as:

$$\begin{aligned} \varepsilon_x &= \varepsilon_{cx} + \varepsilon_x^s \\ \varepsilon_y &= \varepsilon_{cy} + \varepsilon_y^s \\ \gamma_{xy} &= \gamma_{cxy} + \gamma_{xy}^s \end{aligned} \qquad 3.18$$

where ε_x, ε_y and γ_{xy} are respectively the total axial strain along the x-direction, the total axial strain along the y-direction, and the total shear strain; ε_{cx}, ε_{cy} and γ_{cxy} are respectively the average net concrete axial strain in the x-direction, the average net concrete axial strain in the y-direction, and the average net concrete shear strain; and, ε_x^s, ε_y^s and γ_{xy}^s are respectively the average axial strain due to shear slip in the x-direction, the average axial strain due to shear slip in the y-direction, and the average shear strain due to shear slip. By explicitly calculating crack slip deformations, the DSFM eliminates the crack shear check as required by the MCFT.

The selection of either analytical model on the RC beam discussed in this chapter is illustrated in Figure 3.15, where the same default values were used in both cases. The comparison between the MCFT and DSFM will be done based on the effects of the different model and shear characteristic limits, such as crack width and stress limits at cracks. The behaviour of the load deformation curve is compared to the original test data from the previously described test setup of the Oregon beams series 10R.

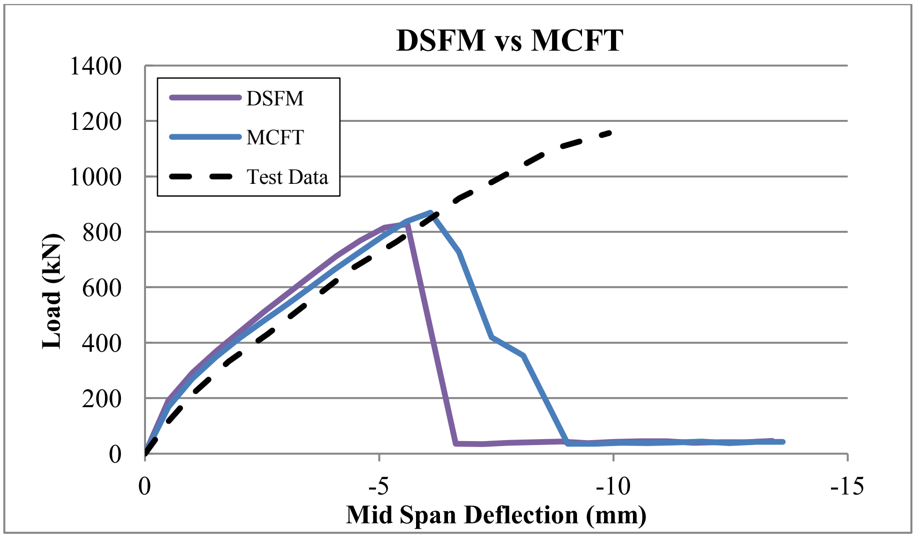

Figure 3.15: The effect of analytical model choice (MCFT vs. DSFM) on the load deformation curve

The behavioural effects of selecting to consider crack slip check are rather limited when default values are selected and can be observed in the Figure 3.15. When crack width is limited to a very small value as does the default settings, the slip is minimal as crack width will be the governing limit. Both concrete shear models properly simulate initial stiffness, while under estimating strength and ductility. The shear model sensitivity and behaviour will be studied next and based on the impact on load deformation curves from varying the stress limits and crack width limits for both models.

In both analytical models, the width of the crack can be limited, beyond which the average principal compressive stresses are reduced. This is done to account for the fact that concrete cannot transmit compressive stresses across large crack widths. The crack width limit default value is set at a conservative value of *a* divided by 10, where *a* is the maximum aggregate size. The size of the aggregate is by default 10 mm if not specified by the user. This implies that the default crack width limit is set to 1 mm by VecTor2. The effect of omitting this check on both models is shown in Figure 3.16 and Figure 3.17 for MCFT and DSFM, respectively. Limiting the width of the crack significantly affects the strength and deformation capacities in both cases. In the case of the beam considered in this chapter, limiting the crack width to 2 mm (a = 20 mm) is very conservative, as crack width beyond this value are expected in properly reinforced beams. In order for aggregates to interlock successfully at a crack and transfer stresses, this check should not be omitted, but rather its limit should be adjusted accordingly to an expectable value based on the beams reinforcement arrangement. A crack width limit was set to 10 mm for all analyses as it was considered to be half of the aggregate size. This value was also an acceptable limit to ensure that aggregate interlock mechanism engages properly in the shear resistance of the beam. The 10 mm limit also proved to be the value that better modelled the behaviour of the reference beam against the published data.

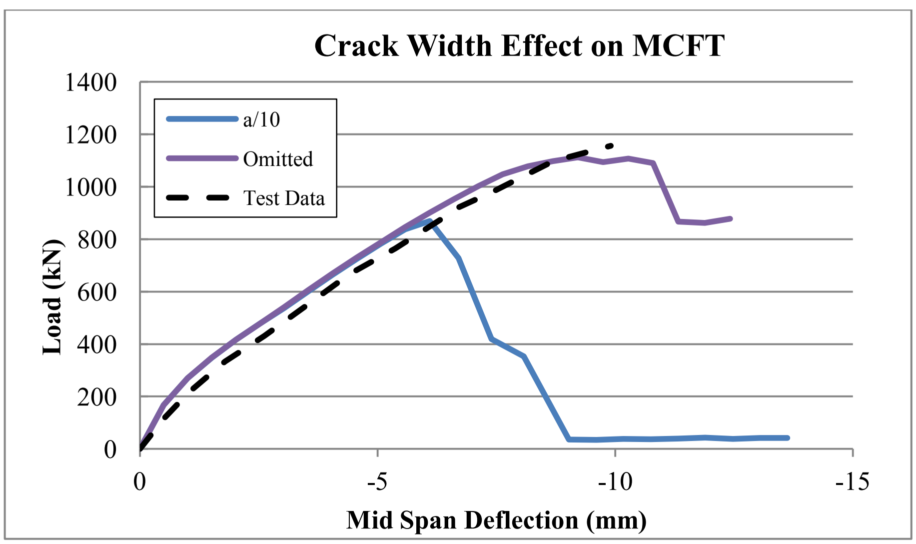

Figure 3.16: The effect of crack width limit on the load-deformation response using MCFT

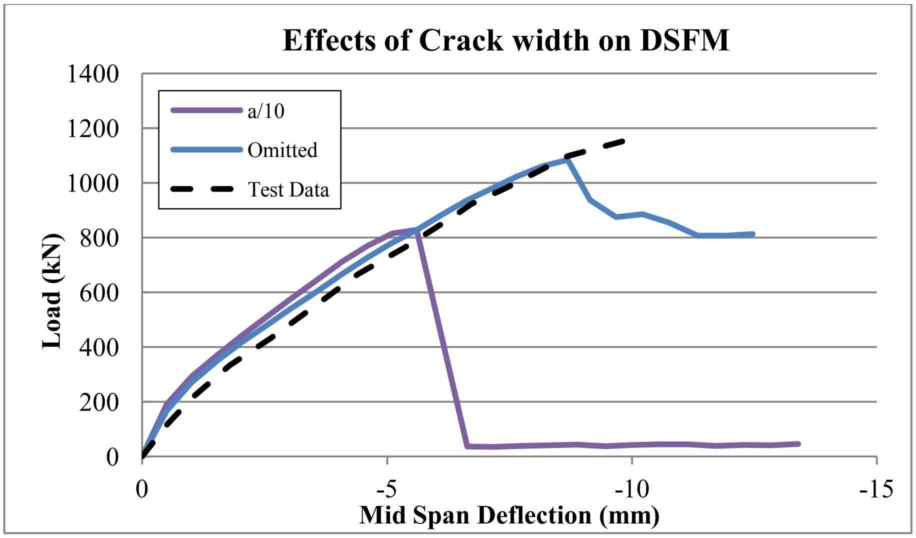

Figure 3.17: The effect of crack width limit on the load-deformation response using DSFM

The effects of the crack width limit on the MCFT and DSFM are presented in the Figure 3.16 and Figure 3.17 respectively. It is clear that in each case, when the crack with limit is considered, it becomes the governing limit. When the check is omitted, the stresses limit at a crack becomes the only limiting case for the MCFT shear mechanism. This impacts the load deformation curve significantly, where strength increases until stresses in the elements reach upper-bound upon which begins to redistribute stresses, which is outlined here near peak regions. The effects are also noticed in the MCFT by a less sudden failure at peak loading where the stresses are redistributed and limited rather than falling to zero when crack width reaches the limit resulting in this sudden failure. The DSFM has a slightly softer behaviour and better estimation of stiffness when the two cases for crack limits are compared. This can be explained by an increase in slip of the concrete elements which also greatly improved the strength and ductility. The DSFM incorporates stress limits as well as slip limits within the model, and by omitting the crack width limits, become a factor in strength calculation. The stress limit considered in the DSFM is rather similar to the default selection of the MCFT, which indicates that the elements reach the slip limit prior to the stress limit as does the MCFT. This observation is simply based on the difference in strength estimation between the two.

The selection of tension softening models has a great effect on the behavior and failure mechanism of shear critical members. The two basic tension softening models in MCFT and DSFM are linear and bilinear. Both tension softening models use a linear relationship up to the tensile strength. However, the bilinear model considers a linear decrease up to zero once cracking has initiated. This is reflected within the model in the failure mechanism and development. If the linear model is chosen, this creates a very sudden failure and does not allow for redistribution of stresses. Considering a linear decrease after reaching the tensile strength affects the area under the tensile stress-strain diagram and increases the fracture energy, which allows for the progressive formation of a crack. The effect of tension softening model on both shear models are represented in the following figures. Figure 3.18 showcases the tension softening model effect when MCFT is selected, whereas Figure 3.19 shows the same effect when DSFM is chosen instead.

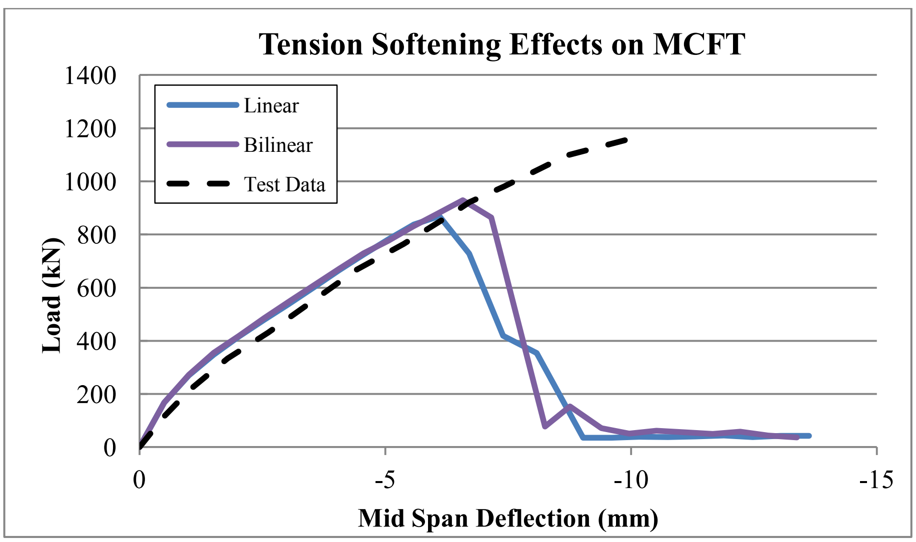

Figure 3.18: Effect of tension softening model on load deformation (MCFT)

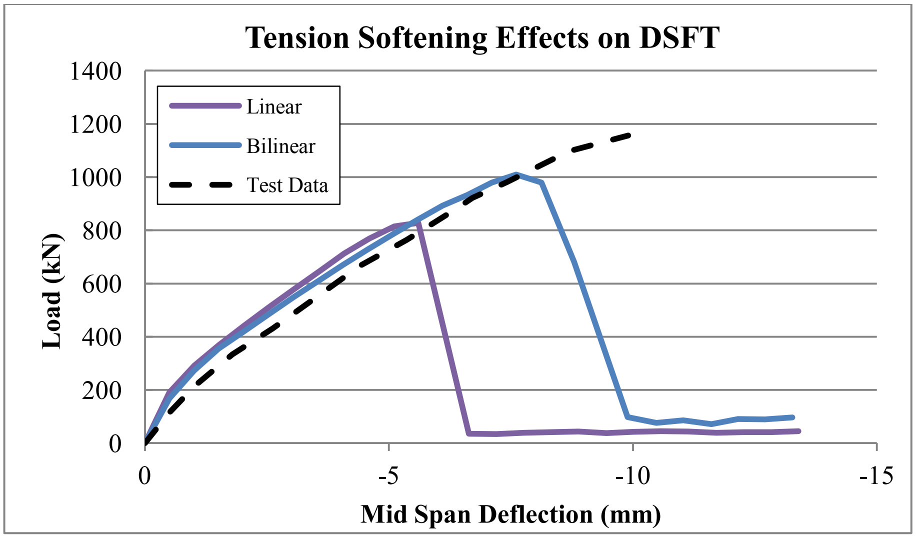

Figure 3.19: Effect of tension softening model on load deformation (DSFM)

The effects are similar in both cases, although they are amplified in the case of the DSFM. This is due to the fact that the DSFM uses the fracture energy in calculating the ultimate tensile strain. Increasing the area under the tensile stress-strain directly increases the fracture energy. In both cases, the increase in strength and deformability is attributed to the fact that the principal tensile stresses do not fall to zero immediately after cracking, and cracked concrete is able to sustain a certain level of tensile stresses.

Dowel action is known as the shear contribution of the flexural reinforcement in resisting stresses at a crack. The model implemented in VecTor2 is based on the slip displacement at the crack and is therefore only implemented when the DSFM is selected as the basis for analysis. The contribution of the flexural reinforcement to the shear capacity is calculated using the Tassios model as described in Wong and Vecchio (2002). The effect of considering dowel action on the load deformation characteristics can be observed in Figure 3.20. The other than the selection of the DSFM, default values were selected for the comparison.

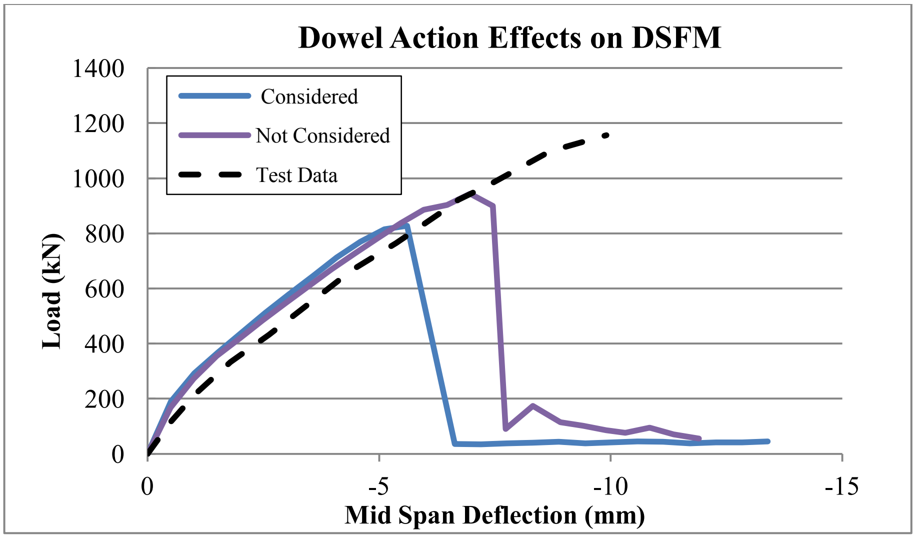

Figure 3.20: The effect of dowel action on load deformation

The effects of incorporating the dowel action model on load deflection curves are presented in the Figure 3.20. The stiff steel dowel of the flexural reinforcement impacts the strength negatively in this case. This decrease in strength and ductility can be explained by the use of default values for concrete properties and material model. Stiffer dowels leads to earlier cracking in elements near the flexural reinforcement and, in combination with the strict crack width limit imposed by the default selections, impacts the ductility and strength of the beam by reaching this limit earlier than if dowel action is not considered.

3.5 Summary of Modelling Methodology

Shear-critical RC beams are modelled with 4-node plane-stress rectangular composite elements. These elements smear steel reinforcement within the material matrix and are used in two distinct ways to model shear reinforcement: (i) the shear reinforcement is smeared throughout in non-critical sections, and (ii) the shear reinforcement is locally smeared (LS) at the location of the stirrups in critical sections. Flexural reinforcement is modelled using simple truss elements, and perfect bond is assumed. A corrosion-induced cracking model is implemented in the FE analysis by introducing fictitious pre-stressed steel smeared horizontally within the affected LS elements. These elements are then pre-strained in compression causing expansion and provoking cracking within surrounding elements. The pre-straining level is calculated based on the level of corrosion damage using a thick-wall cylinder analogy for the concrete cover.

Default values were selected for most of the material models and parameters available within VecTor2. However, some specific models were selected for the analysis based on the parametric analyses of available material model discussed in this chapter. Concrete in compression was modelled using Popovic's constitutive model. This choice is based on the fact that the behavior can be affected by both the modification of the initial tangential stiffness and the peak compressive strain. Popovic's model is less sensitive to the variation of both parameters. The tensile strength of concrete f'_t was set as the default value given by VecTor2, which is defined as $0.33\sqrt{f'_c}$ (MPa).

The selected model to simulate the behaviour of concrete in shear was the DSFM, simply because it better depicts the actual behaviour of shear critical beams. Furthermore, the stress and slip limits at a crack are already incorporated within the DSFM formulation, and it therefore eliminates the choice of models for this limit. It is also able to incorporate the doweling effect of longitudinal reinforcement. The crack width limit was set at 10 mm and the tension-softening model selected for the FE analysis was the bi-linear model. This model yields better overall results for shear-critical members, as it allows the cracks to form at a slower rate and redistributes stresses to other mechanisms. This enables for greater deformability at later loading stages and yields a softer response near peak regions.

Chapter 4 Finite Element Model Validation

4.1 Introduction

This chapter presents the validation of the finite element model presented in Chapter 3. First, the use of a “local smeared” (LS) reinforcement to model stirrups is tested against published data. As this technique isolates the shear reinforcement, it allows for the modification of bar properties based on corrosion of the specific stirrup, and the incorporation of a crack-inducing model. The validation is done in order to obtain a confirmation that the LS modeling technique captures the overall behavioral response as well as the ultimate strength and related deflection of shear-critical RC beams. In addition, validation is further conducted to determine if the cracking model can be successfully incorporated within a 2 dimensional plane-stress problem and properly induce cracking in the surrounding concrete.

4.2 Modeling Shear-Critical RC Beams

Modelling shear-critical RC members is a particularly challenging task. The shear capacity of RC relies on a combination of different mechanisms, and the response is highly non-linear where behavior is attributed not only to material properties but also to geometrical configurations of reinforcement and loading, e.g., shear-span-to-depth ratio. The choice of the VecTor2 as the FE modeling software is based on the fact that it implements the newest constitutive models for concrete, modified compression field theory for example, and allows the user to select the specific constitutive models, shear limits and crack width limits as it is deemed acceptable. This section presents the modelling details required to analyze RC beams under shear.

For shear critical beams, reinforcing steel corrosion does not affect the behavior in the same way as it does in flexural dominant beams. Most often, shear critical beams, deep and short spanned beams, have properly anchored flexural reinforcement to enable the shear resistance mechanisms to develop. Depending on the shear-span-to-depth ratio (a/d) and reinforcement detailing, different types of load transfer mechanisms can develop. These transfer mechanisms are:

- shear resistance of the compression zone;
- aggregate interlock;
- steel contribution to shear resistance from stirrups; and
- dowel action from flexural reinforcement.

This leads to distinct stress distribution within a beam and failure mechanism, such as:

- tied arch ($a/d < 1.5$);
- strut and tie ($1.5 < a/d \leq 2.5$); and
- beam action ($a/d > 2.5$).

In cases where shear governs behaviour, the shear resistance highly depends on the resistance of the concrete struts in compression, and on the tension developed at the shear reinforcing steel. In order to capture the effects of corrosion on both concrete and steel components, it is not sufficient to simply reduce the area of available steel affected by corrosion. The damage to the concrete component, such as corrosion-induced cracking, cannot be neglected, as it is a major contributor to shear strength. In many cases, researchers have simply taken the effects on concrete into account by removing the deemed damaged concrete (Higgins et al. 2011). This is reflected in the available concrete area, where in the case of heavy damage is clearly identified in the form of cracking, spalling and delamination of the concrete cover. Since one of the shear transfer mechanisms depends on aggregate interlock, what are the effects of increasing cracking in the core concrete of the section? How can one take the effects of damage in concrete if telltale signs are not evident at the surface? This work aims at inducing corrosion damage in concrete while taken into account the effects on the steel reinforcement. This is done by using a corrosion-inducing cracking model. The procedure is validated against published data and presented in the following sections.

4.3 Test Specimens

Higgins et al. (2003) tested a series of shear critical RC beams to study the effects of shear reinforcement corrosion on their shear capacity. The results of their test program were the basis of validation for this FE work. The test program looked at different scenarios of shear critical beams, whose shear reinforcement was subjected to accelerated corrosion for different periods of time, and therefore different levels of attained damage. It is important to note that the corrosion damage was isolated to the shear reinforcement and flexural reinforcement was left undamaged. First, the LS model was validated against the control specimen, in which none of the reinforcement was corroded. Second, a cracking model was introduced in the analyses in addition to reduction of the shear reinforcement cross-sectional area, and the numerical results were validated against the published data for the different levels of corrosion.

The specimens chosen for validation were specifically designed to be shear critical (Higgins et al. 2003). The beams underwent accelerated corrosion, which was applied only to the shear reinforcement of the critical section of the member. In total, 14 beams were tested by the authors. A control beam (Beam 10RA) was not subjected to corrosion. The corrosion levels for the other beams ranged between low corrosion penetrations (Beam 10RB), moderate (Beam 10RC) and high levels (Beam 10RD). Each tested series consisted of 4 beams, as shown in Table 5.1. All the beams are denoted by 10R, as they have a rectangular section with stirrup spacing of 10 inches (254 mm) in the critical section, as shown in Figure 4.1.

The test setup consisted of a four-point loading setup. Figure 4.1 describes the test setup as well as the reinforcement details. The loading cells were placed directly at the centre of the two points loads, which were 305 mm apart, yielding a shear-span-to-depth ratio a/d of 1.75. The beams were specifically designed to be shear critical, with one side of the span critically reinforced in shear and considered as the “Test Section”, as illustrated in Figure 4.1.

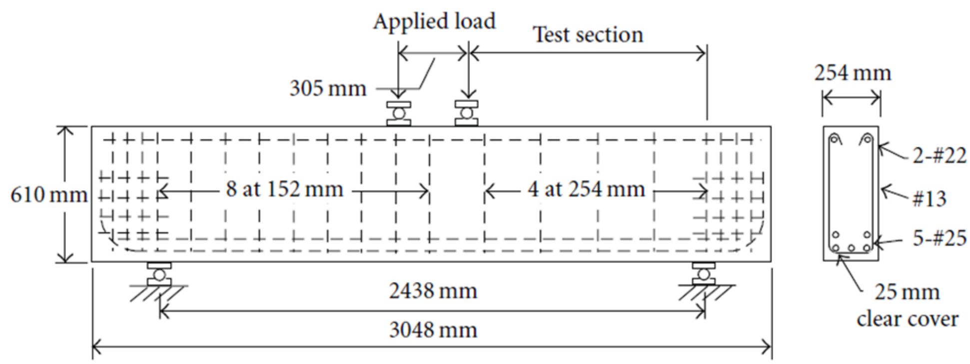

Figure 4.1: Test setup from Higgins et al. (2011)

The load-deflection curves recorded during the tests are shown in Figure 4.2. In this figure, the effects of shear reinforcement corrosion can be observed, with a decrease in both strength and mid-span deflection at ultimate load as the corrosion level increased. In addition, a softer response with increasing corrosion level can be observed and is attributed to the increase in damage.

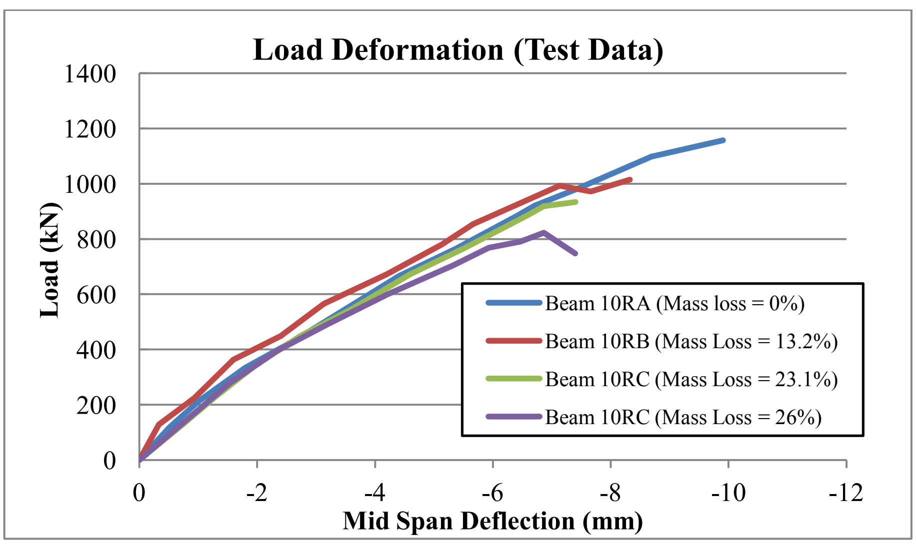

Figure 4.2: Load-deformation curves from Higgins et al. (2003)

In each case, the beams were first cast and then subjected to accelerated corrosion for different periods of times, to induce different levels of damage. Accelerated corrosion was applied only on the critical stirrups within the test section. The levels of corrosion and mass loss were measured only after the beams were tested to failure, after which the stirrups were extracted and mass loss measured. The published data was given in terms of average mass loss per leg of stirrup and maximum local mass loss, as tabulated in Table 5.1.

Table 4.1: Recorded Area and Mass Loss (Higgins et al. 2003)

Beam (Stirrup Leg)	Average Area		Local Minimum Area		Local /Average
	Area in^2 (cm^2)	% M_{loss}	Area in^2 (cm^2)	% M_{loss}	
10RB					
S2-1	0.172 (1.11)	14	0.14 (0.903)	30	0.81
S2-2	0.175 (1.13)	12.7	0.156 (1.01)	22	0.89
S3-1	0.177 (1.14)	11.7	0.127 (0.819)	36.5	0.72
S3-2	0.171 (1.10)	14.6	0.128 (0.826)	36	0.75
10RC					
S2-1	0.158 (1.02)	20.9	0.155 (1.00)	22.5	0.98
S2-2	0.142 (0.918)	28.9	0.0775 (0.500)	61.3	0.54
S3-1	0.161 (1.04)	19.7	0.144 (0..929)	28	0.9
S3-2	0.154 (0.994)	23	0.121 (0.780)	39.6	0.79
10RD					
S2-1	0.125 (0.806)	37.5	0.0 (0.0)	100	0
S2-2	0.112 (0.725)	43.9	0.046 (0.297)	77	0.41
S3-1	0.174 (1.12)	13.3	0.162 (1.04)	19	0.93
S3-2	0.183 (1.18)	8.5	0.158 (1.02)	21	0.86

The pre-straining introduced in the calculations to account for corrosion-induced cracking was calculated based on the average mass loss for each stirrup leg, and it was then distributed over the section using Eq. 3.12 from Chapter 3. The local minimum cross-sectional area was not used, as it was found that using average mass loss yielded better results.

4.4 Validation of LS model

Prior to validating the corrosion-induced cracking model as proposed in chapter 3, the use of LS elements as stirrups was tested to ensure that they properly simulate the behaviour prior to incorporating any corrosion damage. They were tested against the control specimen from the Oregon beams (Beam 10RA). The simulations are compared against overall stiffness and ultimate load and deflection. The failure mechanism is compared as well by means of identifying and comparing the failure crack patterns that were reported during the test.

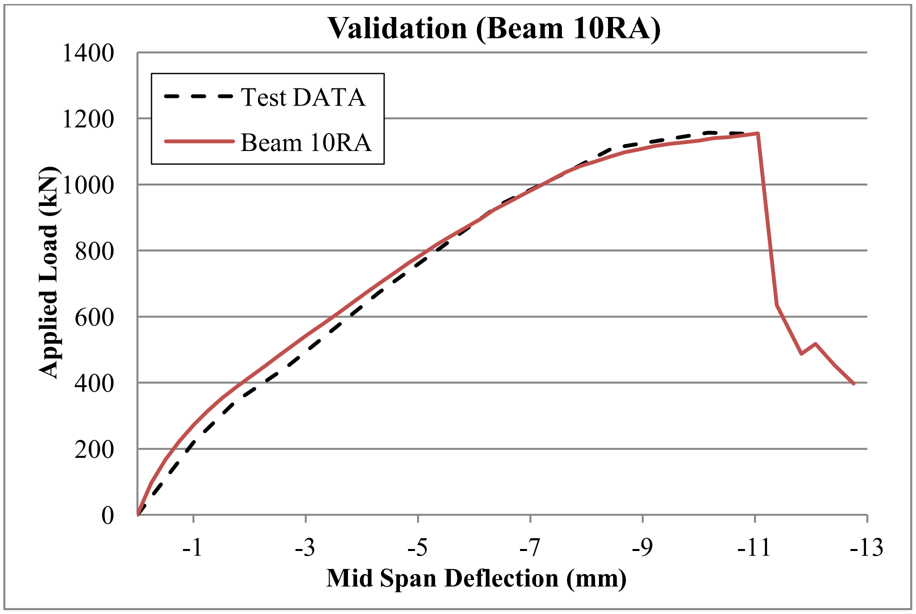

Figure 4.3: Load-deformation for control beam and LS model

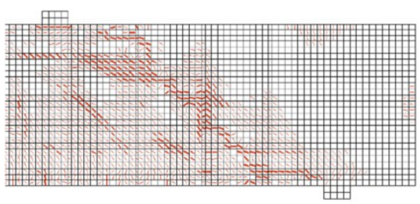
a)

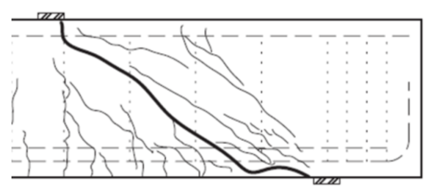
b)

Figure 4.4:(a) Cracking generated by finite element model at failure; (b) Cracking map at failure for test specimen (Higgins et al. 2003)

As it is shown in Figure 4.3, there is strong agreement on the overall stiffness and load-deformation behavior for the control beam 10RA, although the ultimate strength and deflection are slightly over estimated. Furthermore, the modelling approach adopted here properly simulates the failure mode as well as the cracking patterns at ultimate load, as illustrated in Figure 4.4(a) and (b).

4.5 Validation of Corroded Beams

In addition to reducing the stirrup cross-sectional area due to corrosion, corrosion-induced damage in concrete is also incorporated in the form of a corrosion-cracking model, as described in Chapter 3. The affected steel properties are modified based on mass loss and the remaining available area of non-corroded steel. For the test specimens where the stirrups were corroded, the FE model was run when only the steel cross-sectional loss was introduced, according to Eq. 3.8 from Chapter 3, and when both the loss in steel area and corrosion-induced cracking were considered, Eqs. 3.11 and 3.12., The pre-strain necessary to induce cracking was calculated using the data for the average area loss of each leg, as given in Table 4.1. In each case, this pre-strain is calculated based on the respective stirrup and corrosion level modelled. The input data for the cases where pre-strains are considered can be found in Table 4.2.

The data from Table 4.2 is calculated based on the reported data for average mass loss of the stirrup section (Higgins et al. 2003). As previously described in the crack inducing model, the strains are calculated based on the increase in diameter of the bar from its original value and the diameter of the thick wall cylinder surrounding bar. The increase is easily calculated based on an assumption of mass ratio for the steel to corrosion transformation (here $\rho = 2$ is used), to which the affected area is multiplied then added to the remaining virgin steel in order to compute the expanded area and diameter. Assuming uniform corrosion, the expansion is simply the difference between the diameter of the expanded area and the original diameter of the bars. In order to introduce it within the FEM, strains are averaged based on the area occupied by the thick wall cylinder on the member's sectional area.

Table 4.2: Pre-strains inducing cracking

Stirrup and Leg	Geometric and Corrosion Strains									
	M_{Loss}	μ	b_e	c	A_v	d	A_v'	d'	ε	ε
	%		mm	mm	mm^2	mm	mm^2	mm	mstrain	mstrain
Beam 10RB										
ST 1 -1	14	2	254	25.4	110.9	11.88	165.1	14.50	27.06	7.03
ST 1-2	12.7	2	254	25.4	112.6	11.97	161.8	14.35	24.70	
ST 2-1	11.7	2	254	25.4	113.9	12.04	159.2	14.24	22.87	6.01
ST 2-2	14.6	2	254	25.4	110.2	11.84	166.7	14.57	28.14	
Beam 10RC										
ST 1 -1	20.9	2	254	25.4	102.0	11.40	182.9	15.26	39.18	10.14
ST 1-2	28.9	2	254	25.4	91.7	10.81	203.6	16.10	52.52	
ST 2-1	19.7	2	254	25.4	103.6	11.48	179.8	15.13	37.12	9.59
ST 2-2	23	2	254	25.4	99.3	11.25	188.3	15.49	42.75	
Beam 10RD										
ST 1 -1	37.5	2	254	25.4	80.6	10.13	225.8	16.95	66.13	16.90
ST 1-2	43.9	2	254	25.4	72.4	9.60	242.3	17.56	75.82	
ST 2-1	13.3	2	254	25.4	111.8	11.93	163.3	14.42	25.79	6.69
ST 2-2	8.5	2	254	25.4	118.0	12.26	150.9	13.86	16.92	

4.5.1 Low Corrosion

In the case of low-level corrosion, the average mass loss for the affected stirrups was 13.2%. Using the equations in Chapter 3 to determine the strain within the thick-wall cylinder surrounding the stirrup legs and then distributing it over the section, the pre-straining introduced in the calculations was around 5.9×10^{-3} longitudinal strains for both stirrups. The effects of including and excluding the effects of pre-straining are observed in Figure 4.5.

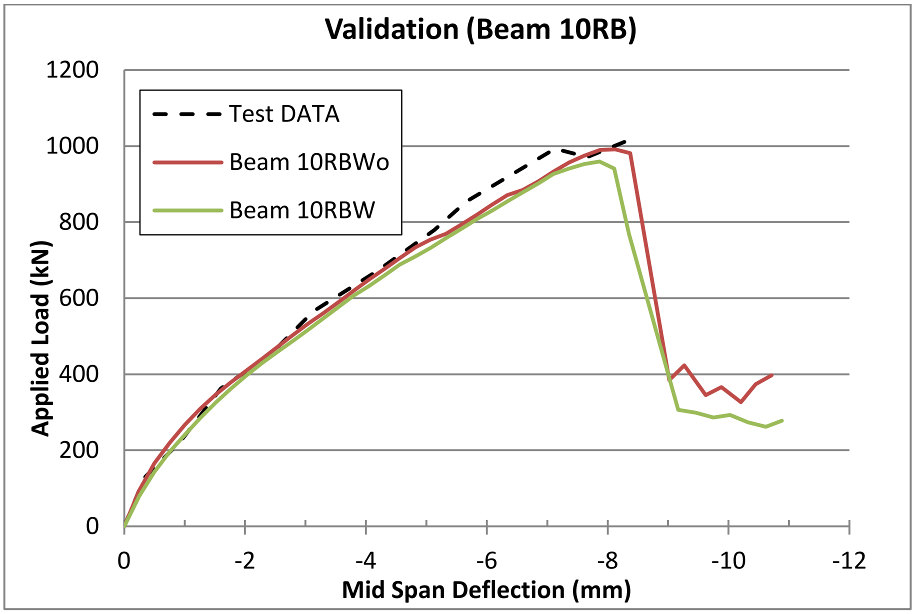

Figure 4.5: Validation of FEM for low levels of corrosion

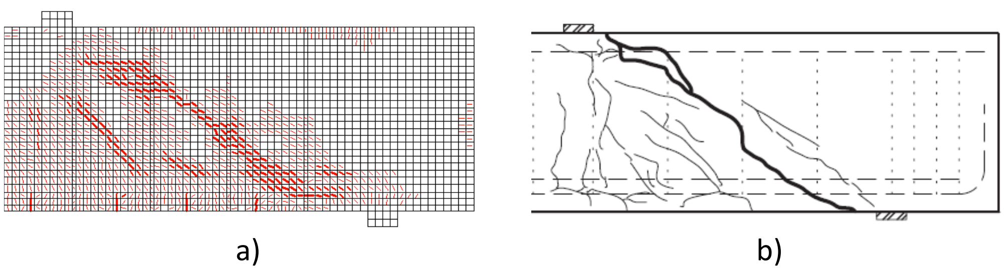

Figure 4.6: a) Cracking prediction for low corrosion without pre-straining, b) Crack map for beam 10RB (Higgins et al. 2003)

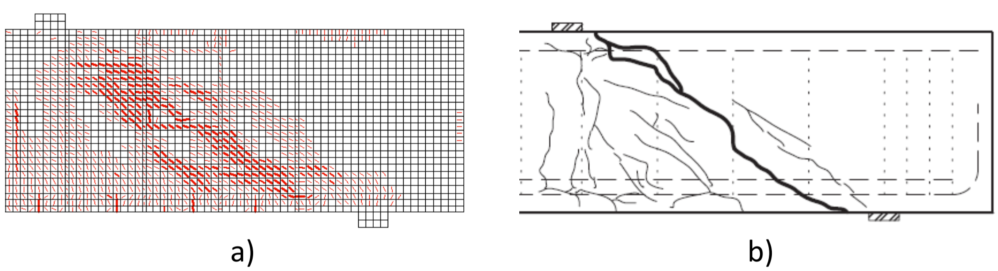

Figure 4.7: a) Cracking prediction for low corrosion with pre-straining, b) Crack map for beam 10RB (Higgins et al. 2003)

Figure 4.5 shows the load-deflection curve for the beam with low corrosion levels (13.2% loss). The finite element results are plotted against the test data for both with (Beam 10RBW) and without pre-straining (Beam 10RBWo). Both responses follow the test data reasonably well. The stiffness of the RC beam is properly reproduced. Although the finite element model without pre-straining seems to better estimate ultimate strength and deflection, the one with pre-straining is a bit more conservative in its estimates. The effect of pre-straining can be noticed by a slight decrease in strength and ultimate deflection. As observed in Figure 4.6(a) and Figure 4.7(a), both finite element results also approximate the crack pattern properly. The crack prediction of both models properly represents the actual failure mode, with the one with pre-straining having more damage as expected (Figure 4.6 (b) and Figure 4.7 (b)).

4.5.2 Moderate Corrosion

In the moderate corrosion-level validation, the average mass loss was 23.6%. Both stirrups corroded in a similar way and resulted in a calculated input pre-strain of 10×10^{-3} in both cases.

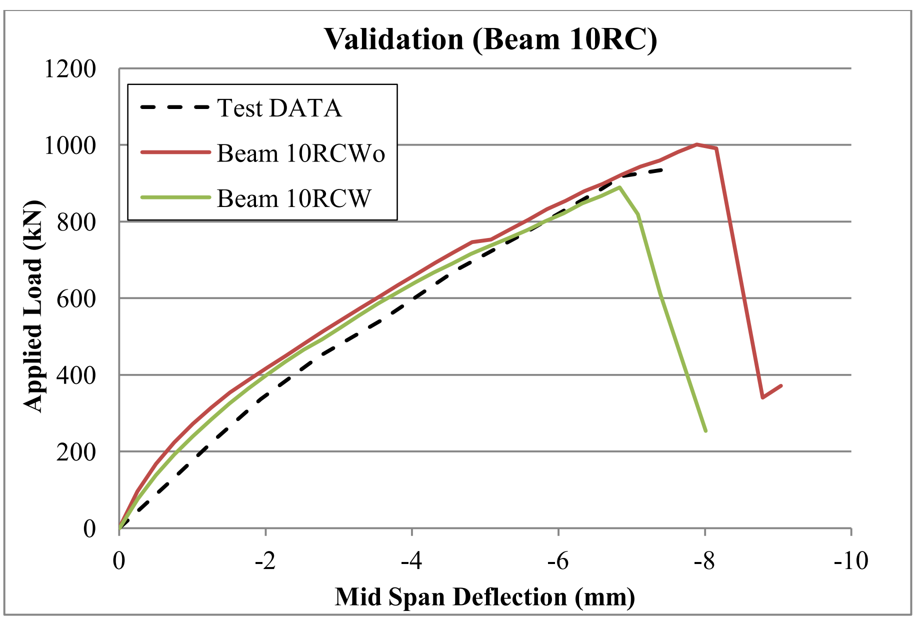

Figure 4.8: Validation of FEM for moderate levels of corrosion

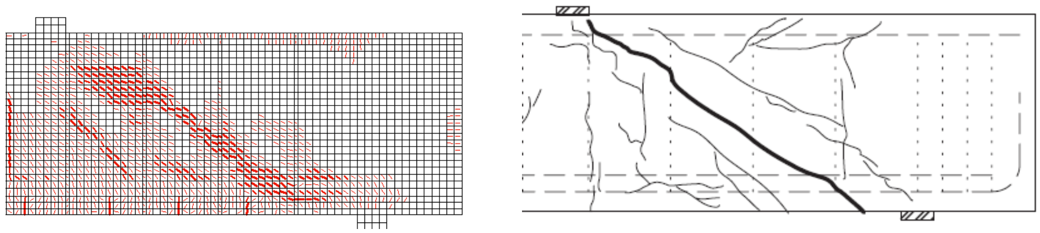

a) b)

Figure 4.9: a) Cracking prediction for moderate corrosion without pre-straining, b) Crack map for beam 10RC (Higgins et al. 2003)

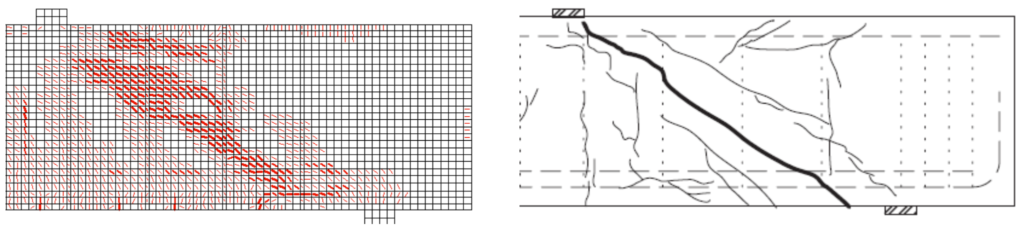

a) b)

Figure 4.10 a) Cracking prediction for moderate corrosion with pre-straining, b) Crack map for beam 10RC (Higgins et al. 2003)

The load-deformation response for the beam with moderate corrosion levels in the stirrups (23.1% loss) is illustrated in Figure 4.8. For moderate levels of corrosion, both finite element models properly simulate the stiffness, with the model with pre-straining having a slightly better estimate. Both models properly estimate ultimate strength and deflection, with similar percentage of divergence with respect to the test data, with the model that includes pre-straining being on the conservative side. The cracking patterns predicted by both analyses are shown in Figure 4.9 and Figure 4.10. Again, when predicting cracking, both models agree with the failure mode, with the pre-straining model inducing more damage and providing a slightly better approximation of the failure crack pattern.

4.5.3 High Corrosion

At high corrosion levels, one of the stirrup legs was affected more than the other. An average mass loss of nearly 41% was attained for the critical stirrup leg, compared to only 11% for the other one. This led to an oddly shaped failure cracking pattern, where there was a clear rupture of one of the severely damaged stirrups. The calculated input pre-strain for the severely corroded stirrup was 17×10^{-3} compared to only 7×10^{-3} for the other stirrup.

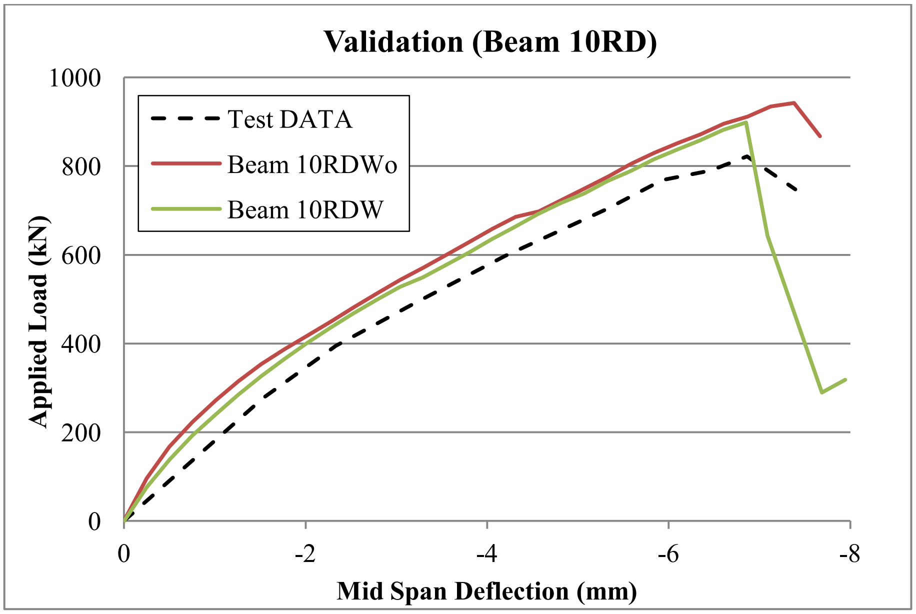

Figure 4.11 Validation of FEM for high levels of corrosion

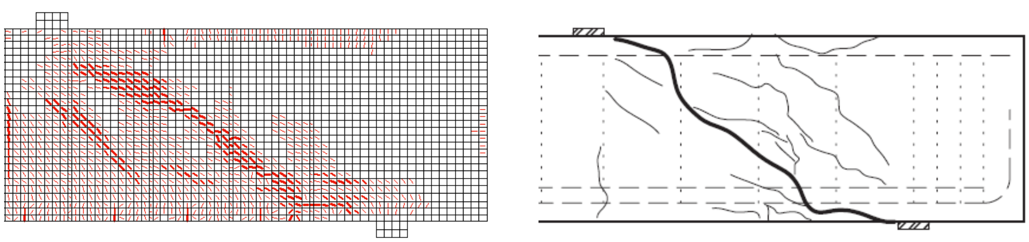

a) b)

Figure 4.12 a) Cracking prediction for high corrosion without pre-straining, b) Crack map for beam 10RD (Higgins et al. 2003)

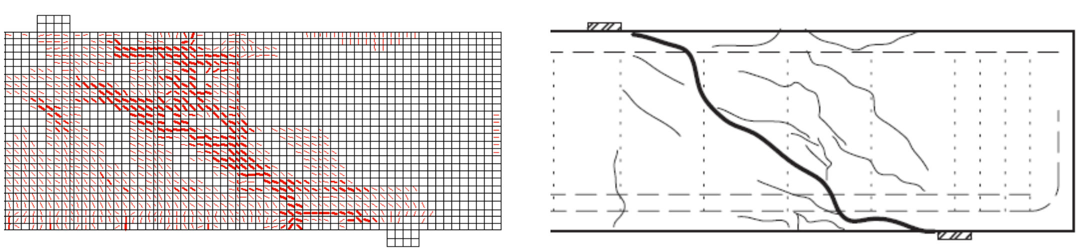

a) b)

Figure 4.13 a) Cracking prediction for high corrosion with pre-straining, b) Crack map for beam 10RD (Higgins et al. 2003)

Figure 4.11 shows the load-deformation response for the beam with high corrosion levels in the stirrups (26% loss). At high levels of corrosion, both models have an overall stiffer behaviour and a higher ultimate strength estimate than what was recorded. The model with pre-straining has a slightly better approximation of stiffness, with a more conservative estimate of the ultimate strength. Both cracking patterns, as shown in Figure 4.12 and Figure 4.13, properly simulate failure behaviour, although the model with pre-straining has a better overall simulation of the failure crack pattern as well as the overall level of induced damage (Figure 4.13 (a)). It is also able to capture a similar failure crack, as a greater amount of strain is concentrated to the severely affected stirrup, which results in greater damage at this location.

4.6 Validation Summary

After validation of the finite element results presented in this chapter, the following conclusions can be drawn:

1. The LS elements successfully model shear critical members and provide good agreement with published data.
2. Corrosion steel loss and corrosion-induced cracking are successfully introduced within a two-dimensional plane-stress problem.
3. The use of LS elements in combination with the cracking model also provides good agreement with published data.
4. Corrosion-induced cracking introduced as a pre-straining around the stirrups becomes more effective at higher levels of corrosion and better reproduces the induced damage at failure.

Since the models ability to reproduce shear critical RC beams affected by stirrup corrosion has been established in this chapter, finite element analyses will be used to perform a parametric analysis to identify critical variables/mechanisms to account in the shear capacity assessment of RC flexural members affected by corrosion of the steel stirrups.

Chapter 5 Parametric Analysis

5.1 Introduction

This chapter presents a parametric study of important design variables using the finite element methodology introduced in Chapter 3 and validated in Chapter 4. Two sets of RC beams tested and published in the literature were selected to perform the parametric analysis (Higgins et al. 2003; Vecchio and Shim 2004). Although the selection of parameters for the parametric analysis is governed by the chosen experimental tests, it does provide a wide range of useful design values. The basic parameter in shear design is the shear-span (a) to depth (d) ratio (a/d). CSA A23.3-04 (2004) limits the use of the shear design equations to members governed by beam action (a/d > 2). Where beams are classified as deep beams (a/d < 2), it is suggested that a strut-and-tie model be used to calculate their shear strength. The shear span-to-depth ratio of the Oregon beams and Toronto beams ranges from, which provides useful information on expected behavioural characteristics as well as different expected failure modes. In addition, these beams present various geometric configurations and material properties.

The analyses are conducted for different corrosion levels, as determined by the steel cross-sectional mass loss. The corrosion damage incorporated in this parametric evaluation focuses on the critical section of the beams. The critical section is that located within a distance *d* from the support or point load. In this case, the critical section is located within *d* from the point load, as it yields the combination of highest moment and shear forces in the member. Four different levels of corrosion were selected based on levels consideration found within the literature. First, FE analysis was conducted neglecting any effects of corrosion, in order to validate the behaviour against the published experimental test data. Then corrosion was incorporated at three levels: 10%, 30% and 50% mass loss, corresponding to low, moderate and high levels of corrosion, respectively. Corrosion-induced cracking was incorporated in the FE analysis following the procedure outlined in Section 3.3.

5.2 Parametric Testing Grid

This section presents the testing grid used for the parametric study. Two sets of experimental tests were selected to perform the parametric analysis. This section describes the geometric and material properties of the two sets of RC beams.

5.2.1 Oregon Beams

The first set of specimens used for the parametric analysis consists of 4 shear critical beams tested by Higgins et al. (2003). These are the beams against which the FE model was validated in Chapter 4. The beams were specifically designed as shear critical beams, and accelerated corrosion was applied only on the stirrups. Differences among beams in this series was the arrangement of shear reinforcement and its associated yielding strength. Table 5.1 lists the geometric and material properties of these beams in detail.

The corrosion for these beams is calculated based on the data that was available from the literature (Higgins et al. 2003). The mass loss was reported for each stirrup leg as average mass loss as well as maximum mass loss in the case of uneven corrosion. The mesh and FE setup is the same as previously validated.

Table 5.1: Oregon Beam Properties

Beam (i.d)	Geometric							Concrete			Corrosion		Shear Reinforcement				Flexural Reinforcement				
	h	b_w	d	b_{wd}	L	S	a/d	f'_c	e_0	E_c	μ	Mass Loss	A_v	ρ_v	f_{yv}	s	A_s	A_s'	ρ_s	f_y	E
	mm	mm	mm	mm^2	mm	mm		MPa	mm/m	GPa		%	mm^2		MPa	mm	mm^2	mm^2		MPa	GPa
Series A																					
Beam 10RA	610	254	521	132334	3048	2438	2.05	33.1	2.9	31.6	2	0	253	0.00393	441	254	2534	776	0.01635	496	200
Beam 10RB	610	254	521	132334	3048	2438	2.05	33.1	2.9	31.6	2	13.2	220	0.00341	412	254	2534	776	0.01635	496	200
Beam 10RC	610	254	521	132334	3048	2438	2.05	33.1	2.9	31.6	2	23.1	191	0.00296	390	254	2534	776	0.01635	496	200
Beam 10RD	610	254	521	132334	3048	2438	2.05	33.1	2.9	31.6	2	26	166	0.00257	384	254	2534	776	0.01635	496	200

5.2.2 Toronto Beams

The second set of beams is that adopted by Vecchio and Shim (2004) for the experimental re-examination of the classic beams originally tested by Bresler and Scoderlis in 1963, which consisted of three-point beam tests. The test setup and related data has become benchmark data in determining the shear capacity of RC beams and cited in numerous studies. It is also often used frequently to validate FE models as it covers a large range of important design parameters in shear design. The test setup of these beams was specifically designed to test the different ranges of shear behaviour in RC. It showcases typical failure mechanisms in shear dominated loading scenarios. The shear span-to-depth ratio is within the appropriate range for the use of the CSA A23.3-04 (2004) general method (a/d >2), and the effects of stirrup corrosion on design parameters can therefore be successfully studied. This test setup was successful in determining three distinct shear failure patterns:

- Diagonal-tension (D-T) failure. It is characterized by the formation of a critical diagonal crack and soon followed by sudden failure. This failure is typically accompanied with splitting cracks in the compression zone near the loading point and splitting cracks along the flexural reinforcement leading towards the supports.
- Shear-compression failure (V-C). This failure mechanism begins by splitting cracks forming in the compression zone near the loading point and propagates to a diagonal crack, which is soon followed by a shear crack forming near the loading point. The failure soon follows the formation of the diagonal shear cracks, but is generally not associated with crack formation along the tensile flexural reinforcement.
- Flexural-compression failure (F-C). This failure mechanism is associated to over-reinforced members. The compression block fails by crushing prior to the yielding of the flexural steel. It can be associated with small shear cracks.

Although the test setup adopted from the original classic beams tests was slightly modified by Vecchio and Shim (2004) in their study, it followed the general concept of the original work. The test considers 4 series, one of which neglects web reinforcement and three containing different ratios of web reinforcement based on the thickness of the beams. The focus of the work presented in this thesis is on the three series containing web reinforcement, as the scope of this research is on the effect of corrosion of web reinforcement on behaviour and strength of RC beams. Figure 5.1 illustrates the sectional dimensions and reinforcement arrangement of each of the beams. The three series are denoted by the letters “A”, “B” and “C”, with beam widths of 305 mm, 229 mm, and 152 mm, respectively. All of the series are separated into three span lengths as illustrated in Figure 5.2: 3.66 m, 4.57 m, and 6.40 m, denoted by “1”, “2” and “3”, respectively. The web reinforcement spacing and diameter are dependent on the member width, with reinforcement ratios of 0.1%, 0.15% and 0.2% for series A, B and C, respectively. The flexural reinforcement is dependent on the span length, and it was specifically increased to enforce shear failure in all cases. The sectional and material properties for all of the Toronto beams are tabulated in Table 5.2, Table 5.3 and Table 5.4.

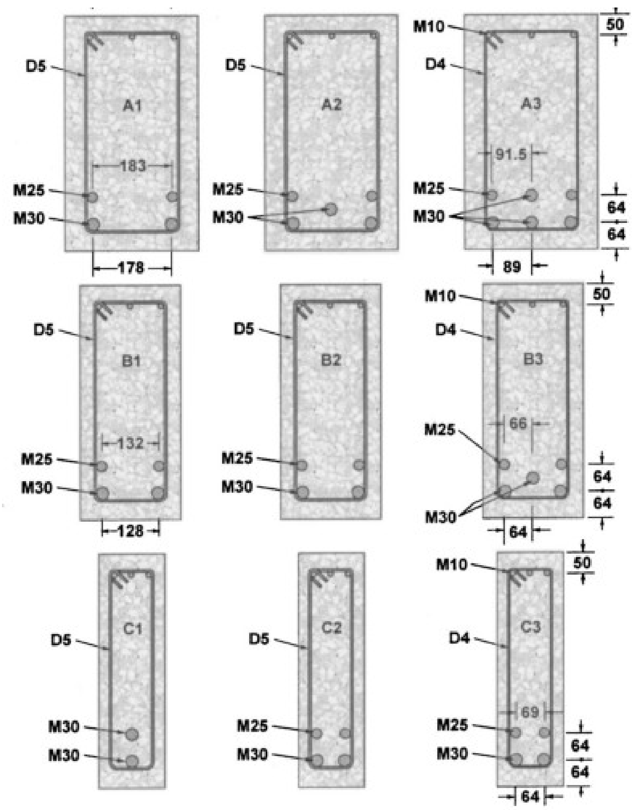

Figure 5.1: Toronto beams sectional properties (Vecchio and Shim 2004)

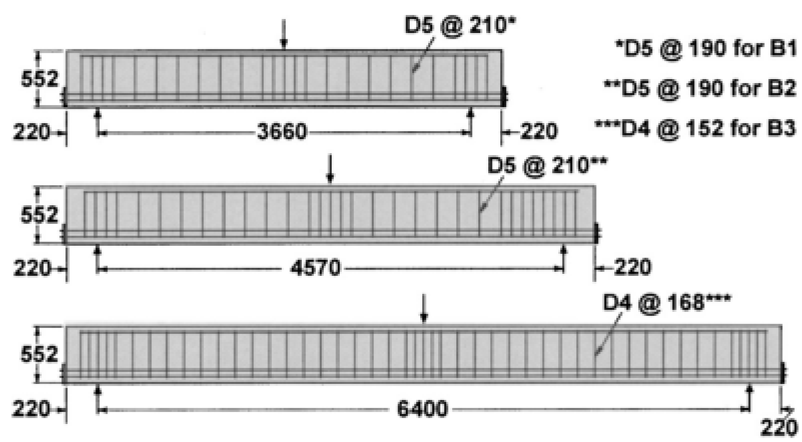

Figure 5.2: Test setup and span lengths used in Toronto beams (Vecchio and Shim 2004)

Table 5.2: Toronto Beams Series A Properties

Beam (i.d)	Geometric							Concrete			Corrosion		Shear Reinforcement				Flexural Reinforcement				
	h	b_e	d	$b_e d$	L	S	a/d	f'_c	e_0	E_c	μ	M_{Loss}	A_v	ρ_v	f_{yv}	s	A_s	A_s'	ρ_s	f_y	E
	mm	mm	mm	mm^2	mm	mm		MPa	mm/m	GPa		%	mm^2		MPa	mm	mm^2	mm^2		MPa	GPa
Series A																					
VSA1V	552	305	457	139385	4100	3660	4.00	22.6	1.6	36.5	2	0	64.4	0.00101	600	210	2400	300	0.01426	440	200
VSA1L	552	305	457	139385	4100	3660	4.00	22.6	1.6	36.5	2	10	58.0	0.00090	570	210	2400	300	0.01426	440	200
VSA1M	552	305	457	139385	4100	3660	4.00	22.6	1.6	36.5	2	30	45.1	0.00070	510	210	2400	300	0.01426	440	200
VSA1H	552	305	457	139385	4100	3660	4.00	22.6	1.6	36.5	2	50	32.2	0.00050	450	210	2400	300	0.01426	440	200
VSA2V	552	305	457	139385	5010	4570	5.00	25.9	2.1	32.9	2	0	64.4	0.00101	600	210	3100	300	0.01841	440	200
VSA2L	552	305	457	139385	5010	4570	5.00	25.9	2.1	32.9	2	10	58.0	0.00090	570	210	3100	300	0.01841	440	200
VSA2M	552	305	457	139385	5010	4570	5.00	25.9	2.1	32.9	2	30	45.1	0.00070	510	210	3100	300	0.01841	440	200
VSA2H	552	305	457	139385	5010	4570	5.00	25.9	2.1	32.9	2	50	32.2	0.00050	450	210	3100	300	0.01841	440	200
VSA3V	552	305	457	139385	6840	6400	7.00	43.5	1.9	34.3	2	0	51.4	0.00100	600	168	3800	300	0.02257	440	200
VSA3L	552	305	457	139385	5010	4570	5.00	25.9	2.1	32.9	2	10	46.3	0.00090	570	168	3800	300	0.02257	440	200
VSA3M	552	305	457	139385	5010	4570	5.00	25.9	2.1	32.9	2	30	36.0	0.00070	510	168	3800	300	0.02257	440	200
VSA3H	552	305	457	139385	5010	4570	5.00	25.9	2.1	32.9	2	50	25.7	0.00050	450	168	3800	300	0.02257	440	200

Table 5.3: Toronto Beams Series B Properties

Beam (i.d)	Geometric							Concrete			Corrosion		Shear Reinforcement				Flexural Reinforcement				
	h	b_e	d	$b_e d$	L	S	a/d	f'_c	e_0	E_c	μ	M_{Loss}	A_v	ρ_v	f_{yv}	s	A_s	A_s'	ρ_s	f_y	E
	mm	mm	mm	mm^2	mm	mm		MPa	mm/m	GPa		%	mm^2		MPa	mm	mm^2	mm^2		MPa	GPa
Series B																					
VSB1V	552	229	457	104653	4100	3660	4.00	22.6	1.6	36.5	2	0	64.4	0.00148	600	190	2400	300	0.01899	440	200
VSB1L	552	229	457	104653	4100	3660	4.00	22.6	1.6	36.5	2	10	58.0	0.00133	570	190	2400	300	0.01899	440	200
VSB1M	552	229	457	104653	4100	3660	4.00	22.6	1.6	36.5	2	30	45.1	0.00104	510	190	2400	300	0.01899	440	200
VSB1H	552	229	457	104653	4100	3660	4.00	22.6	1.6	36.5	2	50	32.2	0.00074	450	190	2400	300	0.01899	440	200
VSB2V	552	229	457	104653	5010	4570	5.00	25.9	2.1	32.9	2	0	64.4	0.00148	600	190	2400	300	0.01899	440	200
VSB2L	552	229	457	104653	5010	4570	5.00	25.9	2.1	32.9	2	10	58.0	0.00133	570	190	2400	300	0.01899	440	200
VSB2M	552	229	457	104653	5010	4570	5.00	25.9	2.1	32.9	2	30	45.1	0.00104	510	190	2400	300	0.01899	440	200
VSB2H	552	229	457	104653	5010	4570	5.00	25.9	2.1	32.9	2	50	32.2	0.00074	450	190	2400	300	0.01899	440	200
VSB3V	552	229	457	104653	6840	6400	7.00	43.5	1.9	34.3	2	0	51.4	0.00148	600	152	3100	300	0.02452	440	200
VSB3L	552	229	457	104653	6840	6400	7.00	43.5	1.9	34.3	2	10	46.3	0.00133	570	152	3100	300	0.02452	440	200
VSB3M	552	229	457	104653	6840	6400	7.00	43.5	1.9	34.3	2	30	36.0	0.00103	510	152	3100	300	0.02452	440	200
VSB3H	552	229	457	104653	6840	6400	7.00	43.5	1.9	34.3	2	50	25.7	0.00074	450	152	3100	300	0.02452	440	200

Table 5.4: Toronto Beams Series C Properties

	Geometric							Concrete			Corrosion		Shear Reinforcement				Flexural Reinforcement				
	h	b_e	d	$b_e d$	L	S	a/d	f'_c	e_0	E_c	μ	M_{Loss}	A_v	ρ_v	f_{yv}	s	A_s	A_s'	ρ_s	f_y	E
Beam (i.d)	mm	mm	mm	mm^2	mm	mm		MPa	mm/m	GPa		%	mm^2		MPa	mm	mm^2	mm^2		MPa	GPa
Series C																					
VSC1V	552	152	457	69464	4100	3660	4.00	22.6	1.6	36.5	2	0	64.4	0.00202	600	210	1400	300	0.01669	440	200
VSC1L	552	152	457	69464	4100	3660	4.00	22.6	1.6	36.5	2	10	58.0	0.00182	570	210	1400	300	0.01669	440	200
VSC1M	552	152	457	69464	4100	3660	4.00	22.6	1.6	36.5	2	30	45.1	0.00141	510	210	1400	300	0.01669	440	200
VSC1H	552	152	457	69464	4100	3660	4.00	22.6	1.6	36.5	2	50	32.2	0.00101	450	210	1400	300	0.01669	440	200
VSC2V	552	152	457	69464	5010	4570	5.00	25.9	2.1	32.9	2	0	64.4	0.00202	600	210	2400	300	0.02860	440	200
VSC2L	552	152	457	69464	5010	4570	5.00	25.9	2.1	32.9	2	10	58.0	0.00182	570	210	2400	300	0.02860	440	200
VSC2M	552	152	457	69464	5010	4570	5.00	25.9	2.1	32.9	2	30	45.1	0.00141	510	210	2400	300	0.02860	440	200
VSC2H	552	152	457	69464	5010	4570	5.00	25.9	2.1	32.9	2	50	32.2	0.00101	450	210	2400	300	0.02860	440	200
VSC3V	552	152	457	69464	6840	6400	7.00	43.5	1.9	34300	2	0	51.4	0.00201	600	168	2400	300	0.02860	440	200
VSC3L	552	152	457	69464	6840	6400	7.00	43.5	1.9	34300	2	10	46.3	0.00181	570	168	2400	300	0.02860	440	200
VSC3M	552	152	457	69464	6840	6400	7.00	43.5	1.9	34300	2	30	36.0	0.00141	510	168	2400	300	0.02860	440	200
VSC3H	552	152	457	69464	6840	6400	7.00	43.5	1.9	34300	2	50	25.7	0.00101	450	168	2400	300	0.02860	440	200

The FE results are labeled as follows: *VS* is used as a prefix to designate the Vecchio-Shim beams, followed by the beam identification provided by the authors (note that the id designation relates to both the beam width and span length, e.g., A1 is related to a width of 305 mm and span length of 3,660 mm.) Finally, the corrosion level is identified by the letters *V*, *L*, *M* or *H*, where they refer to "non-corroded" (also used for validation), "low" (10% mass loss), "moderate" (30% mass loss) and "high" (50% mass loss) levels of corrosion, respectively.

The FE mesh was adopted from that of the validation beams and modified according to the specimen specification of the Vecchio-Shim beams. As the beams are symmetric in design and loading setup, only half the beams was meshed in order to maximize computing effort and reduce output time. In order to do so, the symmetric point at mid span was restrained in the x direction to replicate boundary condition of a full length specimen. This was only done for the specimen elements and the loading plate at mid span was unrestrained as it does not contribute to the resistance. Same meshing criterion where followed as discussed in the chapter 3. The Figure 5.3 shows an example of a typical meshing technique for a Toronto beam.

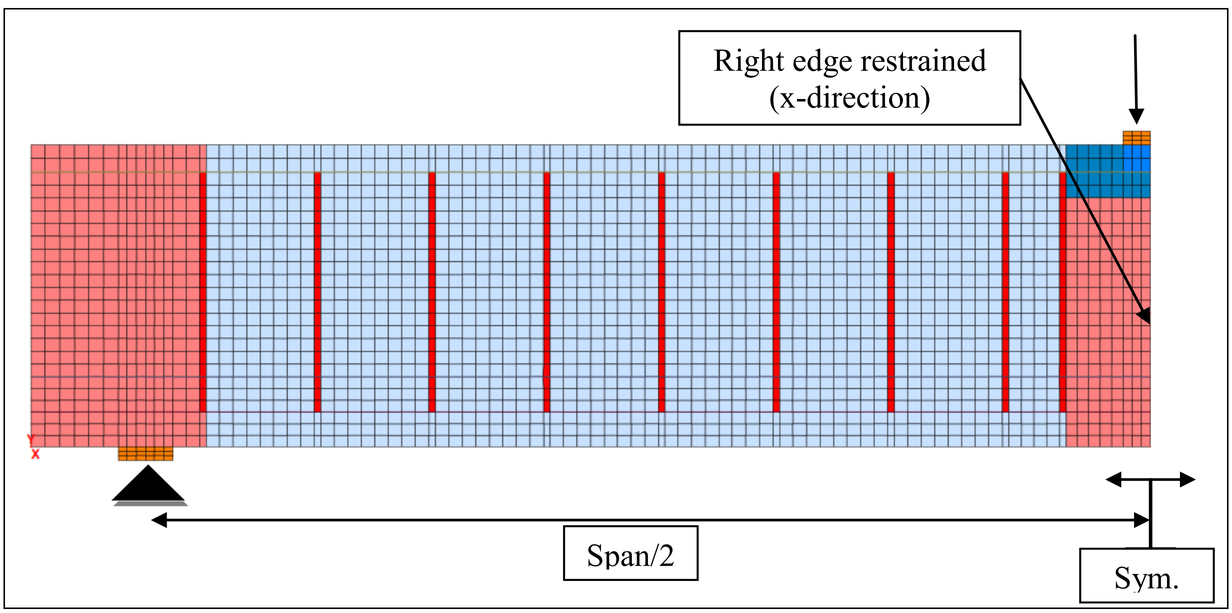

Figure 5.3: Toronto Beam FE mesh

Figure 5.4 plots the calculated strength from the finite element analysis against the test results of all the Toronto beams considered here. Note that in this comparison, corrosion is not introduced in the FE model as the original test setup was design to test shear behavioural ranges without corrosion. As observed from the figure, the finite element analysis provides a good estimate of the observed experimental strengths, with a mean value of the ratio between the two sets of results of 0.95 with standard a standard deviation of 0.05. Input parameters related to the decrease of steel cross-sectional area and concrete cracking due to corrosion for the Toronto beams are presented in Table 5.5 and 5.6.

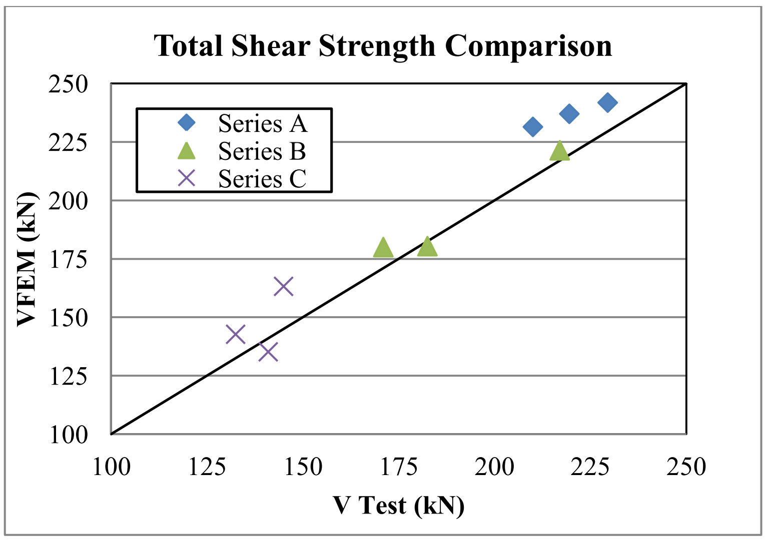

Figure 5.4: Shear strength prediction of the FEM against experimental data

Table 5.5: Corrosion Details and Strains (only span series 1 and 2)

Beam (i.d)	M_{Loss}	μ	b_e	c	A_v	d	A_v'	d'	ε_i	$\bar{\varepsilon}$
	%		mm	mm	mm^2	mm	mm^2	mm^2	mstrain	mstrain
Series A1 and A2										
Validation (V)	0	2	305	45	64.4	6.40	64.4	6.40	0.00	0.00
Low (L)	10	2	305	45	58.0	6.07	70.8	6.72	3.24	2.05
Moderate (M)	30	2	305	45	45.1	5.36	83.7	7.30	9.31	5.89
High (H)	50	2	305	45	32.2	4.53	96.6	7.84	14.93	9.44
Series B1 and B2										
Validation (V)	0	2	229	45	64.4	6.40	64.4	6.40	0.00	0.00
Low (L)	10	2	229	45	58.0	6.07	70.8	6.72	3.24	2.73
Moderate (M)	30	2	229	45	45.1	5.36	83.7	7.30	9.31	7.84
High (H)	50	2	229	45	32.2	4.53	96.6	7.84	14.93	12.57
Series C1 and C2										
Validation (V)	0	2	152	45	64.4	6.40	64.4	6.40	0.00	0.00
Low (L)	10	2	152	45	58.0	6.07	70.8	6.72	3.24	4.11
Modetate (M)	30	2	152	45	45.1	5.36	83.7	7.30	9.31	11.81
High (H)	50	2	152	45	32.2	4.53	96.6	7.84	14.93	18.93

Table 5.6: Corrosion Details and Strains (for span series 3)

Beam (i.d)	M_{Loss}	μ	b_e	c	A_v	d	A_v'	d'	ε_i	$\bar{\varepsilon}$
	%		mm	mm	mm^2	mm	mm^2	mm^2	mstrain	mstrain
Series A3										
Validation (V)	0	2	305	45	51.4	5.72	51.4	5.72	0.00	0.00
Low (L)	10	2	305	45	46.3	5.43	56.5	6.00	2.92	1.83
Modetate (M)	30	2	305	45	36.0	4.79	66.8	6.52	8.38	5.26
High (H)	50	2	305	45	25.7	4.04	77.1	7.01	13.43	8.43
Series B3										
Validation (V)	0	2	229	45	51.4	5.72	51.4	5.72	0.00	0.00
Low (L)	10	2	229	45	46.3	5.43	56.5	6.00	2.92	2.44
Modetate (M)	30	2	229	45	36.0	4.79	66.8	6.52	8.38	7.00
High (H)	50	2	229	45	25.7	4.04	77.1	7.01	13.43	11.23
Series C3										
Validation (V)	0	2	152	45	51.4	5.72	51.4	5.72	0.00	0.00
Low (L)	10	2	152	45	46.3	5.43	56.5	6.00	2.92	3.67
Modetate (M)	30	2	152	45	36.0	4.79	66.8	6.52	8.38	10.55
High (H)	50	2	152	45	25.7	4.04	77.1	7.01	13.43	16.92

5.3 Shear Capacity

This section presents the FE results of the effects of corrosion of the stirrups on the shear capacity of the beams described in Section 5.2. The numerical results are first presented in terms of the load-deformation response of the beams. This highlights the overall effects of corrosion on the load carrying capacity, the deformability as well as overall stiffness of the

RC member. The analysis data is then presented in terms of the residual strength of each beam at a particular level of corrosion damage relative to a beam without any corrosion.

5.3.1 Oregon Beams

Figure 5.5 shows the load-deformation response for the Oregon beams obtained from the FE analysis. From the figure, it is observed that a reduction in overall load-carrying capacity as well as ultimate deflection occurs with increasing levels of corrosion. Also observed in this figure, there is a slight decrease in stiffness as the corrosion damage increases.

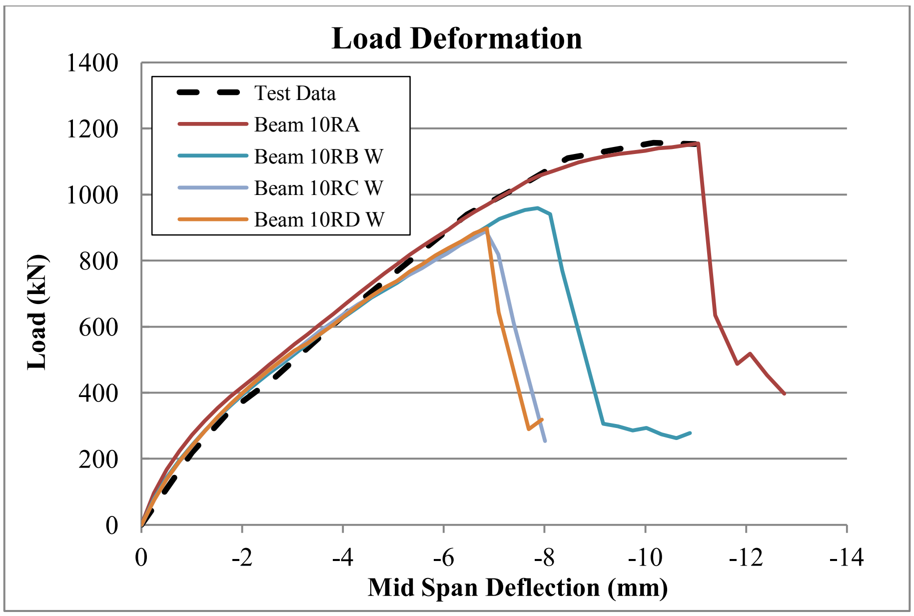

Figure 5.5: Load deformation response of Oregon beams obtained from FE analysis

Figure 5.6 present the shear strength loss of beam 10R relative to an uncorroded specimen for increasing levels of mass loss of the shear reinforcement. The FE results capture the overall strength loss when both the corrosion-induced cracking model is neglected (FEMw/o) and included (FEMw) in the analyses. The FE results that include the cracking model are however slightly conservative, whereas the FE analysis that neglects the effects of cracking has a relatively higher estimate of residual strength. Both models estimate a strength loss of around 20% for a stirrup average mass loss of 25%.

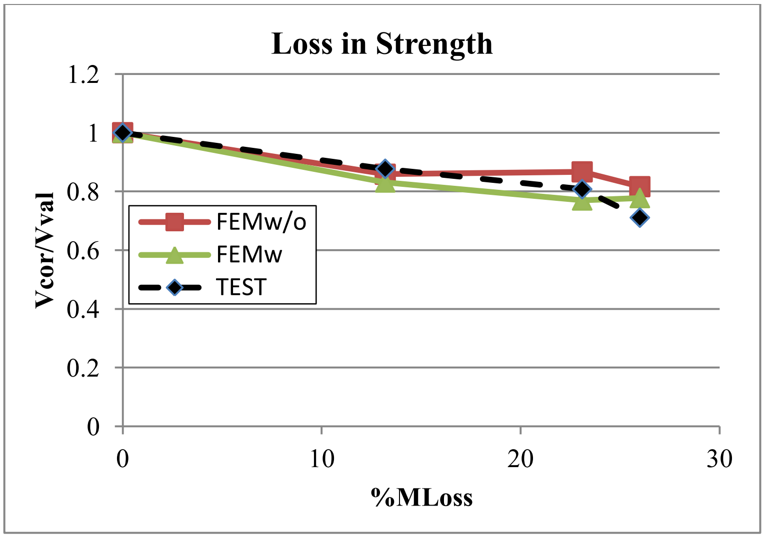

Figure 5.6: Strength degradation for beam 10R

5.3.2 Toronto Beams

The expected failure mechanism for the two shorter spans (series 1 and 2) is a shear-compression failure, whereas it is flexural-compression failure for the longer span (series 3). The change in failure modes can be studied by looking at the failure cracking pattern predicted by the FE analysis. It is important to note that in figures where cracking patterns are presented, red lines indicate a crack smaller than 1 mm, whereas thicker lines indicate a crack width greater than 2 mm. The exception is series A, where thinner lines indicate crack widths smaller than 2 mm, and thicker lines indicate crack widths greater than 4 mm.

5.3.2.1 Series A

Series A is the series with the largest beam width (305 mm). Shear reinforcement is spaced at 210 mm for the two shorter spans (series 1 and 2) and 168 mm for the longest span (series 3). It is also the beams with the least percentage of shear reinforcement, with a ratio of 0.1%, and therefore it has the smallest relative cracking-inducing strain for each of the corrosion levels considered.

Figure 5.7 shows the load-deformation response for beam A1 obtained from the FE analysis. It can be observed that there is a clear reduction in load-carrying capacity with increasing levels of corrosion. The mid-span deflection associated to ultimate strength also follows suit. The slope of the load-deformation response also softens with an increase in corrosion damage. The post-peak behaviour is affected with a reduction in deformability. All of the specimens follow the same sudden failure once the ultimate deflection is reached.

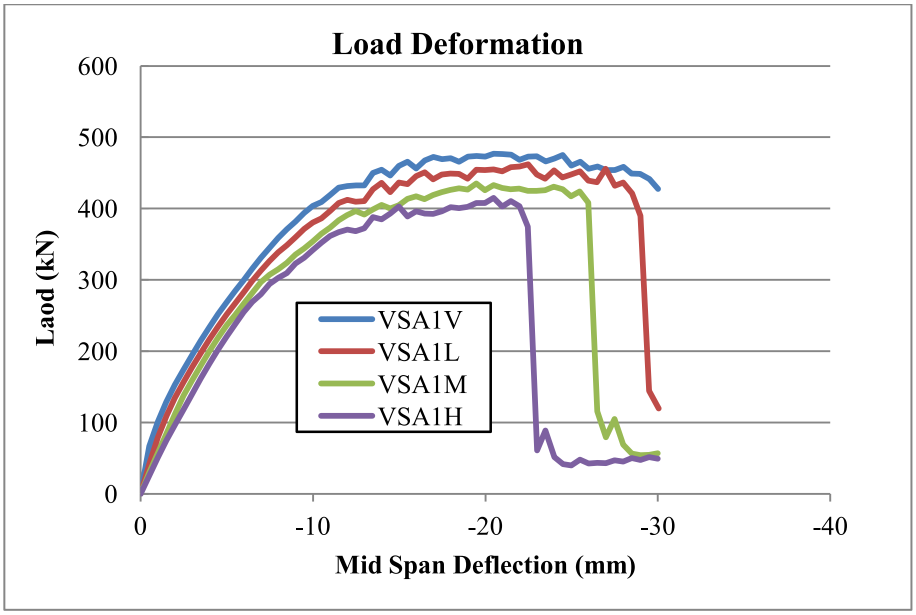

Figure 5.7: Load deformation response for specimen A1

The cracking pattern for specimen A1 can be observed in Figure 5.8. A softening of the primary crack is observed with increasing corrosion level. In addition to this, flexural cracks at mid span become shorter at higher corrosion levels. All specimens failed by a shear-compression failure in the analyses.

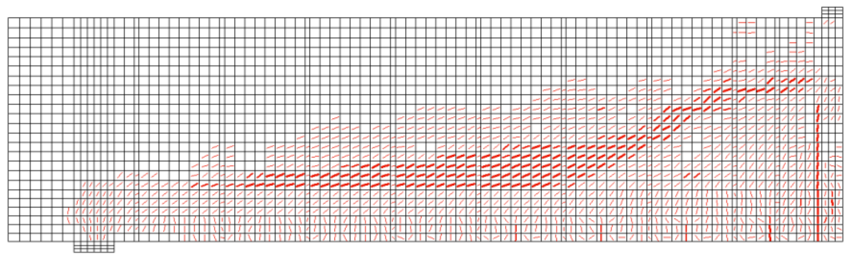

a) Specimen: VSA1V

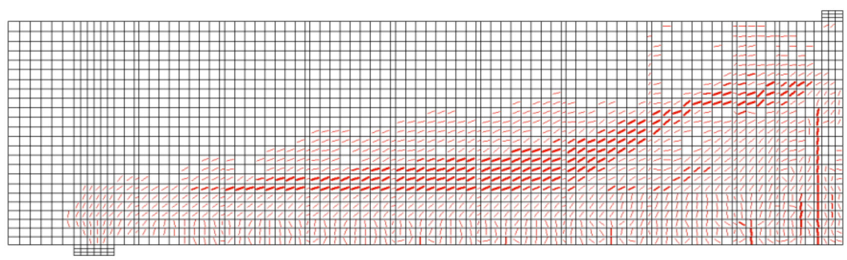

b) Specimen : VSA1L

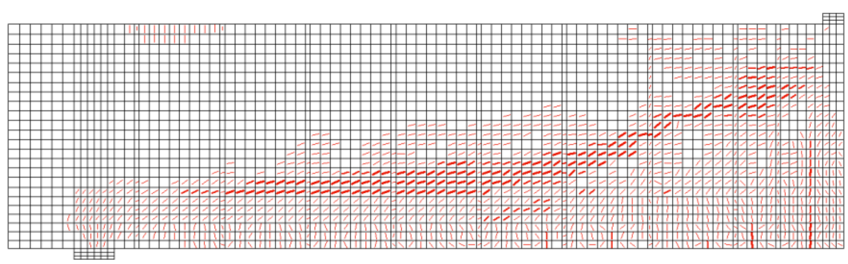

c) Specimen: VSA1M

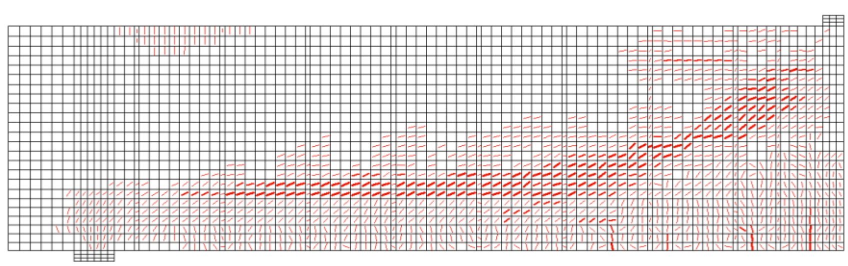

d) Specimen: VSA1H

Figure 5.8: Cracking pattern at ultimate load for specimen A1

Figure 5.9 shows the load-deformation response for beam A2 obtained from the FE analysis. Similar to specimen A1, a reduction of the load-carrying capacity is observed for increasing levels of corrosion damage. This reduction is more significant for specimens with stirrups corroded to moderate and high levels. Post-peak behaviour is greatly impacted from no- and low-corrosion levels to moderate and high ones. There is higher fluctuation in the loading near the peak value at high levels of corrosion, most likely associated to the increased level of cracking, where the aggregate interlock mechanism at the cracks has a higher impact on strength.

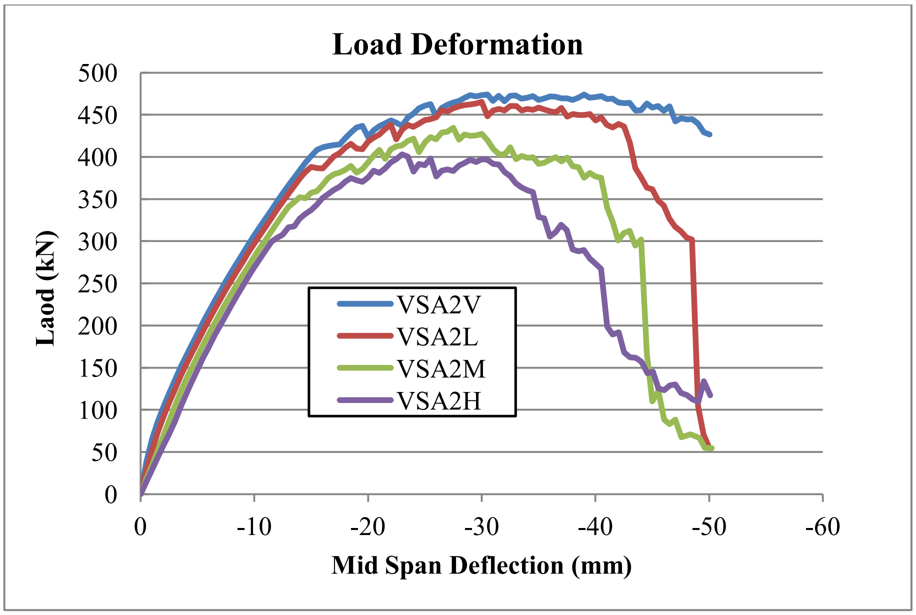

Figure 5.9: Load deformation response for specimen A2

The cracking patterns at ultimate load for specimen A2, illustrated in Figure 5.10, suggest that the crack angle increases with increasing levels of corrosion, contrary to the softening seen in specimen A1. This might indicate that the stress path distribution is shifting from a steel-dominated behaviour to a concrete-dominated one.

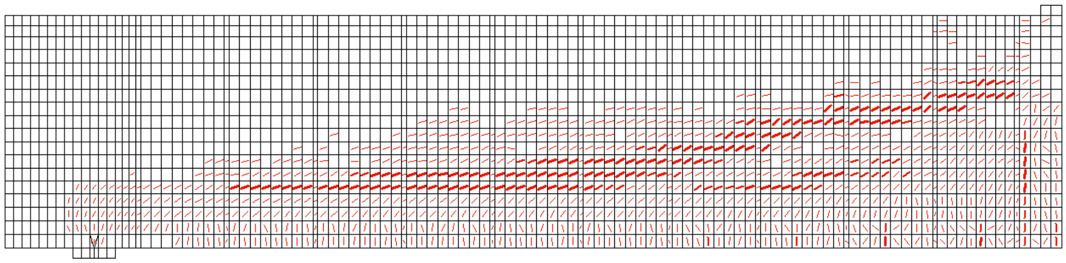

a) Specimen: VSA2V

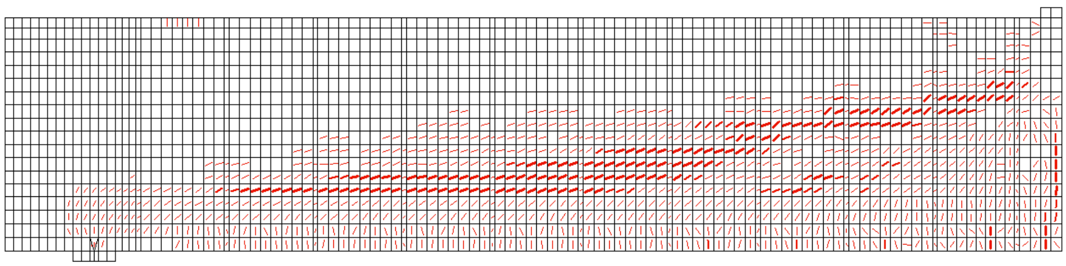

b) Specimen : VSA2L

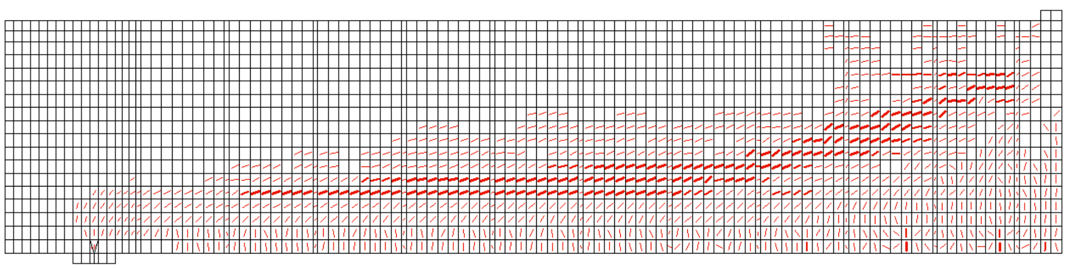

c) Specimen: VSA2M

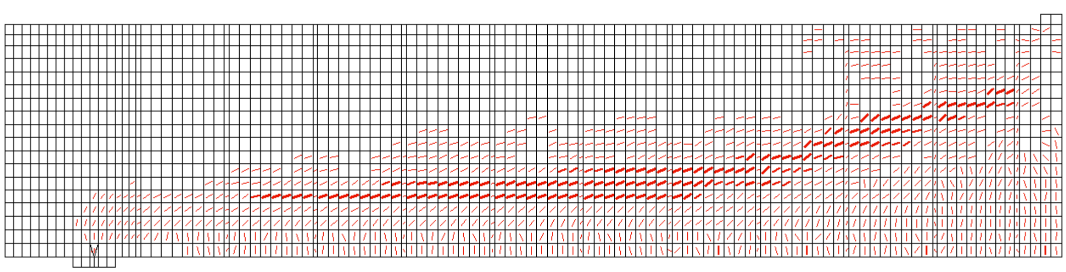

d) Specimen: VSA2H

Figure 5.10: Cracking pattern at ultimate load for specimen A2

Figure 5.11 shows the load-deformation response for beam A3 obtained from the FE analysis. As in the previous case, a decrease in the load–carrying capacity is observed with increasing levels of corrosion. Looking at the mid-span deflections at peak strength, there is only a minimal difference between specimens VSA3V and VSA3L, and similarly between specimens VSA3M and VSA2H. However, the difference between the two sets of pairs is significant. There is a slight softening of the load-deformation slope with increasing levels of corrosion damage. Post-peak behaviours are also identical, although failure happens at different deflection values for each level of damage. This indicates a comparable failure mechanism for all of the specimens in this series.

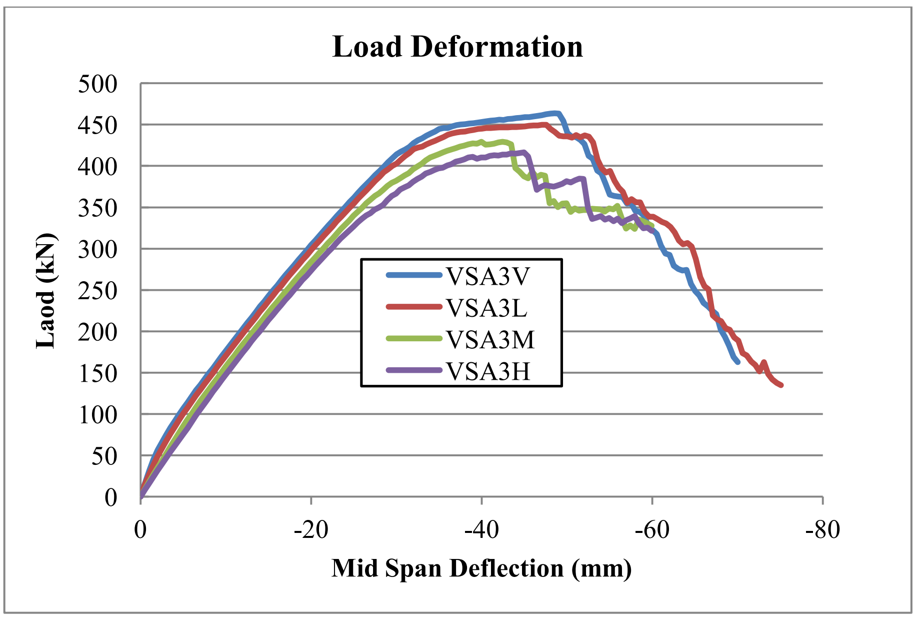

Figure 5.11: Load deformation response for specimen A3

The cracking pattern for specimen A3 can be seen in Figure 5.12, which shows a softening in the predicted cracking angles. It is also observable a shift in the location of the crack angle, although most likely linked to the softening of the crack itself. Flexural cracks at mid span become less imminent as the corrosion increases and seem to indicate an increase in the contribution of the steel stirrups outside of the affected area.

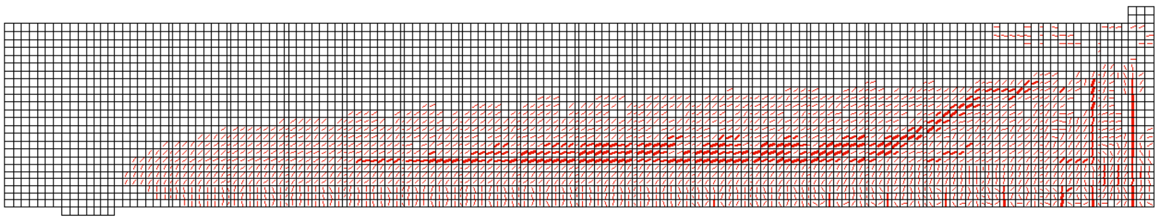

a) Specimen: VSA3V

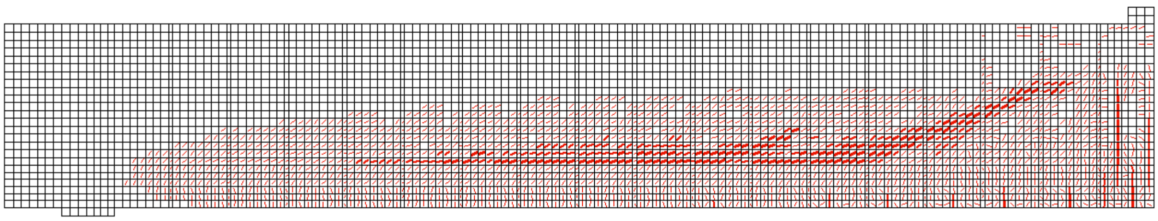

b) Specimen : VSA3L

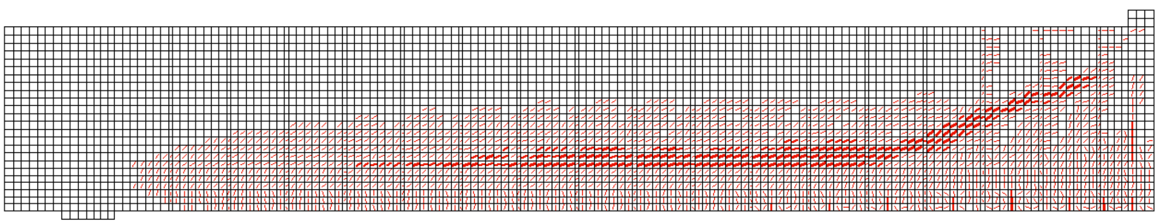

c) Specimen: VSA3M

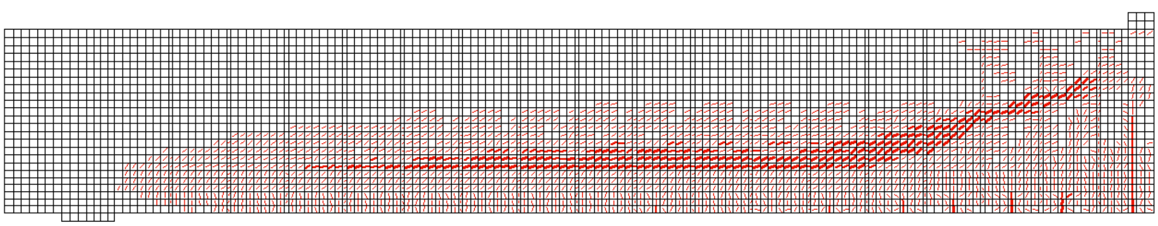

d) Specimen: VSA3H

Figure 5.12: Crack pattern at ultimate load for specimen A3

Figure 5.13 summarizes the loss of shear strength with increasing levels of corrosion damage for series A. The loss is calculated relative to the strength of an uncorroded specimen. There is a very similar decrease in strength for each of the specimens up to moderate levels of corrosion, beyond which some differences are observed. The two shorter spans have a higher decrease in strength from moderate to high levels of corrosion. Even with 50% mass loss of shear reinforcement, the shear strength is only reduced by 15% at most.

Figure 5.13: Shear strength degradation for series A

5.3.2.2 Series B

Series B is the series with a width section measuring 229 mm. It has the smallest spacing of ties at 190 mm for the two shorter spans and 152 mm for the longest span of the series. The shear reinforcement ratio is 0.15 %.

As previously seen, a reduction of the load-carrying capacity with increasing levels of corrosion damage is observed. The ascending slope of the load-deformation curve follows a similar behavioural trend but with an increasingly softer behaviour as the corrosion level increases. There seems to be little effect of corrosion on the deflection associated to peak load. Post-peak behaviour however shows a definitive decrease in deformability as the corrosion increases.

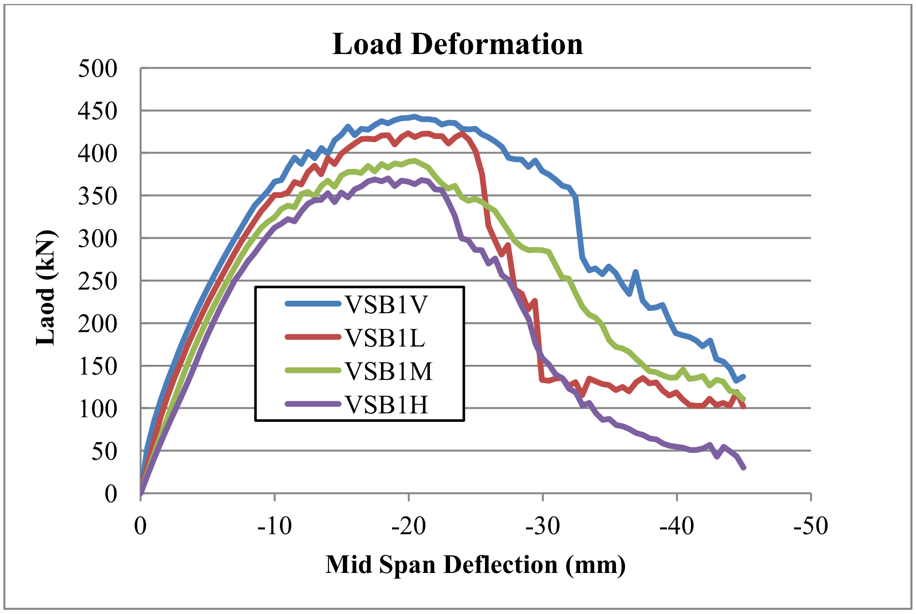

Figure 5.14: Load-deformation response for specimens B1

The cracking pattern for specimen B1 can be observed in Figure 5.15. No definite change in the crack angle can be observed. Cracking at mid height away from the mid span decreases as the corrosion progresses.

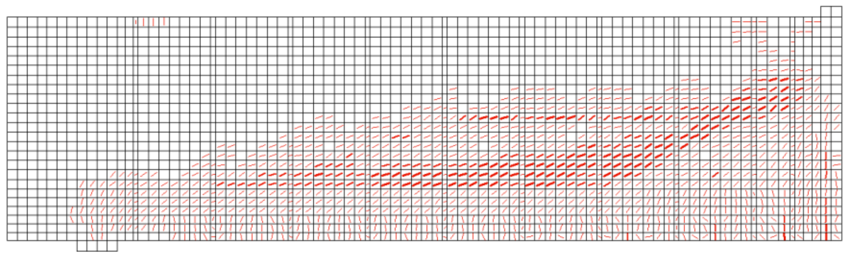

a) Specimen: VSB1V

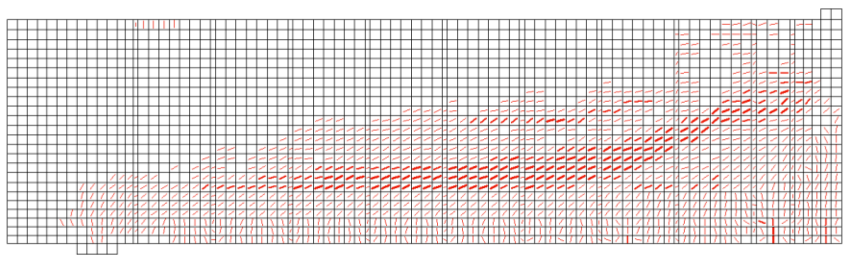

b) Specimen : VSB1L

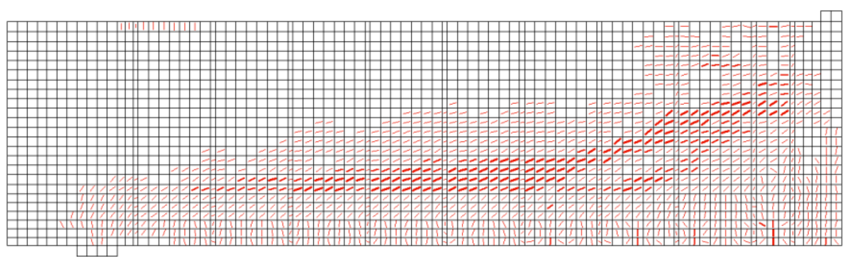

c) Specimen: VSB1M

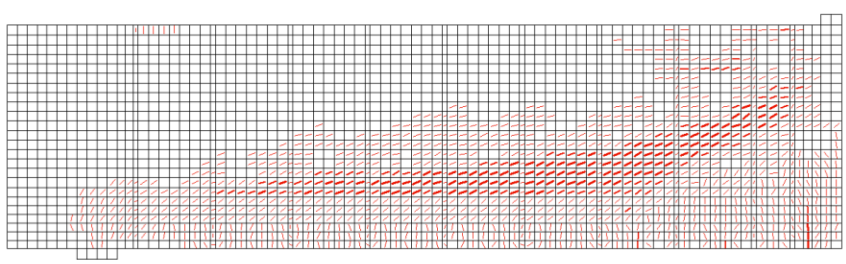

d) Specimen: VSB1H

Figure 5.15: Cracking pattern at ultimate load for specimens B1

Figure 5.16 shows the load-deformation response for beam B2 obtained from the FE analysis. The figure shows similar results as the previous specimens, with a reduction in load-carrying capacity for increasing levels of corrosion. Here a definitive reduction in the deflection associated to peak loads is noticed. The slopes of the load-deformation curves are very similar for each of the specimens, with a slight softening with respect to corrosion increase. Post-peak behaviour indicates flexural concrete crushing for both the uncorroded specimen and the one with low level of corrosion, whereas the two specimens with higher mass loss tend to indicate shear dominated behaviour, identified by a very short plateau followed by a rapid decrease in strength.

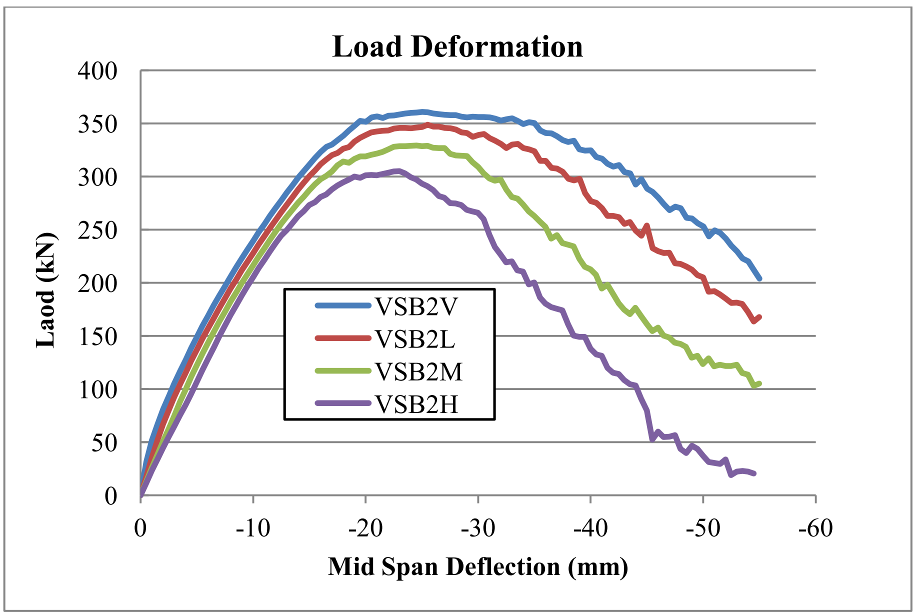

Figure 5.16: Load-deformation response for specimen B2

The cracking pattern for specimen B2 can be observed in Figure 5.17. The first two maps are similar with a governing crack forming within the critical section (i.e., *d* from the load) and shear cracks along mid height of the beams away from the former. Significant flexural cracks at mid span and cracking associated with crushing near the loading are also observed. The two specimens with higher levels of corrosion have fewer flexural cracks and no apparent concrete crushing near the point load. The crack angle stiffens from the moderate to high level of corrosion, which is reflected by means of a reduction in load-carrying capacity as soon as the peak value is reached for specimen VSB2H.

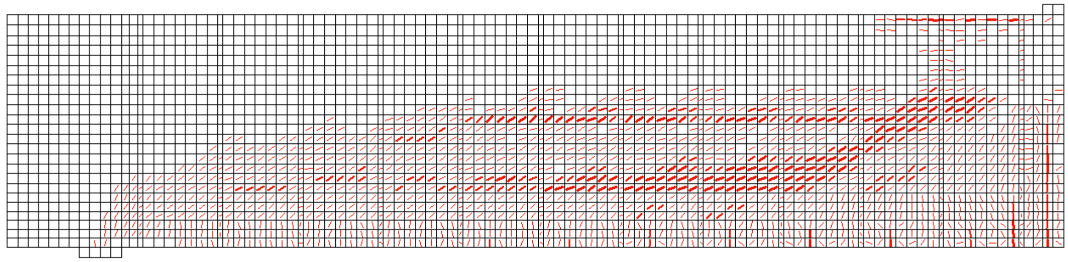

a) Specimen: VSB2V

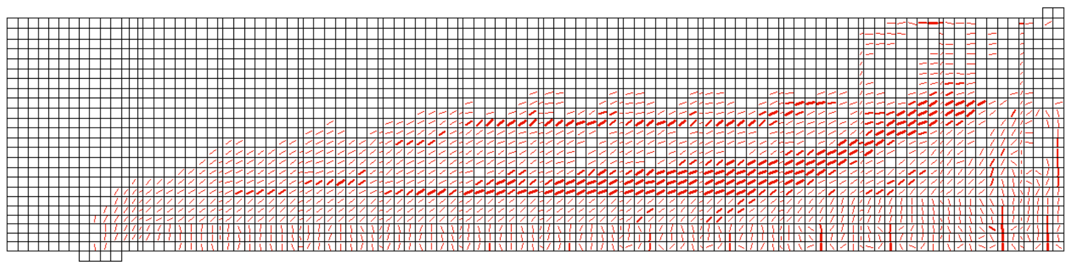

b) Specimen : VSB2L

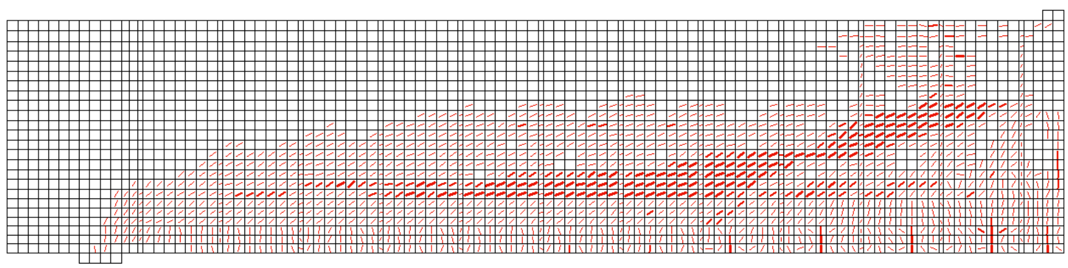

c) Specimen: VSB2M

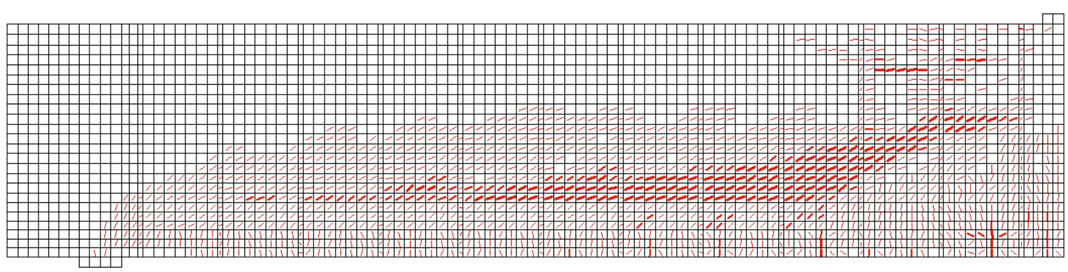

d) Specimen: VSB2H

Figure 5.17: Cracking pattern at ultimate load for specimen B2

Figure 5.18 shows the load-deformation response for beam B3 obtained from the FE analysis. From the figure it is observed that specimen B3 reaches the yield strength of the flexural steel. The load-deformation behaviour is governed by yielding of the longitudinal steel. The effect of increasing the degree of corrosion of the stirrups is not as significant here in reducing the specimen's load-carrying capacity.

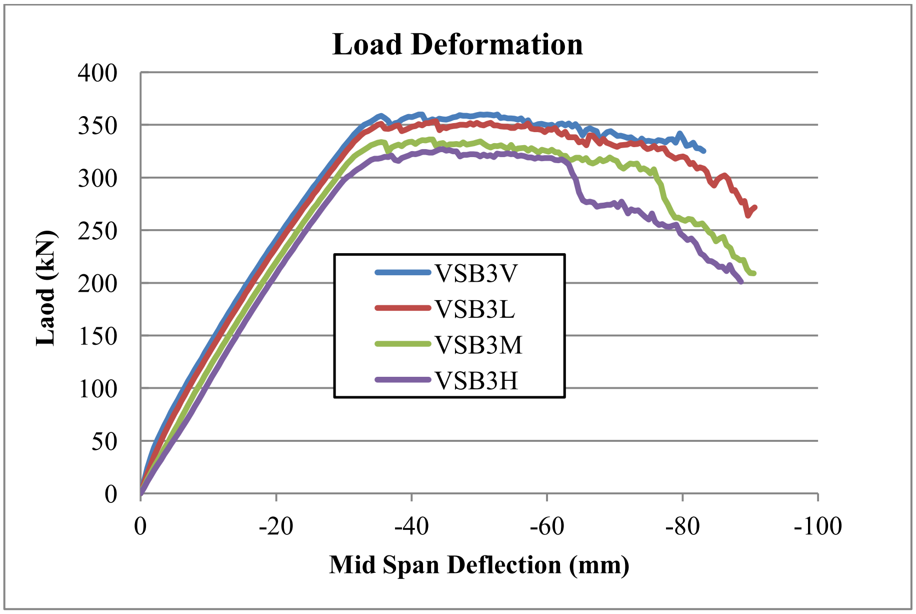

Figure 5.18: Load-deformation response for specimen B3

The cracking pattern at ultimate loads for specimen B3 can be observed in Figure 5.19. Large flexural cracks are observed at mid span for each of the levels of corrosion attained. An increasing amount of shear cracks are observed as the corrosion damage increases. A dominant shear crack begins to form at moderate and high corrosion levels within the critical section, with a fewer amount of secondary shear cracks outside of this region.

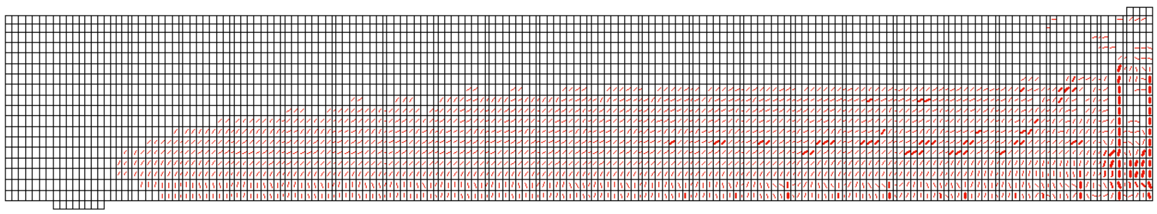

a) Specimen: VSB3V

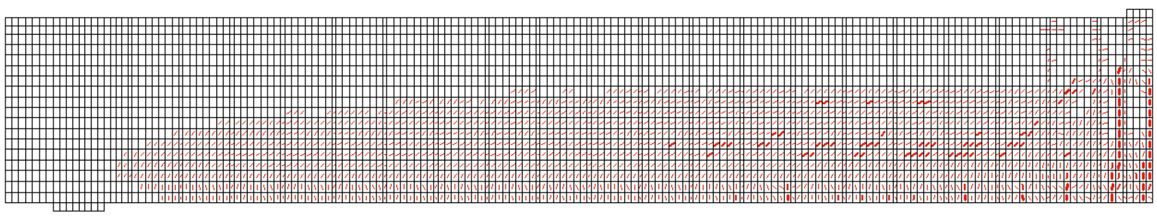

b) Specimen : VSB3L

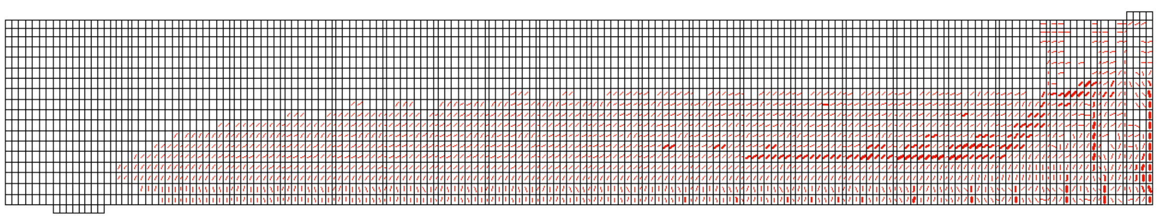

c) Specimen: VSB3M

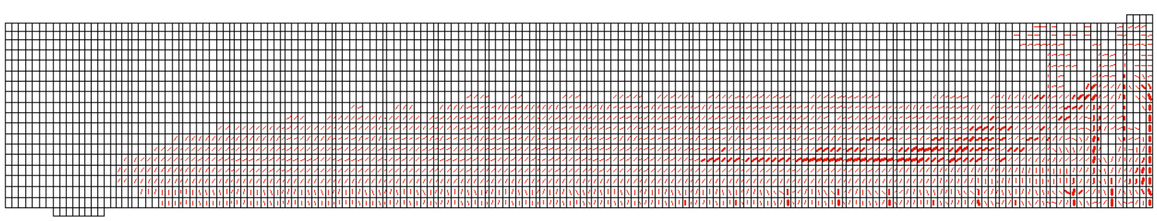

d) Specimen: VSB3H

Figure 5.19: Cracking pattern at ultimate load for specimen B3

The loss in shear strength with increasing levels of stirrup mass loss is plotted in Figure 5.20 for series B. The two shorter span series show a higher decrease in shear strength as the % of mass loss increases. The increase in corrosion damage has less effect on the beam with a longer span, as observed in Figure 5.18.

Figure 5.20: Shear strength degradation for series B

5.3.2.3 Series C

The specimens in series C have the thinnest width, measuring 152 mm. These specimens have the same shear reinforcement as series A and therefore the highest shear reinforcement ratio of all of the series at 0.2%. Because of the smallest width, they have the highest crack-inducing strain for each of the corrosion levels.

Figure 5.21 shows the load-deformation response for beam C1 obtained from the FE analysis. The load-carrying capacity of specimen C1 is clearly governed by yielding of the longitudinal steel, and it is slightly affected by an increasing level of corrosion damage in the stirrups. No effects the on ultimate deflection are noticed. However, the slope of the ascending part of the curve up to peak is clearly decreased with increasing corrosion levels.

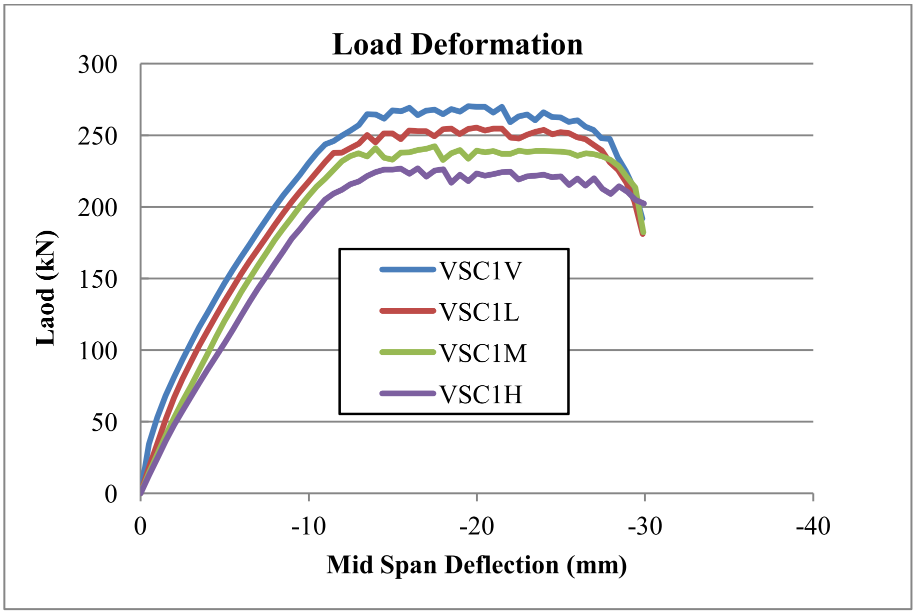

Figure 5.21: Load-deformation for specimen C1

The cracking pattern for specimen C1 can be observed in Figure 5.22. It shows a clear truss mechanism of resistance, with constant cracks forming near mid height starting in the critical region and moving towards the support for the first three cases. As the corrosion progresses, there are fewer cracks outside of the critical section and seem to localise at a specific location. Major flexural cracks become less significant and the crack angle softens slightly at high levels of corrosion.

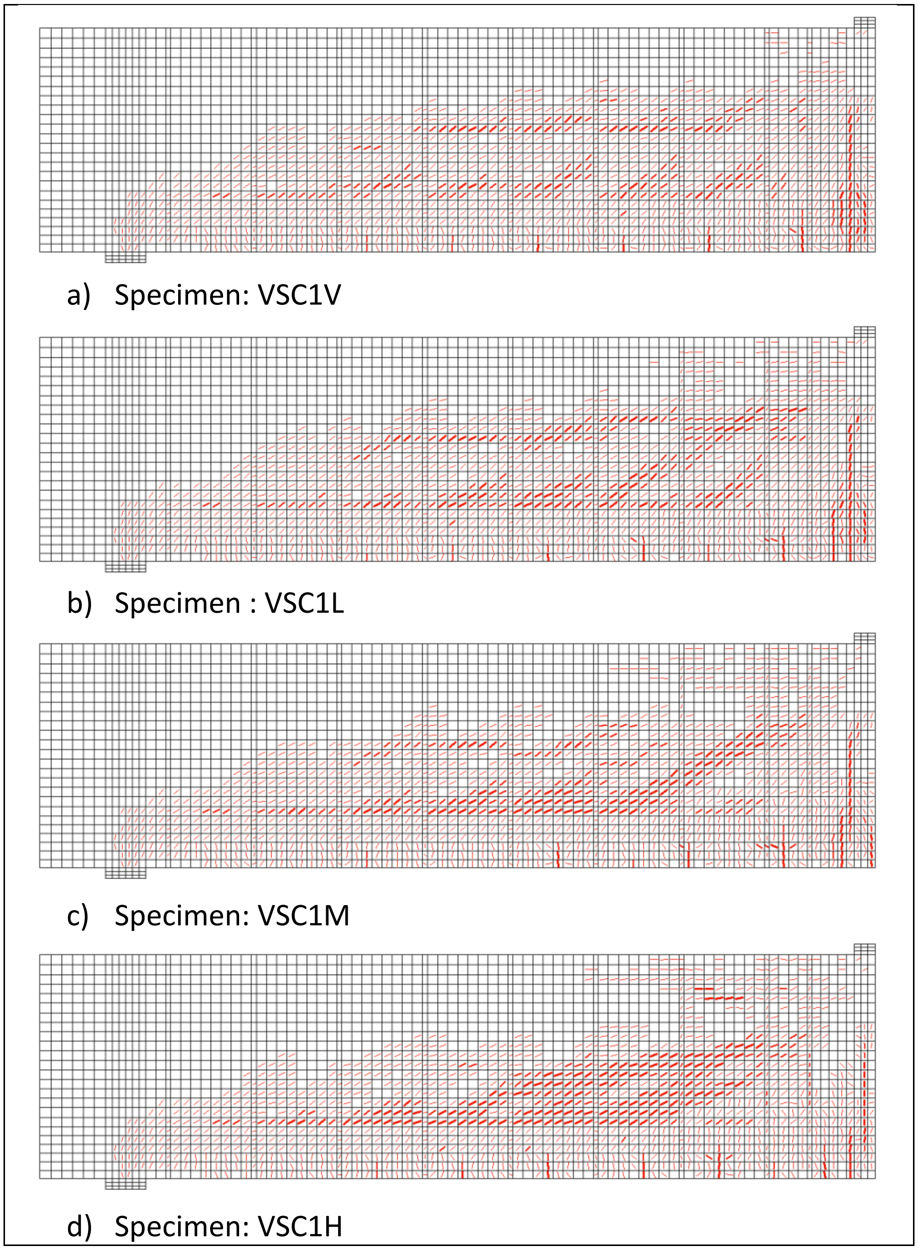

Figure 5.22: Cracking pattern at ultimate load for specimen C1

Figure 5.23 shows the load-deformation response for beam C2 obtained from the FE analysis. There is a significant decrease in load-carrying capacity as corrosion progresses, indicating a shift on the load transfer mechanisms. The beam fails by flexural concrete crushing for the first three cases. As some confinement is provided near the loading bearing plates in the FE model, this allows the beam to maintain its strength while the steel yields the steel at the beam deforms. At a high level of corrosion (50% mass loss), the strength and deformability of the beam is greatly reduced. This last case fails by a shear-compression failure.

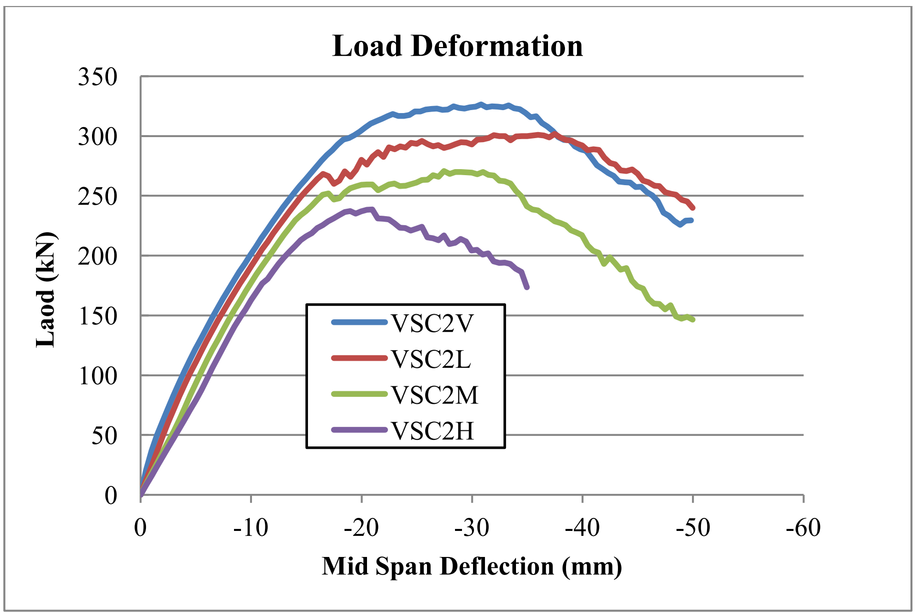

Figure 5.23: Load-deformation response for specimen C2

The cracking pattern for specimen C2 can be observed in Figure 5.24. Crushing cracks near the loading point at mid span are observed for the first three cases, with few flexural cracks. The angle of shear cracks softens as corrosion progresses.

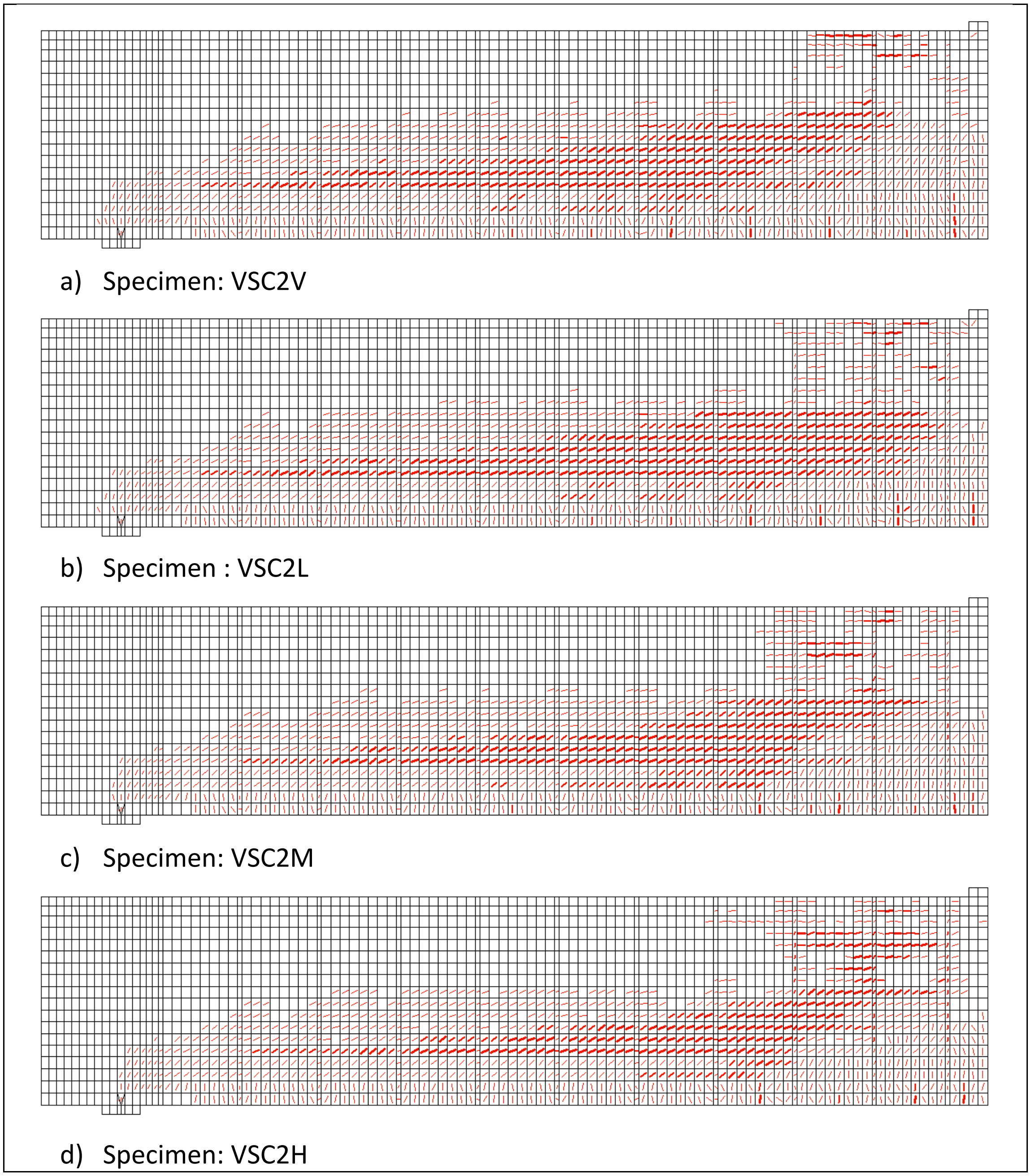

a) Specimen: VSC2V

b) Specimen : VSC2L

c) Specimen: VSC2M

d) Specimen: VSC2H

Figure 5.24: Cracking pattern at ultimate load for specimen C2

Figure 5.25 shows the load-deformation response for beam C3 obtained from the FE analysis. It is observed from the curves that the beams fail by a flexural concrete crushing failure. The confinement effects near the region where the load is applied are noticeable as the beams continue to deform prior to failure. The increase in the deformation ability of the concrete leads to the full engagement of the flexural steel. The strength decrease is slight from no corrosion to a low level of corrosion and becomes more significant as the corrosion damage is increased to higher levels.

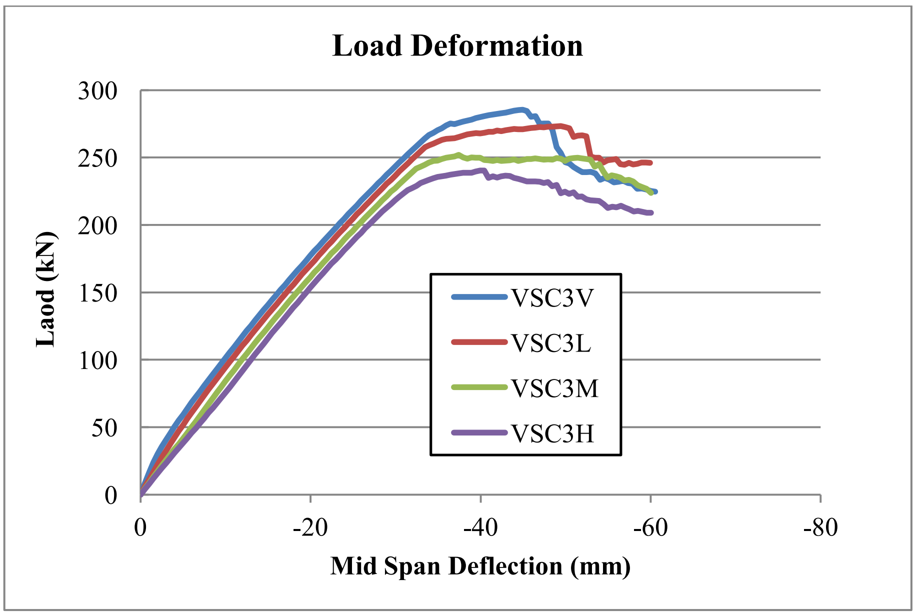

Figure 5.25: Load-deformation response for specimen C3

The cracking pattern for specimen C3 can be observed in Figure 5.26. Significant flexural cracks are observed at mid span for each of the specimens. Shear cracks are well distributed for the un-corroded specimen, whereas they to concentrate in one location and soften in angle as corrosion progresses.

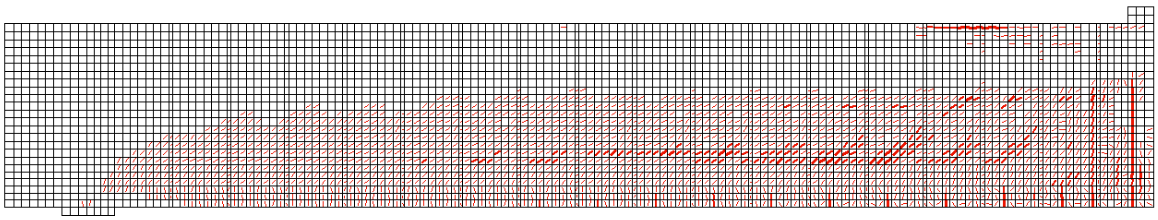

a) Specimen: VSC3V

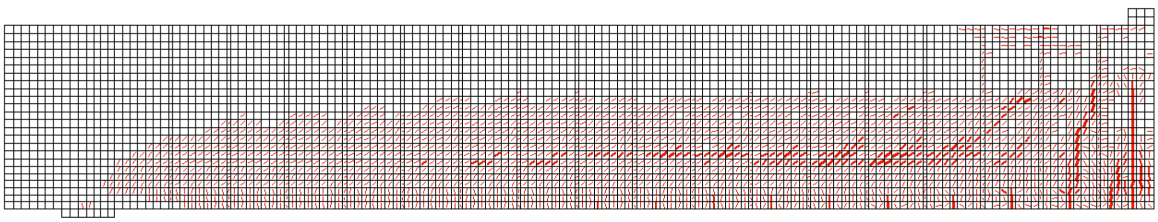

b) Specimen : VSC3L

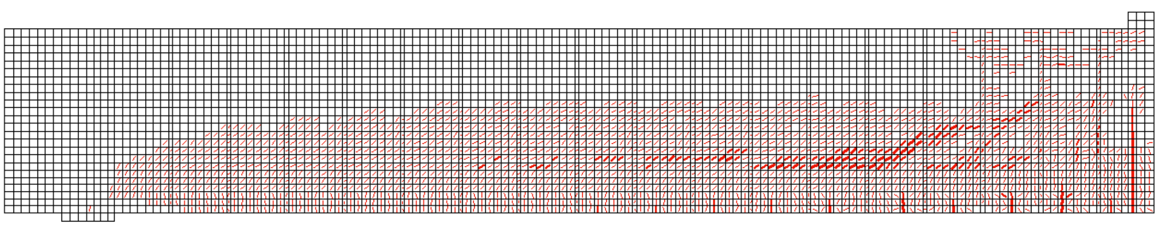

c) Specimen: VSC3M

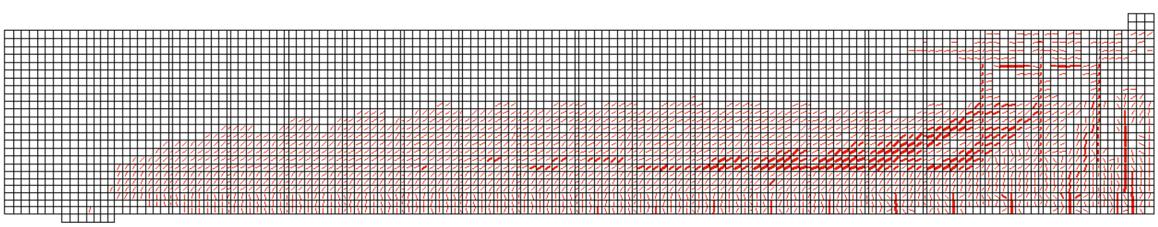

d) Specimen: VSC3H

Figure 5.26: Cracking pattern at ultimate load for specimen C3

Figure 5.27 summarizes the loss in shear strength with increasing levels of corrosion damage for series C. The FE results for this series follow a similar decrease to that obtained for the other two series. A relative loss in strength of 15% at high levels of corrosion for the short and long spans (series 1 and 3) is comparable to what was observed in series A and B. However, the mid-length span specimen C2 has a dramatic loss in strength compared to the other specimens, with a loss of over 25% for an average mass loss of the stirrups of 50%.

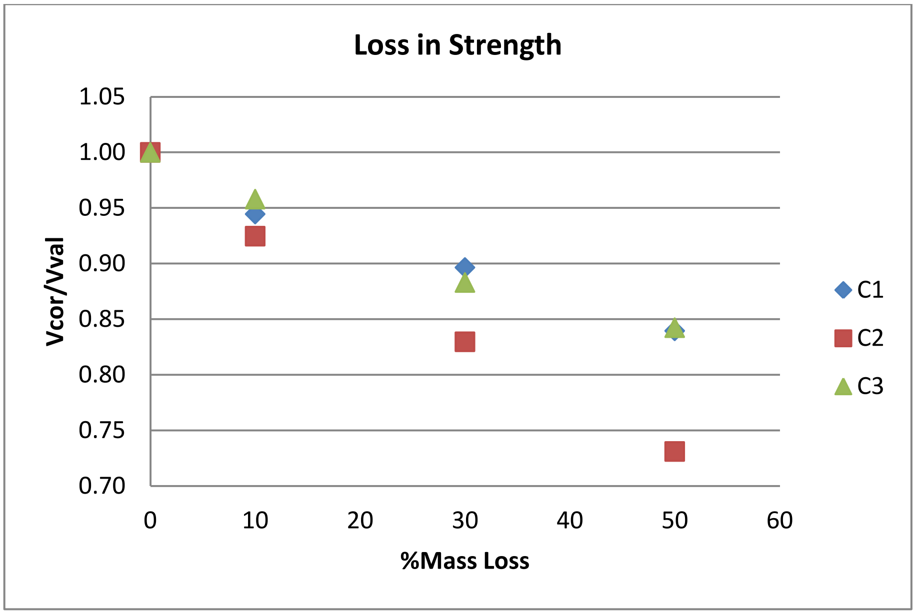

Figure 5.27: Shear strength degradation for series C

5.3.3 Shear Strength Summary

Shear strength was in general decreased as the level of corrosion of the stirrups increased. This is to be expected as the geometrical and material properties of the stirrups decrease with increasing corrosion, affecting directly the capacity of the beams. At high corrosion levels, a relative loss in peak strength for longer spans was around 10%, with the exception of series C, which displays a relative loss of around 15%. Specimen C2 had the largest decrease in strength with a loss of nearly 30% at high levels of corrosion. The Oregon beams followed suit having a constant decrease in strength with an overall loss of around 20% from the un-corroded specimen. By looking at the effect of the a/d ratio on the loss of strength, corrosion has less effect on strength when the shear span-to-depth ratio is larger. This agrees with the findings of Suffern et al. (2010), who observed higher loss in shear strength for smaller a/d.

All of the beams were designed to be shear critical and typically followed the expected failure mechanism of shear-compression in the two shorter spans and flexural-compression failure in the longer span. Once corrosion was introduced, the failure mechanism was generally the same as that of the un-corroded specimens, although the shear-compression failure mechanism was triggered at lower deformations. In some instances at lower levels of corrosion, the deformation associated to ultimate strength increased, although typically for the specimens with the highest a/d ratio.

The ascending slope of each of the loading curves softens to different extent with increasing levels of corrosion. The effect of corrosion on softening the slope of the ascending branch of the loading curve was affected in different ways, depending on the different characteristics of the beams in terms of their width and span length. The deflection associated to ultimate loads was in general reduced past moderate levels of corrosion of the stirrups.

Cracking patterns from the FE results helped to identify trends and failure mechanisms, while providing useful information on cracking angles and stress distribution within the member. Three trends were generally observed between the different series. The first trend is a transition from well-distributed to localized cracking as corrosion damage progresses. In most cases of lower levels of corrosion, cracking was rather well distributed throughout the beam; however, as corrosion level increased, a single crack started to form near the critical damaged section at mid span. This trend is also associated to a change in crack angle. The second trend indicated either stiffening or softening of the crack angle, which seems to be dependent on the spacing of the stirrups. In the case of lager spacing (e.g., series A and C), the crack angle generally softens as the corrosion level increases. Finally, a transition in failure mechanisms was observed when crack became less frequent or disappeared entirely. This indicates that stresses are being redistributed.

5.4 Flexural Rigidity

The flexural rigidity of the beams is defined as the product of the elastic modulus of the section E times its moment of inertia with respect to the bending axis I. The flexural rigidity EI was calculated from:

$$\delta = \frac{PL^3}{48EI} \tag{5.1}$$

where δ is the mid-span deflection corresponding to point load P, L is the span length and EI is the flexural rigidity. Equation 5.1 gives the deflection of a simply-supported beam subjected to four-point loading. In the following sections, the flexural rigidity is plotted against the curvature for the Oregon and Toronto beams, and for different levels of corrosion of the stirrups.

5.4.1 Oregon Beams

Figure 5.28 plots the flexural rigidity extracted from the experimental results of the Oregon beams against their curvature. Although the specimen with low level of corrosion (Beam 10RB) initially had a higher flexural rigidity, the initial bending stiffness in general decreases with increasing corrosion levels. The value of the initial stiffness tends to approach the fully-cracked section stiffness as the corrosion increases. This might be due to cracking of the concrete induced by the expansion of corrosion products on the stirrups.

Figure 5.29 plots the flexural rigidity extracted from the FE results of the Oregon beams against their curvature without prestraining effects. Neglecting to incorporate prestraining effects does not capture the initial drop in stiffness from increasing corrosion, as observed in the test data. Since no concrete is removed or damaged with increasing corrosion this was to be expected. Only a slight drop in stiffness near the higher curvature is captured by this FE model.

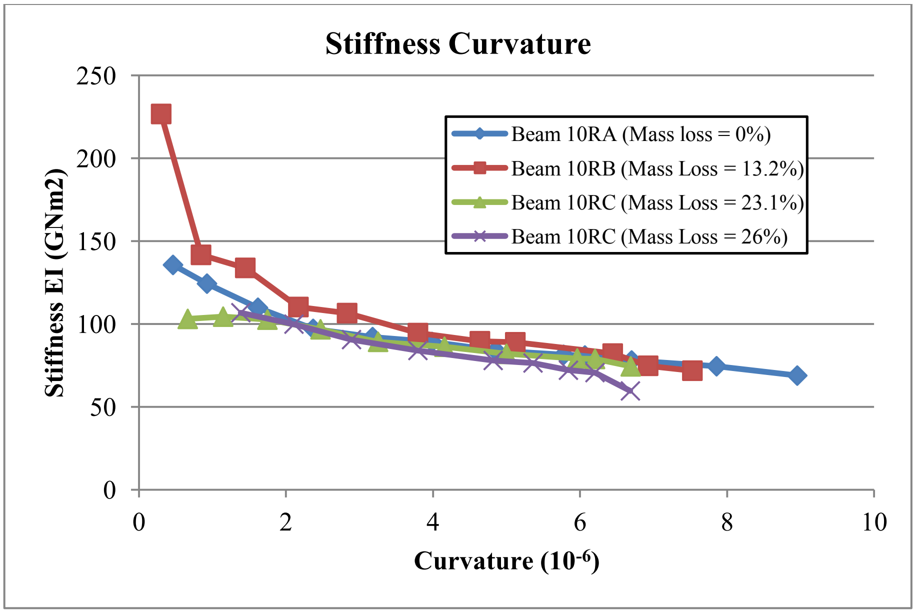

Figure 5.28: Stiffness-curvature relationship obtained from experimental data of Oregon beams

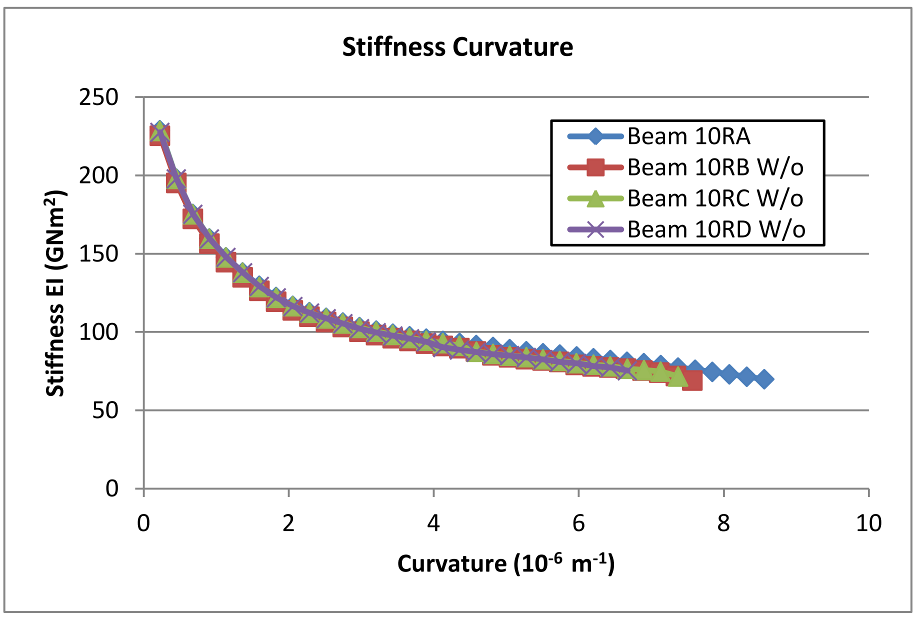

Figure 5.29: Stiffness-curvature relationship for Oregon beams without accounting for corrosion-induced cracking in FE

Figure 5.30 plots the flexural rigidity extracted from the FE results of the Oregon beams against their curvature, when corrosion-induced cracking was modelled through the introduction of prestrains on the concrete surrounding the stirrups. Although not as pronounced as the drop observed in the experimental results, the results display an initial drop in bending stiffness. This indicates that introducing the pre-strain simulates the damage induced in the concrete due to corrosion of the stirrups. Similar to the results presented in Figure 5.29, the drop in stiffness at higher curvatures is successfully represented here as well. The tail end of the graph highlights the curvature at which the independent beams fail which is associated with a significant decrease in stiffness.

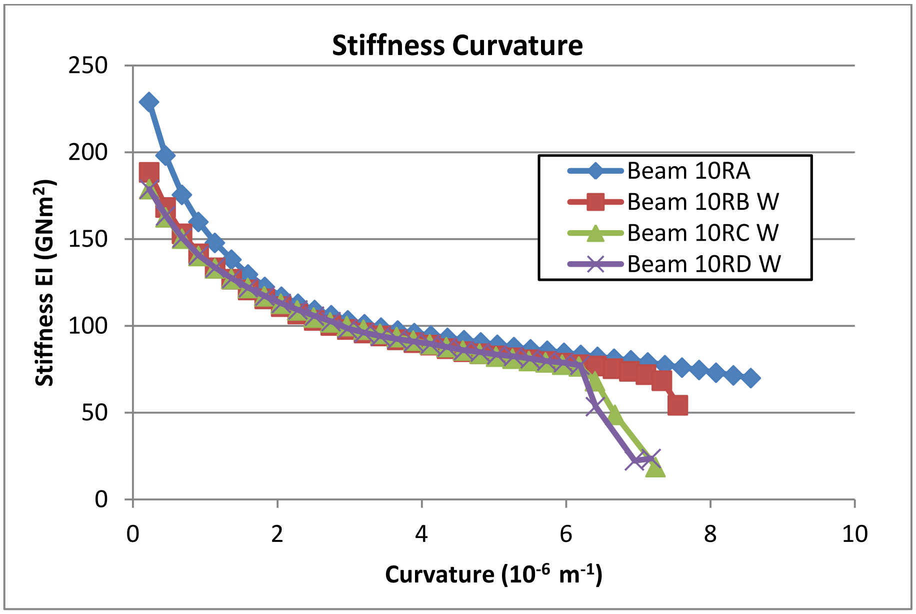

Figure 5.30: Stiffness-curvature relationship for Oregon beams accounting for corrosion-induced cracking in FE

5.4.2 Toronto Beams

The Toronto beams data is separated by series A, B and C. The overall behavioural effects on flexural rigidity are discussed individually first, and then summarized as a whole.

5.4.2.1 Series A

The flexural rigidity extracted from the FE results is plotted against the curvature in Figure 5.31 for specimens in Series A. Most of the effects of stirrup corrosion on the bending stiffness of the beams occur prior to a curvature value of 5×10^{-6} m^{-1}. The effect is more significant for the beam with the shortest span (A1). For beams with longer span (A3), it requires a higher degree of corrosion damage (moderate value of 30% mass loss) for the initial flexural rigidity to drop relative to the un-corroded specimen. Once the curvature is greater than around 5×10^{-6} m^{-1}, all samples (included the uncorroded one) follow the same trend.

5.4.2.2 Series B

The flexural rigidity extracted from the FE results is plotted against the curvature in Figure 5.32 for specimens in Series B. Similar trends as those in Series A are observed. The effect of corrosion on the flexural rigidity-curvature relationship is greater for curvatures lower than approximately 7×10^{-6} m^{-1}. Like Series A, this effect is more significant for shorter spans (beams B1 and B2). The effect for the longer span (beam B3) is very small at low level of corrosion, and requires at least a moderate level of corrosion decrease the initial stiffness considerably. All curves converge past a curvature of 7×10^{-6} m^{-1}

5.4.2.3 Series C

The flexural rigidity extracted from the FE results is plotted against the curvature in Figure 5.33 for specimens in Series C. This series, which corresponds to beams with the smallest width, displays the highest impact of stirrup corrosion on the initial flexural rigidity, including the specimen with the longest span (C3). Furthermore, the decrease in stiffness at later curvature values is more significant in this series than series A and B.

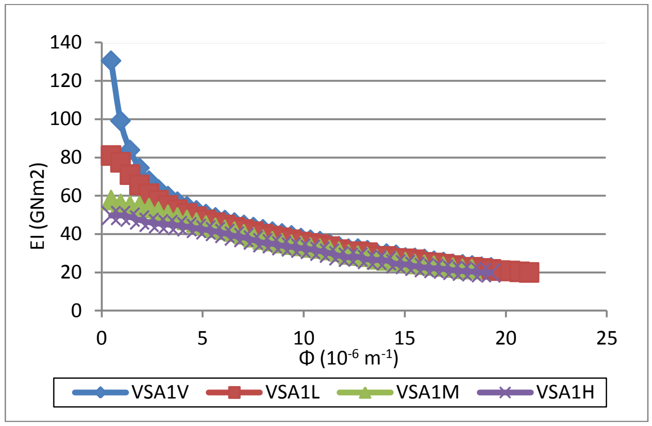

a) Stiffness curvature relationship for specimens A1

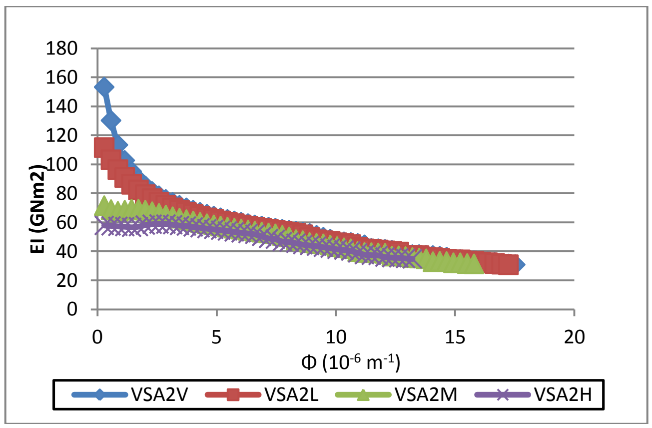

b) Stiffness curvature relationship for specimens A2

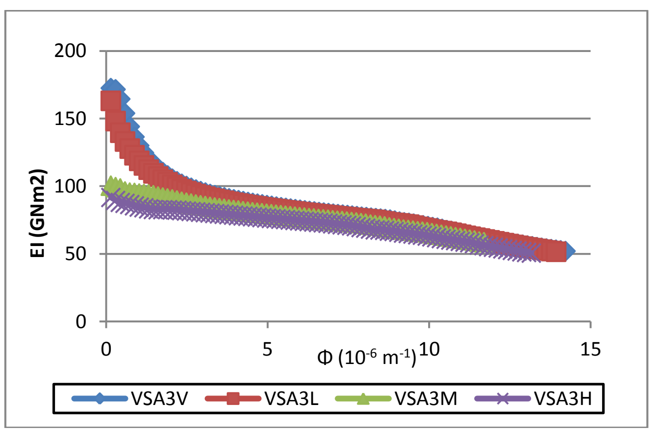

c) Stiffness curvature relationship for specimens A3

Figure 5.31: Stiffness-curvature relationships for series A

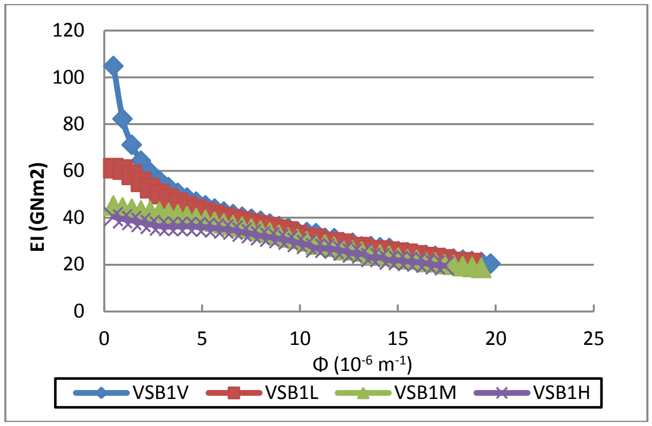

a) Stiffness curvature relationship for specimens B1

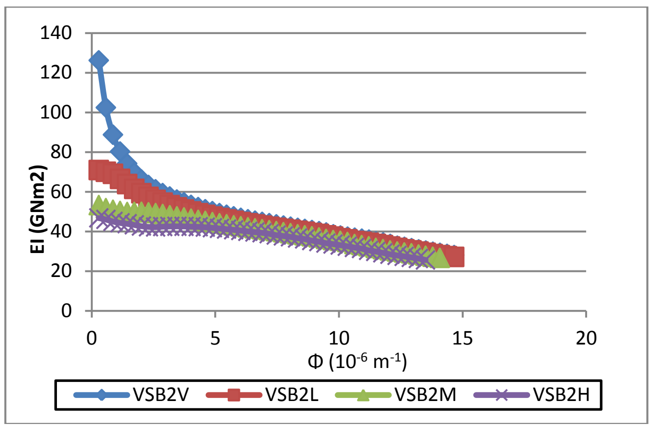

b) Stiffness curvature relationship for specimens B2

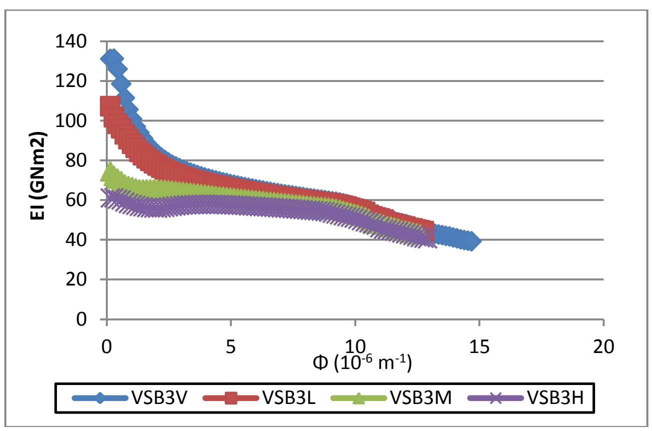

c) Stiffness curvature relationship for specimens B3

Figure 5.32: Stiffness-curvature relationship for series B

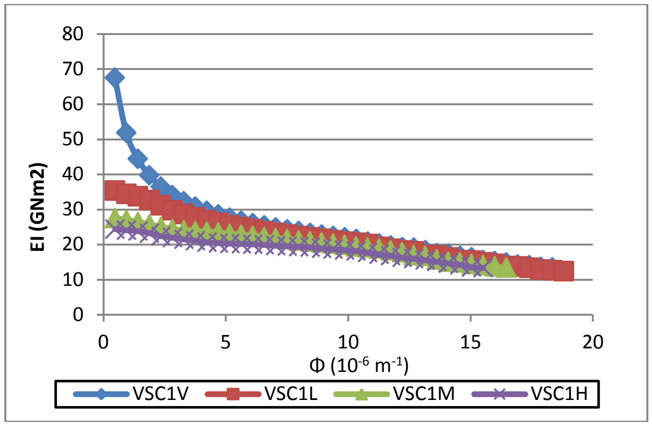

a) Stiffness curvature relationship for specimens C1

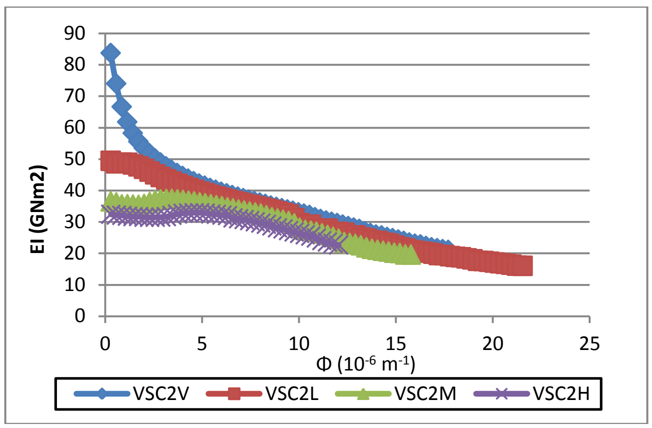

b) Stiffness curvature relationship for specimens C2

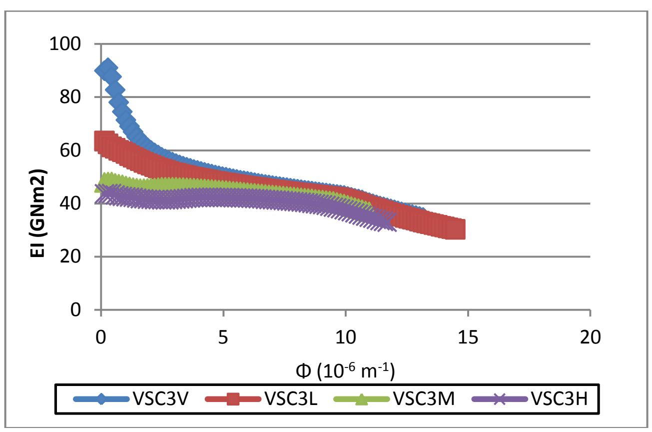

c) Stiffness curvature relationship for specimens C3

Figure 5.33: Stiffness-curvature relationship for series C

5.4.3 Flexural Rigidity Summary

Introducing corrosion-induced cracking in the FE analysis in the form of concrete prestraining around the corroding stirrups correctly captures the overall effect on flexural rigidity degradation with increasing levels of corrosion. The FE results therefore indicated a decrease in the initial stiffness for all the Toronto beams, which agrees with the experimental data from the Oregon beams as well. Introducing corrosion-induced cracking in the analysis methodology leads to a higher degree of cracking in the section, the moment of inertia therefore approaching the fully-cracked value. The effects of concrete cracking on the moment of inertia are limited in a two-dimensional plane stress analysis, as the out of plane effects are not properly modelled. Potential spalling or delamination of the concrete cover as a result of the corroding stirrups, as observed in the field, is not directly modelled in the FE analysis. Series C, beams with the smallest width, displays the highest effect of corrosion on *EI*, which is related to the level of damage incorporated in the FE analysis by means of prestrains. As the thickness of the member is reduced, the related corrosion-induced damage is increased for a given level of steel mass loss, as the prestrain is distributed over the member's width as described in Section 3.3.

5.5 Ductility

Ductility here is defined as the deformation capability up to failure of each specimen. Similar to the strength degradation with increasing corrosion damage, the effect of shear reinforcement corrosion on ductility is studied by means of comparing the peak deflection at a particular corrosion level to that of the control specimen where no corrosion occurs. It is important to note that in the case where two peaks in the load-deformation response occur, the smallest deflection was taken in the comparison, as no increase in shear strength was observed after that point.

5.5.1 Oregon Beams

Figure 1.33 plots the peak deflection δ_{cor} relative to that of the uncorroded specimen δ_{val} against the percentage of stirrup mass loss for the Oregon beams. It is illustrated in the figure the experimental data reported by Higgins et al. (2003) and Miller et al. (2011) along with the FE results with (FEMw) and without (FEMw/o) prestraining. Both FE analyses capture the behavioural characteristics in the experimental tests. However, they tend to overestimate the peak degradation of peak deflection as the corrosion damage is increased. It should be noted that this is a difficult parameter to estimate for these beams given the a/d ratio of 2.04, as the peak deflection was of only 10 mm for the un-corroded specimen, giving a 10% difference for only 1 mm deflection variation. The reduction in the relative displacement can be attributed to an increase of the concrete contribution to the shear resistance mechanism, which can impact significantly the ability of the RC beam to deform.

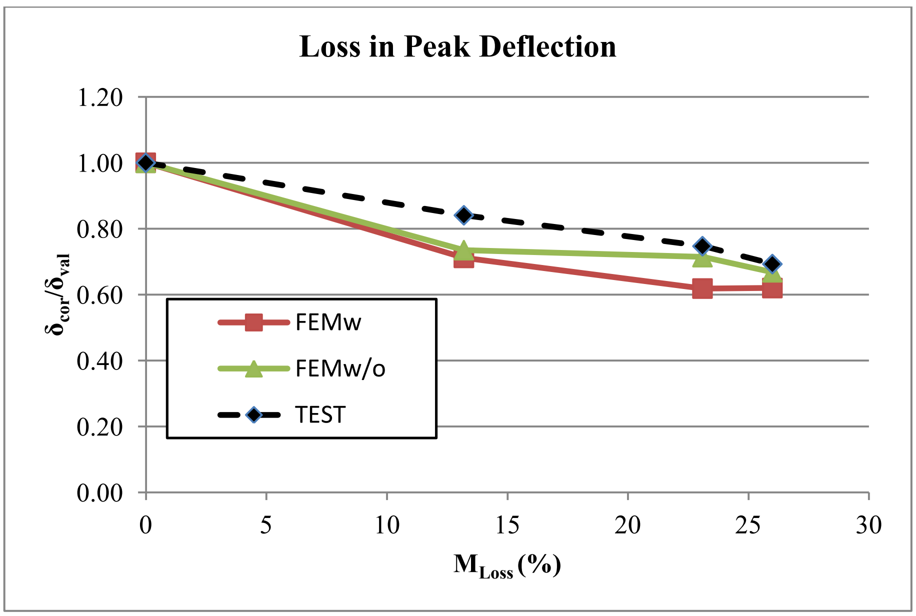

Figure 5.34: Corrosion effects on relative peak deflection for Oregon beams

5.5.2 Toronto Beams

The same procedure was done for the Toronto beams series, where the deflection associated to the peak load in the load-deformation curve is compared to the respective control specimen (no corrosion) for increasing levels of corrosion damage.

5.5.2.1 Series A

The relative peak deflection $\delta_{cor}/\delta_{val}$ is plotted against the % of steel mass loss in Figure 5.35 for series A. There is little effect observed for beam A1. However, there is a distinct reduction in peak deflection with increasing levels of corrosion for beam A2. Beam A3 follows the same pattern up to moderate levels of corrosion (30% mass loss); however, the peak deflection at the high level of corrosion (50% mass loss) is higher than beam A2.

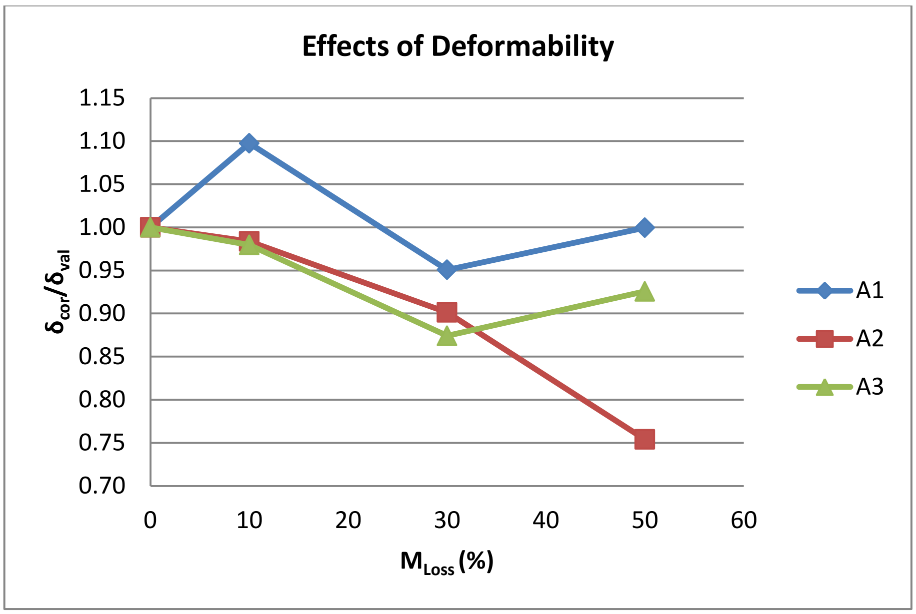

Figure 5.35: Decrease of mid-span deflection at ultimate load for series A

5.5.2.2 Series B

The relative peak deflection $\delta_{cor}/\delta_{val}$ is plotted against the % of steel mass loss in Figure 5.36 for series B. In this figure, it is noted that reduction in peak deflection is similar for beams B1 and B2. Beam B3 has a larger decrease in peak deflection initially at lower levels of corrosion, but it ends up with at 10% reduction at high levels of corrosion (similar to beams B1 and B2).

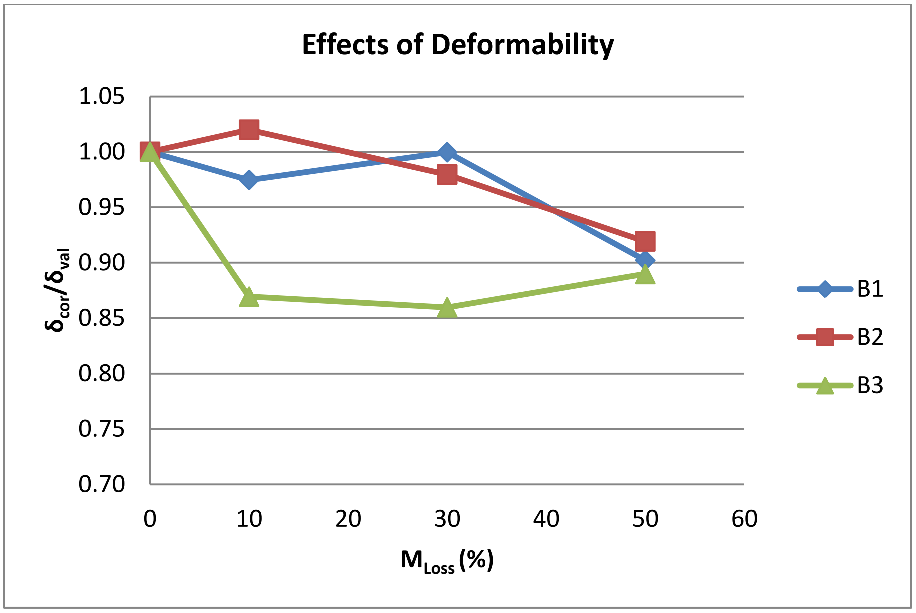

Figure 5.36: Decrease of mid-span deflection at ultimate load for series B

5.5.2.3 Series C

The relative peak deflection $\delta_{cor}/\delta_{val}$ is plotted against the % of steel mass loss in Figure 5.37 for series C. This series follows a similar increase in deformation at low levels of corrosion. This is followed by a decrease in peak deflection at moderate levels of corrosion and a further decrease at high levels, with the exception beam C3. Like series A and B, the decrease in relative peak deflection at high levels of corrosion is around 10%. An exception is beams A2 and C2, with a decrease in relative peak deflection at the high level of corrosion damage of 25%-30%.

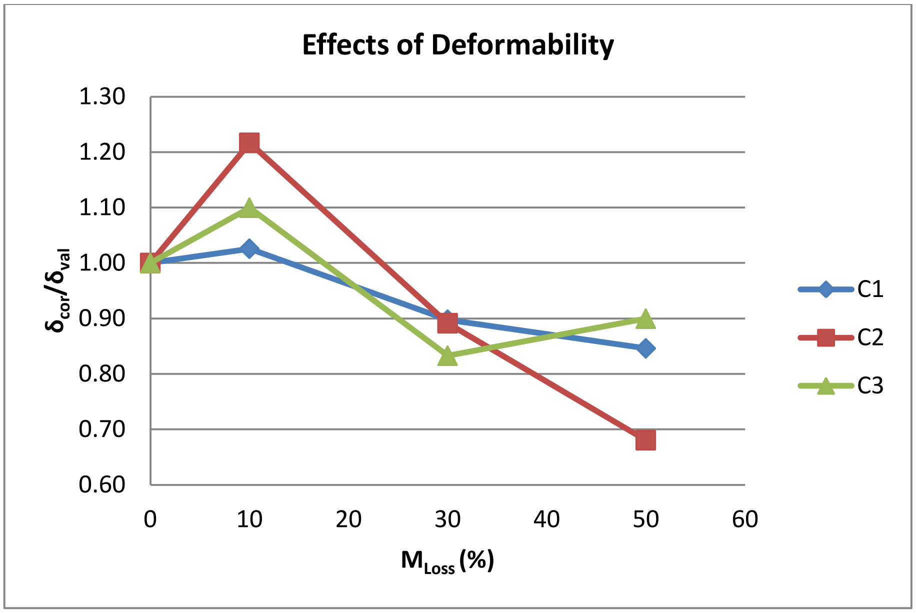

Figure 5.37: Decrease of mid-span deflection at ultimate load for series C

5.5.3 Ductility Summary

It is important to keep in mind that the relative peak deflection is based on the peak deflection of the un-corroded beam, in which behaviour is affected by the length of the span and the sectional properties. By comparing equal relative peak deflections of a short-span beam with a longer one would indicates a greater reduction in deflection for the beam with longer span, as it is expected to deflect more.

From the FE analyses it is observed that in general a decrease in peak deflection occurs for increasing corrosion damage. This trend holds for most of the series with the exception of series C, which undergoes an initial increase in peak deflection at low levels of corrosion. Comparing the span length between the different series, similar trends are noted for beams with equal span length. The shorter-span specimens are less affected by the increase in corrosion levels compared to the other two longer spans. This is indicative of the shear-dominant behaviour of these beams, in which shear-compression failure is expected.

The beams with mid-length span undergo a very similar change in relative peak deflection from series to series, where typically at lower corrosion levels a slight or no increase is noticed, and followed by a constant decrease from low to moderate, and moderate to high levels of corrosion. These beams have a higher moment to shear ratio on the section than the shorter spans, which increases the flexural demand that is imposed on the sections. The effect of damaging the critical section of the beam near mid span induces a change in behaviour, where shear is redistributed over the damaged section similar to a tied arch mechanism is suspected, thus impacting the amount of contribution of the concrete to shear resistance, which in turn greatly affects the deformability of these beams. This effect is less significant on series B, since beam B2 has a smaller spacing between the stirrups, therefore distributing the stresses better between the concrete and steel contributions to shear resistance.

The beams with longer spans are affected at lower corrosion levels, but the effects are minimal past this initial decrease. The moment to shear ratio is the highest here. And because of this high moment demand, the section most likely will be cracked when no steel corrosion is present.

Chapter 6 Discussion of Parametric Results

6.1 Introduction

This chapter reviews the results from the parametric analysis conducted using the FE model. In order to understand the effects of corrosion on the behaviour and strength of RC beams, the results were compared as a function of different design parameters, namely the shear span-to-depth ratio *a/d*, the beam width b_w, and the stirrup spacing *s*. The results are presented in terms of the change in shear strength, deformability, crack angle θ, and longitudinal strain at mid-depth of the beam ε_x, all against the steel mass loss. The impact of the different design parameters with respect to corrosion can also help to understand how RC beams counteract the effects of corrosion by redistributing stresses. Finally, a comparison of the FE results with calculations from the design equations in CSA A23.3-04 (2004) is performed, and considerations for assessment of affected members are suggested.

6.2 Shear Resistance in CSA A23.3-04

The shear design methodology in CSA A23.3-04 (2004) is based on the Modified Compression Field Theory (MCFT). The nominal shear resistance given by clause 11.3.3 is:

$$V_n = V_c + V_s \tag{6.1}$$

where V_n is the total shear strength of a member, V_c is the concrete contribution to shear strength, and V_s is the steel contribution to shear strength. The individual capacities are given by clauses 11.3.4 and 11.3.5 for concrete and steel, respectively. The concrete contribution to shear strength V_c can be calculated using the following equation:

$$V_c = \lambda \beta \sqrt{f_c'} b_w d_v \tag{6.2}$$

where λ is a factor for concrete density (taken as unity for normal concrete), β is a factor that depends on the average tensile stresses in cracked concrete, b_w is the beam effective width, and d_v is the shear depth of the beam (taken as the maximum between 0.9*d* and 0.72*h,* where d is the distance from the extreme compression fibre to the centroid of the longitudinal tension reinforcement and h is the beam's height). Parameter $\sqrt{f_c^{'}}$ in Eq. 6.2 is limited to 8 MPa.

The steel contribution is calculated based on the crack angle θ and stirrup spacing s as follows:

$$V_s = \frac{A_v f_y d_v \cot\theta}{s} \quad 6.3$$

where A_v is the area of the stirrups, and f_y is the yield strength of the shear reinforcement.

Under clause 11.3.6.3, the code offers a simplified method to determine θ and β, provided that the beam has a minimum amount of transverse reinforcement. In this case, the angle θ is taken as 35° and β is assumed to be 0.18. In clause 11.3.6.4, a more detailed method (general method) is provided, and θ and β are calculated based on the mid-height horizontal strain ε_x. The longitudinal strain at mid depth is calculated from:

$$\varepsilon_x = \frac{M/d_v + V}{2(E_s A_s)} \quad 6.4$$

where M and V are the applied moment and shear force, respectively, E_s is the elastic modulus of the longitudinal steel, and A_s is the cross-sectional area of the tension longitudinal reinforcement. The crack angle is given in this clause as:

$$\theta = 29 + 7000\varepsilon_x \quad 6.5$$

Factor β is calculated under clause 11.3.6.4 as:

$$\beta = \left(\frac{0.4}{1+1500\varepsilon_x}\right)\cdot\left(\frac{1300}{1000+s_{ze}}\right) \quad 6.6$$

where ε_x is the longitudinal strain of the member at mid-height, and s_{ze} is the equivalent crack spacing parameter that allows for the influence of aggregate size (s_{ze} = 300 mm if the minimum shear reinforcement is provided.)

The performance of Eq. 6.1 in calculating the residual shear strength of RC beams affected by corroding stirrups was established against each of the FE results. In an effort to introduce the effects of corrosion in Eq. 6.1, the area of the shear reinforcement A_v in Eq. 6.3 was reduced to the corresponding value of mass loss. The incorporation of any damage in the concrete was neglected in calculating the residual shear strength, and the initial sectional and material properties were used.

Since the Toronto beam series fall within the CSA A23.3-04 (2004) criteria for the shear design given by Eq. 6.1 (i.e., $a/d > 2.5$), the FE results from these series are compared in the following sections to important design variables such as the crack angle θ and mid-height horizontal strain ε_x. This data was extracted from the FE results within a distance d_v of the load, which is considered the critical section of the beam. To longitudinal strain at mid depth was taken as the average of those extracted from six rows of elements within d_v at mid-height of the beam. These values were all taken at peak loading values.

6.3 Oregon Beams

The beams tested by Higgins et al. (2003) have an *a/d* ratio of 2.03 (lower than the Toronto beams), and therefore this set of results was considered separately. These beams have two regions of high shear stress: a critical region with s = 254 mm, and a non-critical one with s = 152 mm. The effect of mass loss of the stirrups on the crack angle θ and horizontal strain ε_x is shown in Figure 6.1 and Figure 6.2, respectively. The data is presented with respect to values extracted within d_v of the load, for both critical (blue) and non-critical (red) regions. Also in the figures are the values obtained from Eqs. 6.4 and 6.5 (green). Very little effect of corrosion on the crack angle is observed from Figure 6.1. This was to be expected as the *a/d* is below 2.5, and the load path is rather direct from the loading point to the support. Although it is suggested in CSA A23.3-04 (2004) that deep flexural members ($a/d < 2$) be designed using the strut-and-tie model, the crack angle as given by Eq. 6.5 was also calculated and compared to the FE results. Note that since the equations in the CSA A23.3 standard are based on the MCFT, the calculations obtained from them are denoted as MCFT values in the figures from here onwards. Good agreement was found between the FE results and MCFT calculations. It is important to note as well that the FE software used in the analysis is built upon the MCFT. The critical span showed a much softer response than that of the non-critical one.

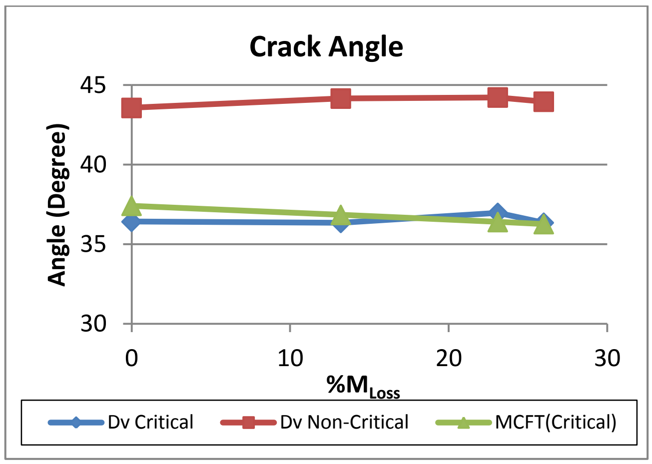

Figure 6.1: Effects of mass loss on crack angle for Oregon beam 10R

The mid-height horizontal strain was extracted from the analysis data and is presented for both critical and non-critical spans in Figure 6.2. A decrease is observed in both spans as the level of corrosion increases. The critical span has the same value of strain for the uncorroded and low-corrosion specimens, whereas the strain in the non-critical span continues to decrease for all corrosion levels. The estimation of the strain using Eq. 6.4 also captures this decrease as the corrosion level increases.

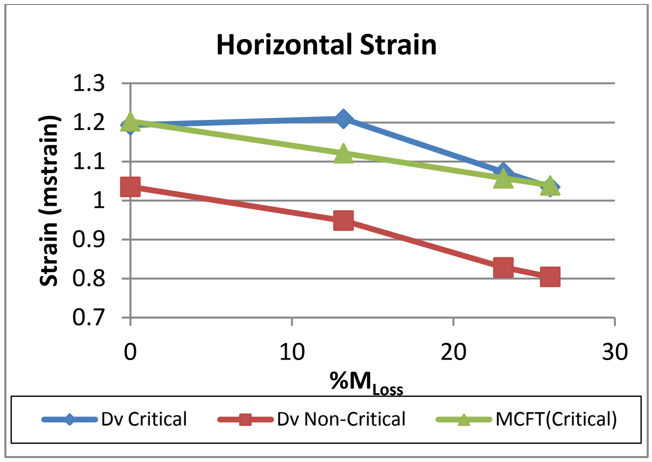

Figure 6.2: Effects of mass loss on mid-height horizontal strain for Oregon Beam 10R

6.4 Shear Span-to-Depth Ratio (a/d)

This section presents the results of the FE parametric analysis in terms of the shear span-to-depth ratio *a/d*. The results first highlight the effect of *a/d* and stirrup corrosion on shear strength and deformability, and then on parameters θ and ε_x as used in Eqs. 6.5 and 6.4, respectively.

6.4.1 Effects on Strength and Deformability

Figure 6.3 shows the shear strength relative to the uncorroded specimen V_{cor}/V_{val} and the corresponding peak deflection relative to that of the uncorroded specimen $\delta_{cor}/\delta_{val}$ as a function of steel mass loss and for increasing shear span-to-depth ratios *a/d*. The data corresponds to the parametric analysis conducted on the Toronto beam series (Series A, B and C). The results have been rearranged to present those related to the same *a/d* ratio on a single figure. In general, a decrease of the V_{cor}/V_{val} ratio is observed for increasing mass loss. The rate of decrease is similar for all *a/d* ratios. When the *a/d* ratio is lowest, there are no differences in the relative strength among the series, which differ in stirrup spacing and section width. As the *a/d* increases, the section with the smallest width (Series C) displays the highest rate of shear strength loss as the corrosion level increases. Series A and B exhibit a similar reduction even though Series B is smaller in width. This is most likely caused because of the reduction in stirrup spacing from 210 mm in Series A to 190 mm in Series B. The range of decrease in shear strength for all the cases analyzed is around 20%.

When looking at the relative peak deformation, there is a slight decrease on the peak deflection at mid span relative to the uncorroded sample at high corrosion levels, with Series C displaying the largest reduction. However, there is not a clear trend for corrosion levels in between. It is interesting to note the difference in deformability of Series B with respect to the other two. This is the series with the smallest stirrup spacing. Closer-spaced stirrups have a greater effect on preventing the reduction on peak deformation as corrosion damage increases.

Strength Degradation	Effects of Corrosion on deformability
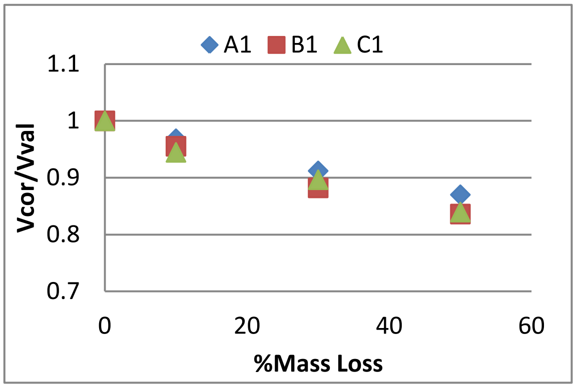 a) *a/d* = 4	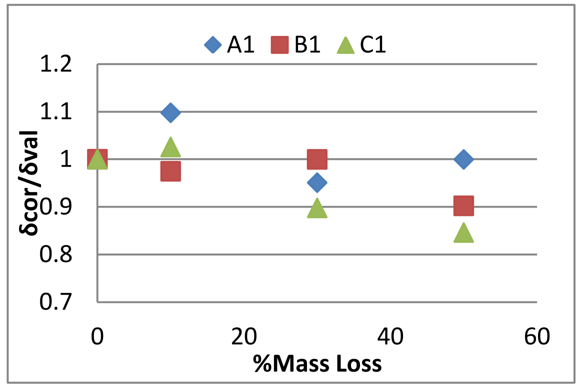 b) *a/d* = 4
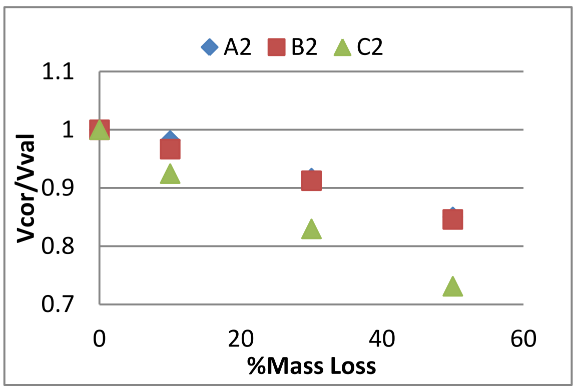 c) *a/d* = 5	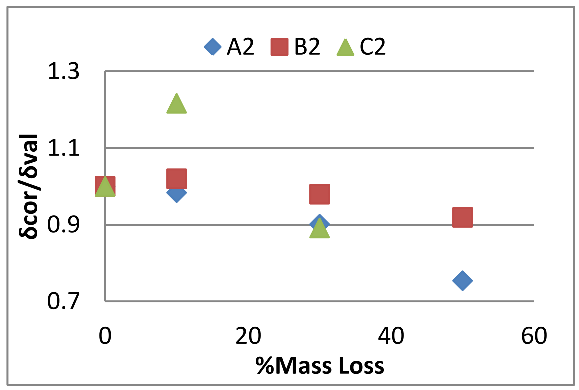 d) *a/d* = 5
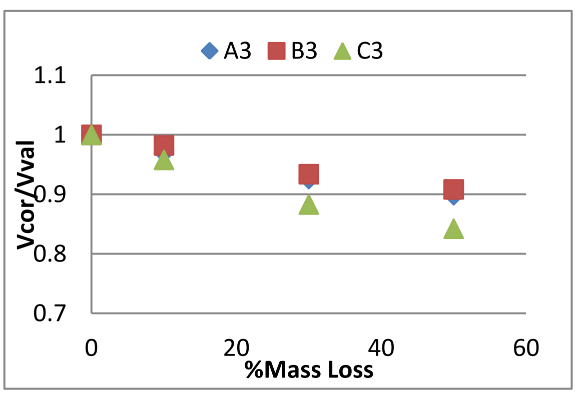 e) *a/d* = 7	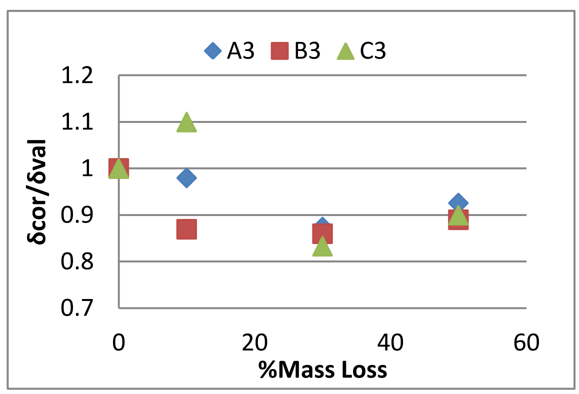 f) *a/d* = 7

Figure 6.3: Effects of *a/d* and mass loss on strength and deformability

The V_{cor}/V_{val} and $\delta_{cor}/\delta_{val}$ ratios are plotted against *a/d* for all the FE results (including those obtained from the Oregon beams) in Figure 6.4 and Figure 6.5, respectively. The values are presented as a function of the corrosion level: "L" for low, "M" for moderate, and "H" for high. The *a/d* parameter definitely has an impact on behaviour and strength when corrosion is present on the stirrup of RC beams. The general trend indicates that at any level of corrosion, the impact on strength is greater at lower *a/d* ratios. The effect on peak deformation is also significant at low *a/d* ratios; however, there is not a clear trend for higher *a/d*. Whereas high corrosion levels do affect the peak deformation of slender beams, this deformation tends to increase relative to the uncorroded sample at low levels of corrosion.

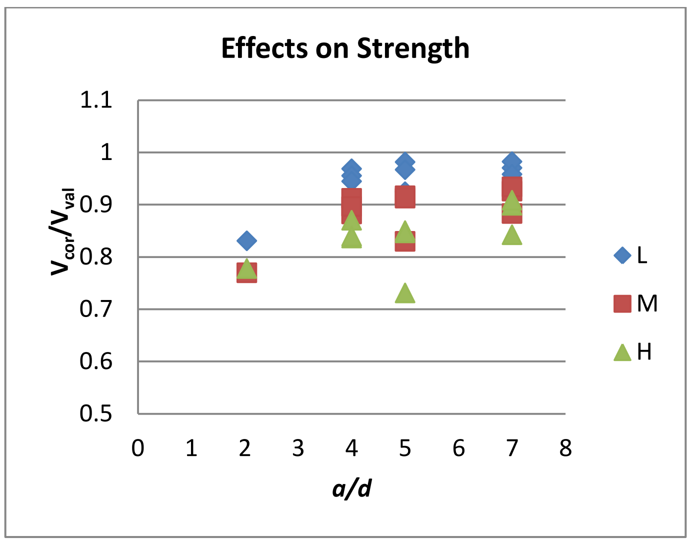

Figure 6.4: The effects of *a/d* on the relative strength

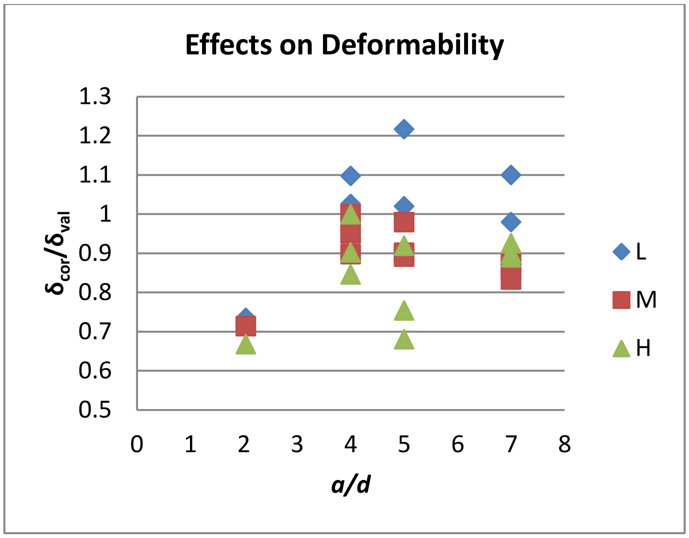

Figure 6.5: The effects of *a/d* on deformability

The difference in strength and behavioural effects with respect to the *a/d* ratio can be explained in terms of the internal stress mechanism. Shorter-span beams tend to distribute more stresses towards concrete components, especially for $a/d < 2.5$. In these types of beams, stresses are transferred from the loading towards the support through a disturbed field. Within these regions, because of the biaxial loading corresponding to the orientation of principal stresses, the strength of the disturbed field relies greatly on the value of tensile stresses and extent of cracking in the concrete. An increase in cracking leads to a decrease in the concrete compression struts' ability to resist compressive forces. The higher the amount of cracking, the less the strength a member can withstand, and therefore when corrosion-induced cracking is present, higher effects on the member strength are noticed. Similarly, as the shorter-span beams rely on concrete to resist the load, less deformation is expected. A slight change in deflection leads to a high impact in relative deformation, as these beams deform relatively less than slender beams. As the *a/d* ratio increases, the beams rely less on the concrete contribution to shear resistance, and the load is distributed more equally between the steel and concrete components, although this load sharing is also based on the width of the beams and spacing of the stirrups.

6.4.2 Effects on θ and ε_x

Figure 6.6 presents the effects of corrosion on the crack angle θ for each *a/d* ratio. The relationships shown are established from the FE results (on the left) and the values calculated from Eq. 6.5 (on the right). Note that the y-axes are adjusted to showcase general behaviour of both FE and MCFT results. Several observations can be made from Figure 6.6. First of all, the crack angle is greatly affected by the beam width and stirrup spacing (differences among Series A, B and C). Whereas for an *a/d* ratio of 4 the FE results show a softening of the angle as corrosion damage increases (with the exception of Series B, where the stirrups are placed at a closer distance), the trend is not as clear for *a/d* ratios greater than 5. The MCFT estimates clearly indicate a decrease in θ as the level of corrosion increases for all *a/d* ratios and the three series, including that with closer stirrups. However, this softening of the crack angle observed from the MCFT estimates is not as significant as that observed in the FE results for an *a/d* ratio of 4 (e.g., Series A softens by nearly 10° at high levels of corrosion in the FE results compared to only 1.5° in the MCFT calculation). The MCFT predicts a slightly stiffer crack angle than the FE analysis for the uncorroded samples in Series A and B series, while it does predict a softer angle for Series C.

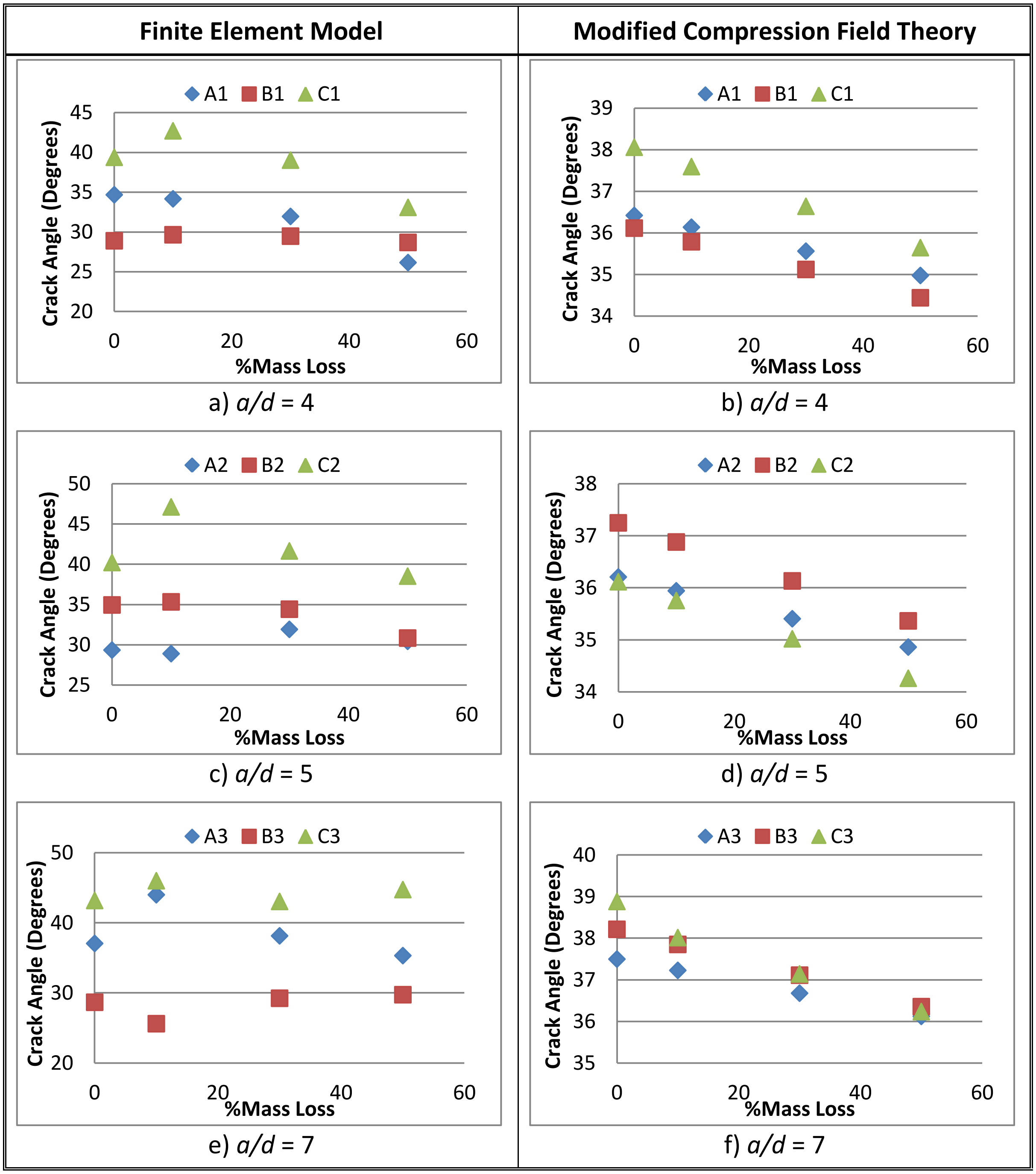

Figure 6.6: Effects of *a/d* and mass loss on cracking angle

Figure 6.7 plots the crack angle obtained in the FE analysis against the shear span-to-depth ratio for various levels of corrosion ("V" denotes no corrosion). The large scatter in the data for *a/d* ratios greater or equal to 4 confirms the effects of beam width on the crack angle independently of corrosion damage. The FE data from the Oregon beams (*a/d* = 2.04) is close for any corrosion level.

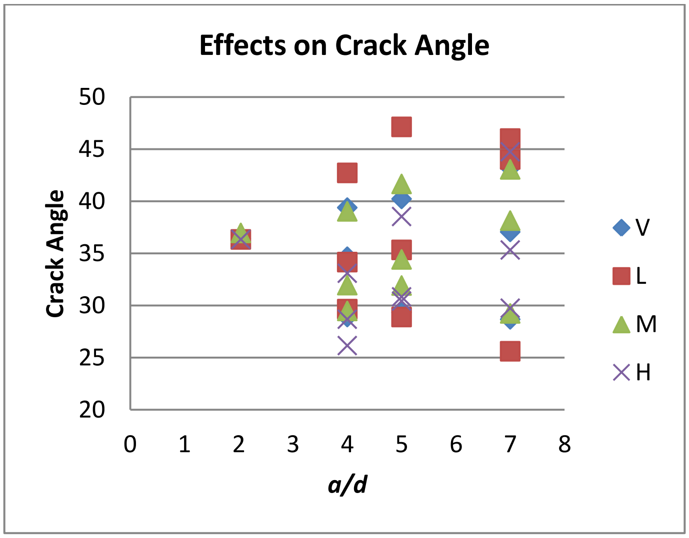

Figure 6.7: Effects of *a/d* on crack angle

Figure 6.8 presents the effects of corrosion on the mid-depth horizontal strain ε_x for each *a/d* ratio. The relationships shown are established from the FE results (on the left) and the values calculated from Eq. 6.4 (on the right). The results from the FE analysis show an increase in the mid-height horizontal strain with increasing levels of corrosion and for all *a/d* ratios. The increase at high levels of corrosion is sometime nearly 3 times that of the uncorroded member. However, it is interesting to note that this trend is reversed for the strain calculated according to the MCFT. The MCFT estimates of mid-height horizontal strain decrease with increasing corrosion damage.

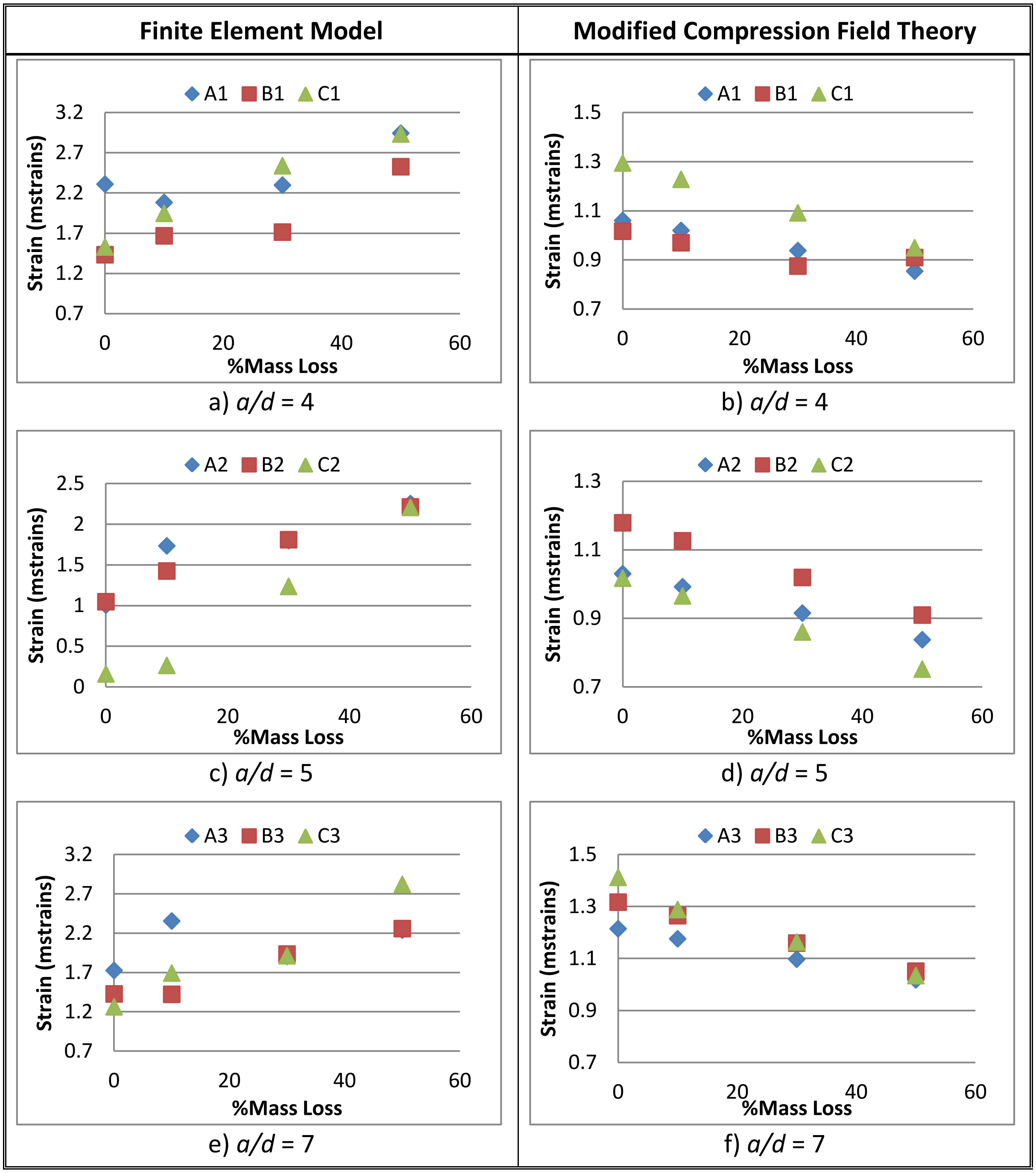

a) $a/d = 4$ b) $a/d = 4$ c) $a/d = 5$ d) $a/d = 5$ e) $a/d = 7$ f) $a/d = 7$

Figure 6.8: Effects of *a/d* on mid-height horizontal strain

The mid-height longitudinal strain data for all beams analyzed is rearranged in Figure 6.9 against the *a/d* ratio and for all corrosion levels. As noted previously, as corrosion-induced damage is increased in slender beams ($a/d \geq 4$), the corresponding longitudinal strain at mid-depth of the member is increased. This effect is not observed for the Oregon beams with an *a/d* = 2.04. The smaller mid-height strain for the beams with *a/d* = 5 (compared to those with *a/d* = 4 or *a/d* =7) can be attributed to softer crack angles with deeper penetration of the compression block and resulting in less mid height deformation for these members.

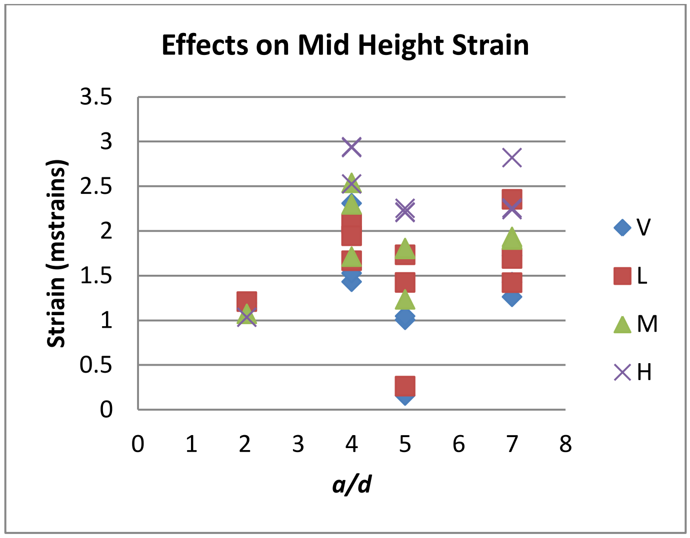

Figure 6.9: Effects of *a/d* on average mid-height strain within d_v of point load

6.4.3 *a/d* Summary

By simply looking at the relative strength and deformation results, the following conclusions are drawn:

- Linear strength decrease for *a/d* ratios of 4 and 5
- Strength seems to stabilize past moderate levels of corrosion for *a/d* ratio of 7
- The effects of stirrup spacing counteracts the effects related to the decrease in beam width for Series B
- A decrease in beam width affects the strength degradation of the beams, with the exception of *a/d* ratio of 4
- The *a/d* ratio has an impact on strength reduction, with a greater decrease at lower *a/d* ratios

By looking at the effects of corrosion on the deformability of the affected beams at peak loads, the following conclusions are drawn:

- The largest effects on relative deflection were observed for the *a/d* ratio of 5
- The impact of closer-spaced stirrups (Series B) is noticed for *a/d* of 4 and 5, wherein very little effect of corrosion was observed on the deformability of this series
- At an *a/d* of 7, a larger impact is noticed at lower levels of corrosion but stabilizes after this level of damage

The impact of corrosion on strength and deformability of the beams with respect to their *a/d* ratio revealed important trends, which help to understand the behaviour of RC members when corrosion is present on the stirrups. From the results obtained by using Eqs. 6.4 and 6.5, it is apparent that simply adjusting the area of available shear reinforcement within the design equation does not properly simulate the behavioural change in the analyzed RC beams. Clear trends with respect to the crack angle are:

- The crack angle softens with respect to increasing corrosion at lower *a/d* ratios
- The *a/d* ratio has an impact on the stability of the crack with respect to increasing corrosion
- The beam width impacts the crack angle of the FE data while not as much in the MCFT calculations
- The crack angle is stiffer for beams with smaller widths independently of the *a/d* ratio
- Beams with closer stirrup did not display a change in crack angle as the corrosion level increased
- The crack angle obtained from the MCFT slightly softens with respect to increasing corrosion

Finally, by looking at the results with respect to the horizontal strain at mid height, some important trends are highlighted here:

- The mid-height strain from the FE results increased with increasing levels of corrosion for nearly every case
- The strain calculated from Eq. 1.4 diverges from that obtained from the FE results, decreasing in value as the corrosion level increases

6.5 Beam Width (b_w)

The effect of the beam width b_w is an important parameter to study here because of the corrosion-induced model introduced in FE analysis. To introduce the prestraining effect in order to simulate corrosion expansion, the equivalent strain from each corroded stirrup leg was averaged over the beam cross-sectional width based on the area occupied by the thick wall cylinder. Therefore, the thinner the member, the larger the strain is induced by the effects of expanding corrosion by-products.

6.5.1 Effects on Strength and Deformability

Figure 6.10 shows the shear strength relative to the uncorroded specimen V_{cor}/V_{val} and the corresponding peak deflection relative to that of the uncorroded specimen $\delta_{cor}/\delta_{val}$ as a function of steel mass loss and for decreasing beam widths b_w. The strength degradation characteristics of each of the series are very similar as the corrosion level is increased. The behaviour is similar between the different specimens of each series, indicating that the introduced prestraining induces similar levels of corrosion for different span lengths and despite different *a/d* ratios. A slightly less impact is noticed for the specimens with a longer span, most likely attributed to the more dominant flexural behaviour. The effects of beam width on deformability are more noticeable for smaller widths (Series C). An increase in peak deflection at low levels of corrosion is noticed for each span length of this series, which is then reversed to a decrease for moderate and high corrosion levels. The initial increase in deformability might be related to the concrete core between consecutive affected stirrups being pre-compressed by the straining induced from the expansion of the reinforcing bars. At low levels of corrosion, this compression might compensate some of the tensile stresses induced by the applied loading and, therefore, lead to an increase in deformability. Once cracking is induced at higher levels of corrosion, the concrete core is weakened and leads to earlier failure of the concrete. The specimens with larger width (Series A and B) display only a small decrease in the peak deflection as corrosion increases

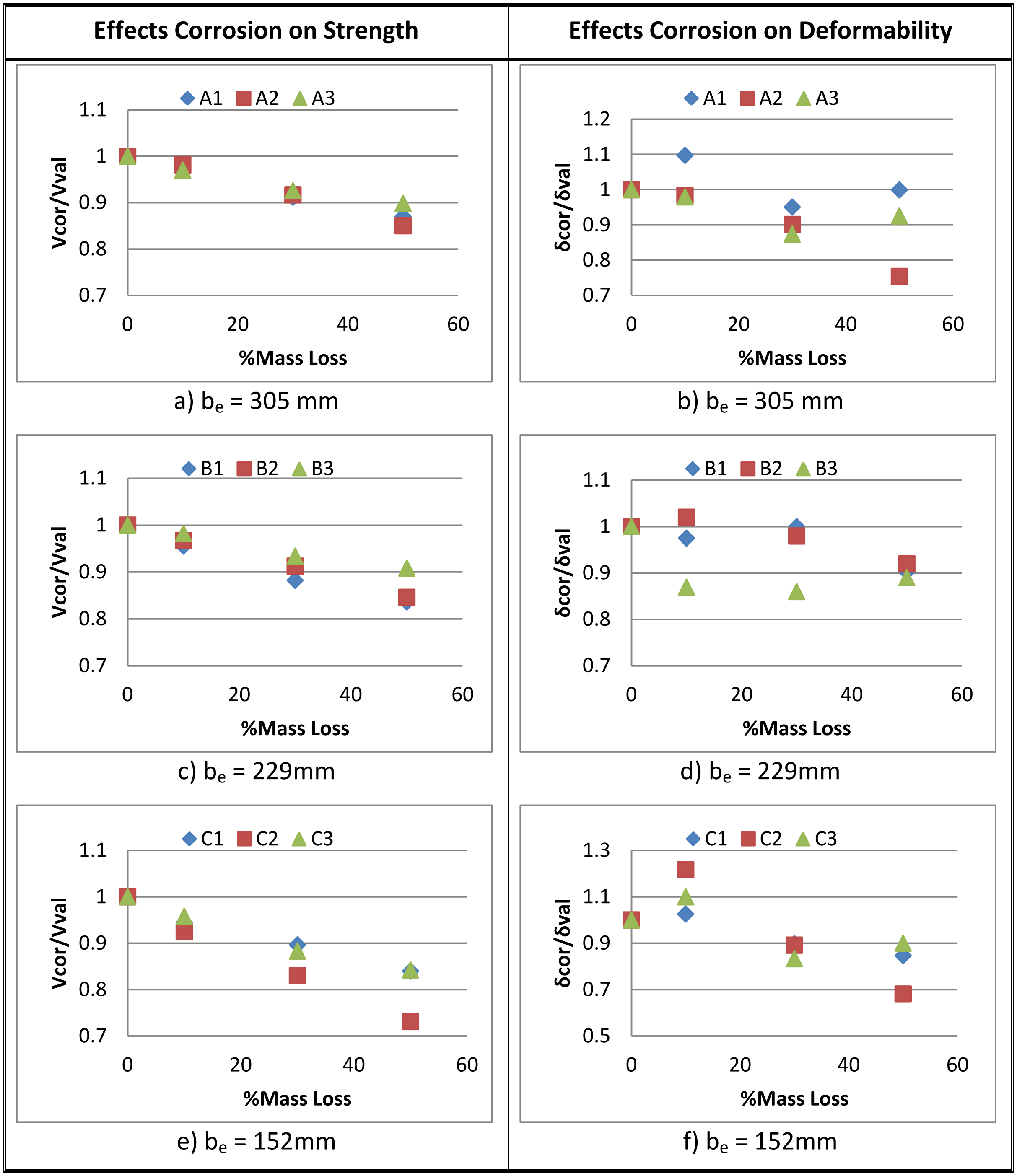

Figure 6.10: Effects of b_w and mass loss on strength and deformability

Figure 6.11 plots V_{cor}/V_{val} ratio against b_w for all the FE results (including those obtained from the Oregon beams) for low, moderate and high corrosion levels. The effect of low *a/d* ratio is shown by including the Oregon beams data (b_w = 254 mm), where a higher decrease in shear strength is evident. In general, the shear strength is reduced as the beam width is decreased and the level of corrosion is increased.

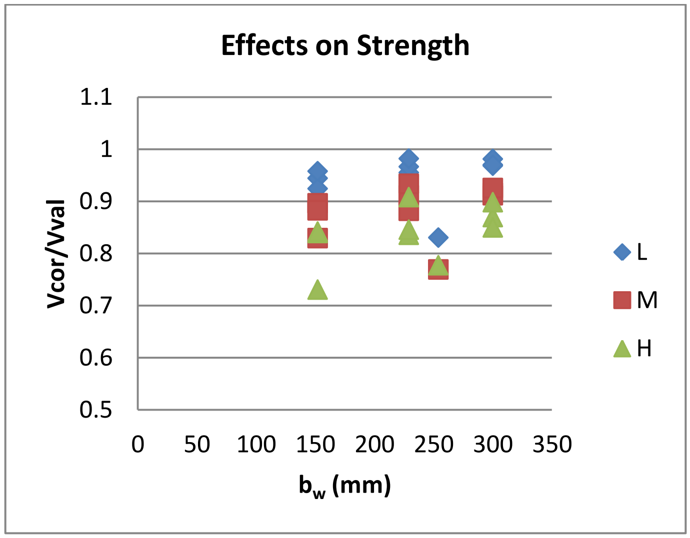

Figure 6.11: Effect of beam width on shear strength

Similarly, Figure 6.12 shows the peak deflection relative to that of the uncorroded specimen $\delta_{cor}/\delta_{val}$ against b_w for all FE results and all corrosion levels. The large scatter of the data at smaller beams width is indicative of the effects of the *a/d* ratio on this series. There is not a clear trend that can be identified from this figure. The effect of a small *a/d* ratio is shown for the Oregon beams, which exhibit lower mid-span deflections at peak loads. With the exception of these beams (b_w = 254 mm), an increase in deformability is noticed for most of the low corroded specimens.

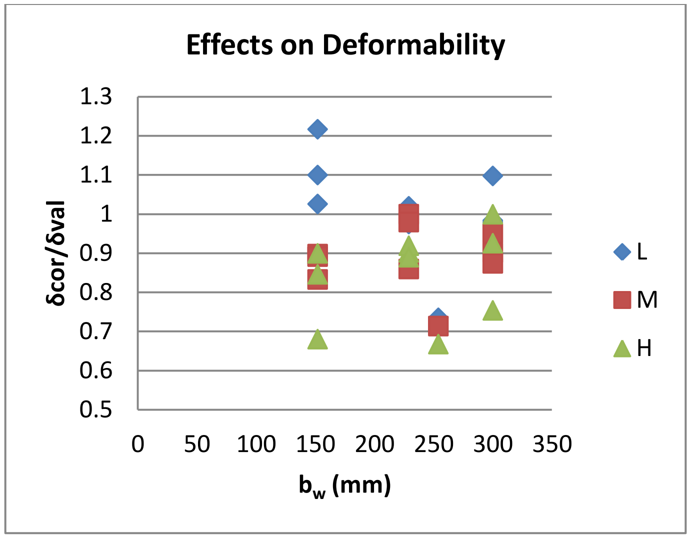

Figure 6.12: Effects of beam width on deformability

6.5.2 Effects on θ and ε_x

Figure 6.13 presents the effects of corrosion on the crack angle θ for each beam width b_w. The relationships shown are established from the FE results (on the left) and the values calculated from Eq. 6.5 (on the right). With the exception of Series C, the FE results do not show sensitivity of the crack angle to corrosion level. Beams C1 and C3, however, exhibit a decrease of the angle with increasing corrosion damage. The MCFT equation estimates that the inclination of the crack slightly decreases as the level of corrosion increases. Yet, this decrease is only one or two degrees, whereas the decrease observed in some of the FE results is nearly 10°. Typically, the MCFT equation properly estimates the crack angle when compared to parametric results of uncorroded specimens, although it generally underestimates its value at high *a/d* ratios and overestimates it for smaller *a/d*.

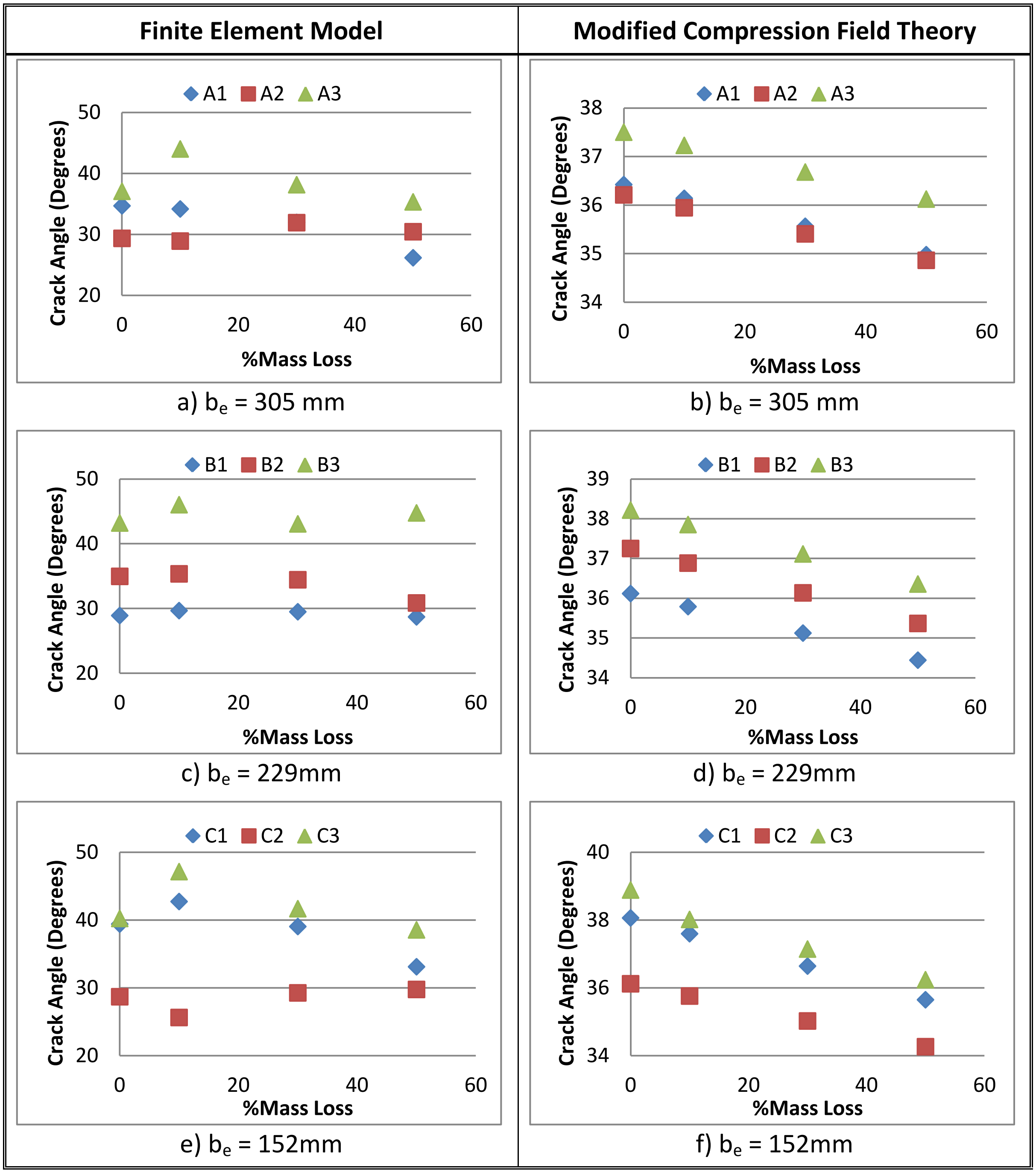

Figure 6.13: Effects of b_w on cracking angles

Figure 6.14 plots the crack angle obtained in the FE analysis against the beam width for various levels of corrosion. The scatter of the data in Figure 6.14 for a value of b_w indicates the large impact of the *a/d* ratio on the results. No clear trends can be observed in this graph, which indicates that the beam width does not influence the inclination of the concrete compressive struts.

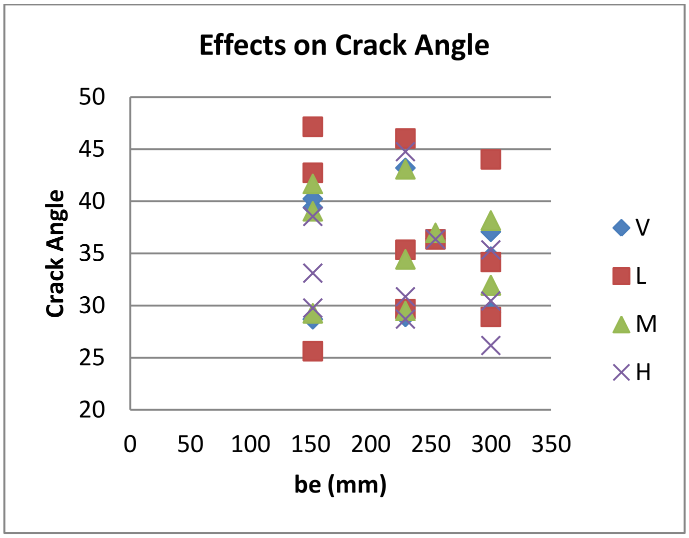

Figure 6.14: Effects of beam width on crack angle

Figure 6.15 presents the effects of corrosion on the mid-depth horizontal strain ε_x for each beam width b_w. The relationships shown are established from the FE results (on the left) and the values calculated from Eq. 6.4 (on the right). As previously observed when the data was presented in terms of the *a/d* ratio, the FE results show an increase in strain for virtually each of the specimens and with each increment of mass loss. The effects of width are noticed however when the behaviour is compared between series. The wider members have a greater impact on strain at mid height. For the shorter beam of this series (A1), the effect on strain is only noticed at high levels of corrosion, as there is only a slight variation of strain from the uncorroded case up to a moderate level of corrosion. The longer member of this series (A3) shows a similar behaviour. The mid-length specimen of this series (A2) exhibits a trend that is matched with the behaviour of the other series. Series B has the most consistent behaviour of the three, where the strain in each of the beams length is very similar and follows a constant increase with increasing corrosion level. This is an indication of the effects of closer-spaced stirrups. Finally, Series C follows very similar behaviour as the previous series. Although the mid-length span beam (C2) does follow the trend observed with the other beams, it has particularly low strains at no corrosion and low corrosion levels; however, this strain then increases significantly towards closer values of strain of other specimens in the same series. The observed increasing trends in the FE data can be explained by a shift in the neutral axis, which is reflected by these higher values of strain at mid height. The shift is rather significant when specimen C2 is considered. Initially, the strain value indicates a neutral axis located near the mid-height of the member, and then the neutral axis shifts upwards to counteract the damage induced by the increasing amount of concrete cracking. The strain predicted by the MCFT equation displays an opposite trend, wherein the strain slightly decreases with increasing mass loss of the shear reinforcement.

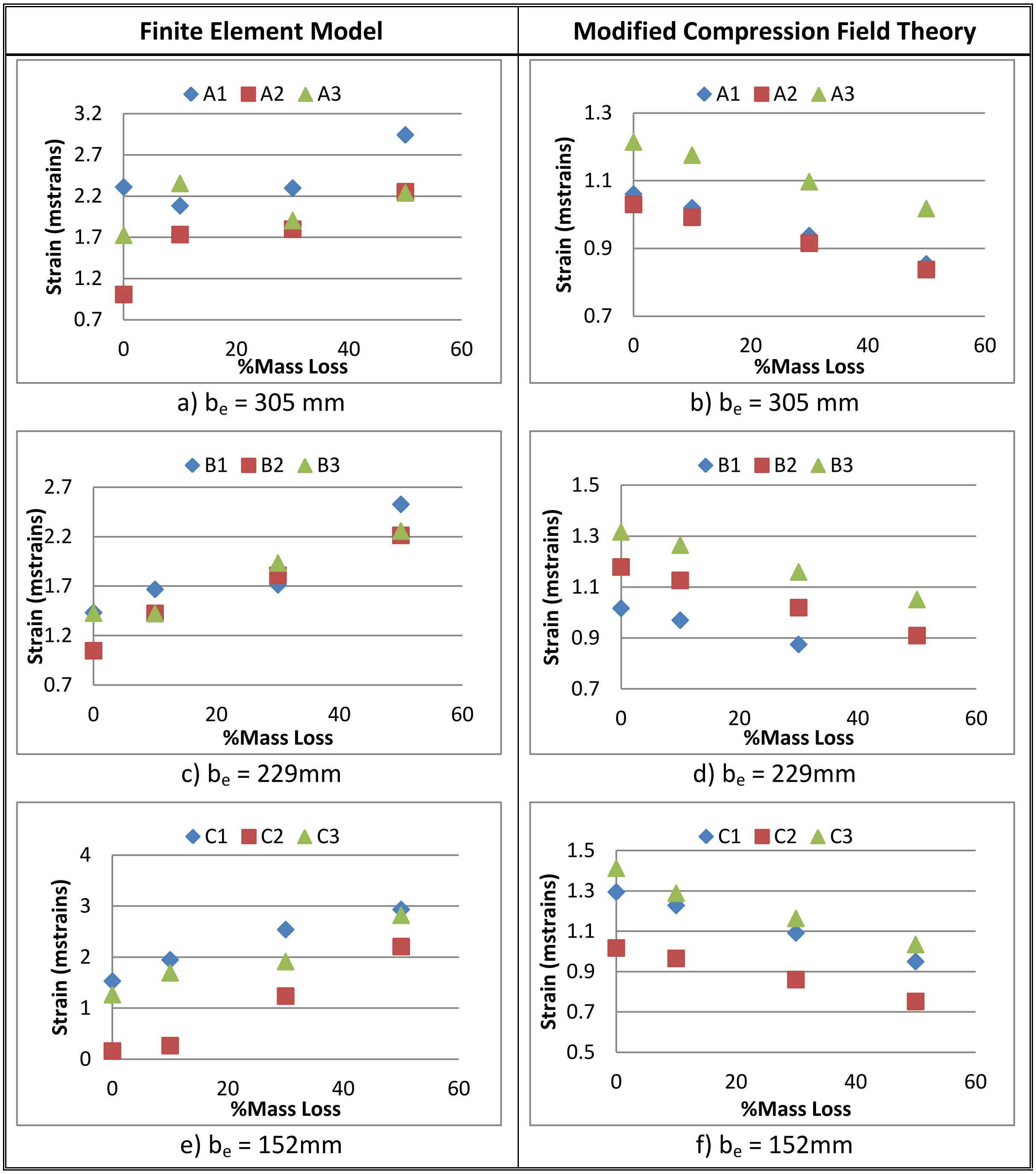

Figure 6.15: Effects of b_w and mass loss on mid-height horizontal strain (FE and MCFT)

The mid-height longitudinal strain data for all beams analyzed is rearranged in Figure 6.16 against the beam width and for all corrosion levels. Again here, the effect of stirrup spacing in observed for beam width values of 229 mm, where the data shows less scatter. The large scatter of the results observed in the figure indicates the effects of the *a/d* ratio on the mid-height strain. In general, for a given level of corrosion, the trend indicates a decrease in value of strain for beams with smaller width. Also, for a given beam width, a higher corrosion level indicates higher values of mid-height strain.

6.5.3 Beam Width Summary

Despite having values of cracking-induced strain twice as large as the beam with a width of 304 mm (series A), the specimens with a width of 152 mm (series C) only showed a slighter decrease in shear strength. The induced strain had a higher impact on the deformation characteristics of the beam, especially for specimens with the smaller width (Series C). The deformation characteristics of wider members were less affected by this prestrain. In general, there was not a strong dependency of the shear strength from the FE results on the beam width. Shear strength degradation was clearly linked to the increase in mass loss of the shear reinforcement and ensuing concrete cracking. A similar conclusion can be made for peak deflection at mid span of the beams.

The beam width had a larger impact on the horizontal strain at mid-height of the member, although the trends observed were different from the FE results (increasing with increasing corrosion damage) and MCFT calculations (decreasing with increasing corrosion damage). The effect of decreasing the beam width from Series A to Series B was counteracted by the closer-spaced stirrups of Series B. In general, there was less scatter of the data for the specimens in these series.

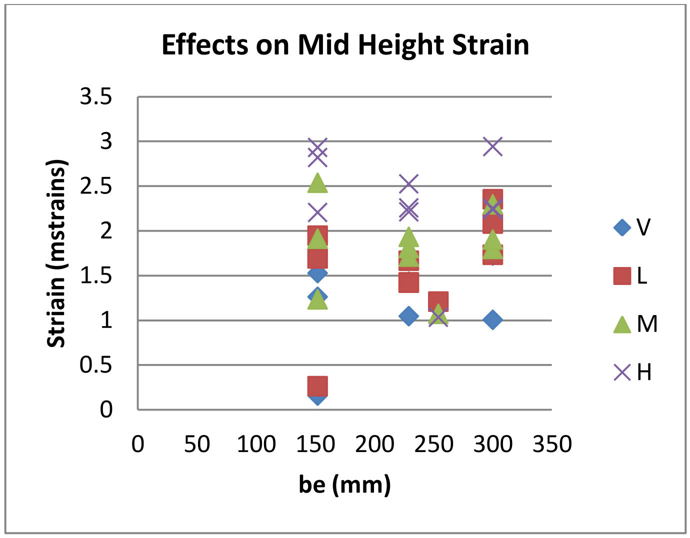

Figure 6.16: Effects of beam width on mid-height horizontal strain

6.6 Stirrup Spacing (s)

One important parameter in the contribution of steel to shear resistance is the stirrup spacing. When an increase in shear capacity is needed, the first design parameter modified is the stirrup spacing. The effect of stirrup spacing in the context of RC beams with corroded shear reinforcement is studied in this section. When shear reinforcement corrodes, the spacing between stirrups along with the value for the concrete cover determines whether corrosion-induced damage will result in either spalling or delamination of the concrete cover.

6.6.1 Effects on Strength and Deformability

The V_{cor}/V_{val} ratio is plotted against the stirrup spacing for all the FE results (including those obtained from the Oregon beams) and for the three corrosion levels in Figure 6.17. Although the data for each of the stirrup spacing is rather limited, a general sense of its effect on residual strength can be observed from the figure. Shear strength degradation takes place for increasing corrosion levels and increasing spacing of the transverse reinforcement. Thus the impact of corrosion on shear strength is associated with the stirrup spacing. The lowest decrease in strength is associated to beams with smaller stirrup spacing (corresponding to specimens with largest *a/d* ratio), and the strength degradation is higher for beams with larger spacing (associated to smallest *a/d* ratio.) By comparing the FE results for the same *a/d*, it is observed that a reduction in the relative shear capacity occurs with wider-spaced stirrups. This trend holds true for beams with an *a/d* of 7 (stirrup spacing from 152 to 168 mm) and an *a/d* of 4 and 5 (stirrup spacing from 190 to 210 mm).

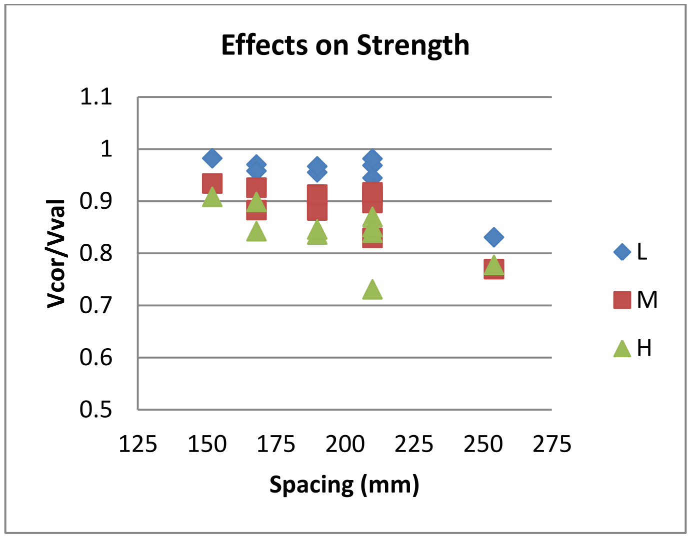

Figure 6.17: Effects of stirrup spacing (s) on shear strength

The $\delta_{cor}/\delta_{val}$ ratio is plotted against the stirrup spacing for all the FE results (including those obtained from the Oregon beams) and for the three corrosion levels in Figure 6.18. The grouping of the results for each of the stirrup spacing is also indicative of the *a/d* ratio. Closer-spaced stirrups were used in the longer members, whereas wider-spaced stirrups were used for the two shorter spans of the Toronto beams. The Oregon beams had the widest spacing (254 mm) of all the members. A comparison of results for the same *a/d* ratio indicates that wider-spaced stirrups have a greater effect on the deformation characteristics. The effects is not as important for an *a/d* ratio of 7 (stirrup spacing of 152 mm and 168 mm) compared to beams with an *a/d* ratio of 4 and 5. The wider-space stirrups only induce a slight decrease for the *a/d* of 7, whereas a larger decrease in peak deflection is observed for the beams with an *a/d* ratio of 4 and 5 (s = 210 mm), especially at high levels of corrosion.

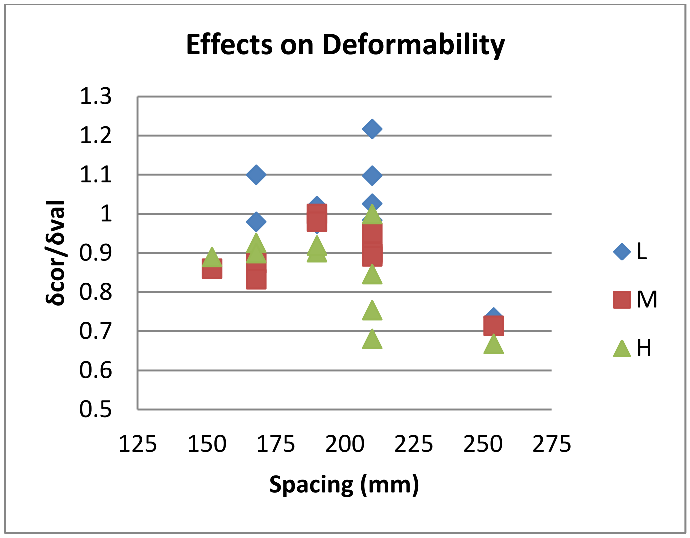

Figure 6.18: Effects of stirrup spacing (s) on deformability

6.6.2 Effects on θ and ε_x

Figure 6.19 plots the crack angle obtained in the FE analysis against the stirrups spacing for various levels of corrosion. There is not a clear dependency of the crack angle on the stirrup spacing for different corrosion levels. The crack angle depends largely on the *a/d* ratio and beam width. One effect that can be noted is in the distribution of the impact of different levels of corrosion on the data. For a given *a/d* ratio, the beams with closer-spaced stirrups show less scatter in the predicted crack angle than those with widely spaced transverse reinforcement.

The mid-height longitudinal strain data for all beams analyzed is rearranged in Figure 6.20 against the stirrup spacing and for all corrosion levels. For a given spacing of the stirrups, the strain at mid depth increases as the level of corrosion increases. Furthermore, for the same *a/d* ratio, a decrease in the strain with increasing spacing occurs for specimens whose shear reinforcement was not corroded (denoted by “V” in Figure 6.20). Once corrosion is introduced, the stirrups spacing appears not to have a direct effect on the resulting strain at mid-height of the member.

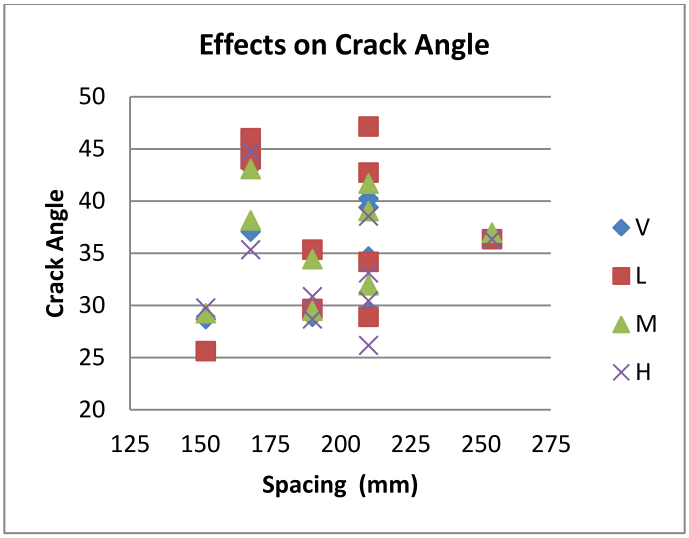

Figure 6.19: Effects of stirrup spacing (s) on crack angle

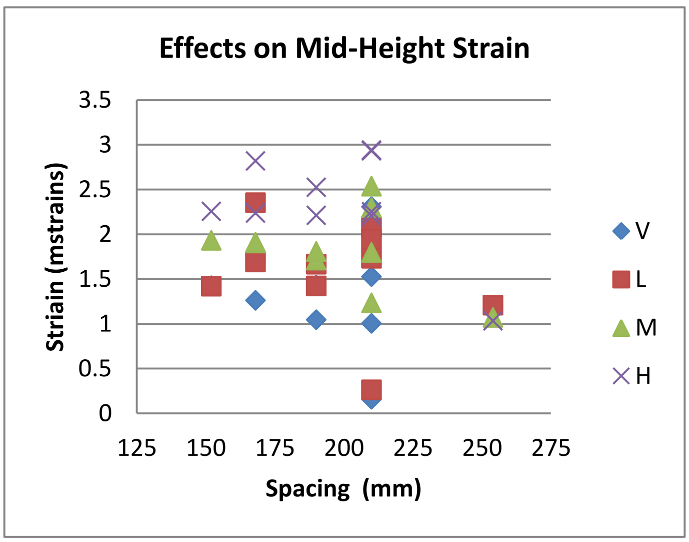

Figure 6.20: Effects of stirrup spacing (s) on mid-height horizontal strain

6.6.3 Stirrup Spacing Summary

The following conclusions can be made from the effect of stirrup spacing on shear strength and peak deflection:

- A decrease in strength is noticed with increasing stirrup spacing.

- The effects of stirrup spacing on the decrease in shear strength are more significant as the *a/d* ratio is decreased.
- The effects of corrosion on deformability are greater with increasing stirrup spacing.

The impact of stirrup spacing on MCFT parameters θ and ε_x depends on parameters other than stirrup spacing. The only main conclusion that can be made is based on the scatter of each set of data, wherein beam with closer stirrups show less scatter regarding the effects of increasing corrosion. The mid-height strain also increases with wider-spaced stirrups when the same *a/d* ratio is compared.

6.7 Effects of Corrosion on Shear Resistance

In this section, the contributions of both concrete and steel towards shear resistance are studied. This is done by comparing the level of contribution of both steel and concrete individually, in terms of the percentage of each contribution to the total strength for each level of corrosion (0, 10%, 30% and 50% mass loss). In order to get the contribution of steel to shear resistance, the average crack angle θ obtained from elements located at mid-height of the beam within a distance d_v of the load was used to identify the number of stirrups contained within the projected distance on the horizontal plane. From the stirrup spacing, the number of stirrups contributing was then computed. The largest stress within a specific stirrup (along its height) was extracted, as the location along the height of this maximum value was assumed to coincide with the intersection of the crack and stirrup. The average steel stress in the LS elements crossing the crack was then calculated. The contribution of the steel was computed based on the calculated number of stirrups, the average area of the steel stirrups (after corrosion-induced mass loss was applied), and the maximum values of stress along the contributing stirrups extracted from the FE analysis. Judgment was sometimes used to identify stirrups contributing to the resistance of the load based on the crack angle and cracking patterns. The concrete contribution was then calculated by subtracting the steel contribution from the total shear strength.

The following subsections present the contributions of both concrete and steel to the shear resistance of the Oregon and Toronto beams, and they are given as a percentage of the total shear strength for a specific corrosion level. The crack angle from the FE analysis ("Teta FEM") and the CSA A23.3-04 general method ("Teta MCFT") is included in the graphs. This additional information helps to understand how the angle impacts each of the component contributions. In addition to reporting the contributions of concrete and steel to shear resistance and the associated crack angle, the following subsections also present the mapping of the concrete principal compressive stress orientations corresponding to the peak load value and for each of the corrosion levels considered. This information enables the understanding of the progression of stress distribution with increasing corrosion damage and helps to determine if a change in shear resistance behaviour occurs.

6.7.1 Oregon Beams

Figure 6.21 illustrates the evolution of the steel and concrete contributions to shear strength with increasing corrosion levels for the Oregon beams data. The figure also displays the change in crack angle θ as the steel mass loss of the stirrups is increased. Note that Beam 10RA corresponds to an uncorroded sample, Beam 10RB corresponds to 13.2% mass loss, Beam 10RC corresponds to 23.1% mass loss, and Beam 10RD corresponds to 26% mass loss. Two observations can be made from Figure 6.21. The first one is in the stability of the crack angle. Despite the increase in corrosion level, there is very little variation in θ. The same conclusion can be made with respect to the individual contributions to shear resistance. A slight increase in the concrete contribution is observed from 59% for the uncorroded sample to 63% for the high level of mass loss. The *a/d* ratio of this beam (*a/d* = 2.04) dictates most of the behaviour. Since there is very little room for variation of the stress fields, the concrete compressive struts extend from the loading point to the support. This leads to the same number of stirrups contributing to the shear resistance of the beams, and it increases the demand on the concrete slightly because of the decrease in available steel.

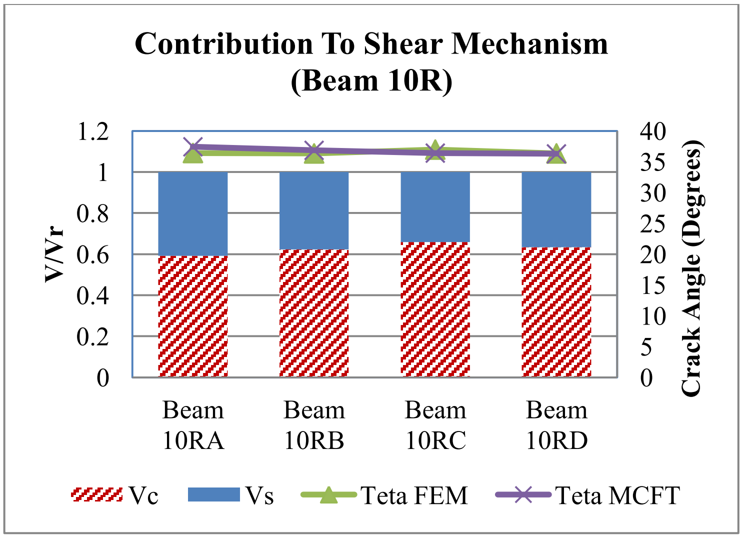

Figure 6.21: Contributions of concrete and steel to shear resistance and crack angle for Oregon beams

Figure 6.22 shows the change in orientation of the principal concrete compressive stresses at ultimate load with increasing levels of corrosion. The direction of the principal concrete compressive stresses is definitively affected by increasing the corrosion level. An arching-type distribution is mostly dominant in the uncorroded specimen (Beam 10RA), whereas the path of the stresses flattens as the corrosion level increases. The effects of having different levels of corrosion on different stirrups need to be considered when comparing Beam 10RD to the other specimens in the series. The leftmost stirrup in the critical span had greater loss in area than the rightmost stirrup, whereas beams B and C had similar corrosion levels for both stirrups. A change from a higher fanning of the stress trajectories in the uncorroded specimen to a more direct distribution line in the corroded ones is noticed. The orientation of the stresses is more evident as corrosion increases to moderate levels (Beam 10RC). This trend is however not as noticeable in Beam 10RD, in which the lesser affected stirrup closer to the load seems to attract more load, where the stress trajectory fanning is more noticeable close to the highly corroded stirrup.

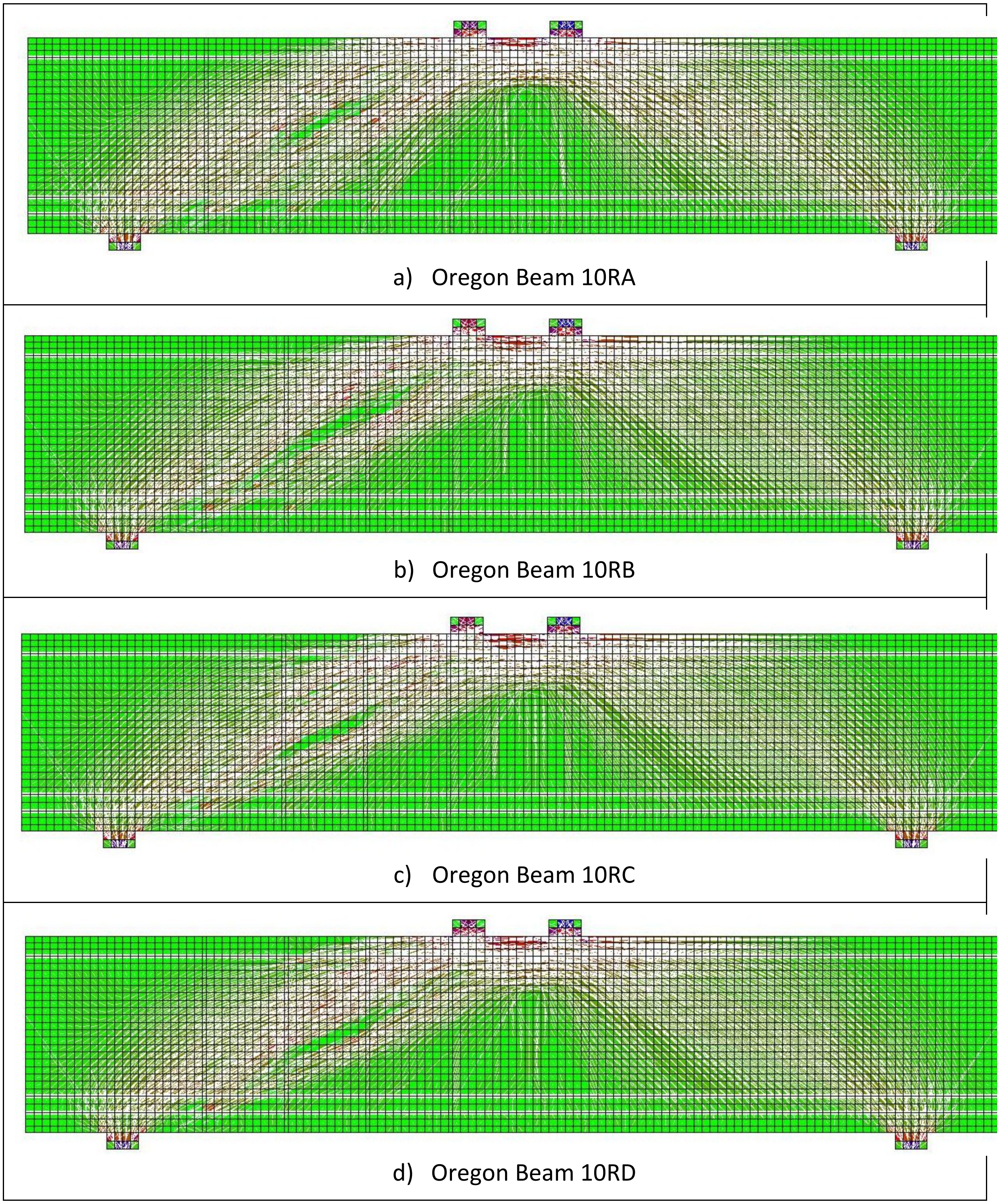
a) Oregon Beam 10RA

b) Oregon Beam 10RB

c) Oregon Beam 10RC

d) Oregon Beam 10RD

Figure 6.22: Principal compressive stress orientation at ultimate load for Oregon beams

6.7.2 Toronto Beams

This subsection presents the individual contributions of concrete and steel to shear resistance and the progression of the concrete compressive stress fields for increasing levels of corrosion and for each of the beams in Series A, B and C.

Series A

Figure 6.23 illustrates the evolution of the steel and concrete contributions to shear strength with increasing corrosion levels for beam A1. The figure also displays the change in crack angle θ as the steel mass loss of the stirrups is increased. The angle of the crack indicates the number of stirrups implicated in the contribution of steel towards the total resistance. The softer the crack, the longer its horizontal projection is, leading to a higher number of stirrups participating in shear resistance and to an increase in the term V_s. However, the FE results show otherwise in spite of the decrease in crack angle with increasing corrosion levels. In this case, an increase in the concrete contribution is observed. Note that even though the number of stirrups resisting shear increases with increasing mass loss, their average cross-sectional area is significantly reduced as well. This reduction has a greater impact on the V_s term than the softening of θ.

To some extent, the crack angle is indicative of the stress paths. Figure 6.26 shows the change in orientation of the principal concrete compressive stresses at ultimate load with increasing levels of corrosion. In order counteract the damaged induced in the critical region within d_v of the support, it is apparent that there is a tied arch forming around this region. By looking at the uncorroded specimen (VSA1V), a clear flexural compression zone is observed near the loading point. Clear stress paths are noticed and directed from the compressive zone towards nearly each of the individual stirrups. At low levels of corrosion, a very similar distribution is observed. The major changes in behaviour happen when corrosion reaches moderate and high levels (VSA1M and VSA1H). Here, it is clear that the stresses are directed toward unaffected stirrups outside of the damaged zone. This directly impacts the stress field in the concrete, creating a softer orientation of stresses and distributing stresses towards the centre of the shear span by means of arching over the damaged area.

Figure 6.24 illustrates the evolution of the steel and concrete contributions to shear strength with increasing corrosion levels for beam A2. The figure also displays the change in crack angle θ as the steel mass loss of the stirrups is increased. The crack angle of beam A2 is more stable for increasing corrosion levels than beam A1, slightly increasing at high corrosion levels. The only difference between beams A1 and A2 is the span of the beam, with A2 having a longer one. The contribution of concrete to shear resistance increases constantly with the increase in mass loss (from 51% to 75%), and this increase is more pronounced than beam A1. This is evidently linked to the stability of the crack angle, which limits the number of stirrups contributing to the resistance of the load, and thus resulting in a constant decrease in the steel contribution because of the loss in cross-sectional area.

Figure 6.27 shows the change in orientation of the principal concrete compressive stresses at ultimate load with increasing levels of corrosion. In general, a softer distribution is noticed for beam A2. The formation of two separate paths is evident in each of the specimens. A deeper flexural compressive region is noticed under the load at mid span, which splits into two paths that lead towards the bottom end of the shear reinforcement. The uncorroded specimen, VSA2V, exhibits a clear beam behavior, as fanning of the stress fields at mid height towards individual stirrups is observed. This behaviour is also true for the low-corrosion level specimen, VSA2L. At moderate and high levels of corrosion, the stress trajectory is directed towards the stirrup located next to the critical section. This leads to a higher amount of stress being carried outside the critical section and near the centre of the shear span.

Figure 6.25 illustrates the evolution of the steel and concrete contributions to shear strength with increasing corrosion levels for beam A3. The figure also displays the change in crack angle θ as the steel mass loss of the stirrups is increased. Beam A3 has the longer span of the Series A. This specimen exhibits a much stiffer crack angle than the beams in the series. Although a crack angle stiffening is noticed in the low-corrosion specimen, the crack is rather stable, and a slight softening is noticed in specimen VSA3H. The concrete contribution once again increases with the level of corrosion. The initial jump in contribution at low levels of corrosion is as a direct effect of the crack stiffening, which leads to one less stirrup contributing to resisting the shear load.

Figure 6.28 shows the change in orientation of the principal concrete compressive stresses at ultimate load with increasing levels of corrosion. This beam displays typical beam behaviour. A larger amount of stresses are concentrated in the upper compressive section of the member. Nearly every stirrup within the critical section has a stress path leading towards it, although a slight concentration is noticed just outside the critical zone for the uncorroded specimen (VSA3V). Similar behaviour is observed for most of the corroded specimens, with a higher concentration of stresses at the limit of the critical section. At moderate levels, the compression zone increases in depth in the area leading away from the critical section. Larger amount of stresses trajectories are observed closer to the centre of the shear span of the member.

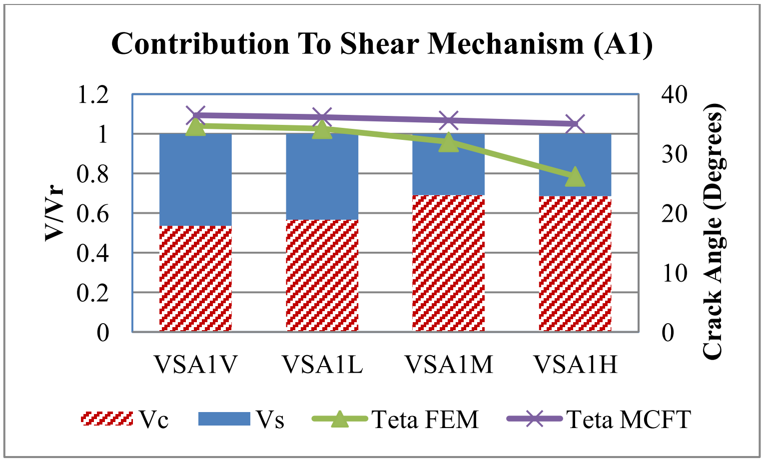

Figure 6.23: Contributions of concrete and steel to shear resistance for Series A1

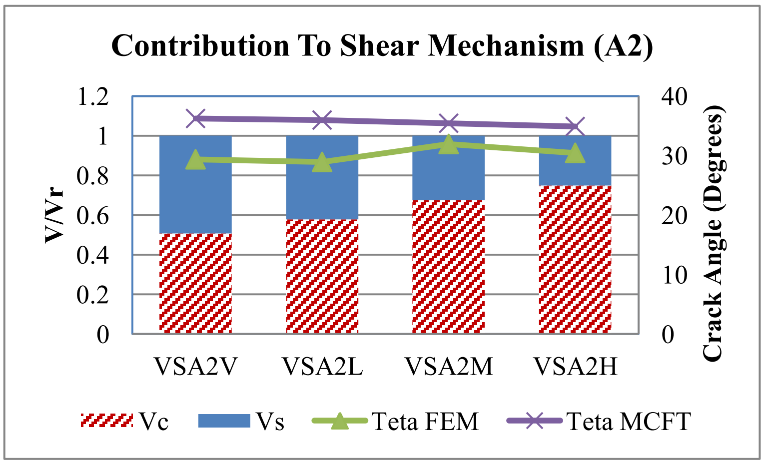

Figure 6.24: Contributions of concrete and steel to shear resistance for Series A2

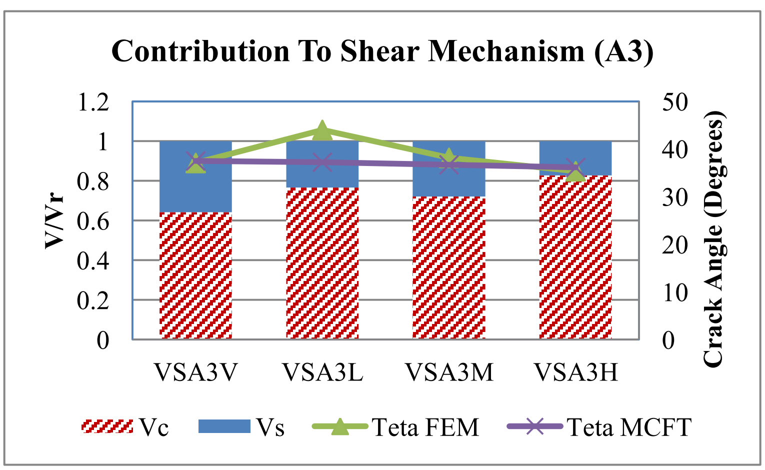

Figure 6.25: Contributions of concrete and steel to shear resistance for Series A3

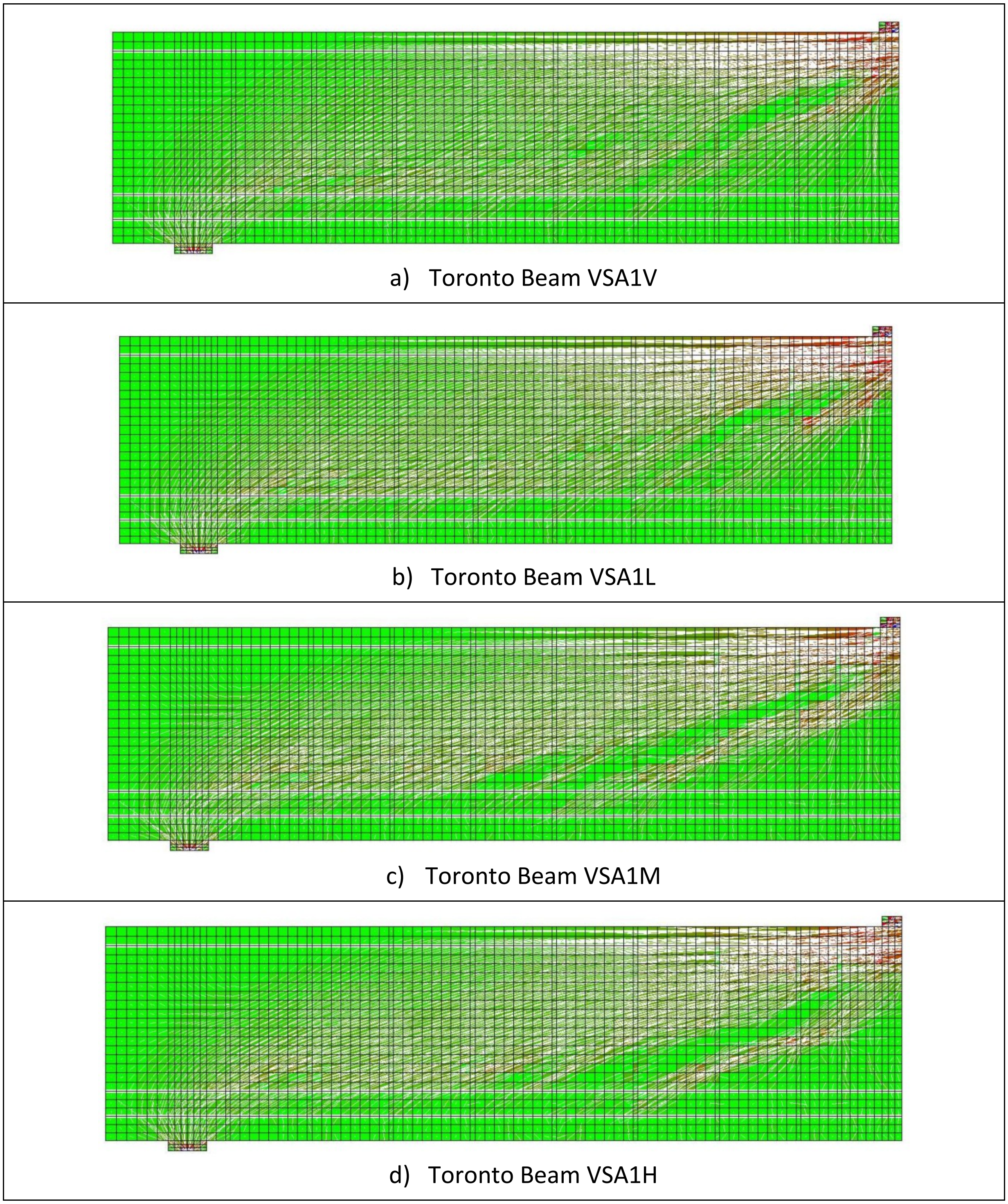

a) Toronto Beam VSA1V

b) Toronto Beam VSA1L

c) Toronto Beam VSA1M

d) Toronto Beam VSA1H

Figure 6.26: Principal concrete compressive stress orientation for Series A1

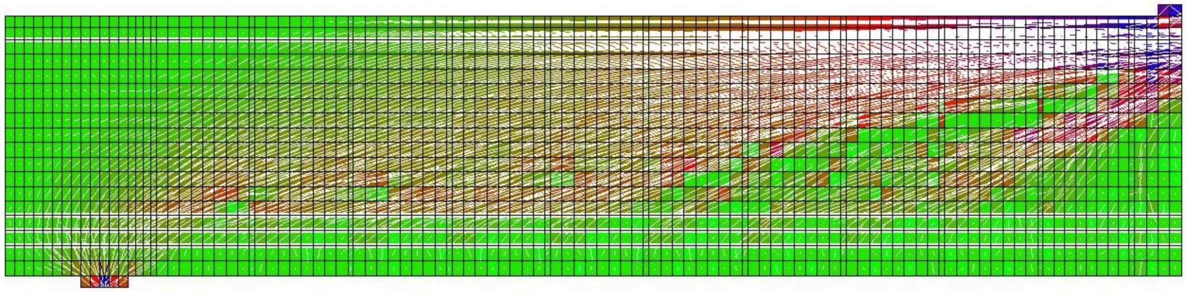

a) Toronto Beam VSA2V

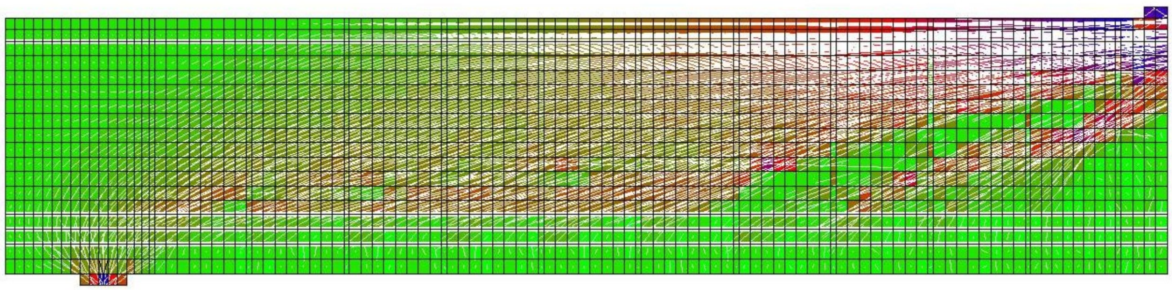

b) Toronto Beam VSA2L

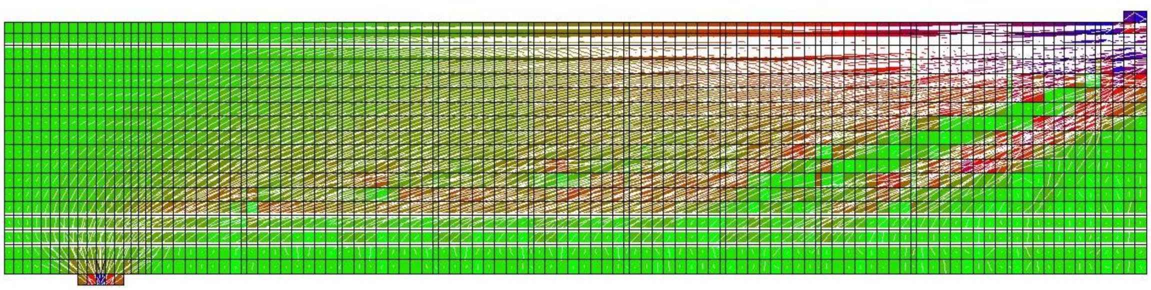

c) Toronto Beam VSA2M

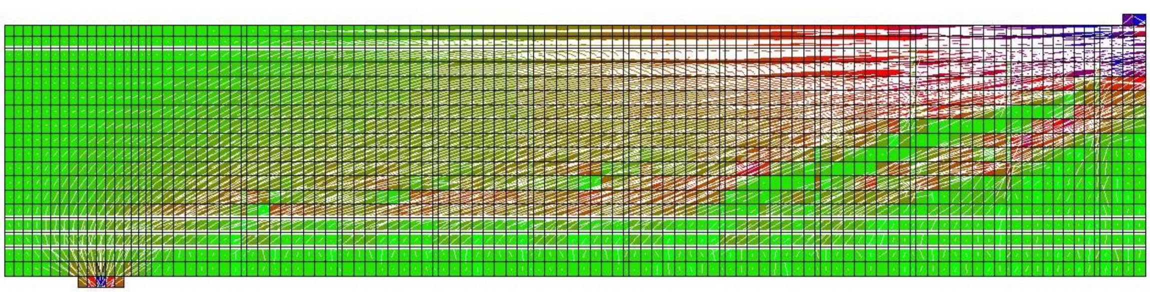

d) Toronto Beam VSA2H

Figure 6.27: Principal concrete compressive stress orientation for Series A2

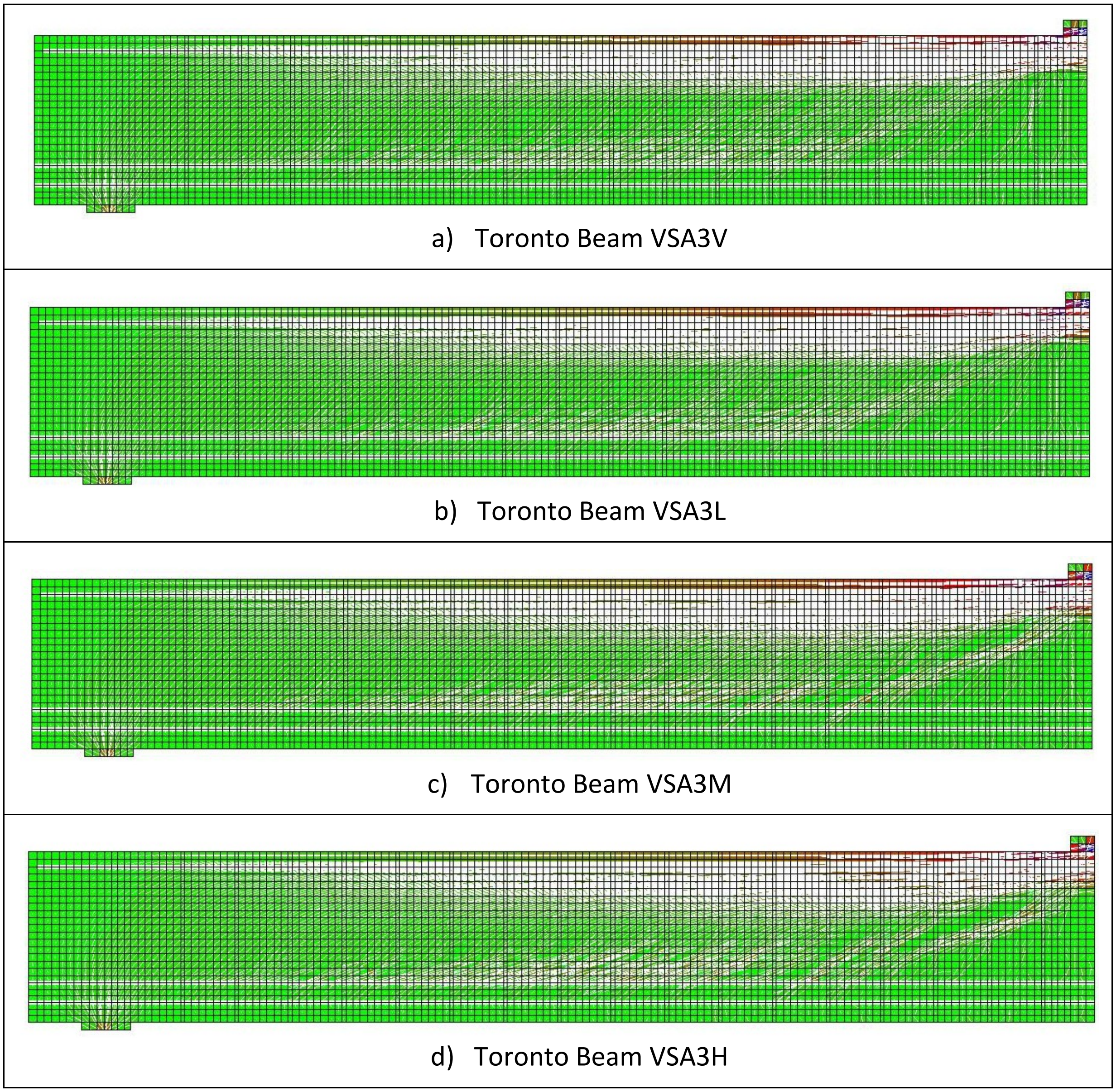

Figure 6.28: Principal concrete compressive stress orientation for Series A3

Series B

Figure 6.29 illustrates the evolution of the steel and concrete contributions to shear strength with increasing corrosion levels for beam B1. The figure also displays the change in crack angle θ as the steel mass loss of the stirrups is increased. A very stable crack was observed for every specimen of Series B, which reflects the closer spaced stirrups. The effect is clearly observed in the contribution of the different resistance components beam B1. Due to the constant crack orientation, the steel contribution continuously decreases due to its reduction in cross-sectional area, which implies that the concrete engages more in resisting the shear with each increase in corrosion level.

Figure 6.32 shows the change in orientation of the principal concrete compressive stresses at ultimate load with increasing levels of corrosion. A very deep flexural compression zone is noticed for these specimens. The effect of closer-spaced stirrups is evident by the well-distributed stress field and fanning towards each of the individual stirrups. Although not as pronounced as Series A, the stress field leading away from the compression zone at mid span changes in orientation and leads to the stirrups located outside the critical section, in a similar fashion as beams in Series A. This indicates more of an arching type mechanism to avoid the damage section near mid span.

Figure 6.30 illustrates the evolution of the steel and concrete contributions to shear strength with increasing corrosion levels for beam B2. The figure also displays the change in crack angle θ as the steel mass loss of the stirrups is increased. As opposed to the shorter-span specimen B1, specimen B2 shows a slight softening in the crack angle at high level of corrosion. The increase in contribution of the concrete is noticed up to the moderate level of corrosion, beyond which, and as a direct cause of the crack softening, an additional stirrup is engaged in resisting the shear, thus leading to an increase in the V_s term at high levels of corrosion.

Figure 6.33 shows the change in orientation of the principal concrete compressive stresses at ultimate load with increasing levels of corrosion. A typical beam type stress distribution is noticed for the uncorroded specimen (VSB2V), in which a distinct fanning of the orientation of the stresses towards individual stirrups is noticed. A similar type stress field is observed at the low level of corrosion. At moderate and high levels, similar to specimen B1, the direction of the field begins to concentrate towards stirrups located outside of the critical and damaged section.

Figure 6.31 illustrates the evolution of the steel and concrete contributions to shear strength with increasing corrosion levels for beam B3. The figure also displays the change in crack angle θ as the steel mass loss of the stirrups is increased. A very stiff and stable crack is noticed for this specimen. The contribution of the steel variation is directly impacted by the change in crack angle, where an adjacent stirrup is considered for softer cracks and not considered for the stiffer cases. This member also has tighter stirrup spacing, wherein a smaller variation in crack angle will consequently have a larger impact in the contributing mechanisms.

Figure 6.34 shows the change in orientation of the principal concrete compressive stresses at ultimate load with increasing levels of corrosion. As a direct cause of longer span and closer stirrups, the stress field indicates flexural-dominant behaviour, with the majority of the compressive stresses located in the compression zone at the top of the beam. Very little impact on the stress field is noticed for this series. Only a slight increase in fanning is noticed at high levels of corrosion.

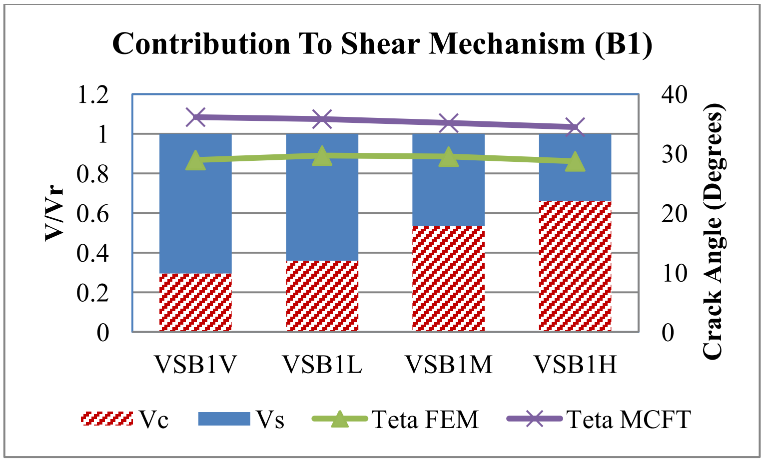

Figure 6.29: Contributions of concrete and steel to shear resistance for Series B1

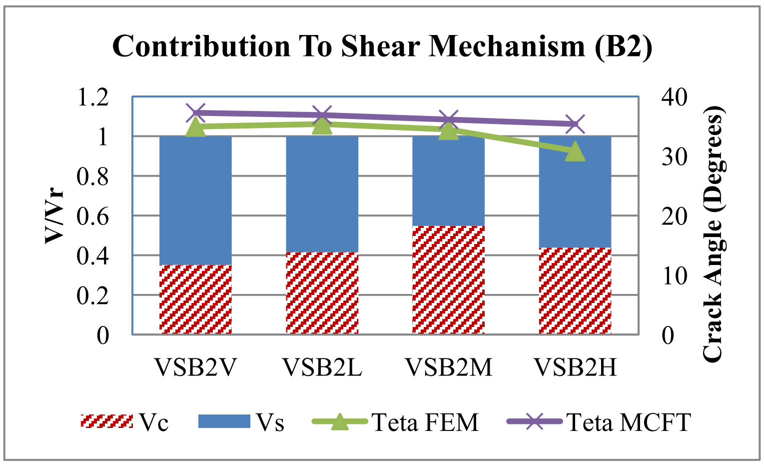

Figure 6.30: Contributions of concrete and steel to shear resistance for Series B2

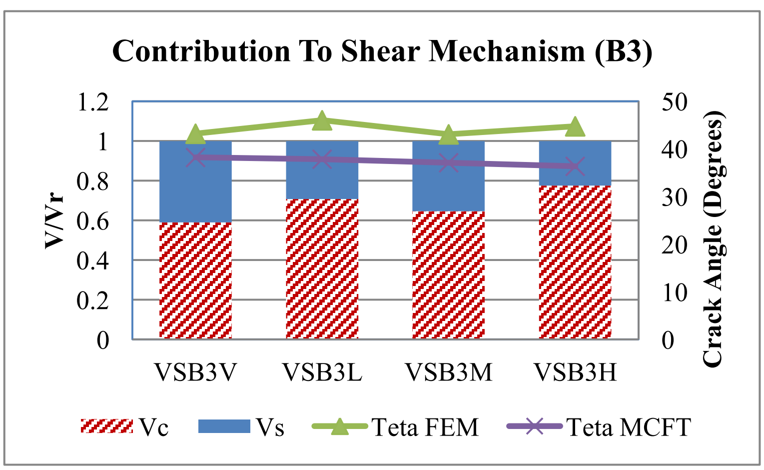

Figure 6.31: Contributions of concrete and steel to shear resistance for Series B3

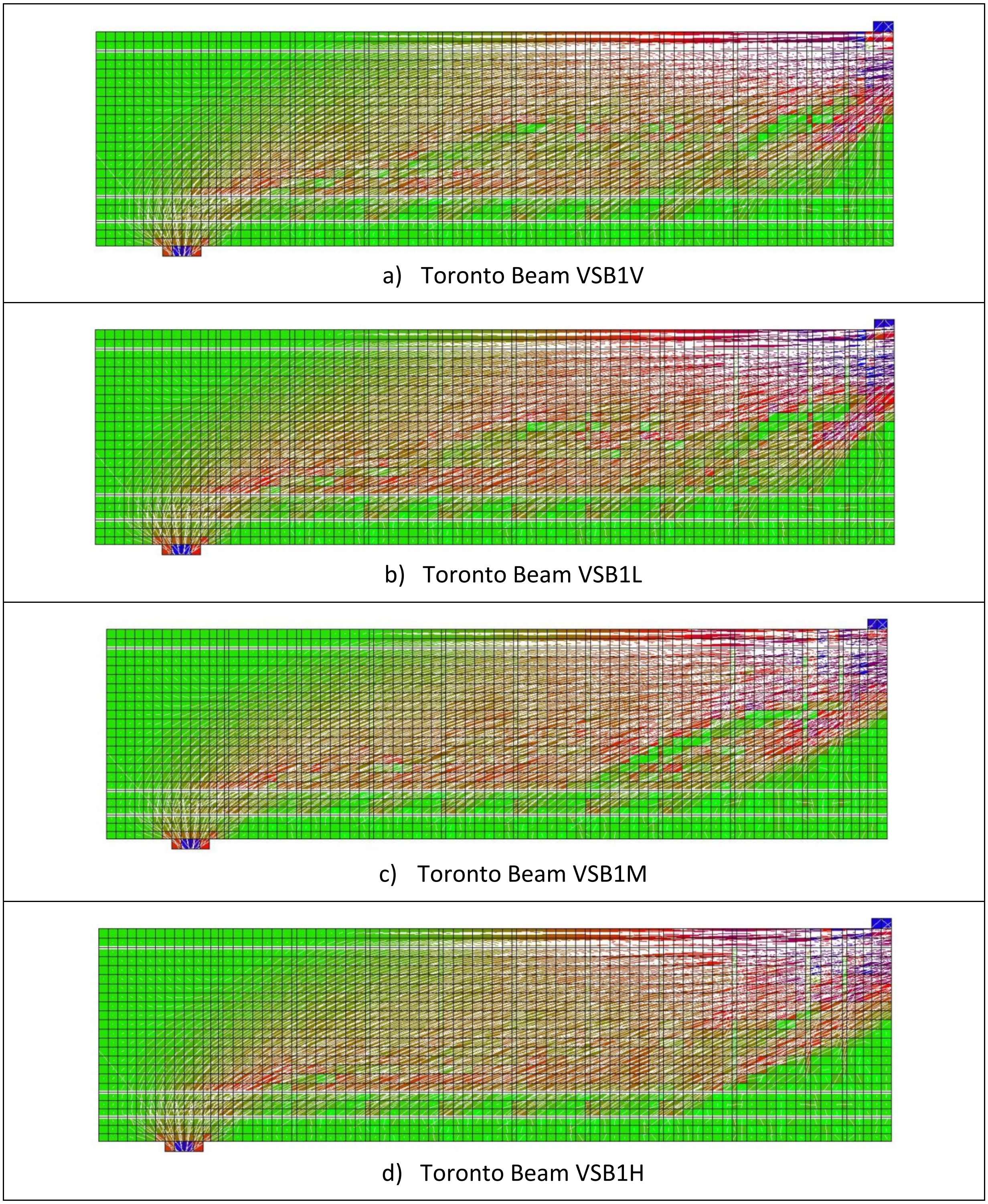

a) Toronto Beam VSB1V

b) Toronto Beam VSB1L

c) Toronto Beam VSB1M

d) Toronto Beam VSB1H

Figure 6.32: Principal concrete compressive stress orientation for Series B1

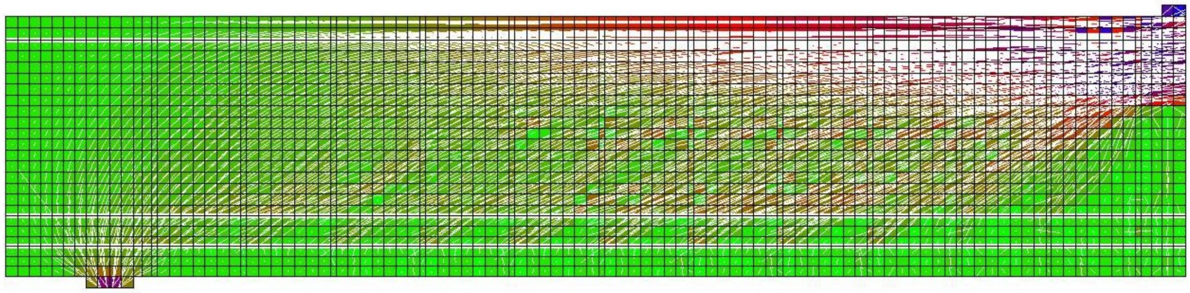

a) Toronto Beam VSB2V

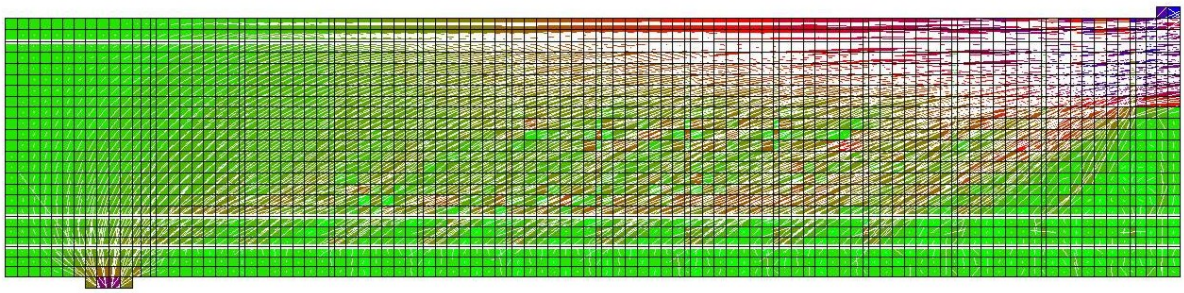

b) Toronto Beam VSB2L

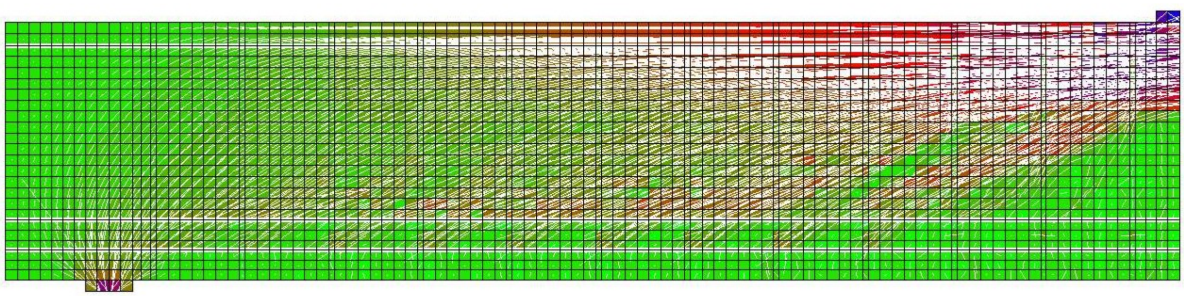

c) Toronto Beam VSB2M

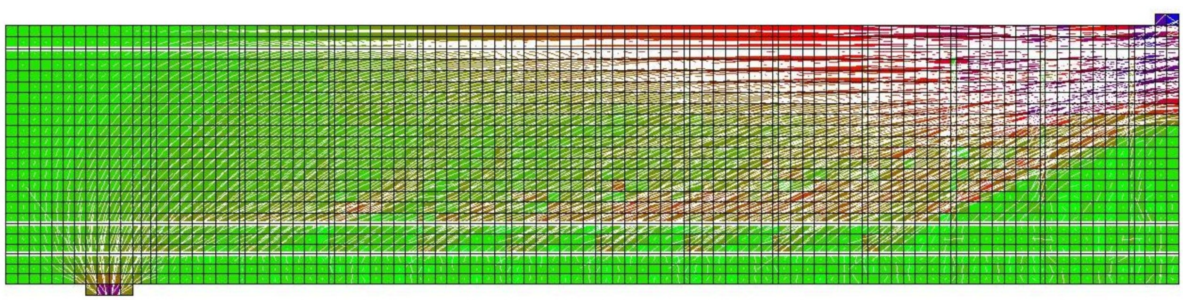

d) Toronto Beam VSB2H

Figure 6.33: Principal concrete compressive stress orientation of Series B2

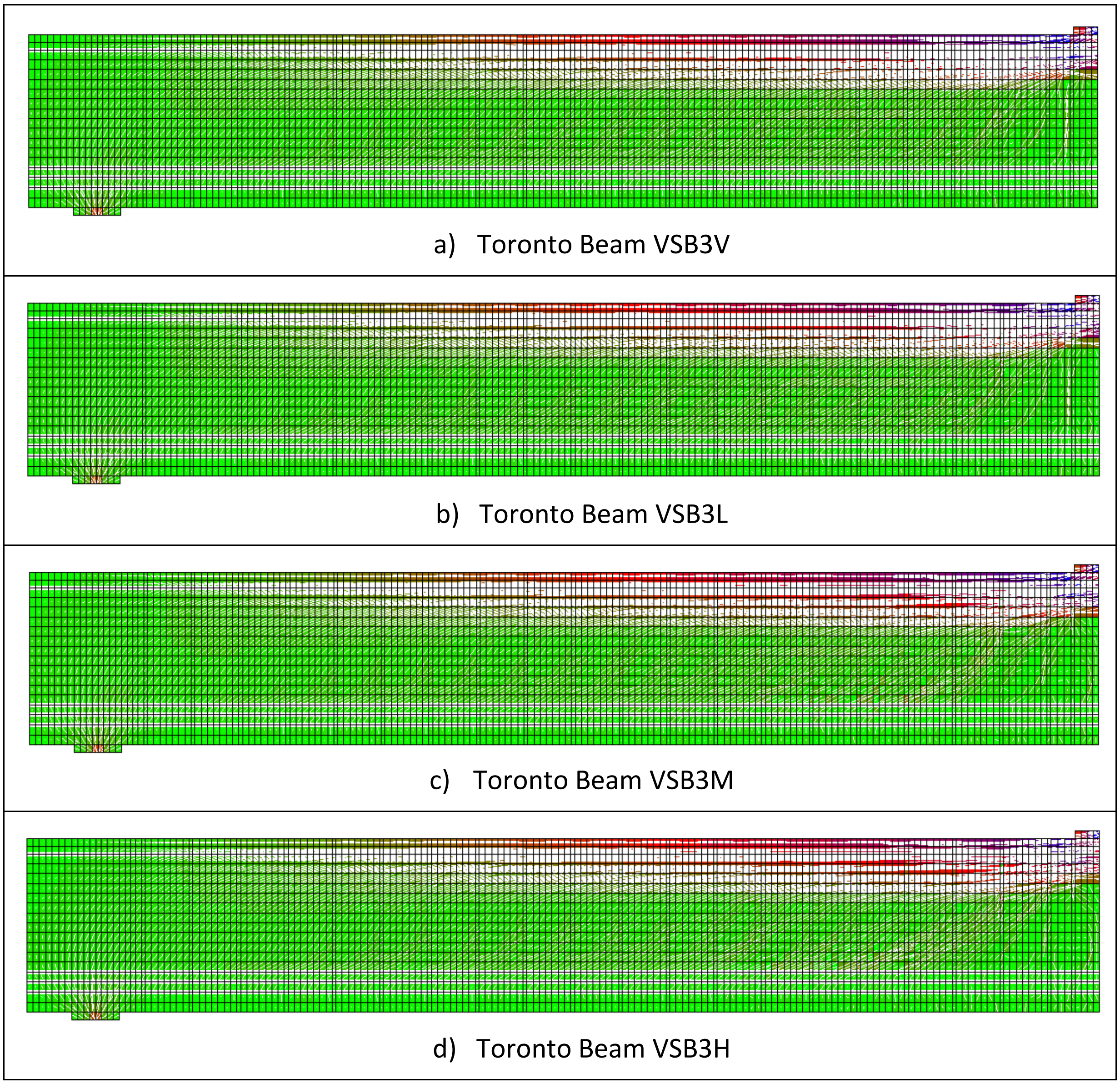

a) Toronto Beam VSB3V

b) Toronto Beam VSB3L

c) Toronto Beam VSB3M

d) Toronto Beam VSB3H

Figure 6.34: Principal concrete compressive stress orientation of Series B3

Series C

Figure 6.35 illustrates the evolution of the steel and concrete contributions to shear strength with increasing corrosion levels for beam C1. The figure also displays the change in crack angle θ as the steel mass loss of the stirrups is increased. The contribution of concrete to shear resistance stays relatively close to that of the uncorroded specimen. Similar to beam A1, the decrease in crack angle with increasing corrosion level does not increase the V_s term. The reduction of V_s due to the loss of steel cross-sectional area counteracts the increase in V_s due to the softening of θ.

Figure 6.38 shows the change in orientation of the principal concrete compressive stresses at ultimate load with increasing levels of corrosion. The uncorroded beam (VSC1V) shows typical beam behaviour, in which fanning is noticed from the flexural compressive region towards virtually every stirrup within the shear span. Similar behavior can be observed at a low level of corrosion, whereas the beams with moderate and high levels of corrosion show a greater impact in the stress trajectory distribution. The stress field becomes increasingly concentrated and directed towards the nearest undamaged stirrup next to the damaged area. This concentration and flattening of the stress field indicate a transition towards a tied-arch type distribution over the damaged section.

Figure 6.36 illustrates the evolution of the steel and concrete contributions to shear strength with increasing corrosion levels for beam C2. The figure also displays the change in crack angle θ as the steel mass loss of the stirrups is increased. A very particular behaviour is observed in this figure, where specimen VSC2L exhibited a particularly soft crack angle, resulting in the steel contributing to most of the shear load (92%). The crack angles of the other specimens are also very soft, which results in the majority of the load being carried by the stirrups at low levels of corrosion. The decrease in the stirrup cross-sectional area as corrosion progresses reduces this contribution to 41%.

Figure 6.39 shows the change in orientation of the principal concrete compressive stresses at ultimate load with increasing levels of corrosion. The first observation from this figure indicates a very deep flexural compressive region for the uncorroded specimen, which increases in depth with the incorporation of corrosion. As a direct effect of this deepening of the compression section, fanning is initially distributed to stirrups located further away than what has been typically observed in other beams. The depth of the compression block is also the cause of the softer crack angle, with concrete compressive stress fields being very flat even near mid-height of the specimen. The orientation of the stress field however follows the previously observed trend of stresses concentration towards the stirrups adjacent to the damaged area. Arching around the damaged area is the predominant stress distribution noticed for all of the affected members.

Figure 6.37 illustrates the evolution of the steel and concrete contributions to shear strength with increasing corrosion levels for beam C3. The figure also displays the change in crack angle θ as the steel mass loss of the stirrups is increased. Despite a jump in the crack angle at low levels of corrosion, the crack angle at moderate and high levels of corrosion is very similar to that of the uncorroded specimen. The contribution of the concrete to shear resistance generally agrees with the trends previously observed for the other beams in Series A and B with longer span. The concrete contribution increases from 40% when no corrosion is present to 69% when the stirrups have lost 50% of the cross-sectional area due to corrosion.

Figure 6.40 shows the change in orientation of the principal concrete compressive stresses at ultimate load with increasing levels of corrosion. A typical flexural type field is observed for the uncorroded and low-level corrosion beams. At moderate and high levels of corrosion, a deeper compression block is forming just outside the critical section of the beams, which is distributed, similarly to previous members, towards the lower part of stirrups located outside of the critical section. This indicates a higher demand in flexural capacity and shear for the section beyond the critical region.

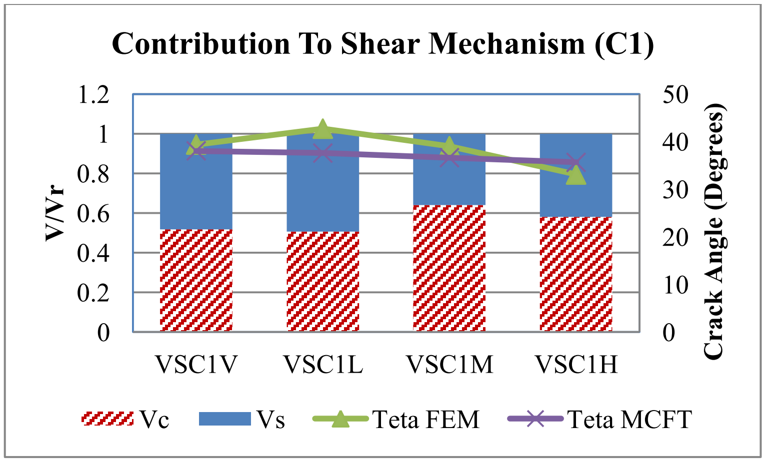

Figure 6.35: Contributions of concrete and steel to shear resistance for Series C1

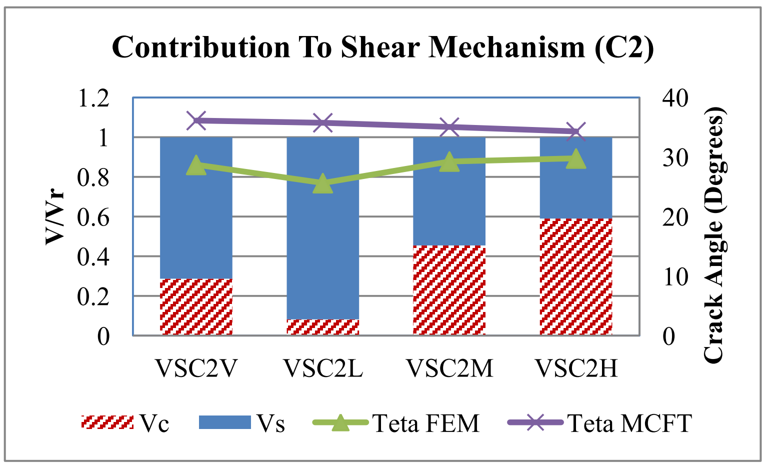

Figure 6.36: Contributions of concrete and steel to shear resistance for Series C2

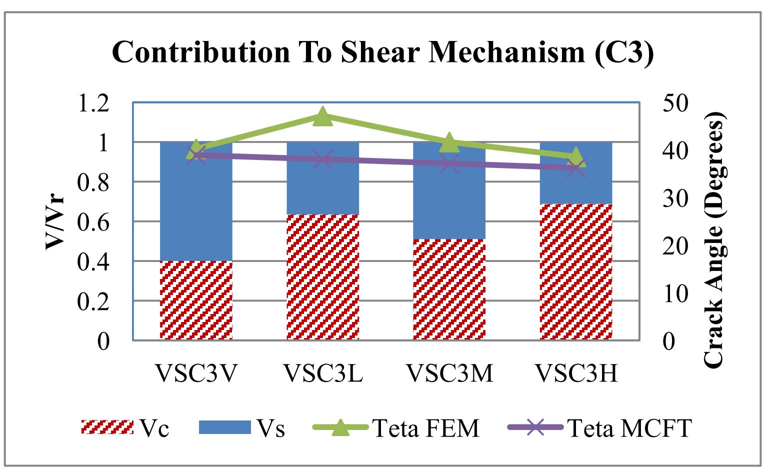

Figure 6.37: Contributions of concrete and steel to shear resistance for Series C3

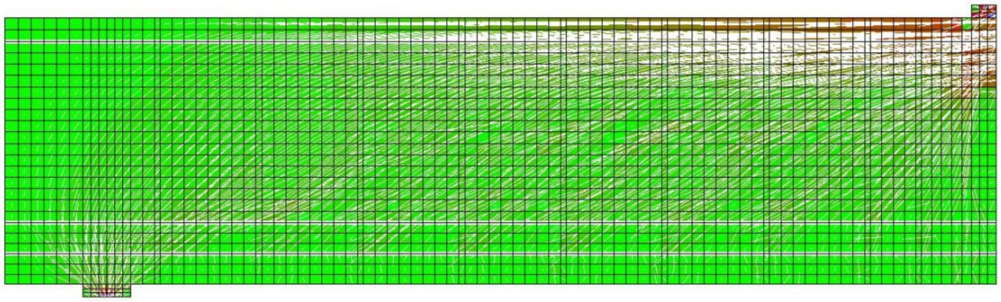

a) Toronto Beam VSC1V

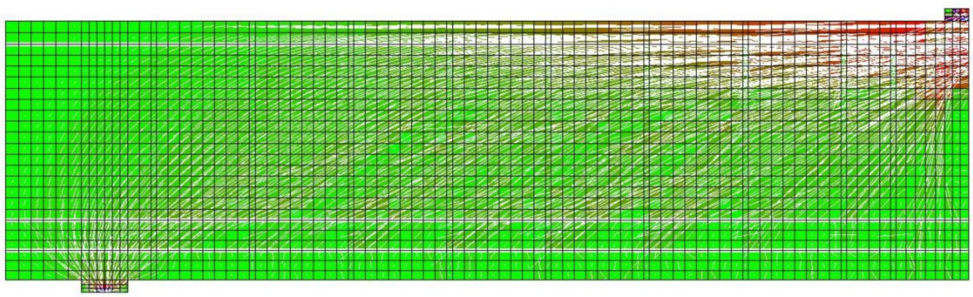

b) Toronto Beam VSC1L

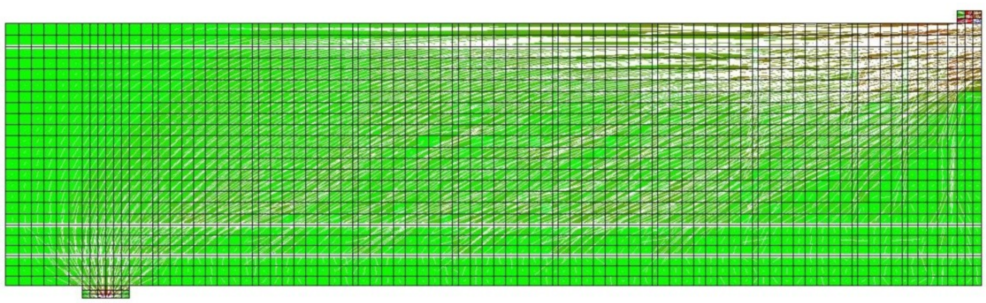

c) Toronto Beam VSC1M

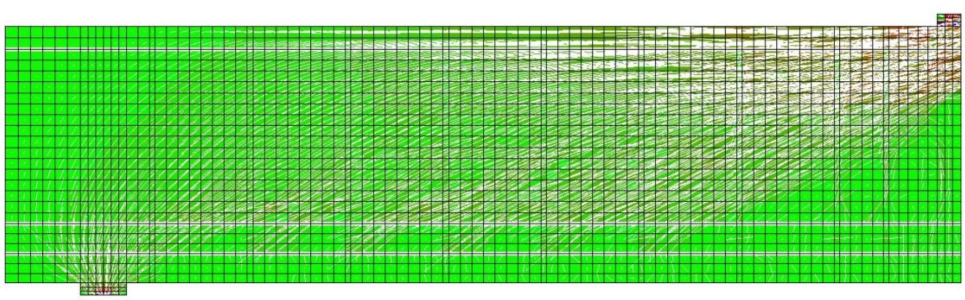

d) Toronto Beam VSC1H

Figure 6.38: Principal concrete compressive stress orientation of Series C1

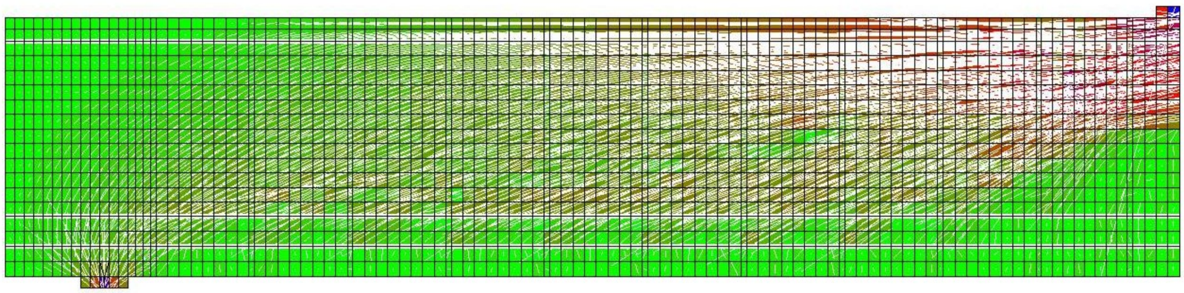

a) Toronto Beam VSC2V

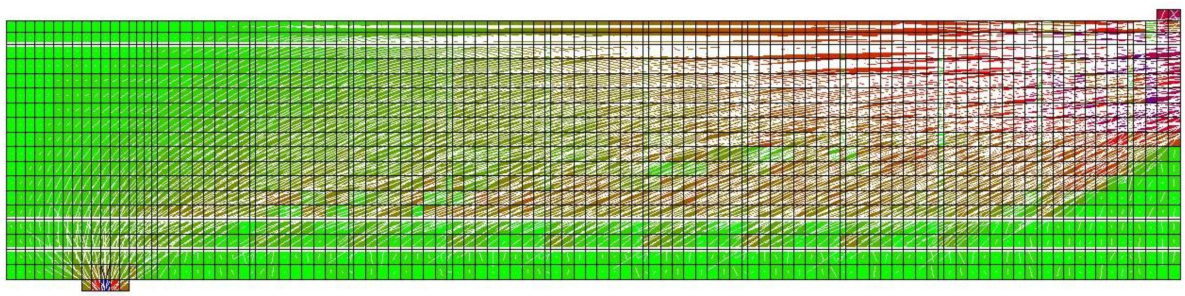

b) Toronto Beam VSC2L

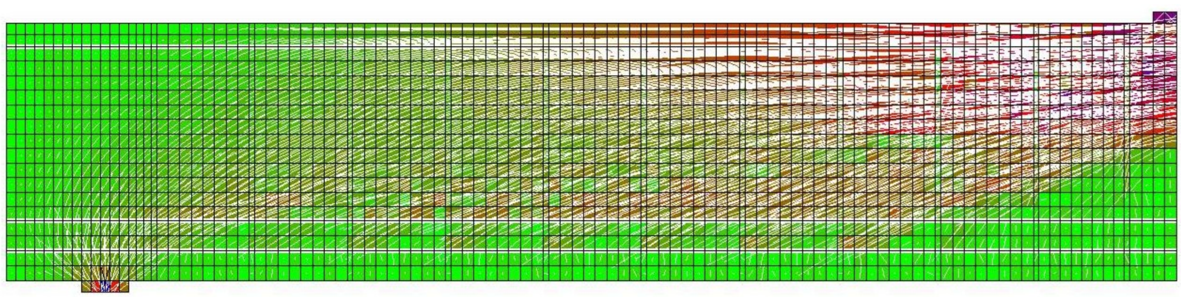

c) Toronto Beam VSC2M

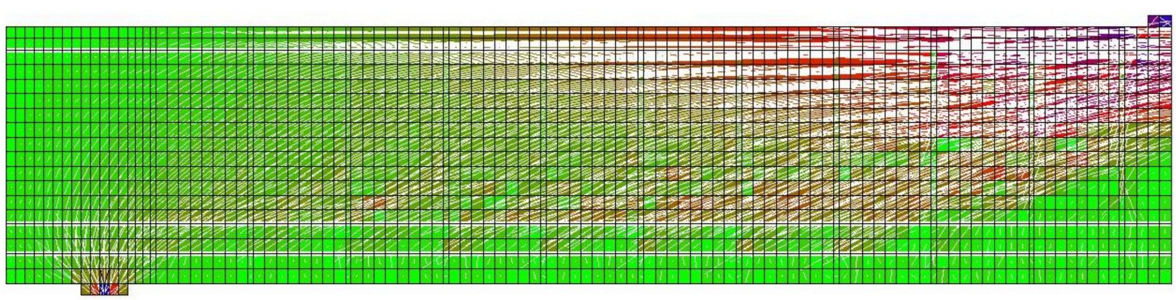

d) Toronto Beam VSC2H

Figure 6.39: Principal concrete compressive stress orientation of Series C2

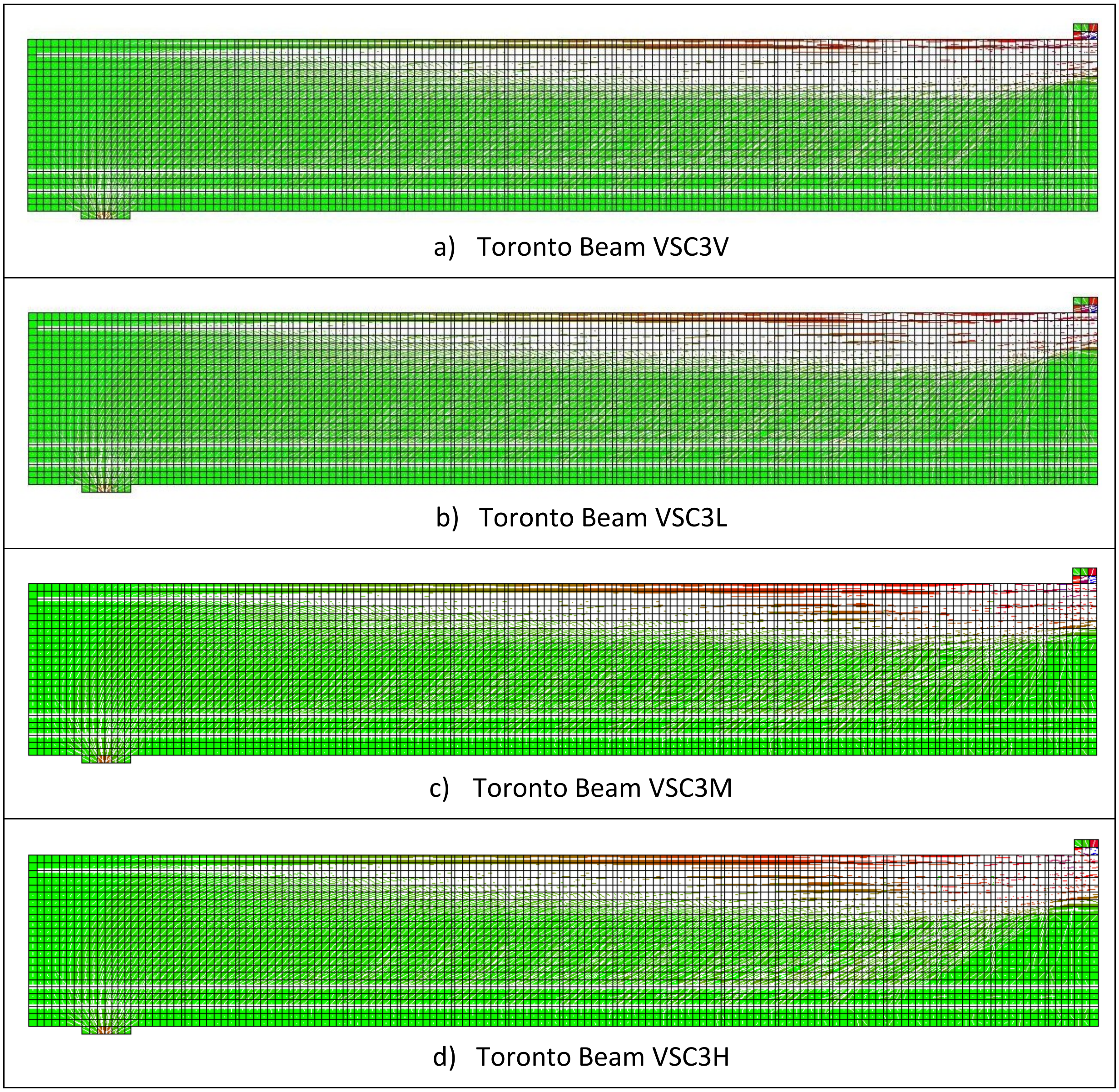

Figure 6.40: Principal concrete compressive stress orientation of Series C3

6.7.3 Shear Resistance Summary

Interesting trends are noticed when the shear resistance mechanism is studied by looking at the individual contributions of both concrete and steel. The beams tend to increase the demand on the concrete contribution to the shear resistance mechanism as the corrosion damage increases. This is expected since the steel contribution is directly impacted and reduced by the loss of stirrup available area. The stress redistribution as a result of the induced damage is particularly interesting; the orientation of stresses definitely implies a higher demand on stirrups located next to damaged areas. These stress trajectories are typically more direct and softer in angle towards these stirrups, indicating a larger implication of the concrete compressive struts within the damage area.

The effects of *a/d* on the stress field redistribution mechanism are prevailing in most cases. While nearly all of the beams exhibited beam-type behaviour in resisting the applied load, the shorter-span beams tended to redistribute the stresses in a more direct manner leading to a tied-arch type stress field. This was also the prevailing mechanism in the Oregon series, which have the lowest *a/d* ratio of all the beams analyzed. In almost every case, alternate stress paths were created to account for the damaged sections. While the first stress path was directed towards the closest stirrup next to the damaged section, it became evident that stresses began to arch over the cracks towards stirrups located away from the damaged section as well. Beams with an *a/d* ratio of 5 exhibited a clear transition toward an arching type mechanism over damaged areas. This was observed not only by a softer and direct line of action in the lower part of the stress field, but also by an increase in spreading and arching of these stress trajectories when moving away from the loading point. This was typically associated to a rather deep penetration of the compression block, naturally leading to a softer crack angle and a flatter principal compressive stress orientation at mid height of the beams. The longer members displayed flexural-dominant behaviour and typically avoided the damaged area by increasing the depth of the flexural compression region in combination with a higher stress distribution towards the centre of the shear span. The closely spaced stirrups in Series B provided a better distribution of stresses. The effects of the member width were predominant in Series A, the series with larger width, in which the formation of distinct compression struts was observed in the two shorter spans of the series compared to rather well-distributed stress fields in thinner members. A change in shear resistance mechanism was observed in every specimen. While this is more closely related to *a/d*, a redistribution of stresses around the critical section of the beams was prevalent nonetheless.

6.8 Comparison to Design Equations

This section compares the results of the FE analysis with the values given by the design equations to shear resistance in CSA A23.3-04 (2004) and presented in Section 6.2. The residual shear strength was calculated from the equations by reducing the cross-sectional area of shear reinforcement according to the percentage in mass loss. The calculated values from the design equations include both the general and simplified methods outlined in the design standard.

6.8.1 Total Shear Strength

The shear resistance obtained from the FE analyses is plotted against the strength calculated from the code equations for the general and simplified methods in Figure 6.41 and Figure 6.42, respectively. By looking at Figure 6.41, there is a good agreement between both methodologies, except for Series A in which the FE results give a higher value of strength compared to the MCFT (on which the code equations are based). The beams width plays a major role in the estimation of shear strength. Note that Series A is the series of beams with the largest width. The trend indicates that the shear capacity provided by Eq. 6.1 is generally conservative for wider members. These beams (Series A) generally underwent flexural compression failure. This failure is avoided in design, and it might be the cause of this over-conservatism in the MCFT estimate. Nevertheless, this scenario could be encountered in corrosive environments, where the strength of the concrete is highly degraded due to cracking, or where the spalling/delamination of the concrete cover artificially increases the reinforcement ratio close to its balance condition. In spite of the difference in estimates for beams in Series A, the shear strength values from Eq. 6.1 are generally close to the results obtained in the FE analysis. It can also be observed from Figure 6.41 that higher corrosion levels lead to lower shear strengths.

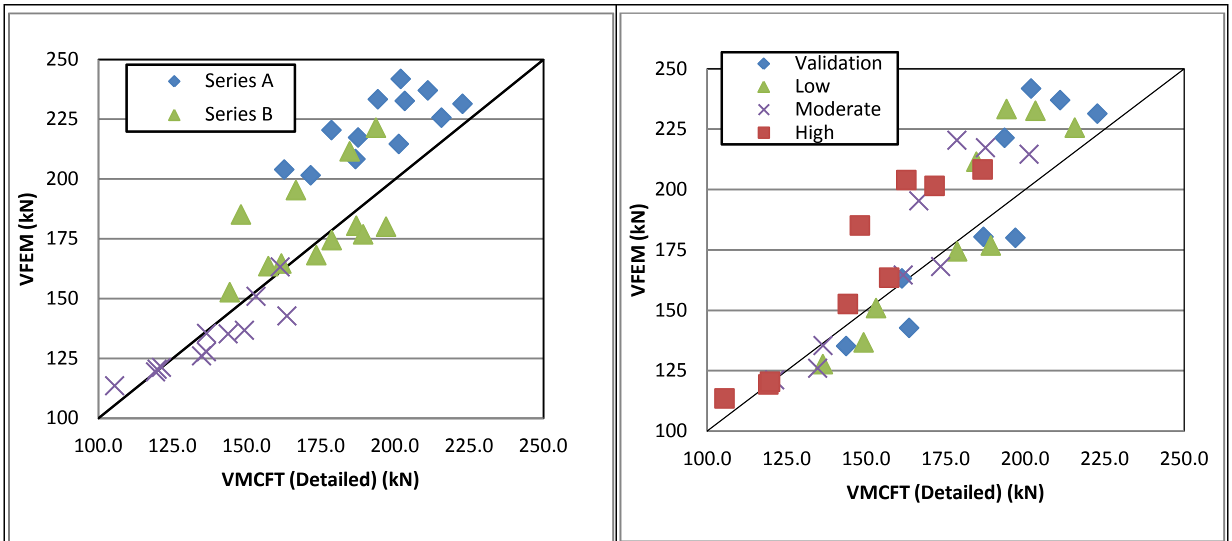

i. Organized by series

ii. Organized by corrosion level

Figure 6.41: Code equation estimation for shear strength (general method, cl. 11.3.6.4)

Figure 6.42. As mentioned in Section 6.2, the simplified method in shear design can be used if the minimum amount of shear reinforcement is provided. The Toronto beams have sufficient amount of shear reinforcement, therefore the crack angle was set to 35° and β set to 0.18. The shear strength of a greater number of specimens was overestimated using the simplified method when comparing it to the FE results. Same observations with respect to corrosion level can be made.

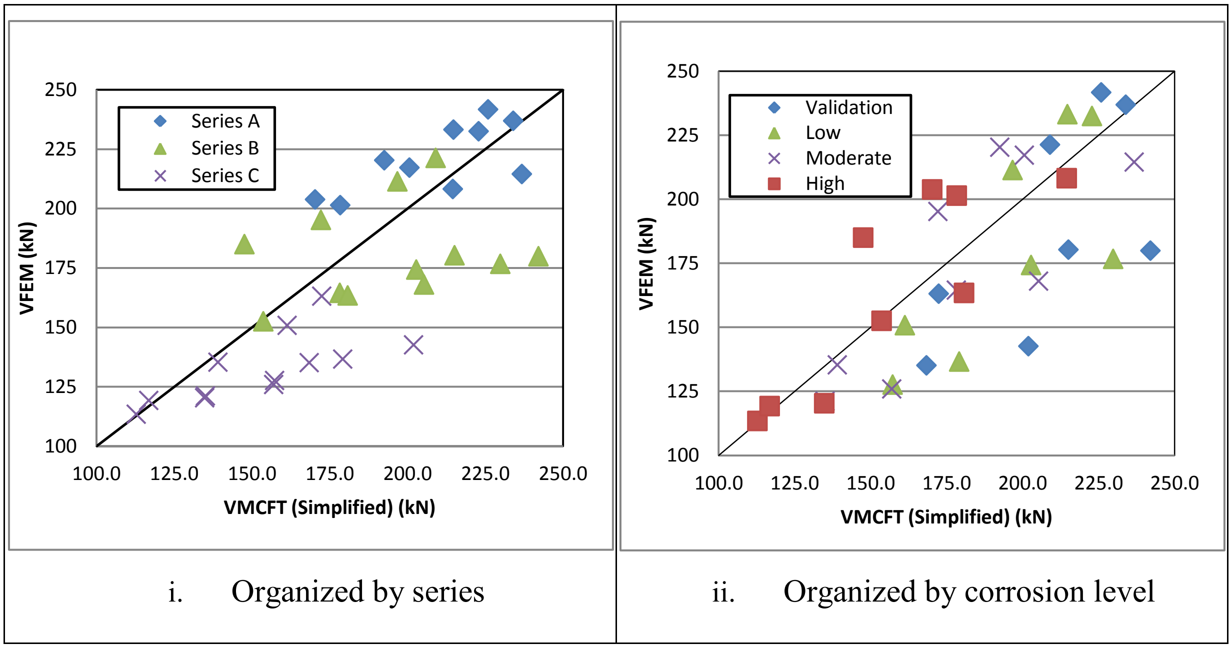

Figure 6.42: Code estimation of shear strength (simplified method, Cl. 11.3.6.3)

6.8.2 Steel Contribution to Shear Strength

The steel contribution to shear strength was calculated based on the number of stirrups contained within the crack length as described in Section 6.7. The steel contribution to shear resistance obtained from the FE analyses is plotted against the strength calculated from Eq. 6.3 for the general method in Figure 6.43. The code equation overestimates the steel contribution for nearly every specimen when compared to FE results. The lower values obtained from the FE analyses are based on the maximum stress the stirrups are experiencing, which might fall way below the yielding value. Equation 6.3 assumes that all stirrups crossing the crack are yielding. Also observed in the figure is the effect of corrosion level, wherein a higher corrosion level leads to lower values of shear force carried by the transverse reinforcement.

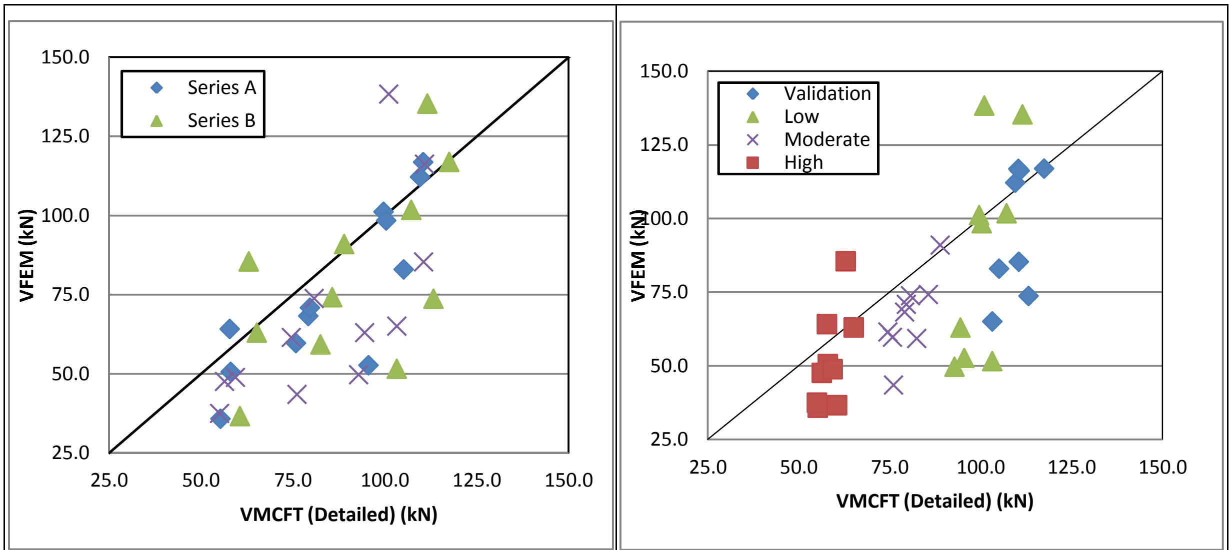

i. Organized by series

ii. Organized by corrosion level

Figure 6.43: Estimation of steel contribution to shear strength (general method, cl. 11.3.6.4)

The steel contribution to shear resistance obtained from the FE analyses is plotted against the strength calculated from Eq. 6.3 for the simplified method in Figure 6.44. The results are very similar to those obtained in the general method. Note that here the crack angle is constant, $\theta = 35°$, and the resistance provided by the steel is only dependent on the available area of corroding stirrups. The resistance provided by the steel as calculated by the general method is also dependent on the variable angle, which tends to decrease as corrosion increases.

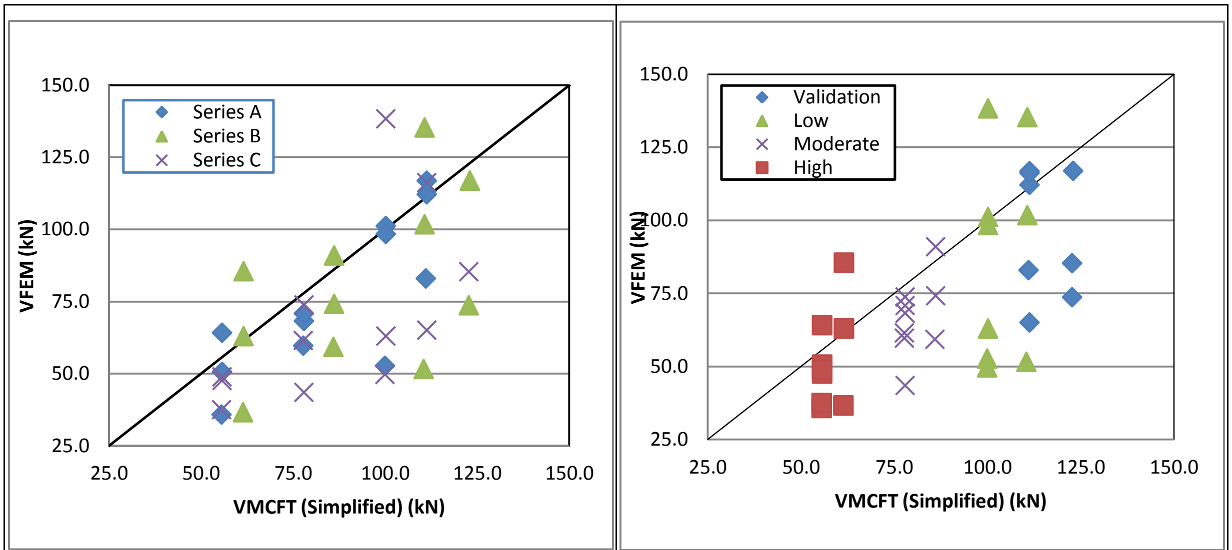

i. Organized by series

ii. Organized by corrosion level

Figure 6.44: Estimation of steel contribution to shear strength (Simplified method, Cl. 11.3.6.3)

6.8.3 Concrete Contribution to Shear Strength

This section explores the change in the concrete contribution to shear resistance for different corrosion levels. Whereas the V_c term in the code is calculated from Eq. 6.2, the contribution of concrete to shear resistance from the FE results was calculated from the difference between the total shear strength and the steel contribution. The concrete contribution to shear resistance obtained from the FE analyses is plotted against the strength calculated from Eq. 6.2 for the general method in Figure 6.45. The code is mostly conservative in the estimates of the concrete contribution to shear resistance when compared to the FE results. Equation 6.2 with the general method tends to underestimate the shear force taken by the concrete for beams with a wider width (Series A).

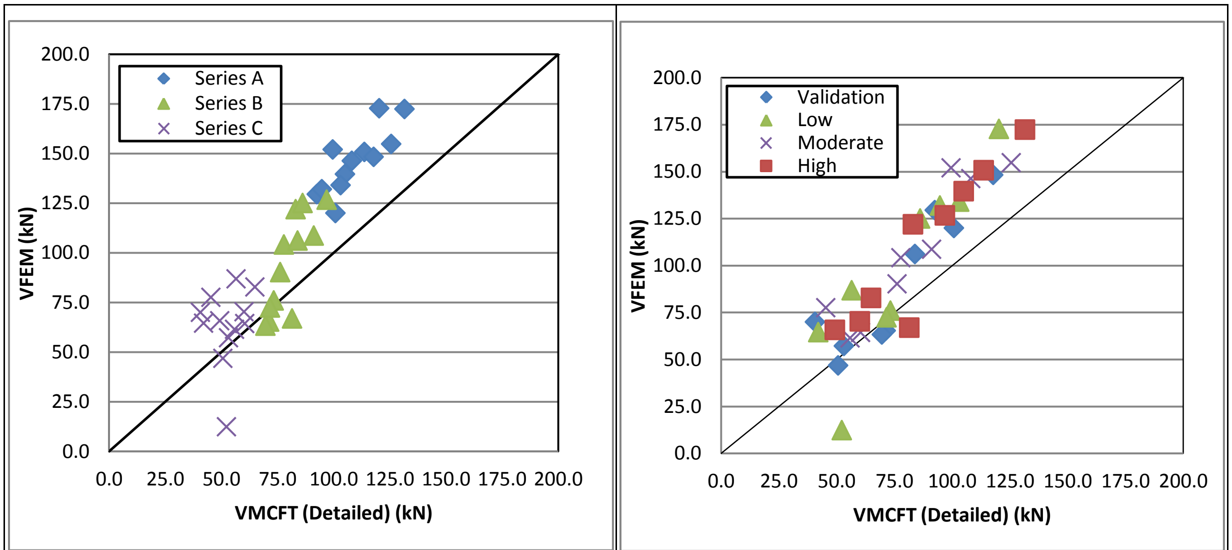

i. Organized by series

ii. Organized by corrosion level

Figure 6.45: Estimation of concrete contribution to shear resistance (general method, cl. 11.3.6.4)

The concrete contribution to shear resistance obtained from the FE analyses is plotted against the strength calculated from Eq. 6.2 for the simplified method in Figure 6.46. This method has a better estimate of the concrete contribution to member shear capacity when compared to the FE results. Generally, the concrete contribution is overestimated for uncorroded specimens (denoted “Validation” in Figure 6.46) and has closer values to the FE results when corrosion-induced damage is introduced in the analysis.

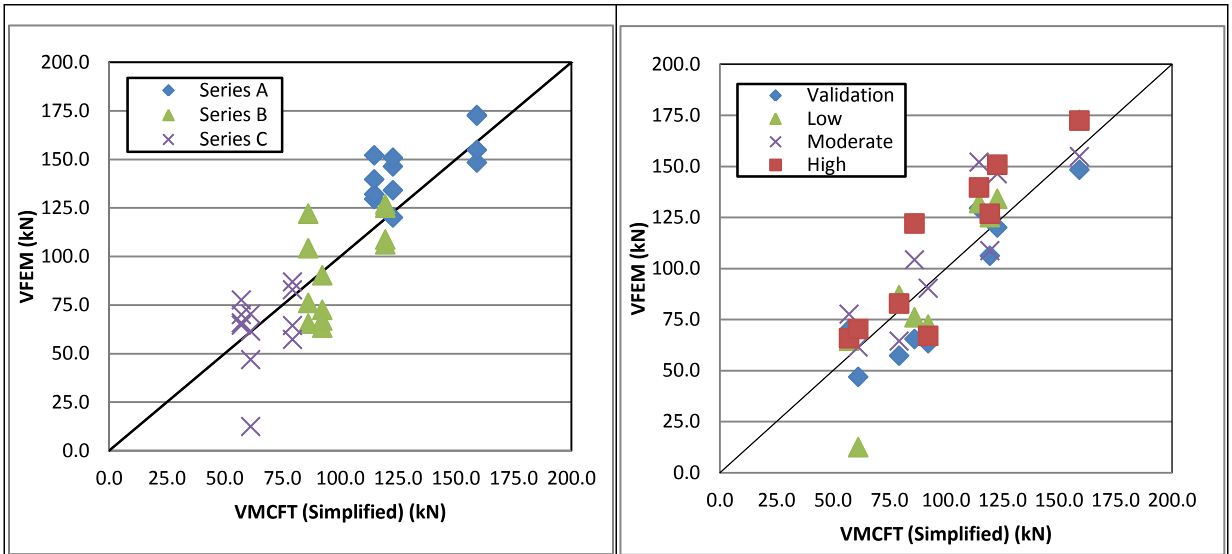

i. Organized by series

ii. Organized by corrosion levels

Figure 6.46: Estimation of concrete contribution to shear resistance (simplified method, Cl. 11.3.6.3)

6.8.4 Design Equation Summary

The divergence between FE results and the code estimation of residual shear strength is typically greater for members with a larger width. When comparing the code equations to the FE results, the steel contribution to shear strength is overestimated using Eq. 6.3, while the concretes contribution is underestimated in nearly every case using Eq. 6.2. The difference between the results in the concrete contribution might be due to the fact that the concrete contribution from FE results is calculated based on the difference between the total shear strength and the steel contribution (note that the stirrup is not necessarily yielding.) It has been observed that as corrosion progresses, there is a shift in behaviour from beam to arch-tie dominant. Arching has greater utilization of the effectiveness of concrete carrying compression in comparison to simply beam-type behaviour.

The CSA A23.3 equations are in general conservative in the estimate of shear strength. The fact that the steel contribution is overestimated and the concrete contribution underestimated might not affect the final estimate of the shear strength; however, it does not capture the change in behavioural mechanism that the member undergoes when corrosion is incorporated. If this behavioural change in shear resistance is to be considered, as observed in Section 6.7, the design methodology provided by CSA A23.3-04 would have to be modified for assessment of affected members.

6.9 Comparison to Experimental Tests

This section compares FE results to available experimental data in the literature, mainly in terms of loss in shear strength as a result of corrosion damage. Incorporating additional data helps to confirm numerical observations and expand the range of beams variables. The experimental data presented here has been extracted from Zhao et al. (2009), who had reviewed published experiments of the effect of stirrup mass loss on RC shear strength. This compilation of data comes from studies conducted by Rodriguez et al. (1995) for *a/d* of 4.7, Chen (2002) for *a/d* of 2.2, Xu and Niu (2004) for *a/d* of 1.0 and 2.0, and finally Higgins and Farrow (2006) for *a/d* of 2.04.

Figure 6.47 plots the ratio V_{cor}/V_{val} against the mass loss of stirrups, where the FE results from the Toronto beams are included as well and denoted by "(FEM)". The loss in shear strength with increasing mass loss agrees well with the experimental data. From the figure, it is clear that at lower levels of corrosion (e.g. around 10% mass loss) there is less effect of on strength, and the FE results capture this trend as well. At moderate levels of corrosion (30% mass loss), the effect of *a/d* starts to have more significance on the shear strength. This is due to the fact that beams with lower *a/d* ratios exhibit a higher strength degradation as a result of corrosion. At high levels of corrosion, only FE results from this work are available and therefore no comparison can be made; however, FE data replicates the trend of a linear decrease in shear strength with increasing corrosion levels, as observed from the experimental data. Nonetheless, the FE results exhibit a slightly softer decrease for beams with higher *a/d* ratios. When the FE results for a beam of *a/d* = 4 is compared to the experimental results of a beam with *a/d* = 4.7, there is a considerable gap between the experimental and numerical data. It is worth mentioning that the results displayed in Figure 6.47 for an *a/d* = 4.7 correspond to a beam tested by Rodriguez et al. (1995), who applied accelerated corrosion to both shear and flexural reinforcement. The FE analysis here only considers the corrosion effects of stirrups. The gap would therefore be attributed to a combination of a decrease in flexural, bond and shear strengths. Most of the beams reported in the literature were undereinforced in flexure, as opposed to the beams used in the FE analysis, which were overeinforced in flexure to induce a shear failure.

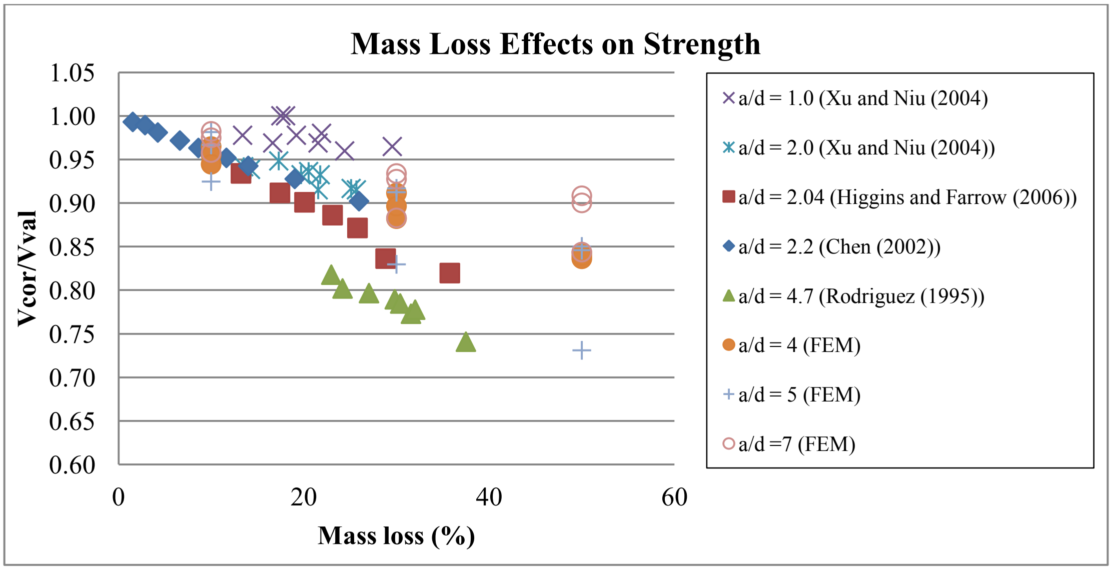

Figure 6.47: Comparison of experimental and numerical data of effects of mass loss on shear strength

6.10 Assessment Considerations

The objective of this work was to identify the effects of stirrup corrosion on the behaviour and strength of RC beams. From behavioural trends highlighted in this chapter in combination with important findings outlined in the literature, it has become apparent that in order to successfully assess the health and condition of an affected structure, one needs to consider specific behavioural changes and corrosion effects on material properties. Important behavioural characteristics within the collected data will help in providing guidance in the estimation of residual shear strength of RC beams. The fact that CSA A23.3-04 shear design equations are conservative in estimating the residual strength of affected RC beam conceals the change in the individual contributions provided by the concrete and steel as corrosion of the stirrups progresses. The overestimation of the steel contribution and underestimation of the concrete contribution (compared to FE analysis results) indicate that the code equations do not capture the transition of the shear resisting mechanism towards an arching-type stress distribution over damaged regions.

The increase in horizontal strain ε_x at mid height of the beam is an indication of the increase in shear demand experienced by the concrete section. This increase is a result of the additional strains caused by the expansion of corrosion by-products on the stirrups. It also indicates higher damage levels in the concrete, which leads to a decrease in the member strength. This effect needs to be accounted for when residual shear strength is estimated, as it depends highly on the concrete ability to transfer stresses to the reinforcing steel. To the contrary of expectations, the crack angle softened at times. In some cases, the crack angle impacted greatly the contribution of steel towards shear strength as the beams compensated for the damaged regions by mean of a softer crack angle in an effort to incorporate stirrups located adjacent to the affected areas. This is a scenario that needs to be considered in assessment and highlights important behavioural change in stress distribution.

Shear capacity of RC members depends greatly on the degree of cracking and the ability to transmit stresses across cracks. The importance of considering an increased level of cracking cannot be underestimated, especially in shear critical scenarios. The effects of cracking in disturbed regions are also very important, since the compressive strength of concrete is greatly affected when tensile strains and increase cracking are present in these regions. Experimental evidence indicating that an RC member with corroded shear reinforcement can have a lower shear capacity than that of a similar unreinforced specimen (Suffern et al. 2010) and should not be taken lightly. This indicates that damage is induced to the concrete itself by the corroding reinforcement, and simply neglecting the contribution of the reinforcement in shear assessment can lead to overestimates of residual strength. The CSA S6 bridge design code assessment procedure implies a higher value for the minimum amount of reinforcement below which it neglects the steel contribution, and calculating the capacity of an unreinforced member might lead to the overestimation of its residual shear strength. The assessment procedure should be rectified to consider the effects of higher amounts of cracking in the concrete core. One possible way of accounting for shear degradation in RC members affected by stirrup corrosion is adjusting the strength of the concrete core due to corrosion-induced cracking.

The importance of accounting for the change in crack angle θ lies in the estimation of the steel contribution to shear strength resistance when code equations are used. The softening of the crack would indicate the possibility of engaging adjacent stirrups in resisting the load. A softening of the angle should be dealt with care, as the direct increase of the steel contribution is counteracted by its decrease due to the loss of cross-sectional area in the stirrups. In fact, this mass loss (especially at high values of 50% loss) is more detrimental to the contribution of the stirrups in resisting the shear. Thus a conservative estimate of residual strength should neglect the softening of the crack and consider the decrease in cross-sectional area of the shear reinforcement. Furthermore, alternate stress paths need to be considered for the proper assessment of shear strength. Simply acknowledging the change in crack angles might not capture the change in behaviour in most cases, as the concrete compressive stresses redistribute along two paths. The first stress field develops towards the stirrups located next to the damaged section, and the remainder stresses are redistributed over the dominant crack by means of arching towards stirrups located away from the damaged section.

The change in stress distribution and deformability can lead to a change in failure mode with less warning signs, creating a higher risk for the public. Acknowledging behavioural change is key in a safe estimation of residual strength. An assessment procedure of residual shear strength should imply stricter strength restrictions and provide guidance in suggesting important considerations for accounting for behavioural changes. The use of strut-and-tie models to account for this change in stress distribution in addition to shear design equations would help in safer decision making when engineering judgment is required. The dimensions of struts and ties and the idealization of internal truss mechanisms should be adjusted to avoid distribution of stresses in highly damaged areas. Indeterminate truss systems are a better representation of the affected members, since the distribution of stress field occurs to more than a single point when corrosion is present in the shear critical section.

The use of FE tools might be a better way of understanding the change in shear stresses distribution in members subjected to reinforcement corrosion, and, in combination with other tools, it might provide a better prediction of residual strength. With the advancement in the precision of FE with respect to concrete, it is a useful tool and should not be underestimated and further utilized in assessment practice. Since the FE modelling methodology presented in this thesis combines both corrosion-induced cracking and loss of steel cross-sectional area, it can also be applied in cases where members cannot be properly inspected, as different scenarios of corrosion level and damage can be successfully modelled. It can be also useful in assessment cases where members do not show typical signs of concrete deterioration such as spalling and/or delamination of the concrete cover. In these cases, it becomes difficult to judge the concrete condition and its contribution to resistance, since it might be affected because of internal cracking. When corrosion-induced cracking is introduced in the analysis and induces damage in the concrete, many scenarios can be simulated without explicitly removing defective concrete (e.g., the cover) from the analysis.

Chapter 7 Concluding Remarks

7.1 Conclusions

The effects of corroding stirrups on shear strength of RC beams was studied and presented using FE analysis. The nonlinear FE package VecTor2 was used because of its strength in modeling reinforced concrete. A FE model was proposed and specifically designed around the basis of the problem, the corroding stirrups. Typical elements were used in a unique way for the purpose of isolating affected stirrups. The stirrups were isolated by means of local smearing (LS) of the stirrups steel within composite 4-node, 8-degrees-of-freedom elements at the specific bar location. Steel mass loss due to corrosion was incorporated by reducing the cross-sectional area of the stirrups accordingly. In order to account for corrosion damage in the concrete, a crack-inducing model was introduced within the two-dimensional plane stress framework. The model incorporates corrosion effects on affected elements by means of prestraining. This is done by incorporating fictitious horizontal prestressing steel within affected LS elements and prestraining them in compression. The elements are then released prior to loading in order to induce cracking. The value of the prestraining was calculated based on the expansion of corroding steel and by idealizing the concrete cover as a thick-wall cylinder subjected to internal pressure resulting from this expansion mechanism. The model was first validated without any effects of corrosion against published data in order to test the performance of the FE model in modeling shear critical beams. Corrosion-damaged was then introduced, and the model was further validated against published data. From the validation stage, the following conclusions can be made:

1. The LS elements successfully model shear critical members and provide good agreement with published data.
2. Corrosion steel loss and corrosion-induced cracking are successfully introduced within a two-dimensional plane-stress problem.
3. The use of LS elements with the cracking model also provides good agreement with published data.

4. Corrosion-induced cracking in terms of pre-straining becomes more effective at higher levels of corrosion and better reproduces the induced damage at failure.

Upon the successful completion of the model validation, and improved confidence in the FE model capabilities, the model was used to perform a parametric study of design variables. The parametric test platform was specifically selected to test different ranges of shear-related variables. The stirrups within the critical section, located at a distance d_v from the load, were subjected to three different levels of corrosion. The data was studied regarding two aspects: i. shear mechanism and behaviour, and ii. Modified Compression Field Theory parameters from the CSA A23.3 equations. The parametric analysis included the study of the following beam characteristics:

- Load-deformation curves;
- Loss in shear strength;
- Loss in ductility;
- Beam stiffness and curvature relationship;
- Contribution to shear resistance from the steel and concrete; and
- Stress field and stress path evolution (principal compressive stresses of the concrete).

The data was further analyzed with respect to two MCFT parameters: crack angle θ and mid-height horizontal strain ε_x. This was done in an effort to study the precision of residual strength estimation using the code equations in the CSA A23.3 by modifying only the available shear reinforcement area.

In each of the cases, the data of the FE analysis was reorganized in an effort to highlight the effects of important parameters and identify trends within the data with respect to these parameters. From the study of the data, the following conclusions can be made:

1. A decrease in strength was encountered in each of the series with increasing corrosion levels.

2. A decrease in deformability was observed in each of the specimens at moderate and high levels of corrosion, whereas only some increase in relative peak deflection was observed at low levels of corrosion.
3. An initial decrease in stiffness was observed in each of the specimens, and with increasing levels of corrosion, the values approached the cracked section properties.
4. The shear span-to-depth ration a/d proved to impact the strength degradation mechanism, with higher effects on strength at smaller a/d ratios.
5. The beam width b_w did not show a large impact on the relative strength degradation, as it would have been expected from the prestrains introduced in the cracking model.
6. The effects of closer-spaced stirrups created better consistency in the results and less variation.
7. Closer-spaced stirrups also counteracted the negative effects of thinner members.
8. The contribution of steel towards shear resistance decreased with increasing corrosion damage, and consequently led to an increase in the concrete contribution.
9. The crack angle was a governing parameter on the steel contribution, and it was impacted significantly by the value of a/d.
10. Despite an increase in mid-height horizontal strain with increasing corrosion levels, the concrete contribution for corroded specimens increased relative to that of uncorroded ones.
11. A change in the stress field pattern was observed in nearly each of the specimens, with a prevailing indication of arching and tied-arch mechanisms for a/d ratios of 4 and 5.
12. The stress path indicated an increase in demand in regions located outside of the damaged areas.
13. In some cases, a softening of the crack angle was noted with increasing corrosion levels.
14. The effects of corrosion were not properly captured by the CSA A23.3 MCFT parameters θ (cracking angle) and ε_x (mid height horizontal strain).

The CSA A23.3 shear design equations were used to estimate the residual shear strength of the specimens by simply reducing the available steel area of the stirrups. These values were compared to the FE results in terms of total shear strength, steel contribution and concrete contribution, with the main conclusions being:

1. The CSA A23.3 detailed method was conservative in nearly each case, with the level of conservatism increasing for wider beams.
2. The CSA A23.3 simplified method was not as conservative as the detailed method, with more cases falling in the overestimation of strength.
3. For both methods, the steel contribution to shear resistance was over estimated.
4. On the contrary, the concrete contribution was under estimated in nearly each of the cases, with a greater divergence for wider members.

The main objective of this study was to help identify the effects of corroding stirrups on the behaviour and strength of RC beams in order to provide useful information for field assessment purposes. With the help of the literature review along with the important findings from the FE and parametric analysis, important things to consider when faced with such a problem are:

1. Accounting for the material deterioration of both the reinforcing steel and concrete.
2. Increase in damage leads to a lower stiffness that approaches the fully-cracked properties.
3. A change in stress distribution is imminent and should always be considered.
4. Stresses are distributed towards undamaged sections of an affected member.
5. The use of shear design equations should be used in combination with other methods. (e.g., strut-and-tie model)
6. If the strut-and-tie model is selected, the idealized truss system should be designed with respect to likely stress paths and avoiding damaged areas.
7. Multiple scenarios of reinforcement corrosion should be considered.

Higher vigilance is required when assessing the condition of an RC member affected by stirrup corrosion. The nature of shear failure should never be taken for granted or neglected even at high a/d ratios. The use of design equations for assessment should not be used without judgment; they do not directly account for corrosion damage.

7.2 Future Work

The assumptions taken to introduce corrosion-induced cracking into the two-dimensional FE model should be further tested in a three-dimensional analysis to account for the out-of-plane damage. Furthermore, the interaction of corrosion damage in the stirrups and longitudinal reinforcement (both tension and compression) should be further studied. The effect of corrosion on the bond interaction between steel and concrete would have to be accounted for to model corrosion of the longitudinal reinforcement. Mechanisms to investigate through numerical modeling are the shift from flexural to shear failure in RC beams affected by corrosion, the effect of bond loss along the longitudinal reinforcement on behavior, and the potential buckling of compression longitudinal reinforcement.

Upon further investigation of the effect of reinforcing steel corrosion on design parameters, specific assessment guidelines could be developed based on the current CSA A23.3 design framework, with parameters specifically modified to account for the concrete and steel deterioration.

References

ACI Committee 562 (2012). "Evaluation, Repair and Rehabilitaion." ACI 562-12, 61.

Azam, R., and Soudki, K. (2012). "Structural performance of shear-critical RC deep beams with corroded longitudinal steel reinforcement." *Cement & Concrete Composites*, 34(8), 946-957.

Azam, R. and Soudki, K. (2013). "Structural Behaviour of Shear-Critical RC Slender Beams with Corroded Properly Anchored Longitudinal Steel Reinforcement." J. Struct. Eng., 10.1061/(ASCE)ST.1943-541X.0000799 (Jan. 5, 2013).

Berto, L., Simioni, P., and Saetta, A. (2008). "Numerical modelling of bond behaviour in RC structures affected by reinforcement corrosion." *Engineering Structures*, 30(5), 1375-1385.

Cairns, J. (1995). "STRENGTH IN SHEAR OF CONCRETE BEAMS WITH EXPOSED REINFORCEMENT." *Proceedings of the Institution of Civil Engineers-Structures and Buildings*, 110(2), 176-185.

Cairns, J., Plizzari, G. A., Du, Y. G., Law, D. W., and Franzoni, C. (2005). "Mechanical properties of corrosion-damaged reinforcement." *ACI Materials Journal*, 102(4), 256-264.

CONTECVET (2001). "A validated Users Manual for Assessing the Residual Service Life of Concrete Structures." Geocisa & Instituto Eduardo Torroja.

Coronelli, D., and Gambarova, P. (2004). "Structural Assessment of Corroded Reinforced Concrete Beams: Modeling Guidelines." *Journal of Structural Engineering*, 130(8), 1214-1224.

CSA Committee S6 (2006). "Canadian Highway Bridge Design Code." Canadian Standards Association, Mississauga, ON, Canada.

CSA Comimitee A23.3-04 (2004). "Design of Concrete Structures." Canadian Standards Association, Mississauga, ON, Canada.

Dekoster, M., Buyle-Bodin, F., Maurel, O., and Delmas, Y. (2003). "Modelling of the flexural behaviour of RC beams subjected to localised and uniform corrosion." *Engineering Structures*, 25(10), 1333-1341.

Delcan (2011). "Assessment of the Champlain Bridge." The Jacques Cartier and Champlain Bridge Incorporated, 41.

El Maaddawy, T., Soudki, K., and Topper, T. (2005). "Analytical model to predict nonlinear flexural behavior of corroded reinforced concrete beams." *ACI Structural Journal*, 102(4), 550-559.

Gohier, P. (2011). "Montral is Falling Down." *Maclean's Magazine*, 26-29. Tuesday, August 23, 2011

Guzman, S., Galvez, J. C., and Sancho, J. M. (2011). "Cover cracking of reinforced concrete due to rebar corrosion induced by chloride penetration." *Cement and Concrete Research*, 41(8), 893-902.

H. Koch, G., P.H. Brongers, M., and G. Thompson, N. (2002). "Corrosion Cost and Preventive Stratagies in the United States." N. International, ed., U.S. Department of Transportation, 12.

Hanjari, K. Z., Lundgren, K., Plos, M., and Coronelli, D. (2013). "Three-dimensional modelling of structural effects of corroding steel reinforcement in concrete." *Structure and Infrastructure Engineering*, 9(7), 702-718.

Higgins, C., Farrow III, W. C., Potisuk, T., Miller, T. H., and Yim, S. C. (2003). "Shear Capacity Assessment of Corrosion-Damaged Reinforced Concrete Beams." G. R. Holcomb, S. D. Cramer, B. S. Covino, S. J. Bullard, M. Ziomek-Moroz, and S. A. Mathes, eds., Department of Civil Engineering, Oregon State University, Oregon Department of Transportation Research Unit, 200 Hawthorne Ave. SE, Suite B-240, Salem OR, 94301-5192 and Federal Highway Administration, 400 Seventh S. W., Washington DC 20590, 88 + Appendix.

Higgins, C., Farrow, W. C., III, and Turan, O. T. (2010). "Analysis of reinforced concrete beams with corrosion damaged stirrups for shear capacity." *Structure and Infrastructure Engineering*, 8(11).

Juarez, C. A., Guevara, B., Fajardo, G., and Castro-Borges, P. (2011). "Ultimate and nominal shear strength in reinforced concrete beams deteriorated by corrosion." *Engineering Structures*, 33(12), 3189-3196.

Kallias, A. N., and Rafiq, M. I. (2010). "Finite element investigation of the structural response of corroded RC beams." *Engineering Structures*, 32(9), 2984-2994.

Khan, I., Francois, R., and Castel, A. (2013). "Experimental and analytical study of corroded shear-critical reinforced concrete beams." *Materials and Structures*. 46(6), 899-910

Kobayashi, K. (2006). "The seismic behavior of RC members suffering from chloride-induced corrosion." Proceedings of the second fib Congress, Paper ID 19-3, Napoli, Italy.

MTO (2008). "Ontario Structures Inspection Manual (OSIM)." M. of Transportation, St. Catharines, Ontario.

NSERC (2012). "Impact Story." *Concrete Improvement*, http:// www.nsercpartnerships.ca/success-reussites/successstory-reussite-eng.asp?id=1003 (May 28, 2013).

Potisuk, T., Higgins, C. C., Miller, T. H., and Yim, S. C. (2011). "Finite element analysis of reinforced concrete beams with corrosion subjected to shear." *Advances in Civil Engineering*.

Stewart, M. G. (2009). "Mechanical behaviour of pitting corrosion of flexural and shear reinforcement and its effect on structural reliability of corroding RC beams." *Structural Safety*, 31(1), 19-30.

Suffern, C., El-Sayed, A., and Soudki, K. (2010). "Shear strength of disturbed regions with corroded stirrups in reinforced concrete beams." *Canadian Journal of Civil Engineering*, 37(8), 1045-1056.

Torres-Acosta, A. A., Fabela-Gallegos, M. J., Munoz-Noval, A., Vazquez-Vega, D., Hernandez-Jimenez, J. R., and Martinez-Madrid, M. (2004). "Influence of corrosion on the structural stiffness of reinforced concrete beams." *Corrosion*, 60(9), 862-872.

Val, D. V., and Chernin, L. (2012). "Cover cracking in reinforced concrete elements due to corrosion." *Structure and Infrastructure Engineering*, 8(6), 569-581.

Vecchio, F. J., and Shim, W. (2004). "Experimental and analytical reexamination of classic concrete beam tests." *Journal of Structural Engineering-ASCE*, 130(3), 460-469.

Wang, X. H., Gao, X. H., Li, B., and Deng, B. R. (2011). "Effect of bond and corrosion within partial length on shear behaviour and load capacity of RC beam." *Construction and Building Materials*, 25(4), 1812-1823.

Wong, P. S., and Vecchio. F.J. (2002). "VecTor2 and FormWorks User's Manual."

Yamamoto, T., Oyado, M., Mikata, Y., Kobayashi, K., and Shimomura, T. (2011). "Systematic Laboratory Test on Structural Performance of Corroded Reinforced Concrete and Its Utilization in Practice." *Modelling of Corroding Concrete Structures*, 5, 113-124.

Zhao, Y.-X., Chen, J., and Jin, W.-L. (2009). "Design of shear strengths of corroded reinforced concrete beams." International Journal of Modelling, Identification and Control, 7(2), 190-198.